ABSTRACT

Title of dissertation: BENCHMARKING CHARGE EXCHANGE THEORY IN THE DAWNING ERA OF SPACE-BORNE HIGH-RESOLUTION X-RAY SPECTROMETERS

Gabriele Latif Betancourt-Martinez,
Doctor of Philosophy, 2017

Dissertation directed by: Professor Christopher Reynolds
Department of Astronomy
Dr. F. Scott Porter
NASA/Goddard Space Flight Center

Charge Exchange (CX) is a process in which a highly charged ion captures one or more electrons from a neutral atom or molecule into an excited state during a close interaction. The electron's subsequent radiative cascade to the ground state produces diagnostic line emission in the X-ray band. CX with solar wind ions occurs frequently in the solar system, and CX may also occur astrophysically.

In order to properly identify CX in astrophysical spectra and make use of its diagnostic properties, we must be able to model the emission. Theoretical treatments of CX are often computationally expensive, experimental benchmarks at high resolution are fairly scarce, and there is often poor agreement between the two.

This dissertation seeks to build a better understanding of the mechanics and

spectral signatures of CX through high-resolution experimental data paired with theoretical calculations of CX. Chapter 1 outlines the necessary ingredients for modeling and identifying CX spectra, describes several astrophysical environments in which CX has been observed or postulated to occur, and presents some of the challenges we are facing in identifying and understanding this emission. Chapter 2 describes the theoretical and computational tools used in this work. Chapter 3 discusses the experimental tools and facilities we use, namely an Electron Beam Ion Trap (EBIT) and an X-ray microcalorimeter. Chapter 4 presents experimental K-shell data that highlights both the subtle nature of the CX interaction and the difficulty in including those nuances in spectral synthesis codes. Chapter 5 presents the first high-resolution L-shell CX spectra of Ne-like Ni and describes what we can learn from these results. In Chapter 6, we take these data a step further and present a pipeline to calculate relative state-selective capture cross sections, previously only available from theoretical modeling. We then compare some of our results to theory. In Chapter 7, we discuss several future steps for our work.

BENCHMARKING CHARGE EXCHANGE THEORY IN THE DAWNING ERA OF SPACE-BORNE HIGH-RESOLUTION X-RAY SPECTROMETERS

by

Gabriele Latif Betancourt-Martinez

Dissertation submitted to the Faculty of the Graduate School of the
University of Maryland, College Park in partial fulfillment
of the requirements for the degree of
Doctor of Philosophy
2017

Advisory Committee:
Professor Christopher Reynolds, Chair/Advisor
Dr. F. Scott Porter, Co-Chair/Advisor
Dr. Maurice Leutenegger, Co-Advisor
Professor Richard Mushotzky
Professor Alberto Bolatto
Professor Jordan Goodman, Graduate Dean's Representative

Preface

Some of the work presented in this thesis has been published in peer-reviewed journals or presented at national and international conferences. Portions of Chapter 3 were presented at the conference *SPIE Astronomical Instrumentation & Telescopes* as a poster in June 2014 [Betancourt-Martinez et al., 2014b] and as an oral presentation in June 2016. Much of chapter 4 was published in the journal *Physical Review A* as "Observation of highly disparate K shell x-ray spectra produced by charge exchange with bare mid-Z ions" [Betancourt-Martinez et al., 2014c]. Preliminary results from Chapter 4 were presented at the *American Astronomical Society* winter meeting in 2014 [Betancourt-Martinez et al., 2014a]. Some of this work was also presented at the conference of the *High Energy Astrophysics Division* of the *American Astronomical Society* in 2016 [Betancourt-Martinez et al., 2016]. The work presented in Chapters 5 and 6 is in preparation for submission to peer-reviewed journals.

The majority of this research was supported by a NASA Space Technology Research Fellowship.

Work at the Lawrence Livermore National Laboratory was performed under the auspices of the U.S. Department of Energy under Contract DE-AC52-07NA27344 and supported by NASA APRA grants to LLNL and NASA/GSFC.

To Rosella Clemmons Washington and Dr. Margaret Anne Cyrus Mills: two strong, brilliant women who I know have been cheering me on from afar.

Acknowledgments

Well, I wasn't always sure that I'd actually get to this point, but here I am, and with an exciting new adventure ahead of me to boot. As cliché as it sounds, I could not have gotten here without many wonderful people on my side to help encourage, guide, and support me.

Maurice: I realized early on that I got really lucky to have you as an advisor. Thank you for being so generous with your time and your vast sea of knowledge, which you always share with extreme patience, genuine excitement, and good humor. I've appreciated the guidance, mentorship, feedback, sharing of data and codes, company at conferences, explanations of random pop culture references that I've missed, and your being solid company (along with Renata) at a Livermore bar on that most dismal night in November 2016.

Chris, thank you for always having my back and making sure that I'm not only productive, but happy. You've always been willing to step in when the situation merits it, and offer a kind and sympathetic ear along with good advice when I've had a rough patch. It's meant so much to know that I can always count on your support.

Scott: you've always looked out for my professional development, and for that I've always been grateful. Thank you for sending me to White Sands for the XQC rocket launch, for making sure I can attend conferences when I want to, for your succinct answers to my science questions, and for opening up research doors and career paths, even when I've been unsure of what direction I want to take.

To the TES team: I'm really glad I got to learn and grow in such a friendly environment. Steve, Joe, Megan, and Simon: special shout-out to you guys for showing me the ropes in the lab. Megan, thank you for always being there for advice and editing help, and for your friendship.

Renata, my fellow nature lover: I so appreciate you for busting your butt to get those MCLZ results in time for my thesis, for being available any time of the day or night for discussions about CX theory, and for the moral support during this process. And from dance classes to random adventures in which we hugged redwoods and did not fall off the side of a mountain—I'm glad to count you not just as a colleague, but also as a friend.

Now onto the EBIT crew. To Greg: thanks for allowing me the opportunity to spend a small chunk of my life at EBIT. I learned a ton, got interesting data, and even managed to have a good amount of fun. I also appreciate the nudges to think more deeply about my analysis, to make my proposals more rigorous, and to finish this thesis when I said I would. Tom: thanks for tag-teaming the CX data acquisition with me, and for staying later than you really needed to just to get me a few more hours of counts. Also thanks for late night lab dance parties, the peanut butter that I stole, the song suggestions and Instagram memes, and for being just as weird as I am. Natalie, thank you for all the figures, the EBIT facts, and the lab gossip. And thanks, Ed and David, for keeping things running smoothly at EBIT while I was there, and for helping us to make whatever weird ideas we had to make the atomic H source work better a reality.

To my fellow "second years:" thanks for showing up for my Fall Into Falls and

Spring Into Springs, for the pie days, salad bowls, and fancy dress parties, and for not hating me when I sent what seemed like a total jerk email about the quals. Krista and Ashlee, or the other 2/3 of the Peanut Butter Patties/Paddies/Padis: you both are rockstars, and I'm really lucky to have had you around as officemates, advice-givers, cheerleaders, workout buddies, travel companions, puppy/kitty-time givers, and obviously, friends.

Rafael and the other Gabriele: thanks for being such fun officemates at Goddard, and no thanks for all the pressure to drink more coffee!

I'm lucky to have found (in undergrad!) smart, caring, and inspiring astrophysicists who also happen to be boricuas. Héctor Arce: thank you for believing in me as a wet-behind-the-ears sophomore, taking me under your wing, and giving me the chance to start my research career with you. I'm honored and proud to still call you my mentor. Tali Figueroa: thank you for seeking me out to join your group for a summer, introducing me to the exciting world of calorimeters, and providing a warm and enriching environment in which to learn.

To my non-grad school friends, who probably won't read this: thanks for keeping me grounded, traveling, dancing, and laughing.

Thank you to my extended family, both related by blood and chosen, for celebrating my victories with me as if they were your own, for pushing me to be better, and for your unconditional love.

Lastly, to my parents, Mamita and Papito: Thank you for supporting me throughout this long haul of a journey, and for sacrificing for and always prioritizing my education—from Kindermusik, piano, and horseback riding, to Montessori,

Westtown, and Yale, plus all the camps and activities in between. Thank you for helping me get here, and for being there for all that I've been through in the last six years, grad-school related or otherwise. You were around to help me buy my first car, you celebrated with me when I won fellowships or acquired jobs, you helped me heal from heartbreak (twice), and you are always around to give me a quick hug from the train platform as I'm passing through Wilmington on the way up or down the East Coast. You came to cheer me on at my first triathlon, you gave me advice on personality clashes, and Mamita, you didn't even hesitate to rush down to Silver Spring with the ingredients for chicken soup when I got super sick. You guys remind me where I came from, who I am, and who I can be. Thank you for being an endless source of love, support, wisdom, and a deep sense of home. I love and appreciate you more than you'll ever know.

Table of Contents

Preface ii

Dedication iii

Acknowledgements iv

List of Tables xi

List of Figures xii

List of Abbreviations xviii

1 Charge Exchange: an Introduction 1
- 1.1 Charge Exchange Basics . . . 4
- 1.2 Introduction to Charge Exchange Theory . . . 7
- 1.3 Theoretical Approximations . . . 11
- 1.4 Spectroscopic Observables . . . 14
- 1.5 Charge Exchange in Astronomy . . . 25
  - 1.5.1 Solar System . . . 25
  - 1.5.2 Astrophysical and Other CX . . . 30
- 1.6 Diagnostic Utility . . . 32
- 1.7 The Challenge . . . 36

2 Theoretical and Computational Tools for Simulating and Understanding CX 42
- 2.1 FAC, the Flexible Atomic Code . . . 42
- 2.2 Charge Exchange Models: SPEX-CX and ACX . . . 44
- 2.3 Multi-Channel Landau Zener Theory . . . 48

3 The Role of Laboratory Astrophysics in Improving Charge Exchange Models 57
- 3.1 The LLNL Electron Beam Ion Trap . . . 57
- 3.2 The EBIT Calorimeter Spectrometer . . . 64
  - 3.2.1 X-ray Microcalorimeter Basics . . . 65
  - 3.2.2 The EBIT Calorimeter Spectrometer . . . 78

3.2.3 ECS Data Acquisition and Analysis . . . 80
3.2.3.1 ECS Filters and Windows . . . 83
3.2.3.2 Absorber . . . 86
3.2.3.3 Amplification, Filtering, and Digitization . . . 86
3.2.3.4 The Software Calorimeter Digital Processor . . . 88
3.2.3.5 Triggering . . . 88
3.2.3.6 Optimal Filtering . . . 89
3.2.3.7 Event Grades and Instrumental Response . . . 91
3.2.3.8 Gain Scale . . . 92
3.2.3.9 Final Analysis . . . 94
3.3 The Transition-Edge EBIT Calorimeter Spectrometer . . . 94
3.3.1 Technical Specifications . . . 97
3.3.2 Device Readout . . . 100
3.3.3 TEMS Cooling System . . . 103
3.3.4 Current Status of TEMS and Outlook . . . 103

4 Observation of Highly Disparate K Shell X-ray Spectra Produced by Charge Exchange with Bare Mid-Z ions 107
4.1 Introduction . . . 107
4.2 Experimental Method . . . 112
4.3 Analysis and Spectra . . . 114
4.4 Discussion . . . 116
4.5 Acknowledgments . . . 123

5 High-Resolution Spectra of L-Shell Charge Exchange with Ne-like Ni 125
5.1 Introduction . . . 125
5.2 Experimental Method . . . 128
5.3 Analysis . . . 132
5.4 Spectra . . . 138
5.5 Summary . . . 150

6 L-shell Ni CX: Comparisons to Models and Relative Capture Cross Section Calculations 152
6.1 Introduction . . . 152
6.2 Comparisons to Spectral Models . . . 153
6.3 A Pipeline to Extract State-Selective Relative Cross Sections from Spectra: Method . . . 171
6.4 Cross Section Calculations: Result for S+He . . . 180
6.5 K-shell S+He Cross Sections: Pipeline Model Comparison to MCLZ Calculations . . . 185
6.6 Cross Section Calculations: Result for $Ni^{19+}+H_2$ . . . 190
6.7 Summary . . . 202

7 Outlook 205

A Spectral Basis Set Elements for Model Fit to S+He CX Data 208

B Spectral Basis Set Elements for Model Fit to Ni+H_2, Ni+He CX Data 219

C X-Ray Emission Mechanisms 232

Bibliography 241

List of Tables

3.1 Comparison between the ECS and the TEMS. 97

4.1 Summary of the normalized H-like series line strengths and hardness ratios for the experiments presented in Chapter 4 118
4.2 Summary of the normalized He-like series line strengths for the experiments presented in Chapter 4 119

5.1 CX lines identified in this work. 146
5.2 DE and model lines identified in this work. 147

List of Figures

1.1 Illustration of the CX interaction. . . . 5
1.2 Radiative decay paths from electron capture into a bare ion at low collision energy. . . . 16
1.3 Radiative decay paths from electron capture into a bare ion at high collision energy 17
1.4 CTMC-calculated spectra for CX between bare O and H at various collision velocities. . . . 18
1.5 Radiative decay paths from electron capture into a H-like ion assuming capture into a singlet state. . . . 21
1.6 Radiative decay paths from electron capture into a H-like ion assuming capture into triplet states. . . . 22
1.7 EBIT spectra resulting from collisional (direct) excitation (DE, top) and CX (bottom) of bare and H-like S with He. . . . 23
1.8 Simulated spectra using the XSPEC APEC model for an ionized thermal plasma, and the AtomDB CX (ACX) model to represent the CX emission. . . . 24
1.9 CX spectra with the same ion and different neutrals. . . . 35

2.1 Schematic of the CX collision along diabatic and adiabatic potential energy curves. . . . 49
2.2 One pseudocrossing p between initial potential state 1 and final potential state 2. . . . 53
2.3 N-1 pseudocrossings between N potential states, where each p_n represents a pseudocrossing happening between the initial state and final state n. . . . 54

3.1 Schematic of the LLNL EBIT-I. . . . 60
3.2 Sketch of the trap region of the LLNL EBIT-I. . . . 61
3.3 Schematic of an ideal microcalorimeter. . . . 68
3.4 Schematic of an X-ray pulse from an ideal microcalorimeter. . . . 70
3.5 A simplified calorimeter bias circuit diagram for a Si-thermistor device. 76
3.6 The ECS cryogenic package. . . . 81

3.7 Image of the ECS detector chip. . . . 82
3.8 Filter transmission for the ECS optical and thermal blocking filters, and optional windows along the ECS line of sight. . . . 84
3.9 Quantum efficiency for the absorbers on the ECS. . . . 87
3.10 Sketch of the gain calibration procedure and gain curve for the ECS. 93
3.11 The resistance vs. temperature curve of five pixels in the TEMS array. 98
3.12 A kilopixel array like the one currently used in the TEMS. . . . 99
3.13 Circuit diagram for a 2-row × 2-column time-division SQUID multiplexer. . . . 101
3.14 The current NIST-developed TEMS focal plane assembly. . . . 102
3.15 Spectral resolution of all multiplexed pixels in TEMS. . . . 104
3.16 FWHM energy resolution of 2.35 eV at 6 keV for one pixel in the current TEMS detector array. . . . 105

4.1 Spectrum of bare argon undergoing CX with neutral argon. . . . 116
4.2 Spectra from bare Mg undergoing CX with four different neutral gases. 117
4.3 S^{16+} and He charge exchange. . . . 117
4.4 Hardness ratio as a function of the atomic number of the ion. . . . 121
4.5 Hardness ratio as a function of the ionization potential and the number of valence electrons of the neutral gas. . . . 122

5.1 Measured X-ray energy as a function of the EBIT cycle. . . . 130
5.2 X-ray filter transmission. . . . 134
5.3 Signal and background signals during a CX experiment. . . . 137
5.4 Spectra of Ni^{19+} created in DE and CX of Ni^{19+}+H_2, from 850–1175 eV. . . . 139
5.5 Spectra of Ni^{19+} created in DE and CX of Ni^{19+}+H_2, from 1175–1550 eV. . . . 140
5.6 Spectra of Ni^{19+} created in DE and CX of Ni^{19+}+He, from 850–1175 eV. . . . 141
5.7 Spectra of Ni^{19+} created in DE and CX of Ni^{19+}+He, from 1175–1550 eV. . . . 142
5.8 CX spectra of Ni^{19+}+H_2 and Ni^{19+}+He. . . . 144

6.1 SPEX-CX model and ACX models plotted against Ni^{19+}+H_2 EBIT CX data. . . . 155
6.2 SPEX-CX model and ACX models assuming CX with atomic H plotted against Ni^{19+}+H_2 EBIT CX data, from 888 eV–1048 eV. . . . 157
6.3 Same as Figure 6.2, but for 1048 eV–1210 eV. . . . 158
6.4 Same as Figure 6.2, but for 1210 eV–1368 eV. . . . 159
6.5 Same as Figure 6.2, but for 1368 eV–1528 eV. . . . 160
6.6 Identifications of high-n CX lines assuming energies as calculated by FAC. . . . 162
6.7 Comparison of high-n lines in the Ni^{19+}+H_2 CX data and the two ACX models. . . . 163

6.8 SPEX-CX model and ACX models assuming CX with atomic H plotted against Ni^{19+}+He EBIT CX data. . . . 164
6.9 SPEX-CX model and ACX models assuming CX with atomic H plotted against Ni^{19+}+He EBIT CX data, from 888 eV–1048 eV. . . . 166
6.10 Same as Figure 6.9, but for 1048 eV–1210 eV. . . . 167
6.11 Same as Figure 6.9, but for 1210 eV–1368 eV. . . . 168
6.12 Same as Figure 6.9, but for 1368 eV–1528 eV. . . . 169
6.13 ACX models assuming CX with He plotted against Ni^{19+}+He EBIT CX data. . . . 170
6.14 ACX models assuming CX with He plotted against Ni^{19+}+He EBIT CX data, from 888 eV–1048 eV. . . . 172
6.15 Same as Figure 6.14, but for 1048 eV–1210 eV. . . . 173
6.16 Same as Figure 6.14, but for 1210 eV–1368 eV. . . . 174
6.17 Same as Figure 6.14, but for 1368 eV–1528 eV. . . . 175
6.18 Simulated L-shell spectra for capture into Ne-like Ni configurations $2p_{1/2}9s_{1/2}(J=0)$ and $2p_{1/2}9s_{1/2}(J=1)$. . . . 178
6.19 Model fit to the data for H- and He-like S+He CX. . . . 182
6.20 Relative n,l,j-resolved capture cross sections for H-like S+He CX. . . . 183
6.21 Relative n,l,j,J-resolved capture cross sections for He-like S+He CX. 184
6.22 Normalized relative cross sections as obtained with our pipeline and fitting procedure and MCLZ calculations for CX between H-like S and neutral He. . . . 187
6.23 Simulated spectrum from MCLZ calculations compared to data. . . . 189
6.24 Data, model fit to the data, and fit residuals for CX between Ni^{19+} and H_2, for the M2 and 3G lines assuming only a $2p_{3/2}$ core hole. . . . 192
6.25 Data, model fit to the data, and fit residuals for CX between Ni^{19+} and H_2, for lines with energies between 890–1530 eV, assuming only a $2p_{3/2}$ core hole. . . . 193
6.26 Data, model fit to the data, and fit residuals for CX between Ni^{19+} and H_2, for the M2 and 3G lines, including all three core hole configurations. . . . 196
6.27 Data, model fit to the data, and fit residuals for CX between Ni^{19+} and H_2, for lines with energies between 890–1530 eV, including states with all three core hole configurations. . . . 197
6.28 State-selective cross sections extracted from the model fit to Ni^{19+} and H_2 data, for states with a $2p_{3/2}$ core hole. . . . 199
6.29 State-selective cross sections extracted from the model fit to Ni^{19+} and H_2 data, for states with a $2p_{1/2}$ core hole. . . . 200
6.30 State-selective cross sections extracted from the model fit to Ni^{19+} and H_2 data, for states with a $2s_{1/2}$ core hole. . . . 201

A.1 Cascade spectrum of H-like S with initial electron configuration $8s_{1/2}$. 209
A.2 Cascade spectrum of H-like S with initial electron configuration $7s_{1/2}$. 209
A.3 Cascade spectrum of H-like S with initial electron configuration $8p_{3/2}$. 210
A.4 Cascade spectrum of H-like S with initial electron configuration $7p_{3/2}$. 210

A.5 Cascade spectrum of H-like S with initial electron configuration $8d_{3/2}$. 211
A.6 Cascade spectrum of H-like S with initial electron configuration $8f_{5/2}$. 211
A.7 Cascade spectrum of H-like S with initial electron configuration $8f_{7/2}$. 212
A.8 Cascade spectrum of He-like S with initial electron configuration $1s_{1/2}6s_{1/2}(J=0)$. . . . 212
A.9 Cascade spectrum of He-like S with initial electron configuration $1s_{1/2}7s_{1/2}(J=0)$. . . . 213
A.10 Cascade spectrum of He-like S with initial electron configuration $1s_{1/2}6s_{1/2}(J=1)$. . . . 213
A.11 Cascade spectrum of He-like S with initial electron configuration $1s_{1/2}7p_{1/2}(J=1)$. . . . 214
A.12 Cascade spectrum of He-like S with initial electron configuration $1s_{1/2}6p_{3/2}(J=1)$. . . . 214
A.13 Cascade spectrum of He-like S with initial electron configuration $1s_{1/2}7p_{3/2}(J=1)$. . . . 215
A.14 Cascade spectrum of He-like S with initial electron configuration $1s_{1/2}7d_{3/2}(J=1)$. . . . 215
A.15 Cascade spectrum of He-like S with initial electron configuration $1s_{1/2}7d_{3/2}(J=2)$. . . . 216
A.16 Cascade spectrum of He-like S with initial electron configuration $1s_{1/2}7d_{5/2}(J=2)$. . . . 216
A.17 Cascade spectrum of He-like S with initial electron configuration $1s_{1/2}7d_{5/2}(J=3)$. . . . 217
A.18 Cascade spectrum of He-like S with initial electron configuration $1s_{1/2}4p_{3/2}(J=1)$. . . . 217
A.19 Cascade spectrum of He-like S with initial electron configuration $1s_{1/2}5p_{3/2}(J=1)$. . . . 218
A.20 Cascade spectrum of He-like S with initial electron configuration $1s_{1/2}7f_{7/2}(J=3)$. . . . 218

B.1 Cascade spectrum of Ne-like Ni with initial electron configuration $2p_{3/2}8s_{1/2}(J=1)$. . . . 220
B.2 Cascade spectrum of Ne-like Ni with initial electron configuration $2p_{3/2}9s_{1/2}(J=1)$. . . . 220
B.3 Cascade spectrum of Ne-like Ni with initial electron configuration $2p_{3/2}10s_{1/2}(J=1)$. . . . 221
B.4 Cascade spectrum of Ne-like Ni with initial electron configuration $2p_{3/2}11s_{1/2}(J=1)$. . . . 221
B.5 Cascade spectrum of Ne-like Ni with initial electron configuration $2p_{3/2}11p_{1/2}(J=1)$. . . . 222
B.6 Cascade spectrum of Ne-like Ni with initial electron configuration $2p_{3/2}11p_{3/2}(J=1)$. . . . 222
B.7 Cascade spectrum of Ne-like Ni with initial electron configuration $2p_{3/2}9d_{5/2}(J=1)$. . . . 223

B.8 Cascade spectrum of Ne-like Ni with initial electron configuration as one or a combination of $2p_{3/2}8f_{5/2}(J=2)$, $2p_{3/2}9f_{5/2}(J=2)$, $2p_{3/2}10f_{7/2}(J=2)$, $2p_{3/2}11f_{7/2}(J=2)$, $2p_{3/2}8g_{7/2}(J=3)$, $2p_{3/2}9g_{7/2}(J=3)$, $2p_{3/2}10g_{7/2}(J=3)$, or/and $2p_{3/2}11g_{7/2}(J=3)$. 223
B.9 Cascade spectrum of Ne-like Ni with initial electron configuration as one or a combination of $2p_{3/2}8f_{7/2}(J=2)$, $2p_{3/2}9f_{7/2}(J=2)$, $2p_{3/2}10f_{5/2}(J=2)$, $2p_{3/2}11f_{5/2}(J=2)$, $2p_{3/2}8g_{9/2}(J=3)$, $2p_{3/2}9g_{9/2}(J=3)$, $2p_{3/2}10g_{9/2}(J=3)$, or/and $2p_{3/2}11g_{9/2}(J=3)$. 224
B.10 Cascade spectrum of Ne-like Ni with initial electron configuration as one or a combination of $2p_{3/2}8f_{5/2}(J=4)$, $2p_{3/2}9f_{5/2}(J=4)$, $2p_{3/2}10f_{5/2}(J=4)$, $2p_{3/2}11f_{5/2}(J=4)$, $2p_{3/2}8g_{7/2}(J=5)$, $2p_{3/2}9g_{7/2}(J=5)$, $2p_{3/2}10g_{7/2}(J=5)$, or/and $2p_{3/2}11g_{7/2}(J=5)$. 225
B.11 Cascade spectrum of Ne-like Ni with initial electron configuration as one or a combination of $2p_{3/2}8f_{5/2}(J=4)$, $2p_{3/2}9f_{5/2}(J=4)$, $2p_{3/2}10f_{5/2}(J=4)$, $2p_{3/2}11f_{5/2}(J=4)$, $2p_{3/2}8g_{7/2}(J=5)$, $2p_{3/2}9g_{7/2}(J=5)$, $2p_{3/2}10g_{7/2}(J=5)$, or/and $2p_{3/2}11g_{7/2}(J=5)$. 226
B.12 Cascade spectrum of Ne-like Ni with initial electron configuration $2p_{3/2}7s_{1/2}(J=1)$. 226
B.13 Cascade spectrum of Ne-like Ni with initial electron configuration $2p_{1/2}8s_{1/2}(J=1)$. 227
B.14 Cascade spectrum of Ne-like Ni with initial electron configuration $2p_{1/2}8s_{1/2}(J=1)$. 227
B.15 Cascade spectrum of Ne-like Ni with initial electron configuration $2p_{1/2}8d_{5/2}(J=3)$, $2p_{1/2}9d_{5/2}(J=3)$, $2p_{1/2}10d_{5/2}(J=3)$, $2p_{1/2}11d_{5/2}(J=3)$. 228
B.16 Cascade spectrum of Ne-like Ni with initial electron configuration $2p_{1/2}9f_{5/2}(J=2)$. 228
B.17 Cascade spectrum of Ne-like Ni with initial electron configuration one or a combination of $2p_{1/2}8d_{5/2}(J=3)$, $2p_{1/2}9d_{5/2}(J=3)$, $2p_{1/2}10d_{5/2}(J=3)$, $2p_{1/2}11d_{5/2}(J=3)$, $2p_{1/2}8f_{7/2}(J=4)$, $2p_{1/2}9f_{7/2}(J=4)$, $2p_{1/2}10f_{7/2}(J=4)$, $2p_{1/2}11f_{7/2}(J=4)$, $2p_{1/2}8g_{9/2}(J=5)$, $2p_{1/2}9g_{9/2}(J=5)$, $2p_{1/2}10g_{9/2}(J=5)$, or/and $2p_{1/2}11g_{9/2}(J=5)$. 229
B.18 Cascade spectrum of Ne-like Ni with initial electron configuration $2p_{1/2}6d_{3/2}(J=1)$. 230
B.19 Cascade spectrum of Ne-like Ni with initial electron configuration $2p_{1/2}9d_{3/2}(J=1)$. 230
B.20 Cascade spectrum of Ne-like Ni with initial electron configuration $2s_{1/2}11s_{1/2}(J=0)$. 231
B.21 Cascade spectrum of Ne-like Ni with initial electron configuration $2s_{1/2}11d_{5/2}(J=2)$. 231

C.1 Radiative cascade. 233
C.2 Scattering of X-ray light by a neutral. 233
C.3 Bremmstrahlung. 234
C.4 Collisional excitation by electron impact. 235

C.5 Photoexcitation. 235
C.6 Collisional ionization. 236
C.7 Photoionization. 237
C.8 Autoionization. 237
C.9 Auger ionization. 238
C.10 X-ray fluorescence. 238
C.11 Radiative recombination. 239
C.12 Dielectronic recombination. 240

List of Abbreviations

AOCC	Atomic Orbital Close Coupling
CAP	Calorimeter Analog Processor
COB	Classical Over-the-Barrier
CTMC	Classical Trajectory Monte Carlo
CX	Charge Exchange
DE	Direct Excitation
EBIT	Electron Beam Ion Trap
ECS	EBIT Calorimeter Spectrometer
ESA	European Space Agency
FAC	Flexible Atomic Code
GSFC	Goddard Space Flight Center
ICM	Intracluster Medium
ISM	Interstellar Medium
JAXA	Japan Aerospace eXploration Agency
JFET	Junction gate Field-Effect Transistor
LLNL	Lawrence Livermore National Laboratory
LTE	Long Term Enhancement
MCLZ	Multi-Channel Landau Zener
MEC	Multi-Electron Capture
NASA	National Aeronautics and Space Administration
NEP	Noise Equivalent Power
NIST	National Institute of Standards and Technology
QE	Quantum Efficiency
QMOCC	Quantum Molecular Orbital Close Coupling
SCDP	Software Calorimeter Data Processor
SEC	Single Electron Capture
SQUID	Superconduting QUantum Interference Device
SWCX	Solar Wind Charge Exchange
TDM	Time Domain Multiplexing
TEMS	Transition-edge EBIT Microcalorimeter Spectrometer
TES	Transition Edge Sensor
XARM	X-ray Astrophysics Recovery Mission

Chapter 1: Charge Exchange: an Introduction

Around 3am on a late-January night, the Japanese amateur astronomer Yuji Hyakutake decided to trudge back up the mountain where he made his first discovery as a comet-hunter. The weather was supposed to get better soon, and he wanted to re-photograph his comet. But when he looked up with his plate-sized binoculars, he saw an object in the sky that he had not seen before. Late the next morning, he faxed a report to experts in order to confirm his observation. A cometary expert verified the sighting, and the media latched on; Hyakutake's accidental discovery of the comet that would soon bear his name would bring him so much fame that for some time, he and his wife could not make telephone calls due to the number of incoming press calls to their home. [Telescope, 2004, Times, 2002, Lab, 1996]

Three months later, Comet Hyakutake, shining as bright as a star and leaving a 62,000-mile long tail in its wake, made its closest approach to Earth. It was near enough that patient watchers could detect its motion against the stars using just their eyes. But Comet Hyakutake would not only be remembered for its dramatic show in the night sky.

Years before, scientists had predicted the generation of X-rays from comets due to collisions between particles released by the comet as it approached the sun

and dust in the solar system [Ibadov, 1990]. Even before that, scientists detected high-energy electrons in the atmosphere surrounding a comet when they performed a flyby observation, suggesting that a process energetic enough to create X-rays may be occurring in the coma [Kirsch et al., 1988]. Armed with this background and motivated by the close approach of comet Hyakutake, Carey Lisse and his team proposed to observe the comet with the ROSAT X-ray satellite. And with this observation, comet Hyakutake made the news again: it was the first comet caught emitting X-rays [James, 1998, Lisse et al., 1996].

The discovery came as a surprise to the astronomical community, and prompted a surge of interest in determining the cause of the emission (e.g., Krasnopolsky [1997], Bingham et al. [1997], Northrop et al. [1997], Haberli et al. [1997]). X-rays are typically observed from hot and extreme objects, like black hole accretion disks or shock-heated gas in supernova remnants—objects and environments that are millions of degrees. Comets, however, have temperatures that are well below freezing [Krankowsky et al., 1986]. How could an object this cold produce such a large amount of energetic light?

About a year after the 1996 ROSAT observation, Cravens [1997] identified the answer. In contrast to a million-degree object producing thermal X-rays, cometary X-rays are produced by a process well-known to plasma physicists but relatively unfamiliar to astronomers called charge exchange (CX). CX is a close interaction between highly charged ions and neutral atoms or molecules wherein the ions capture electrons from the neutral into an excited quantum state. The electrons then cascade down to the ground state, generating X-rays and other radiation. In the case of

comets, the ions are supplied by the solar wind, and the neutral species begin frozen in the surface of the comet, and sublimate away as the comet approaches the sun.

Since this surprising discovery, and as we learn more about its unique spectral signatures and likelihood of occurrence throughout the universe, CX has become a popular explanation for anomalous X-ray emission in astrophysical environments (see Section 1.5). However, upon closer inspection, it is becoming clear that we cannot blindly trust even the best CX models to accurately represent our observational data. There are many open questions regarding the underlying atomic physics behind CX that lead to its unique spectral features, described in the following chapters, that we must address through further experimentation and improved modeling.

This dissertation seeks to build a better understanding of the mechanics and diagnostics of CX through the marriage of these two subfields: high-resolution experimental data together with theoretical calculations of CX. In the rest of Chapter 1, we outline the necessary ingredients for modeling and identifying CX spectra, describe several astrophysical environments in which CX has been observed or postulated to occur, and present some of the challenges we are facing in identifying and understanding this emission. In Chapter 2, we describe the theoretical and computational tools used in this work. Chapter 3 dives into the experimental tools and facilities we use, namely an Electron Beam Ion Trap (EBIT) and an X-ray microcalorimeter. We also describe an instrument in development that will allow us to perform these measurements faster and with better resolution than previously possible. Chapter 4 presents experimental K-shell ($n = x \rightarrow 1$ transitions) data that highlight both the subtle nature of the CX interaction and the difficulty in

including those nuances in spectral synthesis codes. Chapter 5 presents the first high-resolution L-shell ($n = x \rightarrow 2$ transitions) CX spectra of Ne-like Ni and describes what we can learn from these results. In Chapter 6, we take these data a step further and present a pipeline to calculate relative state-selective capture cross sections, previously only available from intensive theoretical modeling. We then compare some of our results to existing theory. In Chapter 7, we discuss where we will go next. Finally, the appendices present supplemental information: Appendies A and B present the individual spectra used in the models described in Chapter 6 for S^{16+}+He and N^{19+}+H_2, respectively, and Appendix C serves as a refresher on various X-ray emission mechanisms discussed in this work.

1.1 Charge Exchange Basics

Charge exchange (CX), sometimes referred to as charge transfer, is a semi-resonant process in which a highly charged ion captures one or more electrons from a nearby neutral atom or molecule during a close interaction. After being captured, the electron(s) relax to the ground state through a radiative cascade, emitting one or more photons. It can be represented as

$$A^{q+} + B \rightarrow A^{(q-m)+} + B^{m+}, \tag{1.1}$$

where A is the highly charged ion with charge q, B is the neutral species, and m is the number of captured electrons. A pictorial representation of this interaction assuming single electron capture (SEC) is shown in Figure 1.1.

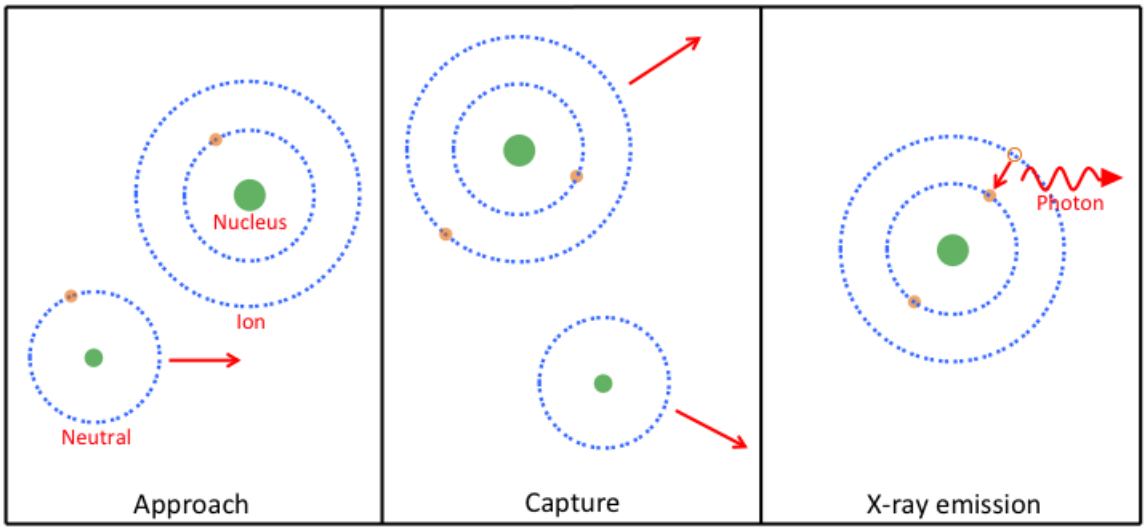

Figure 1.1 Illustration of the CX interaction. The process can generally be described in three steps: an ion and neutral approach each other, the ion captures one or more electrons from the neutral into a highly excited state, and then those electrons radiatively cascade to the ground state. Figure drawn in the style of the CX figure in http://chandra.harvard.edu/xray_sources/solar_system.html.

During the CX interaction, as the ion and neutral approach, their electric fields are superposed, distorting the individual energy levels. At certain internuclear distances, the energy levels of the ion and neutral overlap. It is at this so-called curve crossing that the electron(s) from the neutral will non-radiatively transfer to the ion [Wargelin et al., 2008]. There are several curve crossings at different internuclear distances, so electron(s) can be captured into different quantum states. Because the electron(s) keep approximately the same binding energy during the transfer, capture is often into a highly excited quantum state of the ion [Smith et al., 2014b] (see Equation 1.2). The details of the electron capture depend on the ion and neutral species, the collision energy, and the number of electrons transferred [Janev and Winter, 1985]; other quantities may also be important, but their effects are difficult to disentangle (see Chapter 4).

Typical total cross sections for CX can be approximated by $\sigma_{CX} \sim q \times 10^{-15}$, where q is the charge of the ion [Wargelin et al., 2008]; for astrophysical plasmas, they are often on the order of 10^{-14} to 10^{-15} cm^2, depending on the collision energy and reaction pair [Gu et al., 2016]. This is very large compared to, for example, collisional ionization, which, using Fe K-shell excitation as an example, is on the order of 10^{-22} cm^2 [Krasnopolsky et al., 2004, Stancil et al., 2002, Cravens, 2002, Gilbody, 1986]. For this reason, it is vital to consider the contribution of CX in any astrophysical spectrum measured from an environment in which hot plasmas interact with cool gas. See Section 1.5 for more information on the astrophysical relevance of CX.

In order to properly identify the CX component in astrophysical and laboratory

spectra, we must be able to model (1) the state-selective (i.e., n, l, j, J-resolved in jj-coupling or n, L, S-resolved in LS coupling) cross section of the captured electron (what is its initial quantum state?), as well as (2) its subsequent radiative decay to the ground state (what are the energies of the X-rays that the electron emits during its downward cascade?). (2) is relatively straightforward given the initial distribution of n and l capture states, requiring only accurate atomic data and quantum mechanical selection rules (though obtaining accurate atomic data is not necessarily trivial). The bigger challenge lies in (1): though CX is a conceptually simple process, a detailed theoretical understanding of the subtleties involved can be daunting. Several theoretical methods have been developed to calculate total and state-selective cross sections, with variations in accuracy and utility when applied to different environments. The modeling efforts used in this dissertation are described more completely in Chapter 2; here, I give a brief overview of some of the most common theoretical methods applied to CX.

1.2 Introduction to Charge Exchange Theory

Several parameters influence the aforementioned variations in accuracy and utility between theoretical methods. A primary parameter is the collision velocity: the details of the close interaction between the ion and the neutral as they approach just before, during, and after electron capture are highly velocity-dependent. This strongly affects the distribution of angular momentum state(s) l for the captured electron(s).

Low velocity collisions, where $v \ll v_0$ (where v is the collision velocity and v_0 is the classical velocity of the bound electron) are in the "adiabatic region" [Janev, 1983]. This region is applicable to the experimental CX data presented in this dissertation, and is explained in more detail in Section 2.3. In these slow collisions, the ion-neutral system can be seen as a pseudomolecule that shares the electron during the collision. In this case, the key parameters are the various initial (pre-electron transfer) and final (post-electron transfer) potential energy curves of the pseudomolecule and how they interact [Janev et al., 1985]. At intermediate velocities ($v \sim v_0$), the number of potential final states (also called reaction channels) increases. This is significant because to determine the final reaction channel, one must consider the interaction of all possible states. At these velocities, the fractional amount of time that the electron is in a shared state decreases as compared to collisions at low velocities; the electron is mostly bound to one particle. It is thus more accurate to represent this collision as an ensemble of atomic states. At high velocities ($v/v_0 \sim 3-4$), neighboring potential final states couple more strongly, and in some cases, the electron can be transferred to the continuum [Janev et al., 1985]. In general, theories that consider the pseudomolecular state of the ion-neutral pair better describe slow CX collisions. The most accurate codes for the higher energy ranges consider how discrete atomic and/or continuum states interact [Janev et al., 1985].

Besides the relative velocity of the collision, two other parameters affect the detailed interaction between the ion and neutral during CX: the charge of the ion (q) and the number of electrons in the ion. The charge scales the velocity ranges

for which various theoretical methods are valid, and more electrons in the system makes the interaction between reaction channels more complex [Janev et al., 1985].

The number of electrons captured from the neutral also significantly affects the resulting CX spectrum. Single electron capture (SEC) dominates in most astrophysical environments due to the high cosmic abundance of atomic H. If multi-electron neutrals are present, however, multi-electron capture (MEC) is a non-negligible process in slow CX collisions [Ali et al., 1994, 2005, Hasan et al., 2001]. This is likely present in the data presented in Chapter 5. Unfortunately, only a small fraction of theoretical treatments have incorporated multi-electron capture (MEC) into their calculations (just the Classical Over the Barrier method and the Classical Trajectory Monte Carlo method [Cariatore and Otranto, 2013, Ali et al., 2005]). Section 1.7 discusses this further.

The simplest theoretical treatment of CX is with the Classical Over-the-Barrier method (COB), applicable to collisions between 100 eV/amu–10 keV/amu [Bodewits, 2007]. COB is based off the classical estimations of the joint potential well of the ion and neutral. In COB, the electron is transfered from the neutral to the ion if the potential barrier between the two nuclei is lower than the binding energy of the electrons. One can estimate the total capture cross section and the most likely n level for electron capture with COB, but it does not give a n or l distribution [Bodewits, 2007].

The Classical Trajectory Monte Carlo method (CMTC) is slightly more sophisticated than the COB method. It traces the three-body dynamics between the ion, neutral, and one active electron. It determines the time-dependent position and

momentum of each of these particles for a large ensemble of configurations to simulate a collision [Olson, 2006, Abrines and Percival, 1966, Olson and Salop, 1977]. CTMC is best for high energy collisions (above ∼5 keV/amu), but does not adequately describe experimental data taken at low collision energies [He et al., 2009, Olson, 2006, Janev, 1983, Beiersdorfer et al., 2000a].

The Multichannel Landau-Zener approximation (MCLZ) is best for low-energy collisions (from several tens of eV/amu to ∼5 keV/amu) [Mullen et al., 2016]. It considers the quasimolecular energy configurations of a slow collision between an ion and a neutral. It calculates diabatic potentials of pre- and post-capture states and calculates the probability of a pseudocrossing, or a location where the quasimolecule can move from the pre-capture potential curve to the post-capture potential curve, representing the electron transfer process. MCLZ can estimate state-selective capture cross sections and can generally predict large-scale trends in capture cross section, but results when compared to experiment are mixed [Wu et al., 2011]. We use MCLZ calculations to compare to our data in Chapter 6. More details on MCLZ can be found in Section 2.3.

The most accurate methods are close coupling methods, such as Quantum Mechanical Molecular Orbital Close Coupling (QMOCC) and Atomic Orbital Close Coupling (AOCC). These methods calculate the quasi-molecular or atomic structure of the electron transfer, respectively, and can yield state-selective capture cross sections. QMOCC is most accurate for low-energy collisions (below ∼1 keV/amu), and AOCC is most accurate for high-energy collisions (up to ∼500 keV/amu) [Cumbee, 2016]. However, few of these close-coupling calculations exist due to their compu-

tational intensity.

1.3 Theoretical Approximations

In the absence of a full state-selective cross section calculation via one of the aforementioned methods, one can approximate the initial distribution of n and l capture states. The peak in the n capture distribution can be approximated as:

$$n_{\max} \sim q\sqrt{\frac{I_H}{I_n}}\left(1+\frac{q-1}{\sqrt{2q}}\right)^{-1/2} \sim q^{3/4}, \tag{1.2}$$

where I_H and I_n are the ionization potentials of hydrogen and the neutral target, respectively, and q is the ion charge [Janev and Winter, 1985]. This relationship follows [Janev and Winter, 1985] from considering the diabatic potentials of the initial (V_{n0}, covalent) and final (V_n, excited ionic) states of the reaction partners in the adiabatic collision velocity regime, at large internuclear distances [Janev and Presnyakov, 1981]:

$$V_{n0}(R) = -\frac{1}{2n_0^2} + O(R^{-4}) \tag{1.3}$$

and

$$V_n(R) = -\frac{q^2}{2n^2} + \frac{q-1}{R} + O(R^{-2}). \tag{1.4}$$

The internuclear distances at which the strongest interaction between the initial and final potentials occurs when the initial and final potential energies become degenerate (i.e. equating Equations 1.3 and 1.4). Solving for R_n gives the internu-

clear distance where electron transfer occurs:

$$R_n \simeq \frac{q-1}{\frac{q^2}{2n^2} - \frac{1}{2n_0^2}}. \tag{1.5}$$

It should be noted that this approximation results from ignoring the higher order terms in Equations 1.3 and 1.4. For states that have the same initial and final symmetry, one cannot ignore these terms. In this case, electron exchange effects become important close to R_n, which add additional terms to the initial and final potentials. This leads to several so-called "avoided curve crossings," which are discussed further in Section 2.3.

Solving Equation 1.5 for n, setting $n_0 = 1$ (assuming an initial ground state of the transferred electron) and considering the distance R_0 where electron capture dominates in the decay model [Janev and Presnyakov, 1981, Janev, 1983],

$$R_0 \simeq 2n_0^2\sqrt{2q}, \tag{1.6}$$

yields Equation 1.2.

The scaling of $n_{\max} \sim q^{3/4}$ in Equation 1.2 also follows from other approximations, such as the COB method and the distorted-wave approximation [Janev, 1983].

Though this commonly-used approximation for $n_{\max}$ is independent of velocity, it is more accurate (though not straightforward) to consider how $n_{\max}$ behaves in the three collision velocity regimes described above [Janev et al., 1985]. The shape of the distribution of n values around $n_{\max}$ also changes as a function of velocity:

for low Z (Z$\lesssim$ 10) and very low collision velocities, the n distribution is narrowly peaked around $n_{\max}$. This distribution widens with increasing collision velocity. The shape of this distribution is often asymmetric around $n_{\max}$ due to the fact that for $n < n_{\max}$, the energy spacing between levels is larger than those with $n > n_{\max}$, so the capture cross section into those ($n < n_{\max}$) states decreases more rapidly [Janev et al., 1985]. For intermediate to high collision velocities, electron momentum transfer begins to contribute to the electron transfer process, and $n_{\max}$ strays from Equation 1.2 and becomes velocity-dependent [Janev and Winter, 1985, Janev et al., 1985].

The l-state distribution, which is highly dependent on the relative velocity between the ion and neutral, is more difficult to calculate theoretically. This is especially problematic in the low collision energy regime (below 1 keV/amu), where collisions are slow enough that electron-electron interactions and pseudo-molecular effects become important. Two spectral synthesis codes for CX, SPEX-CX and ACX [Smith et al., 2014a, Gu et al., 2016], discussed in Section 2.2, employ certain approximations for the l distribution based on work by Janev and Winter [1985]. These approximations lead to four different distribution functions $W_n(l)$, for a given value of n:

Landau-Zener:

$$W_n(l) = l(l+1)(2l+1)\frac{(n-1)!(n-2)!}{(n+l)!(n-l-1)!} \tag{1.7}$$

Separable:

$$W_n(l) = \frac{2l+l}{q} e^{\frac{-l(l+1)}{q}} \tag{1.8}$$

Even:

$$W_n(l) = \frac{1}{n} \tag{1.9}$$

Statistical:

$$W_n(l) = \frac{2l+1}{n^2} \tag{1.10}$$

The Landau-Zener and Separable approximations are applicable to the low collision energy regime [Janev, 1983, Janev and Winter, 1985]. In this regime, there is not enough momentum in the system to populate a higher orbital angular momentum state. As collision energy increases, the distribution moves towards statistical weighting, where higher l values are preferred [Janev, 1983, Janev and Winter, 1985]. This can be explained through a classical description of the CX process, where momentum from the initial collision is transferred into the electron's orbital angular momentum. The even distribution does not have a physical basis, but instead represents a regime between the low- and high-velocity extremes [Smith et al., 2014a]. Though these approximations have utility as starting points for calculating CX spectra, they do not incorporate the quantum mechanical or quasi-molecular effects of the CX interaction, and should be used with great care (see Chapter 6).

1.4 Spectroscopic Observables

Though modeling CX emission can be challenging, we have learned that there are spectral features that can be generally diagnostic of the occurrence of CX.

For SEC onto bare ions, if the electron populates a low angular momentum

state, the resulting cascade has a characteristic spectrum of one or several strong high-n Lyman lines from direct decay from $n = n_c$, $l = 1$ to the ground state, where n_c is the principle quantum number of the captured electron. These lines are much stronger in CX than from collisional excitation [Smith et al., 2014b]. If the electron initially populates a high angular momentum state, it will decay along the Yrast chain in steps of $\Delta n = -1$ and $\Delta l = -1$, giving off low-energy photons, and eventually leading to a strong Lyman α line from the $n = 2 \rightarrow 1$ transition. In this case, the high-n line(s) is suppressed [Wargelin et al., 2008]. These scenarios are shown in Figures 1.2 and 1.3. As the l distribution moves towards statistical weighting at high collision energy, a higher collision energy usually results in capture into a high l state. Because of this, the ratio of high-$n \rightarrow n = 1$ lines to Lyman α can be used as a diagnostic of the collision energy. Chapter 4 uses this ratio, called the hardness ratio, to perform spectral diagnostics of experimental K-shell data. Figure 1.4 illustrates this spectral dependence on the collision energy, as calculated with a CTMC model.

For SEC onto H-like ions (creating He-like ions), the angular momentum coupling between the already-present electron with the newly captured one results in singlet and triplet states in an LS coupling scheme. Singlet and triplet states have distinct decay patterns.

Singlet np can directly decay to the $1s$ state, so singlet states can have high-$n = n_c \rightarrow 1$ emission as in the H-like case. However, most capture states decay to singlet $2p$, which subsequently decays to the ground state to yield a strong w (resonance) line.

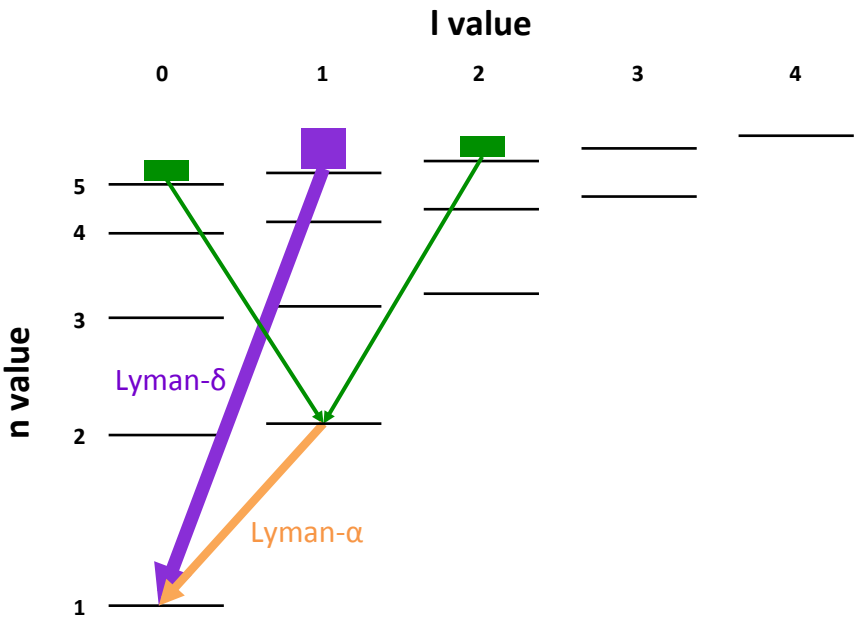

Figure 1.2 Radiative decay paths from initial electron capture into a bare ion at low collision energy, which preferentially populates low angular momentum states. In this case, capture primarily into $5p$ leads to a strong Lyman-δ line (shown in purple). Not all electron transitions are shown, and energy spacing is not to scale.

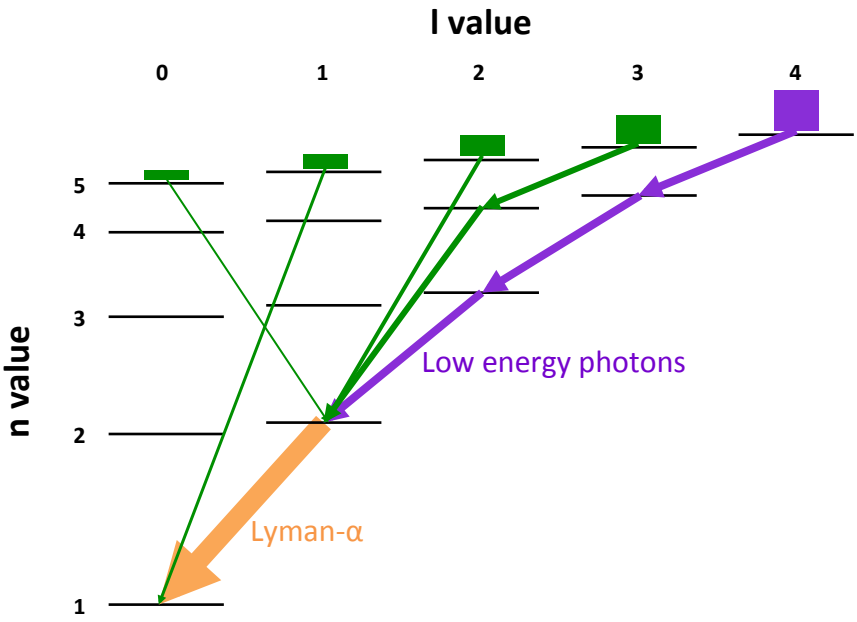

Figure 1.3 Radiative decay paths from initial capture into a bare ion at high collision energy, where the l states are populated statistically. In this case, capture into mostly high angular momentum states leads to significant Yrast cascades. In this case, decay along the Yrast chain after capture primarily into $5g$ leads to the low-energy photons shown in purple. These cascades primarily populate the $2p$ state, which then decays to the ground state, yielding a strong Lyman α line (shown in yellow). Not all electron transitions are shown, and energy spacing is not to scale.

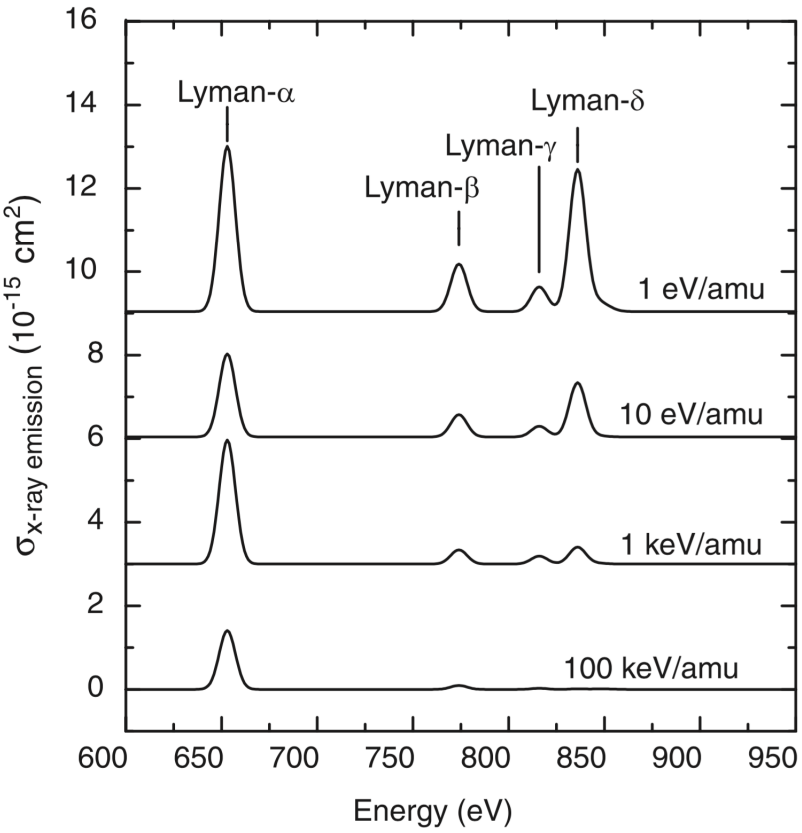

Figure 1.4 Theoretical spectra as calculated with the CTMC method for CX between bare O and H, at several collision velocities. This shows the suppression of the high-n Lyman line with increasing velocity, indicating a statistical population of l states. Reproduced from Wargelin et al. [2008].

In low-Z ions, which are well-described by an LS coupling scheme, triplet states are spin-forbidden to decay to the $1s^2\ ^1S_0$ ground level via an electric dipole transition. This means that electrons will cascade downward from their initial capture state to populate the $1s2s\ ^3S_1$ level or the $1s2p\ ^3P_{0,1,2}$ levels. From there, they undergo a magnetic dipole transition to the singlet $1s^2\ ^1S_0$ ground state. This can be via a z (forbidden) line ($1s2s\ ^3S_1 \rightarrow 1s^2\ ^1S_0$) or an x or y (intercombination) line ($1s2p\ ^3P_{2,1} \rightarrow 1s^2\ ^1S_0$). Triplet states are thus dominated by emission from these lines, and high-$n \rightarrow 1$ transitions are suppressed.

Schematics of these transitions for He-like ions are shown in Figures 1.5 and 1.6.

The Kα complex, or the combination of the w, x, y, and z lines, thus dominates CX spectra from He-like ions. He-like CX spectra typically show relatively weak high-$n \rightarrow 1$ lines in comparison to H-like spectra, though these lines are still stronger in CX than in collisional excitation. With increasing Z, spin-changing transitions become allowed, and emission from high-$n \rightarrow 1$ lines increases [Beiersdorfer et al., 2000a].

Recombination typically preferentially populates triplet states due to their larger statistical weight [198, 1989] (although some CX experiments have shown departures from this, e.g. Leutenegger et al. [2010], Bliek et al. [1998]). This means that for CX emission from He-like ions, the sum of the intercombination and forbidden lines is typically much stronger than the w line.

It is important to note that enhanced forbidden and intercombination lines can also be created with other processes such as radiative recombination of H-like

to He-like ions or inner-shell ionization of Li-like ions. To distinguish radiative recombination from CX, one may look for a continuum feature that will be present in spectra from a radiatively recombining plasma (see Appendix C), but not CX. The challenge, however, is that these and other processes are often occurring in parallel and are thus not straightforward to disentangle.

Figure 1.7 shows a K-shell laboratory spectrum resulting from collisional excitation (or direct excitation, DE) compared to CX, for the case of bare and H-like S interacting with He. One can see the enhanced forbidden line in the He-like species, as well as the strong high-n Lyman line in the H-like species.

Specific and widely accepted spectral diagnostics for L-shell ions at high-resolution are scarce in the literature; Chapter 5 presents experimental data for Ne-like Ni to begin to rectify this.

In order to obtain a global view of the differences between a collisional and CX-dominated plasma, it is necessary to consider spectra from more than one ion. The XSPEC spectral fitting package [Arnaud, 1996] is useful for comparing various emission mechanisms to note spectral differences, and can incorporate a CX model called ACX. ACX uses approximations to calculate the n, l electron capture state rather than theoretical or experimental cross sections (see Section 2.2) and thus has limited accuracy and applicability, but it can give a general sense of CX spectral signatures and diagnostics. Figure 1.8 shows an ACX spectral model compared to a collisional thermal plasma model (APEC). Both focus on the energy range 0–2 keV and assume an electron temperature of 4 keV and a solar abundance of metals. One can notice the stark differences in spectral shape between the two models. This

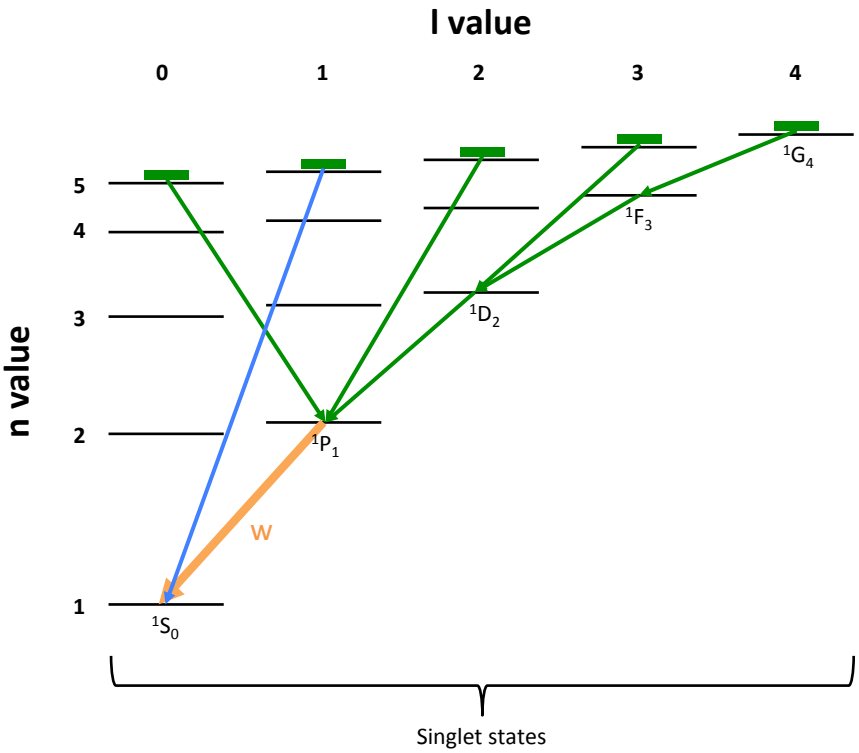

Figure 1.5 Radiative decay paths from initial capture into a H-like ion assuming capture into a singlet state and an even l-distribution. Electrons that initially populate l=1 can decay directly to ground (in this case, the blue K-δ line), but electron capture into other states primarily decay to $^1P_1$, which decays to the singlet ground state $^1S_0$ via the w (resonance) line, shown in yellow. Not all electron transitions are shown, and energy spacing is not to scale.

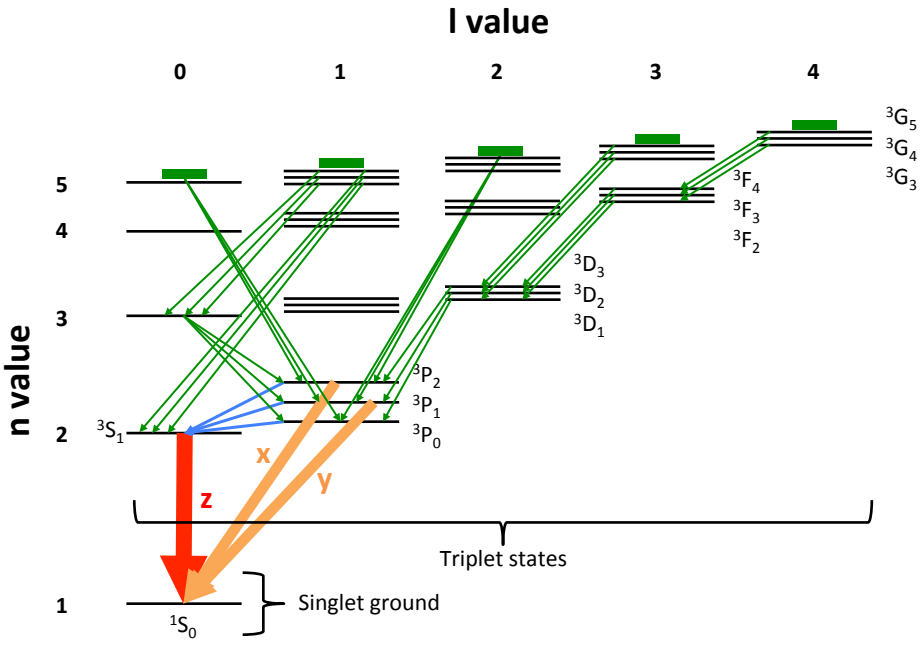

Figure 1.6 Radiative decay paths from initial capture into a H-like ion assuming capture into triplet states and an even l-distribution. Direct decay from a high-n state is forbidden; transitions to the $^1S_0$ ground state require a magnetic dipole transition. Transitions from $1s2p\ ^3P_2$ and $1s2p\ ^3P_1$ to ground result in an x or y (intercombination) line, respectively (shown in yellow). Electrons in the $1s2p\ ^3P_0$ state transition to $1s2s\ ^3S_1$. Transitions from $1s2s\ ^3S_1$ to ground lead to a z (forbidden) line, shown in red. Not all electron transitions are shown, and energy spacing is not to scale. In particular, the spacing between the $^3P_{0,1,2}$ states is exaggerated for clarity.

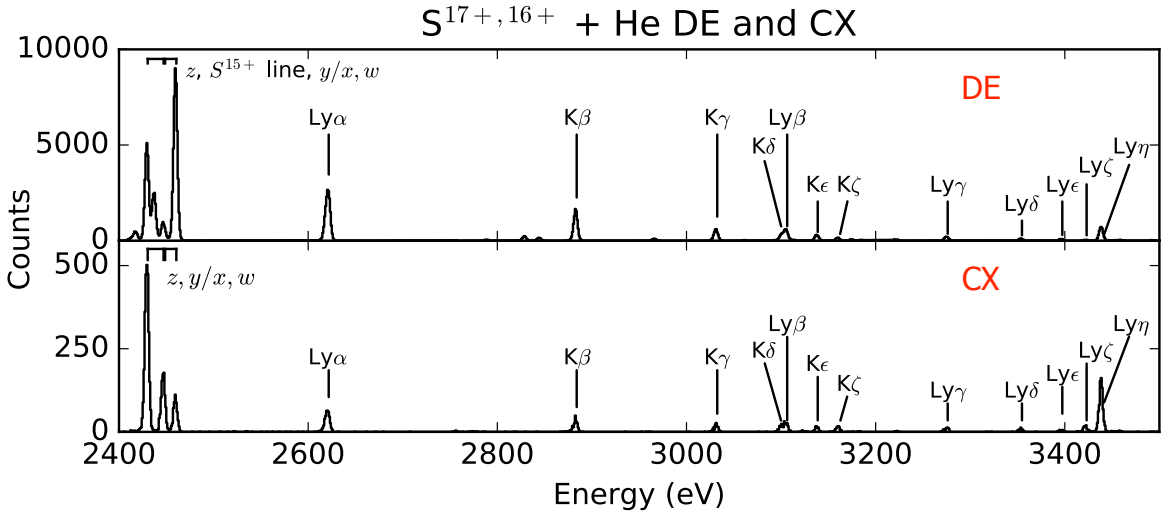

Figure 1.7 Spectra resulting from collisional (direct) excitation (DE, top) and CX (bottom) of bare and H-like S with He, as measured with an X-ray microcalorimeter at an Electron Beam Ion Trap. Note the highly enhanced Ly-η line and the He-like z line in CX.

demonstrates the importance of considering CX in astrophysical observations: if CX is present but not accounted for, the derived abundances of, for example, a purely thermal model may have to be significantly enhanced in order to reproduce strong line emission that actually stems from CX.

Though it is vital to consider the contribution of CX to our observations, it is perhaps even more important to tackle the challenges of detailed modeling: if we apply inaccurate CX spectral models to our data, we run the risk of misinterpreting the physical attributes of the objects and environments we observe. This will become especially obvious thanks to recent advancements in spectrometers: we will soon be able to resolve astrophysical and laboratory plasmas, especially extended sources, at higher resolution than ever before. This makes the need for accurate models more

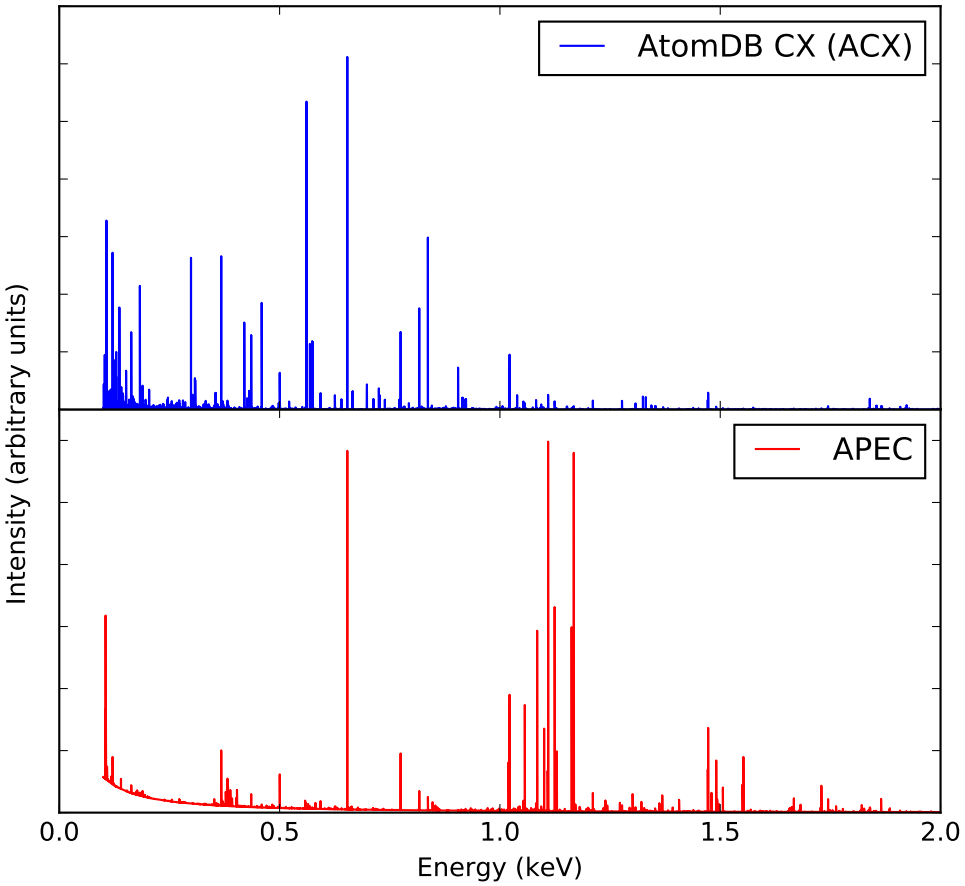

Figure 1.8 Simulated spectra under 2 keV resulting from a 4 keV plasma using the AtomDB CX (ACX) model to represent the CX emission (top) and the XSPEC APEC model for an ionized thermal plasma (bottom).

acute. Luckily, attention on CX has recently increased due to a a wider recognition of its unusual spectral signature and large total cross section, which may lead to greater modeling effort. The next section describes several environments where CX has been observed or postulated to occur.

1.5 Charge Exchange in Astronomy

CX occurs ubiquitously in our solar system due to interactions between neutrals in various locations and the ions in the solar wind (called solar wind CX, or SWCX), and most likely in many other astrophysical environments where hot plasma comes in contact with cool gas. While only SWCX has widespread acceptance, it is worthwhile to give a sampling of the myriad objects and environments where CX may occur in order to understand the importance of having an accurate and widely applicable spectral theory for CX.

1.5.1 Solar System

The solar wind is the source of the highly charged ions for most instances of CX in the solar system. Its composition is mostly protons, electrons, and alpha particles, but 0.1% of the composition consists of highly charged ions. These are mostly bare, H-like, and He-like C and O, though bare and H-like Ne and Mg may be present during coronal mass ejections, as well as some L-shell Fe ions and bare, H-like, and He-like N [Schwadron and Cravens, 2000, von Steiger et al., 2000]. The wind velocity ranges from 300–800 km/s; the fast wind stems from the polar regions,

and the slow wind comes from the equatorial regions and has a higher abundance of highly charged ions [Schwadron and Cravens, 2000, von Steiger et al., 2000].

As described earlier in this chapter, CX was discovered in our solar system in 1996 with the unexpected detection of X-rays from the comet C/Hyakutake 1996 B2 via observations with the ROSAT satellite by Lisse et al. [1996]. After Cravens [1997] determined that SWCX was the X-ray emission mechanism in Hyakutake, more than 20 comets were subsequently observed in the EUV and soft X-ray bands (e.g., Lisse et al. [1999], Krasnopolsky et al. [2000], Dennerl et al. [2003], Bodewits et al. [2007], Christian et al. [2010]). More recently, Beiersdorfer et al. [2003b] verified experimentally using an Electron Beam Ion Trap (see Section 3.1) that cometary spectra can be extremely well-described solely via CX X-ray emission. Because cometary X-ray emission stems almost completely from CX, comets are one of the cleanest astrophysical laboratories for theoretical benchmarking and comparison to experiment.

SWCX has also been observed in planetary atmospheres. In nonmagnetic planets such as Venus and Mars, the solar wind interacts with the exospheres much like it does with cometary comae; the main difference is that the exospheric density is higher than in a coma, so the ions more quickly lower their charge state as they undergo multiple CX reactions in a thin layer. Planets also exhibit a smaller CX flux than nearby comets due to their smaller spatial extent on the sky. The first instance of planetary CX was observed in Mars; both Chandra and XMM reported X-ray emission from the halo [Dennerl, 2002, Gunell et al., 2004, Dennerl et al., 2006]. While the spectra were dominated by X-ray fluorescence, there was line emission

from highly charged C, N, O, and Ne ions in the halo, similar to that of cometary spectra. The forbidden line was also enhanced in the He-like O lines, confirming CX as the origin of the emission.

Given CX being detected in Mars, Venus was expected to show even stronger signs of CX due to its larger size and closer proximity to the sun, placing it in a denser region of the solar wind. However, initial observations of Venus with Chandra showed that the X-ray emission is dominated by fluorescence [Dennerl et al., 2002]. Later observations performed at solar minimum showed two spatially distinct origins of X-rays: the troposphere and the exosphere. The X-rays from the exosphere were brightest in the He-like O spectral line band, which are also the brightest lines in cometary X-ray spectra resulting from CX. It was thus determined that the exospheric X-ray emission resulted from SWCX with neutrals [Dennerl, 2008].

Emission lines below 2 keV from the polar region in Jupiter have been attributed to CX [Gladstone et al., 2002, Elsner et al., 2005, Branduardi-Raymont et al., 2007], however it is not clear if the CX is due to interactions with ions from the solar wind, those accelerated in Jupiter's magnetosphere, or both [Bunce et al., 2004, Cravens et al., 2003]. Ions are accelerated by the magnetosphere to velocities of at least ∼5000 km/s (∼ 130 keV/amu), so in principle, with sufficient understanding of the spectral dependence on velocity (i.e., better models) and high enough spectral resolution, one could determine the origin of the ions with further high-resolution observations.

Although comets are one of the brightest sources of SWCX, CX in the Earth's exosphere and the heliosphere has the most pervasive effect on X-ray observations

we make. Anomalous diffuse X-ray emission was discovered during the ROSAT All-Sky Survey and dubbed "long term enhancements" (LTEs) [Snowden et al., 1994], as it varied on time scales from several hours to days. The connection between solar wind variation and the long term enhancements was made by Cravens et al. [2001], suggesting that SWCX was being produced locally with neutrals in the Earth's exosphere. This was confirmed with Chandra spectra of the dark moon [Wargelin et al., 2004]: as the moon blocked out the cosmic X-ray background, only CX produced locally was left, and the observed emission matched models for X-ray emission via SWCX. Similarly, SWCX with the stream of neutral ISM flowing through the heliosphere leads to variable X-ray emission on longer time scales than the LTEs.

This local CX emission means that any observation we make has a spatially, temporally, and spectrally variable X-ray foreground: exospheric CX affects all low-Earth orbit observations, and heliospheric CX affects any observation made from within the solar system. This presents a subtle challenge: this local X-ray emission is superposed on more distant objects, and thus can lead to misinterpretations of observations [Snowden et al., 2004]. Background subtraction is complicated due to the fact that the emission is ubiquitous and temporally variable on many scales. If the emission varies over time, we might hope to identify the CX component, but the X-ray flux does not always change during the observation. Even if it does, it is unlikely that we can identify all of it, especially the heliospheric contribution that may vary on long time scales. This foreground CX will continue to affect future observations until a more satisfactory way of identifying or modeling the foreground CX is found.

Observations of the soft X-ray background is one example of the complication of exospheric and heliospheric SWCX. It was thought that the Local Hot Bubble, a non-symmetric cavity around the sun about 60 pc in radius thought to contain a 10^6 K plasma, was responsible for the soft X-ray background [Sanders et al., 1977, Cox and Anderson, 1982, Snowden et al., 1990]. However, it was realized that this diffuse emission has a signature that is similar to CX, both morphologically and spectrally [Cox, 1998, Cravens, 2000, Lallement, 2004a, Welsh and Lallement, 2005, Koutroumpa et al., 2009b]. Observations by Chandra [Smith et al., 2005, Hickox and Markevitch, 2006], XMM [Snowden et al., 2004] and Suzaku [Fujimoto et al., 2007, Henley and Shelton, 2007] measured temporal variations in the soft X-ray background flux, adding credence to the idea of its exospheric/heliospheric origin.

Various authors made estimates of the CX contribution to the soft X-ray background that ranged from 5 percent to nearly all of it, depending on direction and energy band [Cravens, 2000, Wargelin et al., 2004, Cravens et al., 2001, Lallement, 2004a, Koutroumpa et al., 2007, Robertson et al., 2009, Lallement, 2004b]. Finally, the DXL sounding rocket flight made an observation of the helium focusing cone, an area within the heliosphere of a greater than average density of neutral He. The 2012 observation led to a firm measurement that up to 40% of the diffuse X-ray background stems from heliospheric SWCX [Galeazzi et al., 2014]. An accurate measurement of the SWCX contribution to the diffuse X-ray background directly affects our assumptions of the conditions of our local ISM, as well as astrophysical objects.

1.5.2 Astrophysical and Other CX

CX may also be very important in setting the ionization balance and for cooling via line formation in nonequilibrium plasmas such as supernova remnants, in interactions between the ISM and stellar winds, and in galaxies and galaxy clusters.

It has been postulated for some time that CX can occur in supernova remnants [Chamberlain, 1956, Serlemitsos et al., 1973], at the interface between the shock-heated hot plasma and the neutral ISM beyond the shock front. However, Wise and Sarazin [1989] found that CX emission should contribute less than 10% via He-like C and N lines, and even less from other elements. Observations by Lallement [2004b] showed that emission from CX at the shock front is negligible, save possibly having an effect on limb brightening if CX is occurring along our line of sight. However, several authors continue to suggest CX as a likely mechanism for emission in the Cygnus loop [Katsuda et al., 2011, Cumbee et al., 2014, Roberts and Wang, 2015]. Thus, currently, the picture of CX occurring in supernova remnants remains unclear, though this could be due to limitations in detector resolution for extended sources and inaccuracies in theoretical modeling.

CX likely plays a part in X-ray emission around winds, ranging in scale from stellar to galactic. Pollock [2007] found that CX is likely to be as important in stellar winds interacting with neutral ISM as it is for SWCX around comets in the solar system. On the galactic scale, it is possible that ionized galactic wind could collide with cool ambient gas in halos of starburst galaxies and result in CX. M82 is a potential example of this: Tsuru et al. [2007] did a deep observation with Suzaku

and found that CX may contribute significantly to emission in the K-shell O lines in the extended X-ray halo. Ranalli et al. [2008] observed the central region of the galaxy and found unusual emission from H-like O lines that did not fit a solely thermal model, but could be explained by CX emission. Liu et al. [2010] observed the bulge and found unusually strong emission from the He-like triplet. Though these results are intriguing, none lead to a definite answer regarding the occurrence of CX in these regions.

Closer to home, the Galactic Ridge is an area of the Milky Way that extends a few degrees above and below the Galactic Plane, and around the Galactic Center, extending about 45 degrees in longitude. Diffuse X-ray emission was observed in Worrall et al. [1982] as both continuum radiation and emission lines from H- and He-like Mg, Si, S, Ar, Ca, and Fe [Koyama et al., 1996, Ebisawa et al., 2001, Muno et al., 2004]. Tanaka et al. [1999] and Tanaka [2002] postulated that this could come from CX between low energy cosmic rays and neutral gas in the Galactic Plane. However, others [Bussard et al., 1978, Rule and Omidvar, 1979] calculate that there are not enough cosmic rays of the right energy to produce the H- and He-like lines observed, and that the cross section for CX at those high energies is too small to lead to the observed line intensities.

CX is also very likely to take place in galaxy clusters, when rarified hot intra-cluster medium gas encounters cold interstellar clouds or filaments at high velocity. Walker et al. [2015] showed that CX may contribute a fraction of the X-ray flux in the 0.5–1.0 keV band in galaxy clusters like Perseus, where the hot ICM interacts with Hα filaments.

CX may even be confused with dark matter. Bulbul et al. [2014] and Boyarsky et al. [2014] both independently discovered an unexpected emission line at ∼3.5 keV in stacked XMM-Newton data of 73 galaxy clusters. They suggested that since there are no expected atomic transitions of a thermal plasma at that energy, it was possible that this was a signature of a sterile neutrino decay, a proposed dark matter particle. However, Gu et al. [2015] proposed that line was not due to a sterile neutrino decay, but rather due to CX between bare S ions from the hot intracluster medium that interacted with neutral H in cold, dense clouds. This was supported by laboratory work done by Shah et al. [2016]. However, Hitomi observations of the Perseus cluster with a X-ray microcalorimeter did not show any excess flux at this energy [Aharonian et al., 2017], though it should be noted that the observation was not long enough to compare to the stacked XMM-Newton data. In addition, the authors of the Hitomi study mention that there was a slight excess at the 1.5σ level at 3.44 keV that could be due to a high-n to $n = 1$ transition of H-like S following CX.

1.6 Diagnostic Utility

With the wide variety of possible astrophysical sources of CX, it would be beneficial to be able to use its observed spectrum to probe the conditions of the emitting region. In many cases, the very factors that make modeling CX complex (e.g., velocity dependence, number of electrons in the system) can be used as diagnostic tools, provided we understand the underlying physics behind these relationships.

The flux that we observe from CX can be written as

$$F_{CX} = \frac{1}{4\pi D^2} \int n_{\rm ion} n_{\rm neutral} v \sigma_{\rm tot}(v) dV, \tag{1.11}$$

where $n_{\rm ion}$ and $n_{\rm neutral}$ are the number densities of the ion and neutral species, v is the relative velocity between them, and $\sigma_{\rm tot}$ is the total cross section for CX between that particular ion and neutral pair. The number of photons that we observe from CX thus holds keys to information about these parameters, though the challenge is that typically, most of these variables are unknown.

We may use CX spectra to learn about the ions present in the emitting region. We can deduce the ion temperature through comparing the relative strength of lines from differing charge states of a particular ion. By comparing the strength of lines from different ions across the entire spectrum, one could possibly learn about the relative elemental abundances. This, however, requires information about the total cross section for CX for each ion species.

For CX to occur, a hot plasma must come in contact with a cool cloud of neutrals. Although these two ingredients may exist in many environments (as discussed in Section 1.5), their presence alone does not guarantee CX; the ions may be shielded from the neutral gas by magnetic fields, for instance. Thus the occurrence of CX is indicative of the interaction of these two temperature regions. Further, the spectral signature of CX can tell us at what velocity these two temperature regions are interacting. Again, Figure 1.4 shows an example of how the CX spectrum may change as a function of relative velocity between the ion and neutral species.

Accurate models that can predict this behavior for a wide variety of astrophysical ions and neutrals can aid us in better determining the interaction velocity in regions where we currently only have approximate information.

According to Equation 1.11, if we have information on the relative collision velocity and an estimate on the total CX cross section, we can then extract information on the ion and neutral densities along the line of sight. However, even if this proves too challenging, we can at least hope to diagnose the neutral species involved in the reaction. It has been shown experimentally [Beiersdorfer et al., 2003b] that the spectral signature of CX changes as a function of neutral species; this is shown in Figure 1.9. Understanding why this happens requires a detailed understanding of the atomic physics of CX, but in the meantime, we can use these empirical measurements to identify the neutral species involved in our astrophysical observations. This is especially valuable for atoms and molecules that are hard to detect via other means, such as neutral He and H_2.

Unfortunately, we are often limited in our ability to use these diagnostic tools in our astrophysical observations, both for a lack of accurate theory and a lack of photons. This dissertation focuses on the need for more accurate theory, but it is worthwhile to mention that except for the case of SWCX (where CX may contribute up to nearly all of the X-ray emission, as was found in Beiersdorfer et al. [2003b]), CX may often be just a small perturbation on the larger X-ray signal. Take, for example, the case of CX occurring in the Perseus cluster between the Hα filaments and the hot ICM, as investigated by Walker et al. [2015] and as mentioned in Section 1.5. A quick back-of-the-envelope calculation of the fraction of X-rays coming from CX

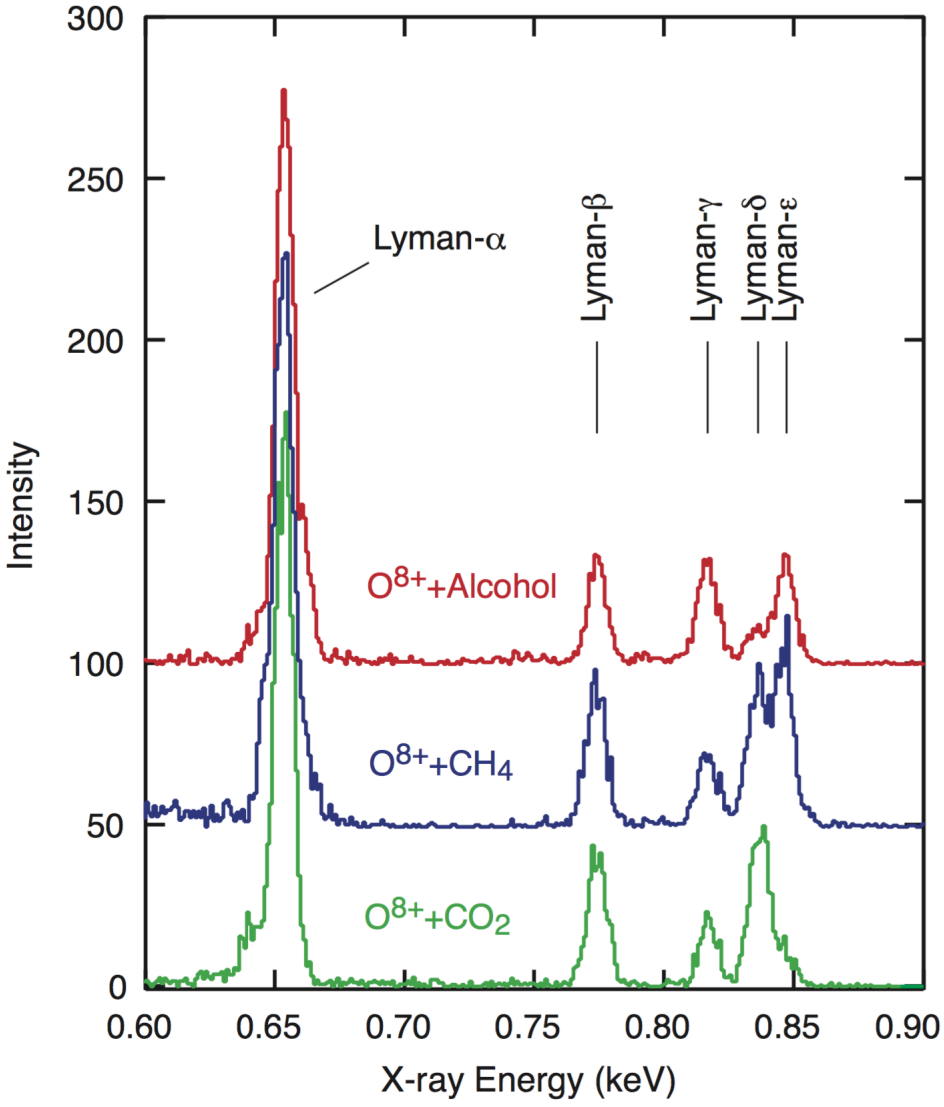

Figure 1.9 Experimental EBIT spectra from Beiersdorfer et al. [2003b] showing how CX between the same ion but differing neutrals yields dramatic spectral differences.

versus other sources in the observation by Walker et al. [2015] leads to an estimate of 1-10%.[1] This is thus barely at the detection limit of most current instruments without a significant amount of observing time.

Not only does CX contribute a small fraction of photons in many astrophysical cases, but the spectral resolution in many of our observations is not sufficient to actually resolve the spectral lines that would be most diagnostic. This can be seen, again, in Walker et al. [2015], where there are hints of the presence of CX, but the ∼100-eV resolution of the Chandra CCD limited a clearer answer.[2]

1.7 The Challenge

We have seen that CX may be an important emission mechanism in a wide variety of astrophysical plasmas, and that we need a better understanding of the complex underlying atomic theory. The work detailed in this dissertation addresses this challenge by presenting measurements of high-resolution CX spectra in order to benchmark and compare to theory.

This research fits into a growing body of work that highlights the challenge of developing accurate CX theory. Calculations with the most accurate models are

[1] This is done by assuming that CX would occur on the surface of the observed Hα filaments, that the ions are moving at thermal velocities, and that most of the CX flux comes from oxygen ions.

[2] On the other hand, as was mentioned previously, Aharonian et al. [2017] possibly detected signatures of CX with the $\sim$ 5 eV resolution of the microcalorimeter on Hitomi. With a similar detector and longer observation time, it would likely be possible to determine the origin of this signal with more certainty.

few and far between, the most common models often produce results that disagree with experiments, and experimental benchmarks for theory often do not exist at high enough resolution, or at all. Selected examples of this follow.

Accurate calculations of the total cross section are vital for estimates of the total flux we should expect from environments with CX. Though experimental and theoretical results can diverge in the low collision velocity regime [Wargelin et al., 2008], many experiments agree with theoretical calculations of the total cross section (e.g., Ali et al. [1994], Bruhns et al. [2008], Greenwood et al. [2001], Wu et al. [2012]). However, in order to model spectra, it is necessary to calculate state-selective cross sections. Only certain theoretical methods can calculate such information (CTMC, MCLZ in some cases, and AOCC/QMOCC, for example), and of the ones that can, they often show discrepancies when compared to experiments.

For example, CTMC predictions do not match experimental results well at low collision energies [Beiersdorfer et al., 2000a], such as those produced by an EBIT. Otranto et al. [2006] demonstrated that while CTMC calculations qualitatively agree with EBIT experiments showing a decrease of the n capture state with increasing ionization potential, their CTMC model overestimates the flux in high-n Lyman transitions following CX onto O^{8+}. Beiersdorfer et al. [2000a] performed experiments with an EBIT showing that, contrary to CTMC calculations, the so-called hardness ratio (a proxy for the l capture state) following CX with bare Ne, Ar, Kr and Xe was always nearly unity. Further, the disagreement between calculated and measured hardness ratios worsened at higher atomic numbers.

Mullen et al. [2016] performed MCLZ calculations of CX with K-shell Fe, and

showed that in order to match data from EBIT experiments at low collision energy, it was necessary to adjust the applied l-distribution by hand. Hasan et al. [2001] compared various theoretical calculations to experiments performing cold-target recoil-ion momentum spectroscopy, which had collision energies of a few keV/amu. The authors found that the QMOCC model agreed well with the data, but the COB, MCLZ, and CTMC methods were less accurate. Mančev et al. [2013] used another theoretical technique called the Born approximation to calculate state-selective cross sections, and compared them to experimental data points at a wide range of energies. In all cases, the two methods agreed well at high velocities, but diverged at energies below $\lesssim$ 100 eV/amu. Finally, Chapters 4 and 6 provide further evidence of the mismatch between theory and experiments when calculating state-selective cross sections or predicting spectra.

There has been a focus on obtaining theoretical results in the high collision energy regime, applicable to, for example, the fast solar wind. These velocities can be attained in the lab with, for instance, merged-beam experiments, or by colliding an ion beam with a neutral target, as in Bodewits [2007]. However, as we have just seen, there are many more discrepancies between experiment and theory in the lower energy regime ($\lesssim$ 100 eV/amu). This regime is relevant to, for example, solar wind CX inside the bow shock of a comet, which may happen at velocities as low as 50 km s^{-1} and be responsible for up to 50% of the X-ray emission in comets [Allen et al., 2008]. CX experiments with EBITs (described in Chapter 3) can reach these low velocities, though the capability to vary this velocity is fairly limited.

There is a dearth of theoretical calculations for the more complex L-shell ions,

and experimental measurements are few and far between. Only Bliek et al. [1998], Lubinski et al. [2000], Ehrenreich et al. [2005] measured EUV spectra of Li- and Be-like C, N, and O, Tawara et al. [2002, 2003] performed measurements of Kr at high collision energy, and more recently, Frankel et al. [2009a] measured L-shell spectra of Fe and S. Chapter 5 presents the first high-resolution spectra of L-shell Ni CX.

Finally, obtaining a detailed understanding of CX following MEC has been challenging. MEC likely plays an important role in SWCX, as the multi-electron neutrals CO_2, H_2O, and H_2 are abundant in cometary comae and planetary atmospheres [Ali et al., 2005]. MEC has been shown to be important in the low-collision energy regime [Ali et al., 1994, Otranto et al., 2006]. Perhaps unsurprisingly, we find that MEC is likely a significant factor in the laboratory data presented here (see, e.g., Chapters 4 and Chapter 5). Since MEC leads to a doubly excited state that is unstable against autoionization, it can change the shape of the resulting spectrum as compared to SEC [Tawara et al., 2006, Ali et al., 2005, Otranto et al., 2006]. In order to extract reliable information from spectra involving both SEC and MEC, we must thus understand how each process affects the spectrum. Although it is generally recognized that MEC is an important factor in astrophysical and laboratory spectra, very few theories that incorporate MEC exist due to the computational complexity required.

This is a challenge that we can begin to address from the experimental side. To mimic most astrophysical CX and to ensure SEC, one may use atomic H as the neutral partner in CX experiments. However, this is itself a challenge. Work by Leutenegger et al. [2016] has shown that it is possible to ballistically inject atomic

H that has been thermally dissociated from molecular H_2. However, it is difficult to fully characterize the dissociation fraction, i.e. the relative amount of H versus H_2, and the reported fraction of H is an upper limit. Other methods are possible: for instance, one can create an atomic H beam by passing a beam of H^- through a laser cavity, so the ions are neutralized via photodetachment [Bruhns et al., 2008]. An advantage to this method is that it is possible to vary the collision energy by several orders of magnitude. However, in this setup, it is only possible to measure total cross sections, not state-selective cross sections or spectral measurements.

It is important to put the study of CX and its theoretical, observational, and experimental challenges in context with the wider field. The ESA-led XMM-Newton [Jansen et al., 2001] and NASA-led Chandra [Weisskopf, 1999] satellites have made significant advances in many areas of astrophysics, including numerous observations of CX in our solar system and possibly beyond. However, for the spectroscopic study of CX, we are beginning to reach the limits of our current capabilities with data from the instruments onboard these missions. Since the high-resolution slitless grating spectrometers on XMM and Chandra are dispersive instruments that confuse spectral and spatial information, they are not suitable for extended sources—ruling out many targets that emit X-rays following CX. Chandra and XMM also have charge coupled devices (CCDs). These CCDs provide exceptional imaging capabilities and do not produce spatial-spectral confusion of extended sources, but they only deliver moderate resolving power (R= $\lambda/\Delta\lambda$ ∼20–50). Moving past simply (possibly) identifying the presence of CX in astrophysical observations and beginning to harness its diagnostic power requires a non-dispersive spectrometer with higher resolution.

This need can be met with microcalorimeters: high-resolution, wide-band, non-dispersive X-ray spectrometers whose physics is detailed in Section 3.2. Microcalorimeters on satellites have had a relatively unlucky history—most recently with the JAXA-led Astro-H/Hitomi mission [Takahashi et al., 2016], which tragically broke apart after excessive rotation due to an erroneous signal. However, as evidenced by Hitomi's groundbreaking observation of the Perseus cluster of galaxies, which led to a Nature paper within its first month after launch [Collaboration, 2016], microcalorimeter data have the potential to revolutionize the field of X-ray astronomy. There are several future planned (X-ray Astrophysics Recovery Mission [Porter et al., 2010], Athena [Barret et al., 2013]) and proposed (Lynx [Bandler et al., 2016]) observatories that include microcalorimeters.

These missions hold promise for improved observations and a clearer understanding of CX locally as well as across the universe. However, this impending era of routine high spectral resolution measurements presents a new time-critical challenge. With lower-resolution data, it is easier to ignore details of CX that are not quite correct. High-resolution data does not allow for this margin of error. We must be able to verify the accuracy of the underlying atomic physics of CX in our spectral models at the same or higher resolution than these instruments, or we risk misinterpreting our observations.

Laboratory studies at high resolution, such as the ones presented in this dissertation, will help us benchmark and improve our theory in order to meet these new challenges in this dawning era of space-borne high-resolution X-ray spectrometers.

Chapter 2: Theoretical and Computational Tools for Simulating and Understanding CX

Experiment and theory go hand in hand for improving our understanding of the complicated and subtle nature of CX. It is impossible to understand experimental results without a theoretical basis, but without experiments to benchmark and guide theory, we risk misinterpreting the atomic physics encoded in a given spectrum. In this chapter, we present the computational tools used in this dissertation to analyze our experimental spectra, and the theoretical models we use to simulate CX spectra and compare to our experimental results.

2.1 FAC, the Flexible Atomic Code

We use the Flexible Atomic Code (FAC, [Gu, 2008]) in Chapters 4, 5, and 6 in order to calculate the energy levels and radiative transition rates for a given ion and charge state. FAC is a software package that calculates several atomic radiative and collisional processes, including radiative cascades, collisional excitation, collisional ionization, photoionization, autoionization, radiative recombination, and dielectronic recombination (see Appendix C for a description of these processes). FAC is beneficial because of its accuracy when compared to experimental data [Chen

et al., 2006, 2007] and its relative speed and ease of use. Calculations in FAC are based on the relativistic Dirac equation and use jj-coupling, thus making the code applicable to ions with large Z. The physics of how the code calculates atomic structure, including energy levels and transition rates, along with other atomic data related to electron impact excitation, ionization, and other processes, can be found in Gu [2008]. For demos on how to use FAC, along with sample atomic datasets generated by FAC, see https://www-amdis.iaea.org/FAC/.

To derive energy levels and transition rates, we interact with FAC via the Python library PFAC, which allows us to write a code for each ion and set of ion structures we wish to calculate. We specify the atom (e.g., S), which electron shells are closed (e.g., none for H-like S), and any desired electron configurations we wish to consider. We typically specify the ground configuration along with several excited states that consist of one excited electron above the ground configuration, with increasing n values up to a limit we determine. This limit is often $n = 15$. FAC then considers the central potential of the specified configurations interacting with one another, and diagonalizes the Hamiltonian to calculate the atomic structure. Its output is a list of all possible configurations with fully specified n, l, j, and total J values, along with the energy of that configuration with respect to the ground state. For every transition between each of these configurations, it also calculates the energy, the oscillator strength, the Einstein A coefficient, and the multipole expansion, for all multipoles.

If it is necessary for better accuracy, one can manually adjust the values of the energy levels. For example, for the S^{16+} and S^{15+} transition energies used in Section

6.4, we corrected the ionization energy required to make those ions according to Johnson and Soff [1985] and Artemyev et al. [2005], respectively. This then corrects the ground state energy level. For the Ni^{19+} data presented in Chapters 4 and 5, the ionization energy was corrected according to calculations by Scofield [private communication], and the $3 \rightarrow 2$ transition energies were corrected to match those in Gu et al. [2007a].

2.2 Charge Exchange Models: SPEX-CX and ACX

In section 6.2, we use the commonly available CX spectral synthesis codes SPEX-CX and ACX to compare to our experimental spectra. SPEX-CX is a model available for use with the SPEX X-ray fitting package [Kaastra et al., 1996], and ACX is a standalone package that can be used with the XSPEC spectral fitting code [Arnaud, 1996].

These codes first calculate the initial n and l distributions of electrons in the ion after electron capture, then perform a radiative cascade using energy and transition information from their respective atomic databases or atomic structure calculations to generate a spectrum. For this second step, SPEX-CX uses FAC as a baseline tool, a second atomic structure code [Cowan, 1981], and measurements from the National Institute of Standards and Technology (NIST). ACX uses the AtomDB database developed by Foster et al. [2011]. Though the radiative cascade from each method may produce slightly different results even with the same initial conditions, here we are more interested in the first step, which will more strongly influence

the resulting spectra: determining the initial distributions of electron states after capture. It is from this distribution that we can begin to trace the detailed physics of the CX reaction. Though the SPEX-CX and ACX codes calculate this in similar ways, there are key differences both in their methods of calculation and applicability to experimental data.

The creators of SPEX-CX compiled available theoretical and experimental total and state-selective (n-, nl-, or nlS-resolved) cross section data from the literature for collisions between several ions and atomic H at specific collision energies. These sources are shown in Table 1 of Gu et al. [2016]. For cases where these data do not exist, scaling laws were applied to infer this information.

To determine the n distribution scaling, the authors collected n-resolved cross sections for discrete values of n around n_{max} (from Equation 1.2) for nine different ions (C^{5+}, N^{6+}, N^{7+}, O^{6+}, O^{7+}, O^{8+}, Ne^{10+}, Fe^{25+}, and Fe^{26+}) undergoing CX with atomic H at 14 different collision velocities. The authors then fit a third-order polynomial to these values to derive a smooth distribution function for n at each of these velocities. They assume that the n distribution around n_{max} and its velocity dependence will be the same for all ion species. When using SPEX-CX, it is possible to select a desired collision velocity between 50–5000 km s^{-1}, which correspond to the minimum and maximum values for which these n distributions were calculated or extrapolated. The authors use a linear interpolation to calculate n distributions for the velocities between the 14 discrete points [Liyi Gu, private communication].

The SPEX-CX authors determined an l distribution with a similar combination of experimental and theoretical datapoints and scaling laws. They have seven ions in

their database for which theoretical or experimentally-measured l distributions exist, presumably at a range of collision velocities. In order to compute an l distribution for the rest of the ions, they compared the seven available l distributions to one of five distribution approximations to determine the best fit. Four of these distributions are presented in Chapter 1 as Equations 1.7 (which the SPEX-CX authors refer to as "low energy II"), 1.8 (separable), 1.9 (even), and 1.10 (statistical); the fifth equation, which they call "low energy I" is a variant of Equation 1.7, and is given as

$$W_n(l) = (2l+1)\frac{[(n-1)!]^2}{(n+l)!(n-l-1)!}. \tag{2.1}$$

They determined which approximation best matches the theoretical or experimental distribution over a velocity grid of 20 points (somewhat finer sampling than in the n distribution calculation), spread between 50–5000 km s^{-1}. They did this for two sets of n values: $n \leq n_{\max}$ and $n > n_{\max}$. For example, for most ions, for $n \leq n_{\max}$, they determine that the separable distribution should be applied from 50–500 km s^{-1}, and the statistical distribution is valid from 500–2000 km s^{-1}. When using the SPEX-CX code, it is possible to specify which distribution function should be used, but the default (and recommended) option is to let the specified CX collision velocity determine this distribution.

Finally, the user can specify the relative abundance of each ion, but in SPEX-CX, the distribution of the ion charge states can only be specified by the ionization temperature parameter. SPEX-CX currently cannot be used to simulate CX with neutrals other than atomic H, and assumes only SEC.

The ACX package similarly uses estimations for the n and l distributions, but bases these purely from theoretical estimates without comparison to data.

The $n_{\max}$ in ACX is calculated with Equation 1.2, and offers two possibilities for the distribution of electrons around $n_{\max}$ if $n_{\max}$ is not an integer: assuming that all electron capture is into the rounded $n_{\max}$ channel, or weighting the two nearest n shells around $n_{\max}$ according to the integer fraction. After the n distribution calculation, the code determines the LSJ coupled states that would result in a photon up to $n \leq n_{\max}$, and uses the AtomDB database (and in some cases, the AUTOSTRUCTURE code [Badnell, 1986]) to determine the energies and transition probabilities between each of these levels. ACX only calculates the energies of shells up to $n = 10$.

ACX allows the user to determine the l distribution to be one of the four equations presented in Chapter 1 (Equations 1.7–1.10), and also allows the user to choose whether this distribution is applied to the total L or the l of the captured electron. This is specified via the ACX *model* parameter. The authors recognize that using these equations ignores many important considerations such as velocity dependence, and can only be used as rough approximations until more accurate calculations or measurements become available [Smith et al., 2014a].

The ACX package includes several models. The main model is ACX, in which the user can set an ion temperature distribution in keV, an abundance of metals in the plasma compared to solar, and other parameters. VACX is the variable abundance version of ACX, where the user can specify the relative elemental abundances. ACXION allows for the calculation of a spectrum from a single ion at a specific charge

state after it undergoes CX with H, He, or a mix of the two. All the ACX models can incorporate both H and He as the neutral partner by adjusting the model parameters, but like SPEX-CX, it only considers SEC.

2.3 Multi-Channel Landau Zener Theory

In Chapter 6, we present comparisons of our experimental data to Multi-Channel Landau Zener (MCLZ) theory. MCLZ was briefly introduced in section 1.2, but we now go deeper into its physical basis. Recall from Section 1.1 that CX at low energies resembles a molecular collision process. This is because in the limit of $v \ll v_0$, where v is the relative velocity between the collision partners and v_0 is the classical orbital speed of the electrons, the electrons are moving fast enough to be able to continuously adjust their motion to the relative position of the collision partners. This creates a so-called "quasimolecule" composed of the ion and neutral, whose energy levels are a function of the internuclear separation which varies slowly over time.

The duration of the collision with respect to the characteristic electron transition time, i.e., how long the electron is bound versus being transferred between the two collision partners, affects the adiabaticity of the collision process [Janev and Winter, 1985]. In slow collisions, the process is adiabatic, and at higher speeds, it becomes diabatic [Lichten, 1963]. In the CX collision, the quasimolecule moves along the potential of the initial, inbound state (on the diabatic potential) as the collision partners approach each other. In regions of strong curvature of two of

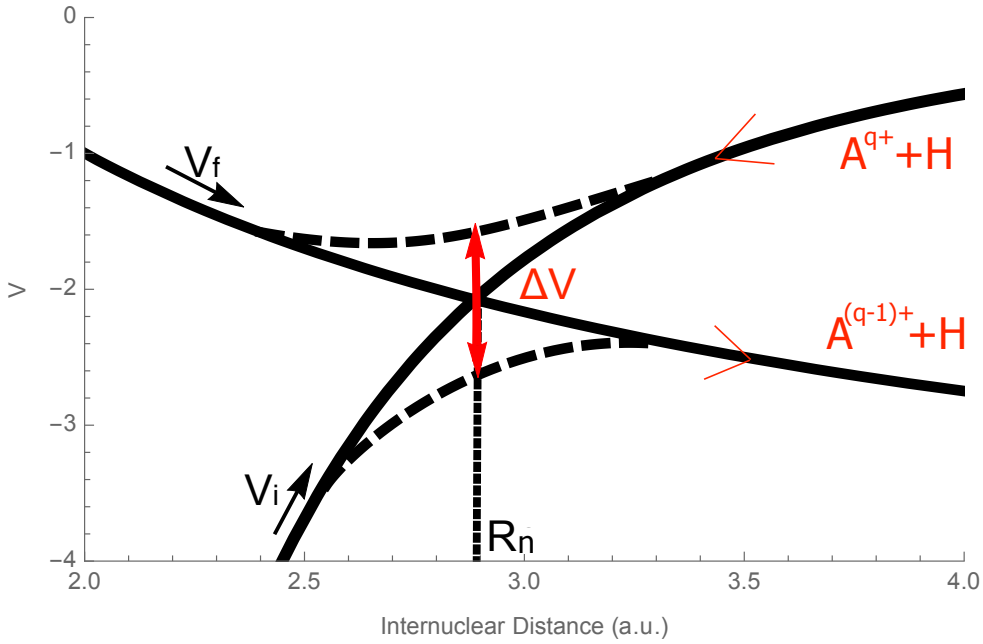

Figure 2.1 Schematic of the diabatic (solid lines) and adiabatic (dashed lines) energy curves, with an ingoing polarization potential V_i (Equation 2.3) and an outgoing Coulomb potential V_f (Equation 2.5). The quasimolecule travels along the initial, inward diabatic potential curve until it reaches a pseudocrossing R_n, where R is the internuclear distance. Here, the quasimolecule moves to the initial adiabatic curve, then to the final outward one. This is the electron capture process. Finally, the quasimolecule exits on the outgoing channel. Figure adapted from Cumbee [2016].

these potential lines or at very small internuclear separations, electron transfer can occur at a so-called "avoided curve crossing" or "pseudocrossing" [Eichler, 2005, Janev, 1983]. At these regions, the quasimolecule moves along the initial, then final adiabatic potential curves as the electron is transferred from the neutral to the ion. The outgoing quasimolecule then moves along the final, outbound diabatic potential curve. A schematic of this process is depicted in Figure 2.1.

Multichannel Landau-Zener theory [Landau, 1932, Zener, 1932] considers the

probability of electron transfer at these pseudocrossings, and can be used to derive state-selective (nlS-resolved) cross sections for CX interactions at low energies (below ~5 keV/amu). It is most accurately applied to a system with a fully stripped ion and neutral atomic H, because the symmetry of this system limits the density of pseudocrossings and keeps the transition regions fairly well isolated [Janev, 1983]. The most important parameters in the MCLZ calculation are the locations of any pseudocrossings, the magnitude of the energy separation of the two potential energy curves that make up the pseudocrossing, and the slope of those two potential energy curves [Cumbee, 2016].

The location of these pseudocrossings in atomic units can be approximated with

$$R_n \simeq 2n^2 \frac{q-1}{q^2-n^2} \tag{2.2}$$

for $n < q$, where n is the index of the pseudocrossing and q is the ion charge [Janev, 1983, Janev et al., 1983]. Based on this equation, we see that the n distribution of captured electrons for $n \geq q$ cannot be calculated with the MCLZ method [Janev, 1983].

Alternatively, R_n can be calculated by equating the two potentials of the inbound collision pair (one at large internuclear distances and another at small ones) with that of the outgoing collision pair and solving for R. The MCLZ code implemented to produce the cross sections in Section 6.5 uses this generalized form of R_n. The potentials involved are described in the following three equations.

At large internuclear distances, the potential is given by the polarization potential:

$$V_{pol} = -\frac{\alpha q^2}{2R^4}, \tag{2.3}$$

where α is the static dipole polarizability of the neutral (for H, $\alpha = 4.5$) [Cumbee, 2016].

At small internuclear distances, the potential between the approaching ion and neutral is given by the repulsive Born-Mayer potential:

$$V_{BM} = Ae^{BR}, \tag{2.4}$$

where A and B are fitting coefficients, given to be $A = 25q$ and $B = -0.8 + \xi_i$, where ξ_i is 1 for H and 1.7 for He [Butler and Dalgarno, 1980].

After electron transfer, both ion and neutral are positively charged, so the outgoing potential can be described by Coulomb repulsion:

$$V_{Coul} = \frac{(q-1)(q_{cap})}{R} - E, \tag{2.5}$$

where q_{cap} is 1 for SEC, and E is the collision energy in eV/amu.

With these potentials at play, we can now show how MCLZ calculates the probability of a transition occurring between an initial potential curve (i) and a final curve (f) at a particular pseudocrossing R_n. This probability is given by

$1 - p_n$, where p_n is given by the Landau-Zener formula:

$$p_n = \exp\left(\frac{-2\,\pi\,V_{if}^2}{\Delta F\,v_{rad}}\right). \tag{2.6}$$

ΔF is the difference in the slopes of the potential energy curves at the pseudocrossing R_n, and v_{rad} is the radial velocity at R_n, given by

$$v_{rad} = \nu\sqrt{1 - \frac{b^2}{R_n^2} - \frac{V_i}{E}}, \tag{2.7}$$

where ν is the collision velocity, b is the impact parameter, V_i is the initial potential energy, and E is the collision energy. V_{if} in Equation 2.6 is the potential energy difference between the initial and final potential curves at R_n, which for the MCLZ calculations shown in this dissertation, is given by the Olson-Salop-Taulbjerg approximation [Salop and Olson, 1976, Olson et al., 1971, Taulbjerg, 1986]:

$$V_{if} = \left(\frac{9.13\,f_{nl}}{\sqrt{q}}\right)\exp\left(\frac{-1.324\,R_n\,\alpha}{\sqrt{q}}\right). \tag{2.8}$$

α is a correction factor for the ionization potential of neutrals other than atomic H,

$$\alpha = \sqrt{2I}, \tag{2.9}$$

where I is the ionization potential of the neutral. f_{nl} is a correction factor to describe capture into nondegenerate l states for charge states lower than H-like. For H-like ions, $f_{nl} \to 1$ due to degeneracies. This results in the limitation that only n–resolved cross sections may be calculated for H-like ions [Mullen et al., 2016]. To obtain nl–resolved cross sections for this charge state, an l distribution function

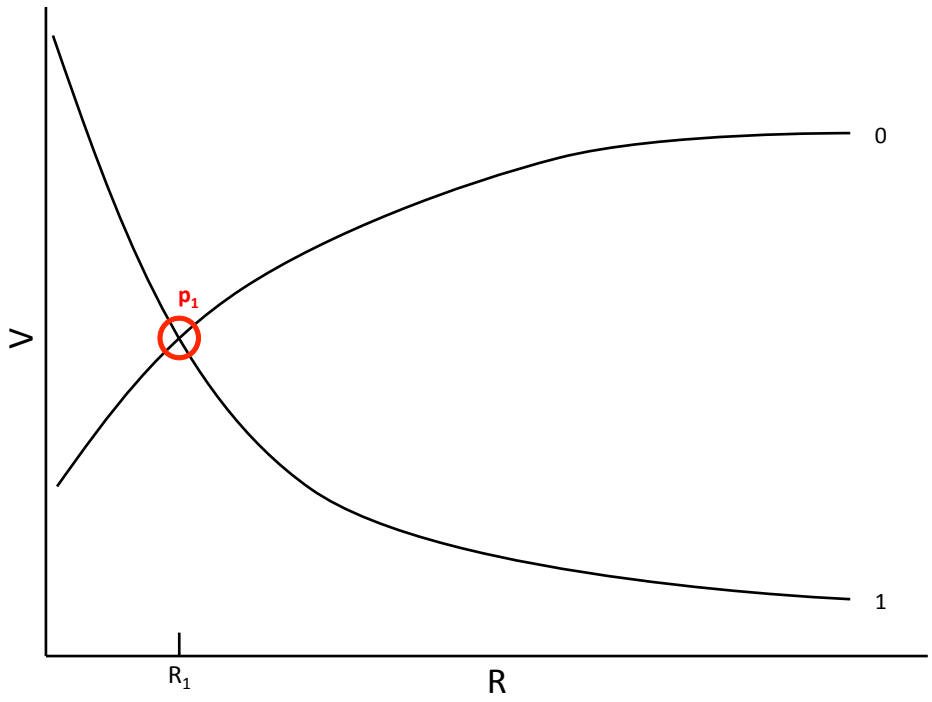

Figure 2.2 One pseudocrossing p between initial potential state 1 and final potential state 2.

must be applied. We discuss possible l distributions shortly.

This transition probability just discussed is illustrated in Figure 2.2, which depicts one initial state (0, potential given by Equations 2.3 and 2.4), one final state (1, potential given by Equation 2.5), and one pseudocrossing at R_1 between them with a probability of p_1.

Using the probability defined in Equation 2.6, the probability of two crossings at R_n are $2p_n(1-p_n)$. Generalizing this to N crossings going to a final state f requires considering the mutual interaction of all potentials. In this case, we have

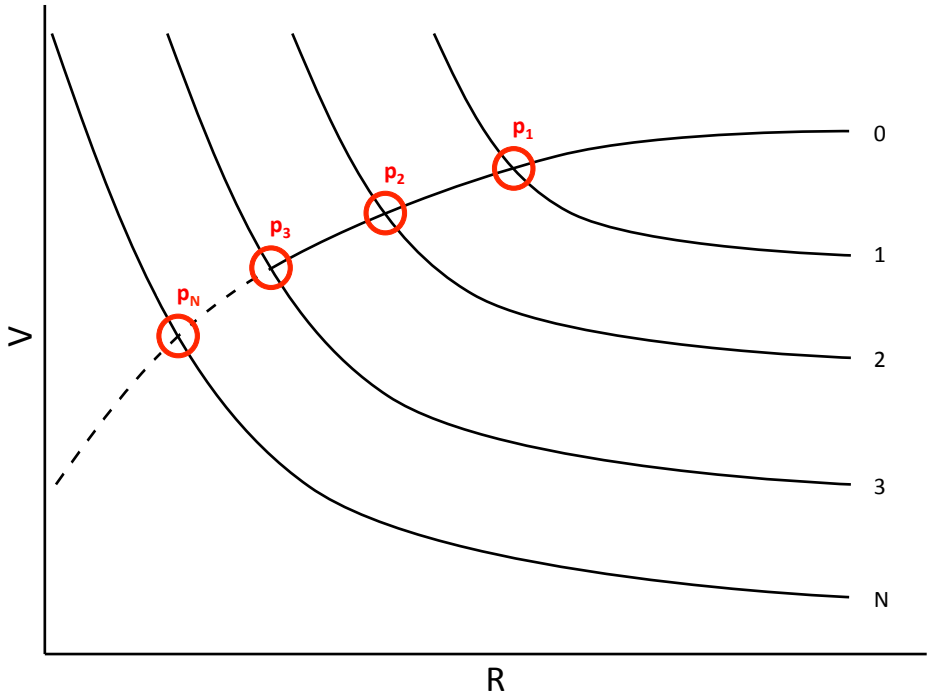

Figure 2.3 N-1 pseudocrossings between N potential states, where each p_n represents a pseudocrossing happening between the initial state and final state n.

[Janev et al., 1985]

$$\begin{aligned} P_f = p_1 p_2 \dots p_f (1-p_f)[1 + (p_{f+1} p_{f+2} \dots p_N)^2 + \\ (p_{f+1} p_{f+2} \dots p_{N-1})^2 (1-p_N)^2 + \\ (p_{f+1} p_{f+2} \dots p_{N-2})^2 (1-p_{N-1})^2 + \\ \dots p_{f+1}^2 (1-p_{f+2})^2 + (1-p_{f+1})^2]. \end{aligned} \tag{2.10}$$

This process is depicted in Figure 2.3. In this figure, the ingoing channel is 0, and the final outgoing channel f is chosen to be one any one of the numbered states.

The partial cross section for one particular transition between state i and state f, i.e. the goal of the MCLZ calculation, is then given by integrating this probability over all possible impact parameters:

$$\sigma_f = 2\pi \int_0^{R_n} P_f \, b \, db \, . \tag{2.11}$$

The total cross section for capture is given by

$$\sigma = \sum_{n=1}^{N} \sigma_f . \tag{2.12}$$

As previously mentioned, MCLZ can only calculate an n distribution for bare (going to H-like) ions; to get nl-resolved cross sections, it is thus necessary to apply an l distribution. Janev [1983] does this by multiplying the n-resolved cross section by an l distribution:

$$\sigma_{nl} = W_{nl} \, \sigma_n , \tag{2.13}$$

where W_{nl} takes different forms depending on the energy regime of the collision. Several commonly-used distributions are presented in Equations 1.7–1.10. The two most commonly used in MCLZ calculations are repeated here for convenience. For high collision energies of ∼1 keV/amu or higher, the l levels are found to be populated statistically [Janev and Winter, 1985]:

$$W_{nl}^{stat} = \frac{2l+1}{n^2} . \tag{2.14}$$

For energies below this threshold, Abramov et al. [1978] derived a low-energy

distribution function:

$$W_{nl}^{low\ e} = (2l+1)\frac{[(n-1)!]^2}{(n+l)!(n-1-l)!}. \tag{2.15}$$

Equation 2.14 is thus the same as the statistical distribution function presented in Equation 1.7, and Equation 2.15 is the same as the "low energy I" equation used in SPEX-CX from Equation 2.1.

For further reading on MCLZ theory, see, for example, Janev [1983], Bliek et al. [1998], Salop and Olson [1976], Eichler [2005], Janev et al. [1985], Janev and Winter [1985], and Cumbee [2016].

Chapter 3: The Role of Laboratory Astrophysics in Improving Charge Exchange Models

While theoretical models are important for a nuanced understanding of CX, they are most useful in concert with experiments that test them. Experiments are not only important for benchmarking theoretical models, however: through experiments, we learn new and often surprising things empirically that may not be expressed in theory (e.g., Leutenegger et al. [2010]). Of course, with any experiment, it is important to disentangle physical results from the processes under study from any instrumental and experimental effects. To do this, one must have a deep understanding of the tools used and the errors that contribute to a result. In this vein, we will describe the operating principles of the tools used for the CX experiments presented in this dissertation, namely an electron beam ion trap (EBIT) and an X-ray microcalorimeter.

3.1 The LLNL Electron Beam Ion Trap

The EBIT-I facility at the Lawrence Livermore National Laboratory (LLNL), where the EBIT was invented, is an ideal environment in which to perform laboratory astrophysics measurements, as the EBIT can produce well-characterized

plasmas in specific ionization states for nearly every element through bare uranium. The EBIT-I and EBIT-II at LLNL were the first devices utilized specifically for laboratory astrophysics [Beiersdorfer, 2003]. Within the set of plasma sources available for laboratory use (including Z-pinches, tokamaks, vacuum sparks, etc.), EBITs are especially useful for laboratory astrophysics because the densities achieved in the trap are low enough to be in the coronal limit, i.e. the rate of collisional processes is much lower than that of radiative or autoionization processes. This means that an ion, after an excitation, ionization, or recombination event, has time to de-excite to the ground state and emit radiation that can be used for spectral diagnostics.

The main components of the EBIT are an electron gun and three sets of cylindrical electrodes, called drift tubes, that are oriented along a vertical axis. These drift tubes are elevated to a tunable voltage potential by a low-noise high voltage amplifier (which we call the drift tube rack voltage), and an additional floating low voltage power supply superimposes additional bias to the three individual drift tubes. The electron beam originates from the gun, and the electrons are accelerated towards the bottom, middle, then top drift tubes, as shown in Figure 3.2. The ion trap region is created in the 2 cm–long middle drift tube region, which is kept at a lower bias than the bottom and top drift tubes. Adjusting the top and middle drift tube voltages allows us to vary the depth of the ion trap. These drift tubes create the ion trap in the axial direction; ions are radially confined due to the electrostatic attraction to the electron beam.

The trap region is surrounded by a pair of superconducting Helmholtz coils. The 3 T magnetic field from the coils compresses the electron beam to a diameter

of ∼60 μm, and also serves as the ion trapping method in the radial direction when the beam is off (so-called magnetic trapping mode, discussed shortly). After the electron beam passes through the drift tube assembly, it is defocused by a magnet and directed into the collector electrode, which is cooled with liquid nitrogen to offset the heat input from the beam. The EBIT axis is vertical, and to allow direct line-of-sight access to the trap region, there are six radial ports, onto which are attached various spectrometers and gas injectors. A schematic of the LLNL EBIT is shown in Figure 3.1, and a schematic of the trap region is shown in Figure 3.2.

We inject neutral species directly into the trap, where the electron beam collisionally excites and ionizes them to our desired charge state. In the experiments presented here, we inject gases in two ways. The first is via a ballistic gas injector, mounted on one of the radial ports. This injects a collimated stream of neutral gas directly into the electron beam. The amount of gas injected is controlled by the injection pressure, which is regulated by a thermal valve. We typically inject gases from a compressed gas cylinder, and in some cases, liquids with a high vapor pressure at room temperature. Solids used in our experiments, such as Ni, are injected with a sublimation injector. The injection pressure is adjustable, and vapor from the sublimator is collimated and aligned to intercept the electron beam. The background EBIT chamber pressure is low (on the order of a few 10^{-10}–10^{-11} torr), and gas injection pressures are usually on the order of 10^{-6}–10^{-9} torr.

The charge state of the ions is determined by the energy of the electron beam, the amount of time the ions interact with the beam, and recombination processes in the trap. Electrons are stripped off the ions sequentially until the next ionization

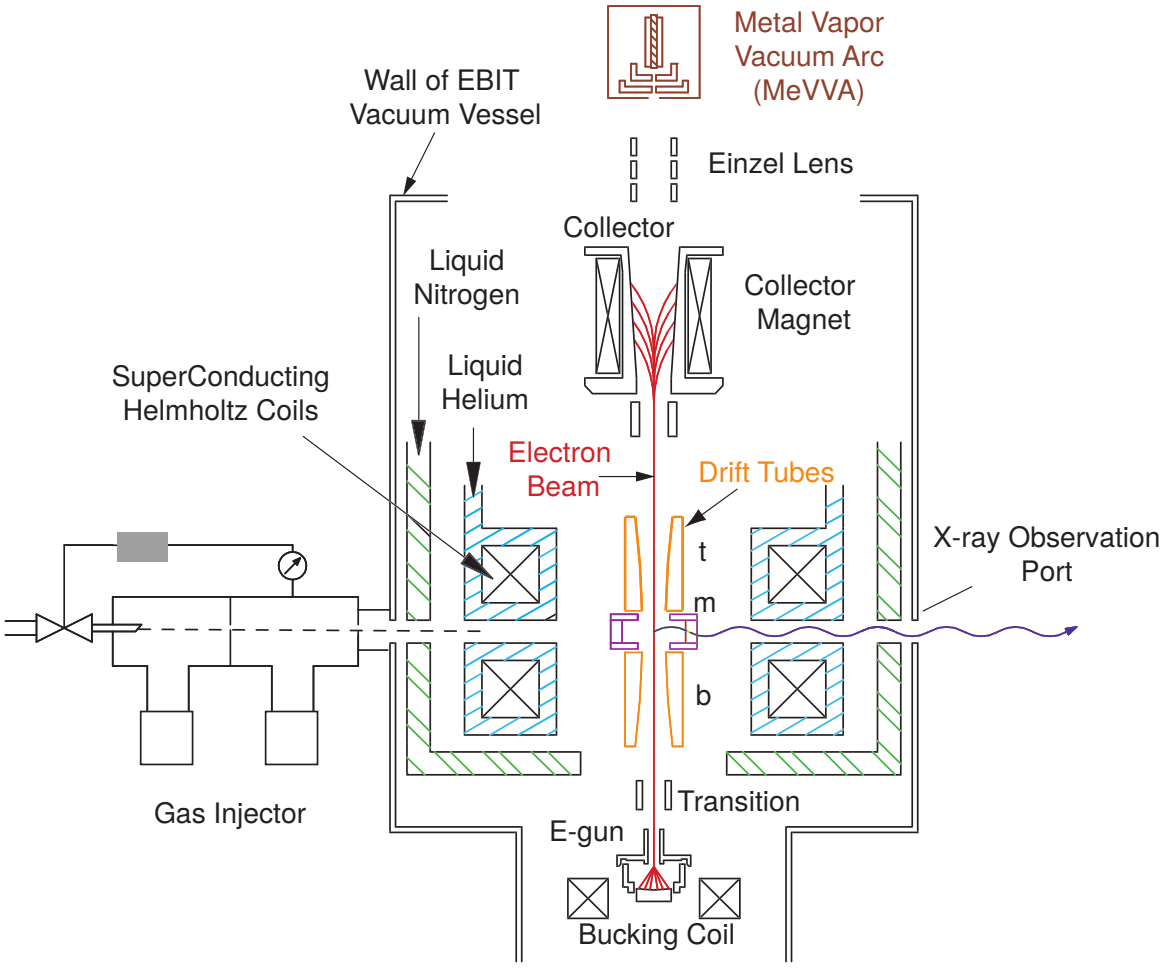

Figure 3.1 Schematic of the LLNL EBIT-I, courtesy of Klaus Widmann.

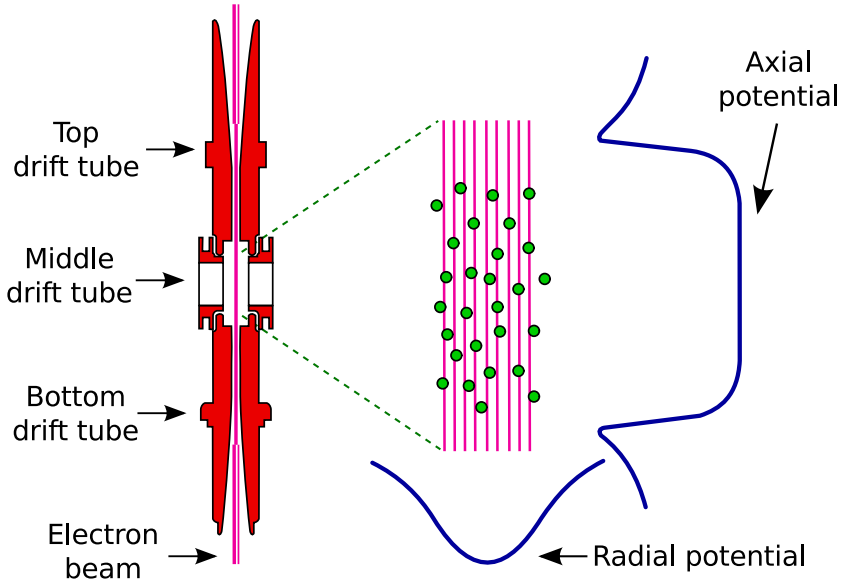

Figure 3.2 Sketch of the trap region of the LLNL EBIT-I, courtesy of https://ebit.llnl.gov/ and Natalie Hell.

potential is higher than the electron beam energy. The energy of the electron beam is determined by

$$E_{beam} = e(V_{DT} + V_{MDT} + V_{SC}), \tag{3.1}$$

where e is the electron charge, V_{DT} is the voltage of the drift tube rack, V_{MDT} is the voltage of the middle drift tube, and V_{SC} is the space charge voltage as determined below. Negative space charge is generated by electrons in the beam, and positive space charge is generated by trapped ions. The electron beam space charge in Volts can be approximated by

$$V_{SC} = -5.4\frac{I_b}{\sqrt{E_b}}, \tag{3.2}$$

where I_b is the electron beam current in mA and E_b is the electron beam energy in keV [Brown, 2000]. It is estimated that the positive space charge from the ions reduces the effect of the electron beam space charge by half [Brown, 2000], so this number is often divided by two before using the value in Equation 3.1.

Precise selection of an electron beam energy is important to produce a desired ion charge state. The electron beam energy is nearly monoenergetic, with an energy distribution that is roughly Gaussian in shape with a FWHM of ∼30 eV [Beiersdorfer et al., 1992]. Because of the monoenergetic nature of the electron beam in normal operation, plasmas created in the EBIT are not thermal. The beam energy can be tuned to as low as 100 eV and as high as 20 keV [Beiersdorfer, 2003]. For our experiments, the energy was typically in the range of 1-12 keV.

The electron beam current is controlled by the voltage of the anode on the electron gun. The current of the LLNL electron gun in Amperes is given by

$$I = pV_a^{3/2}, \tag{3.3}$$

where p is the perveance, which for the LLNL EBIT is 0.5 μperv [Gu, 2000], V_a is the anode voltage of the gun in Volts. Typical beam currents are on the order of ∼100–200 mA. The electron density in the trap, which is determined by the electron beam current, is $\sim 10^{10}$–10^{12} cm^{-3} for most experiments [Beiersdorfer, 2003].

Ions are heated by elastic collisions with the electron beam. The ion temper-

ature in eV is approximated by

$$T \sim \alpha q V, \tag{3.4}$$

where α is an efficiency factor, typically taken to be 0.2, q is the ion charge in units of elementary charge, and V is the trap potential in Volts [Levine et al., 1989]. For the species typically used in most laboratory astrophysics experiments, ion temperatures are about 50 eV/amu. Ions with sufficient (thermal) kinetic energy can overcome the potential barrier of the trap and escape in a process called evaporative cooling. Because of the effects of evaporative cooling and the approximate nature of the value of the efficiency factor, it is helpful to have an in-situ measurement of the ion temperature, rather than simply extrapolating one from the trapping potential. One can do this by taking high-resolution measurements of the doppler broadening of a spectral line with, for example, a crystal spectrometer. This process was performed in, for instance, Leutenegger et al. [2013].

As ions with lower charge experience a lower trapping potential and thus can escape the trap with a lower kinetic energy, low-Z species may be intentionally injected to carry away excess thermal energy and keep the average ion temperature low. Conversely, high-Z elements such as Ba (Z=56) and W (Z=74), which evaporate off the electron gun and enter the trap, can eventually dominate the ion population. To mitigate this, the potential of the top drift tube can be lowered below that of the middle drift tube as a function of time. In this so-called "dump," ions are accelerated upwards towards the collector and out of the EBIT.

It is possible to adjust the timing pattern of the voltage supplies to change the EBIT parameters, charge balance, and even EBIT mode as a function of time. The EBIT can be run in two modes: electric trapping mode and magnetic trapping mode. In electric trapping mode, the electron beam is on and the injected gas is collisionally ionized and trapped. In magnetic trapping mode [Beiersdorfer et al., 1996b], the electron beam is turned off, and the ions initially created with the electron beam are radially confined in the trap by the magnetic field instead of the electron beam. In this mode, the EBIT is effectively a Penning trap. We study the emission from charge exchange (CX) recombination in magnetic trapping mode. The electron beam energy and current can also be swept as a function of time to create a pseudo-Maxwellian thermal electron distribution [Savin et al., 2000] with a characteristic electron temperature.

3.2 The EBIT Calorimeter Spectrometer

The EBIT Calorimeter Spectrometer (ECS) is an invaluable tool for many of the laboratory astrophysics experiments performed at the LLNL EBIT facility, including the CX work presented here. The ECS system is low-maintenance and easy to use, and the non-dispersive spectrometer yields high spectral resolution and quantum efficiency across a wide energy band. Further, the ECS data acquisition system time-tags each photon with its arrival time, which allows us to differentiate between photons from electric versus magnetic trapping mode for CX experiments, or to isolate transient states such as during the charge breeding process.

In this section, we will provide the framework for understanding how the ECS works, both theoretically and operationally, and how to understand its results and uncertainties. We will first review the basics of microcalorimeter theory, then move on to the specific ECS system, then finally give an overview of a new microcalorimeter spectrometer system in development at NASA's Goddard Space Flight Center (GSFC) that will soon be delivered to the LLNL EBIT facility.

3.2.1 X-ray Microcalorimeter Basics

X-ray microcalorimeters (referred to interchangeably as X-ray calorimeters) are attractive for X-ray spectroscopy due to their imaging capabilities and impressive spectral results across a wide bandpass (i.e., Collaboration [2016]). Here, we will discuss general microcalorimeter theory for the ideal case, a few details to consider in detector design, and finally selected non-ideal cases. For more details and derivations, one can peruse these resources: Enss [2005], Figueroa Feliciano [2001], and Moseley et al. [1984].

A microcalorimeter is a near-equilibrium, non-dispersive, thermal detector. Thermal detectors measure the heat of each incoming photon that is incident upon the detector. Non-dispersive detectors determine the energy of incident X-ray photons without diffracting the light onto a position-sensitive detector, as crystal and grating spectrometers do. Though dispersive spectrometers exhibit extremely high resolution (typical R$\sim$3000), they are not suitable for observations of extended sources, as light from different regions of the observation would be diffracted to

different locations on the position-sensitive detector. This confuses the spectral information with the spatial. Using a non-dispersive spectrometer is vital for the extended X-ray emission in the EBIT trap during magnetic trapping mode, when the ion cloud spreads out.[1]. Near-equilibrium detectors measure nearly all the energy from each photon event, with very little energy getting lost. This is in contrast to, for example, ionization detectors such as CCDs, where some of the photon energy goes into a detectable form of internal energy (i.e., free charge), but a significant fraction goes into undetectable forms of internal energy, such as heat. This leads to a fundamental constraint on the energy resolution of such detectors. In contrast, because nearly all the energy of photons incident upon calorimeters goes into thermal energy, which is exactly the quantity being detected, they can theoretically have much higher energy resolution.[2]

Microcalorimeters fundamentally only consist of three parts: an X-ray absorber, a thermometer, and a heat sink kept at cryogenic temperatures (∼50 mK) to achieve optimal detector sensitivity. Mirroring this simplicity, microcalorimeters

[1]It should be noted that although crystal spectrometers have limited use for extended sources, as discussed here, and also can only operate within a narrow energy bandpass at one time, their extremely high resolution makes them extremely useful for many EBIT experiment where extreme precision is required and a narrow bandpass can be tolerated. These include measurements of absolute cross section measurements as in Brown et al. [2006] and absolute wavelength measurements as in Brown et al. [2002] and Gu et al. [2007a].

[2]The fundamental limit on the energy resolution of CCD detectors is due to the fano factor, as discussed here, as well as counting statistics for the measured electrons. The fundamental limit for microcalorimeters is due to energy being transferred across the weak link between the thermometer and the heat bath. This is called phonon noise, and will be discussed shortly.

detect the energy of an X-ray event in just three steps. First, the X-ray is absorbed by the absorber through the photoelectric effect and is thermalized, next, the thermometer measures the temperature rise of the absorber, which corresponds to the energy of the photon, and finally, the heat from the event bleeds out to a heat sink, which is weakly linked to the absorber to cool the system back down to its equilibrium temperature to be ready for the next event. This is the picture for one detector, which we call a pixel; by creating arrays of these absorber-thermometer pairs, we create an imaging spectrometer. Figure 3.3 presents a schematic of a single-pixel calorimeter.

Now including a few variables: if the energy of incident photon is E_0 and absorber has some heat capacity C, assuming instant thermalization, the temperature rise of the absorber is

$$\Delta T \simeq E_0/C(T). \tag{3.5}$$

The absorber, which is connected to the thermal bath with a thermal conductance G, will then cool to the bath temperature. This creates a temperature pulse profile for each incident photon. The shape of this pulse is proportional to the energy of the photon.[3] The time-dependent equation for this profile is

$$T(t) = \frac{E_0}{C(T)} e^{\frac{-t}{\tau}}, \tag{3.6}$$

[3]There are several metrics we can use to convert the shape of the pulse to a photon energy, such as the pulse height or the area under the curve. In our analysis, we use the amplitude of the pulse at all frequencies.

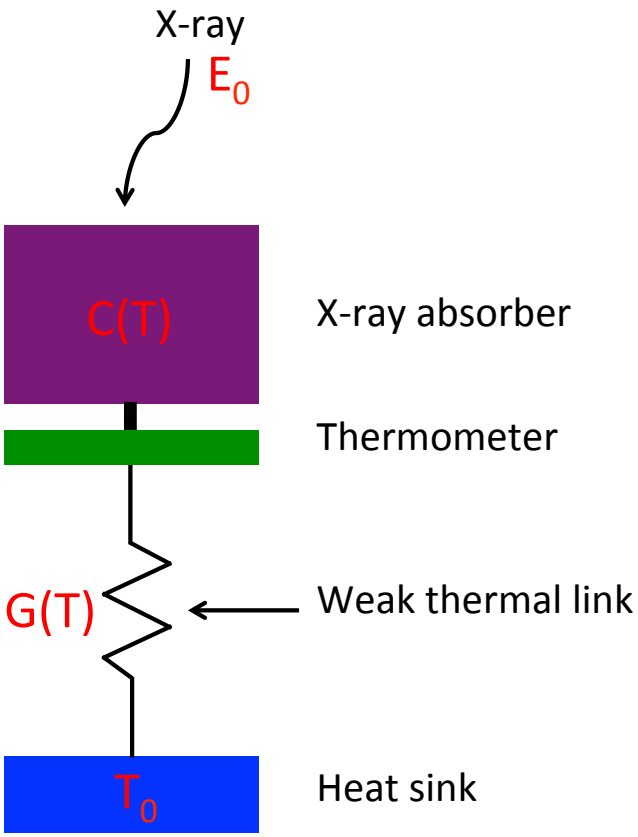

Figure 3.3 Schematic of an ideal microcalorimeter. An absorber with heat capacity $C(T)$ is connected to a thermometer. This pair is then connected through a weak thermal link with a thermal conductance $G(T)$ to a heat bath at temperature T_0, nominally 50 mK. An X-ray with energy E_0 incident upon the absorber is thermalized and the temperature change is read out by the thermometer.

where the time constant of the exponential decay is

$$\tau \simeq \frac{C(T)}{G(T)}, \tag{3.7}$$

valid only without the presence of electrothermal feedback, which is discussed shortly. An approximation of this temperature profile is shown in Figure 3.4. This simple equation tells us that by knowing the parameters C and G and by measuring T, we can determine the energy of the photon. Conversely (and more realistically), with a well-characterized energy source, we can derive the properties C and G from this ideal case.

With this information in mind, let us now consider some qualitative design criteria and trades for the three basic parts of a microcalorimeter. Two important qualities for the absorber are high stopping power to measure as many photons as possible (achieving high quantum efficiency), and quick internal thermalization (in the crystal structure of the absorber) and a compact geometrical design, so the energy input on the absorber is not position-dependent, which degrades the energy resolution. In addition, the combination of a low C (of both the absorber and the thermometer) and a high G to the heat bath allows the detector to quickly return back to base temperature, so more photons can be collected over a short amount of time. This avoids a phenomenon called pileup, in which a second photon is absorbed too soon after a first one, and thus the detector has not yet returned back to its base temperature.

See Morgan [2015] and references therein for a discussion about material

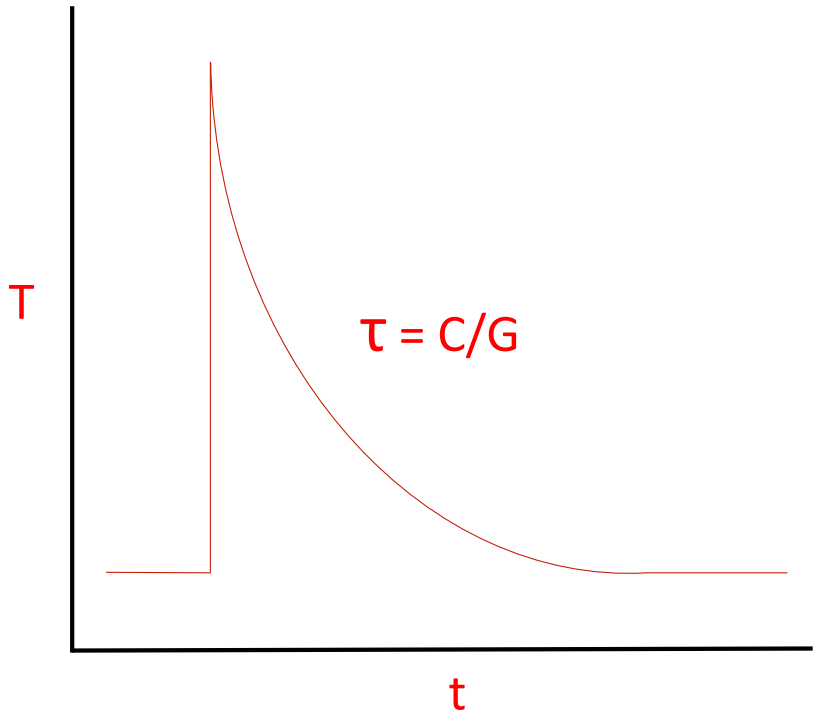

Figure 3.4 Schematic of an X-ray pulse from an ideal microcalorimeter. The height of the pulse is a function of the photon energy and the heat capacity, and the time constant of the decay is equal to the heat capacity of the absorber divided by the thermal conductance to the heat bath.

choices and design trades for the absorber. The detectors fabricated at NASA/GSFC use either a combination of mercury and tellurium (MgTe) or bismuth and gold (BiAu).

The main desired quality for a microcalorimeter thermometer is the ability to accurately measure a very small change in temperature without adding much noise to the system. Our choice of thermometers is fairly wide, but here we will focus on resistive thermometers, otherwise known as thermistors, whose resistance varies as a function of temperature. Operationally, this means that the quantity we measure after an X-ray pulse is the resistance of the thermometer, in some form. At GSFC, the thermistors we use are either semiconductors (called "silicon-thermistor devices") or superconductors (called "Transition-Edge Sensors," or TESs). Si-thermistor devices were developed first, but there are practical limits on their ability to scale up to large arrays of pixels, which we will discuss shortly. Because of this, in recent years, the field has moved to TESs. TESs have proved to routinely yield high resolution and can scale up to array sizes of thousands of pixels, though this technology is not without new complications (see Section 3.3).[4]

The weak link to the thermal bath determines in part how quickly the detector cools back down to its equilibrium temperature, and the optimal link must balance competing interests. On one hand, the thermal time constant should be longer than the time it takes for the absorber and thermometer to reach thermal equilibrium

[4]The fundamental limits on Si-thermistor detectors and TESs are the same, and they both can be optimized to achieve similar energy resolution for a variety of applications. The choice between one or another often depends on the size, mass, and power constraints of the experiment.

after a pulse. However, if the thermal time constant is too long, the risk of pileup increases, which ultimately leads to lower energy resolution.

The main job of the detector heat sink is to achieve a low temperature that is steady and well-controlled. This can be done in many ways, always involving successive thermal stages that make discrete transitions from the outer layer at room temperature to the inner detector cold stage. The details of the various cooling methods are beyond the scope of this dissertation, but one such way, implemented in the ECS system, is described in the following section.

In practice, there are countless other design considerations to take into account when choosing the materials and design of a calorimeter than what has been briefly mentioned here. These include factors such as structural stability, robustness against vibration or temperature changes, cost, ease of fabrication, among others. Additionally, one must consider the thermal, mechanical, magnetic, and superconducting/semiconducting properties of the chosen materials, and realize that altering the materials, thicknesses, geometries, temperatures, and, where applicable, superconducting or semiconducting properties of a chosen design will change the properties and performance of the detector. Furthermore, external factors such as noise and magnetic fields, along with the choice of detector readout hardware and the method of pulse analysis will add variation and complexity in detector properties and performance.

Now that we have already begun to drift away from the ideal case, let us consider more concretely a few more complications; mainly noise and other effects present in a real detector system. Remember that our goal is to calculate a photon

energy. However, the information we measure is not just due to photons incident upon the detector; there are various sources of noise that we must disentangle from our true signal to accurately measure the photon energy.

There are two fundamental noise sources intrinsic to resistive X-ray microcalorimeters that must be considered: phonon noise and Johnson noise. Phonon noise arises from the presence of the weak link between the detector and the cold bath: this can be thought of as Poisson fluctuations in the number of energy carriers in the detector that have a mean energy $k_B T$ [Enss, 2005]. These fluctuations have the same frequency spectrum as a pulse, and contribute an average change in energy in the detector of

$$\langle \Delta E^2 \rangle = k_B T^2 C(T), \tag{3.8}$$

where k_B is the Boltzman constant, T is the temperature of the detector, and $C(T)$ is the temperature-dependent heat capacity of the device. To minimize this effect, it is helpful to reduce T and $C(T)$.

Johnson noise is caused by the Brownian motion of electrons in the thermistor, and leads to fluctuations in the temperature readout. The power spectrum from Johnson noise is nearly white. Johnson noise is also present in other parts of the system connected to the detector, like resistors in the circuit or from an amplifier. Though both phonon and Johnson noise are nearly constant across all frequencies, the natural time constant τ of the thermistor will damp out any phonon fluctuations with frequencies greater than $2\pi\tau$.

Considering a microcalorimeter as part of a system with other instruments introduces many other noise sources that are extrinsic to the detector but often present in real calorimeter systems, and which limit their spectral performance. A random selection of these noise sources include fluctuations in temperature of the heat bath, RF pickup, shot noise from stray photons, noise in the amplifier chain, 1/f noise [Stahle et al., 1999], and mechanical vibrations from nearby pumps. Other complexities arise from the fact that a detector is not made up of a single pixel, but rather an array of them. Because of the close proximity of pixels, heat input to one pixel may be detected by a neighboring one in a process called thermal crosstalk. This becomes worse at high count rates, and is a major limiting factor for the performance of large arrays of pixels.

A much more complete discussion on noise sources is presented in Enss [2005]. In general, sources of noise should be eliminated or reduced as much as possible, but if present, they should be well-characterized in order to determine their effect on the signal during post-processing. This can be done via a so-called "optimal filtering" procedure, which will be described in the following section.

Besides noise sources, a commonly discussed feature of resistive thermometers is electrothermal feedback. To understand this, we must first place the calorimeter in a circuit. Recall that we use thermistors to determine the ΔT of a pixel after a photon event, due to their well-known resistance versus temperature curve. We must thus measure the resistance across the thermistor before, during, and after a pulse. In practice, we achieve this by running current across the thermistor, measuring the voltage drop, and calculating the resistance. For Si-thermistors, in order to give the

thermistor a constant supply of current, we voltage bias it through a load resistor of high value. This causes the current through the thermistor to be mainly dependent on the value of the load resistor. A simplified circuit diagram of this (Si-thermistor) detector scheme is shown in Figure 3.5. One may note the presence of an amplifier: the small voltage drop across the thermistor must be amplified near the cold detector stage before moving the signal to subsequent warmer thermal stages. The JFET is placed there in order to minimize capacitive vibrational noise induced in the long cable that extends to higher temperature stages. For Si-thermistor devices fabricated at GSFC we use junction gate field-effect transistors (JFETs, which are voltage amplifiers), and for TESs, we use superconducting quantum interference devices (SQUIDs, which are current amplifiers).

Electrothermal feedback occurs due to current passing through the thermistor in order to measure the temperature. The current causes the thermistor to heat via Joule heating, but this in turn changes the resistance of the thermistor, which then changes the voltage drop across the resistor. Whether this is positive or negative feedback depends on the sign of the thermistor's resistance dependence on temperature, and whether the detector is voltage- or current-biased. Both Si-thermistor and TES devices experience negative electrothermal feedback. In the case of a TES, the resistance in its superconducting-to-normal transition increases with temperature. With a constant applied voltage bias, the Joule power ($P_J = V^2/R_{TES}$) will decrease as the temperature increases. For Si-thermistor arrays, the resistance decreases as a function of temperature, but Si-thermistor arrays are current-biased rather than voltage-biased. Negative electrothermal feedback stabilizes the device against ther-

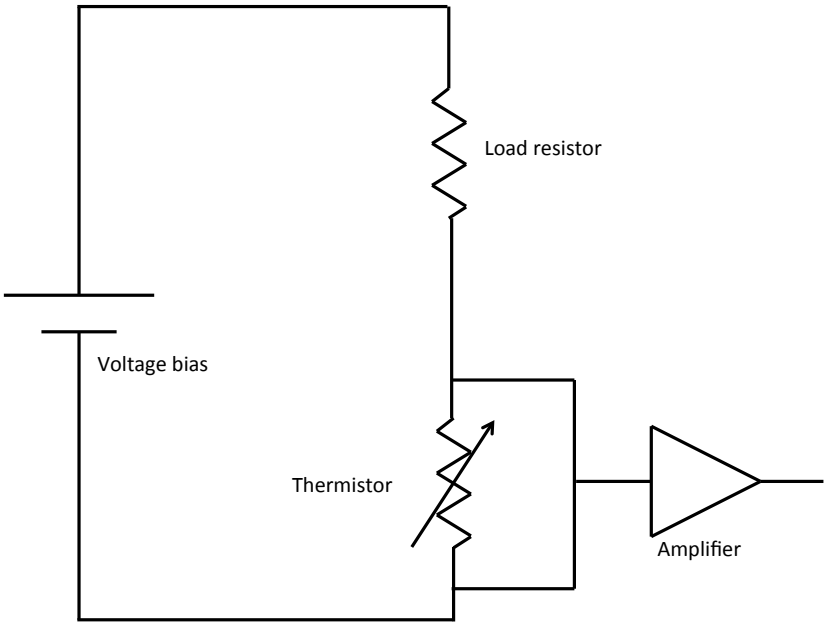

Figure 3.5 A simplified Si-thermistor calorimeter bias circuit diagram with a load resistor, a voltage-biased thermistor, and an amplifier.

mal runaway, and has the added effect of shortening the thermal decay constant τ.

To wrap up our general view of microcalorimeters, noise, and optimization, we will briefly show the dependence of the theoretical full-width half-max energy resolution on several aforementioned parameters. A full derivation of this can be found in Figueroa Feliciano [2001] and Enss [2005]; here, we will simply point out that the energy resolution is limited by the various sources of noise that are present in the measurement of a pulse. To calculate the intrinsic energy resolution of a device, one must calculate the so-called noise-equivalent power (NEP) for each of these sources. The NEP is the equivalent inferred power given as an input that produces a given output noise at a particular frequency, and is related to the energy resolution [Moseley et al., 1984] by

$$\Delta E_{RMS} = \left(\int_0^\infty \frac{4df}{\mathrm{NEP}^2(f)} \right)^{-1/2}. \tag{3.9}$$

One then sums the NEP of each noise source in quadrature (assuming they are uncorrelated), as in the following:

$$\mathrm{NEP}^2_{total} = \mathrm{NEP}^2_{phonon} + \mathrm{NEP}^2_{Johnson} + \ldots \tag{3.10}$$

Inputting the relevant variables for the intrinsic sources of noise gives [Enss, 2005]

$$\Delta E \sim \sqrt{\frac{k_b T_0^2 C}{\alpha}}, \tag{3.11}$$

where α is the dimensionless sensitivity of the thermistor, essentially, the sharpness of the slope of its R vs T curve in the operating region:

$$\alpha \equiv \frac{dlogR}{dlogT} = \frac{T}{R}\frac{dR}{dT}. \tag{3.12}$$

Equation 3.11 tells us that we would like to run our detector as cold as possible, choose materials that have a low heat capacity, and select a thermometer with a very high dependence of R on T.

The most basic goal of a microcalorimeter is to determine the energy of a single photon. Next we shall address how this is accomplished in practice, considering all parts of the system, each with some error contribution. We will thus move from a generalized case to a more specific one of the ECS, and follow the path of a photon generated in the EBIT chamber, from creation as a photon to a count in a histogram that makes up a spectrum.

3.2.2 The EBIT Calorimeter Spectrometer

The EBIT Calorimeter Spectrometer contains a Si-thermistor microcalorimeter array provided by GSFC that has been a permanent facility-class instrument at the LLNL EBIT since 2007. Its predecessor, the XRS/EBIT, was based on the engineering models of the detector systems and microcalorimeter arrays from the Astro-E and Suzaku missions. During its seven years of operation at the EBIT, the XRS/EBIT yielded groundbreaking laboratory astrophysics measurements, including the first high-resolution (5.5–6.0 eV FWHM at 6 keV) observations of CX in

astrophysical elements [Beiersdorfer et al., 2003b]. However, the XRS/EBIT was not meant to be a permanent instrument: it required frequent upkeep of its liquid cryogens for operation, and its duty cycle was rather short. The ECS was developed as an permanent upgrade to the XRS/EBIT system, building off experience operating and assembling the XRS detector array and with prototype and spare hardware from the Astro-E and Astro-E2 programs [Porter et al., 2000, 2008b]. Many of the upgrades made it significantly more user-friendly than the XRS/EBIT: less frequent cryogenic maintenance, an almost completely automated cooling procedure, and a much longer hold time at its operating temperature of 50 mK. The detector array also exhibited improved resolution over the XRS/EBIT, achieving ∼4.5 eV FWHM at 6 keV.

The ECS uses four steps to achieve the 50 mK operating temperature for the detector array heat sink. The outer jacket of the ECS cryostat is cooled with liquid nitrogen to 77 K. Next, an inner jacket is filled with liquid helium at atmospheric pressure, which cools to 4 K. This shields a He-3/He-4 sorption cooled refrigerator that cools to ∼350 mK. Finally, the sorption cooler is thermally linked via a heat switch to an adiabatic demagnetization refrigerator (ADR) which cools the connected detector array to its operating temperature of 50 mK.

He-3/He-4 sorption coolers work by condensing He-3 gas after bringing it in contact with a sorption pumped He-4 reservoir at ∼1 K. The temperature of the He-3 liquid is then reduced by pumping on it using a sorption pump.

ADRs use a paramagnetic salt crystal surrounded by a magnet to control the direction of the magnetic moments in the salt. Bringing up the magnetic field aligns

the magnetic moments, which generates heat that is transferred to the He-3/He-4 cooler. Once the ADR and detector have cooled back to the He-3 temperature, the thermal link to the He-3/He-4 cooler is broken. The magnetic field is then reduced slowly, allowing the entropy of the salt pill to increase and thus lower its temperature. Once the magnetic field has been reduced to zero, the cooling power has been exhausted and the cycle must be repeated.

In the ECS system, the ADR and sorption cooler are recycled together under software control. Temperature fluctuations of the ADR are minimal ($\leq$ 200 nK RMS at 50 mK), thus contributing negligibly to degradation in the detector resolution. The ECS cryogenic package is shown in Figure 3.6.

The ECS detector is a 30-pixel array of silicon-doped thermistors divided into mid- and high-energy pixels, which together have a dynamic range of $0.05 - > 100$ keV. The 16-pixel mid-band array uses 8 μm thick HgTe absorbers each with an area of 625×625 μm and 95% quantum efficiency at 6 keV, and is sensitive to 0.05–12 keV. The 14-pixel high-energy array, sensitive to 0.3–100 keV, uses 100 μm thick HgTe absorbers with a size of 625×500 μm and has 32% quantum efficiency at 60 keV. Figure 3.7 shows the ECS detector chip, including both mid-band and high-band pixels.

3.2.3 ECS Data Acquisition and Analysis

Let us now begin our task of following the path of a photon from creation to a count in a spectrum.

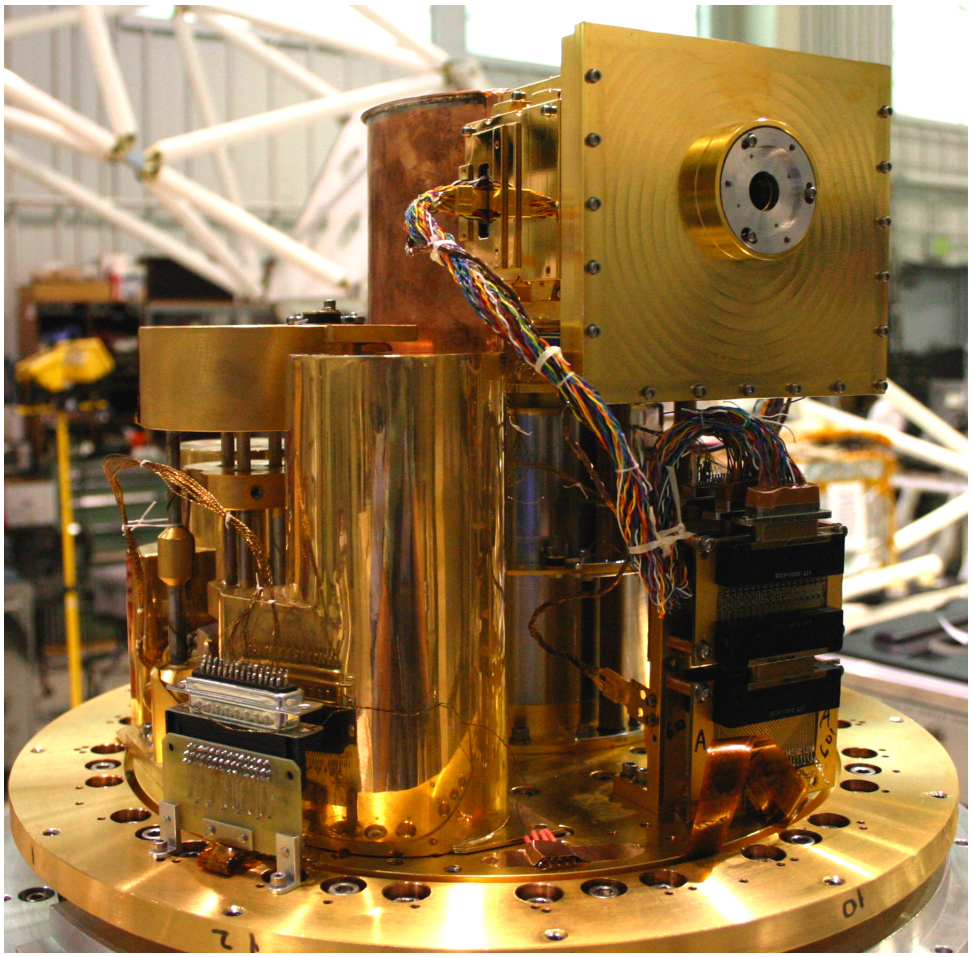

Figure 3.6 The ECS cryogenic package. The detector assembly is on the upper right side, the He-3/He-4 sorption cooler is on the left, and the ADR is in the back, obscured by the other parts.

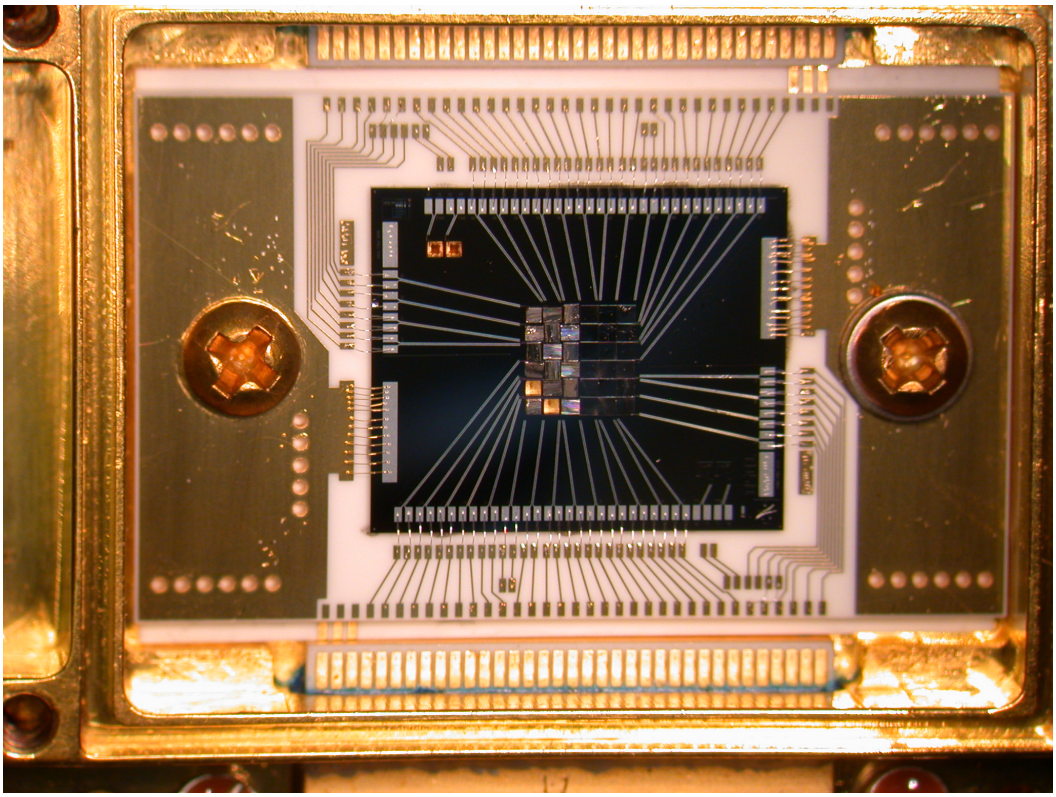

Figure 3.7 Image of the ECS detector chip. The pixels are in the center. The lighter colored pixels on the left are the hard band pixels and the darker ones on the right are the mid-band pixels.

3.2.3.1 ECS Filters and Windows

After the X-ray is created in the EBIT trap, if it is traveling in the direction of the ECS radial port, it will first pass through optical and thermal blocking filters. Four of these filters are positioned along the radiative path of the X-rays inside the ECS, at different temperature stages of 77 K, 4 K, 300 mK, and 50 mK. The filters are made of aluminized polyimide that block optical and infrared photons but allow X-rays to pass through. They are present for two reasons: first, to reduce the level of shot noise on the detector from these lower energy photons, and second, to block the radiative thermal load from the room temperature EBIT environment from heating the detector cold stage. The total aluminum thickness is 1470 Å and the total polyimide thickness is 2386 Å. In addition, there is a 525 Å polyimide window outside the ECS dewar to isolate the lower ECS vacuum from the higher EBIT vacuum so as to reduce the amount of background gas in EBIT. Finally, there are two Be windows (0.5 mil and 5 mil) that can be used to reduce the soft X-ray count rate on the ECS, allowing a higher fraction of "high-res" events (which will be explained shortly) for some experiments. The thicknesses of all filters have been experimentally verified to an accuracy of 10%.

While the purpose of the blocking filters is to block unwanted light but allow X-rays, the X-ray attenuation is not negligible and must be included in all analyses. The filter transmission of the aforementioned filters is shown in Figure 3.8, with transmission constants obtained from Henke et al. [1993]. This transmission constants are considered to be accurate to the 3% level [Saloman et al., 1988]. The

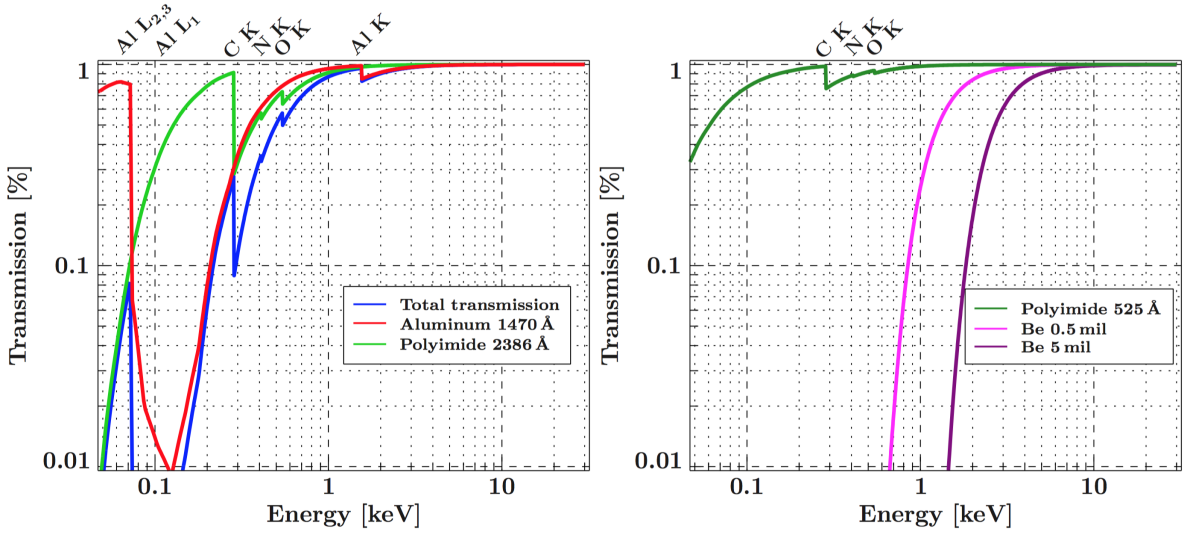

Figure 3.8 Filter transmission for the ECS optical and thermal blocking filters (left), and for the optional windows along the ECS line of sight (right). Transmission constants are from Henke et al. [1993]. The absorption edges of the elements present in the filter materials are marked. Reproduced from Hell [2017].

dips in transmission are located at the so-called absorption edges of the elements present in the filter materials. These energies correspond to the ionization potentials of inner-shell electrons of those elements. Photons passing through the filter with energies near these ionization potentials have a higher probability of ionizing one of these inner-shell electrons, thus getting absorbed.

In addition to the photon attenuation from the filters, we must also consider attenuation from contaminants that may freeze on the filters. We believe these contaminants are from water ice frozen on the 77 K filter, nitrogen and oxygen gas frozen on the 4 K filter, or both. Since the photoelectric absorption cross section scales very nearly as E^{-3}, each substance would produce the same transmission curve at energies above the oxygen K threshold, assuming a given optical depth at a given

energy. Given this, for simplicity, we assume that the contaminant is water ice. During each experiment, the thickness of water ice must be determined by regularly measuring the O Ly-α to Ly-β line strength ratio in electron impact excitation at high electron beam energy ($\sim$ 12 keV). The measured value for this ratio is 6.25 [Beiersdorfer, 2003]. From there, one considers the photon transmission through a material:

$$T(E) = e^{-\tau(E)}, \tag{3.13}$$

where τ is the optical depth,

$$\tau(E) = \frac{t}{l(E)}, \tag{3.14}$$

where t is the thickness of the contaminant material and $l(E)$ is the transmission length at a given energy.

The decrement is the measured ratio of the O Ly-α to Ly-β line fluxes, corrected for filter transmission, divided by the measured value of 6.25:

$$\text{Decrement} = \frac{Ly-\alpha/Ly-\beta}{6.25}. \tag{3.15}$$

We equate this with the predicted decrement,

$$\frac{T_{Ly-\alpha}}{T_{Ly-\beta}}, \tag{3.16}$$

and solve this for t to calculate the contaminant thickness:

$$t = \frac{ln(\frac{T_\alpha}{T_\beta})}{\frac{1}{l_\beta} - \frac{1}{l_\alpha}}. \tag{3.17}$$

One then calculates the energy-dependent transmission curve for a layer of water ice of the calculated thickness, and folds this in with the filter transmission correction during spectral analysis.

3.2.3.2 Absorber

After passing through the ECS filters and frozen contaminants, the photon is then absorbed by a pixel in the ECS detector. The quantum efficiency (QE) of the ECS detectors is nearly unity for the energy range of astrophysical K- and L-shell ions ($\sim$0.1–6 keV), and does not change quickly as a function of energy in this range (see Figure 3.9). As our CX results do not depend on flux ratios from lines that are highly disparate in energy (as some other experiments do, e.g., absolute cross section measurements that are normalized to the radiative recombination line), we do not correct for quantum efficiency. In general, errors on the QE stem from uncertainties in the absorber thickness and in the mass absorption coefficient.

3.2.3.3 Amplification, Filtering, and Digitization

After the photon is absorbed, the signal passes through a JFET that is connected to that pixel. JFETs are run at a warmer temperature than the thermistor, so they are thermally isolated from the detector cold stage. JFETs are run at this temperature in order to minimize their noise output. At lower temperatures, there are less electrons available in the conduction band to be able to move charge, and shot noise increases. At higher temperatures, Johnson noise increases. 130 K is the

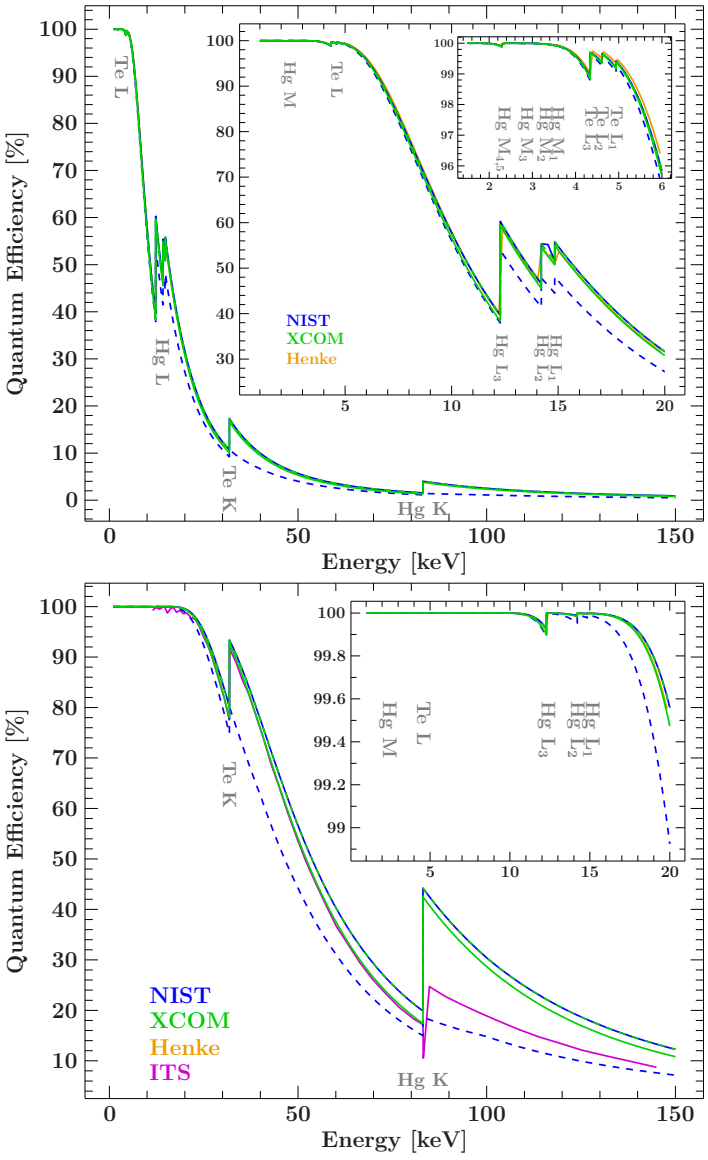

Figure 3.9 Quantum efficiency for the 8 μm thick HgTe absorbers on the low-energy pixels (top) and the 100 μm thick HgTe absorbers on the high-energy pixels (bottom) of the ECS, as given by various sources. Absorption edges are marked. Reproduced from Hell [2017].

point where the sum of these effects is minimized. After the signal is passed through the JFET, it goes to the analog processing unit called the Calorimeter Analog Processor (CAP), where the signal is further amplified. Next, the signal gets filtered, digitized, and passed to the Software Calorimeter Digital Processor (SCDP).

3.2.3.4 The Software Calorimeter Digital Processor

The SCDP, developed for data analysis for the Astro-E/Astro-E2 missions, takes an input data stream and converts it into photon pulse heights that correspond to their energies. It performs this in several steps which will be explained next in more detail: generally, it triggers the data stream, tags the photon with its arrival time relative to the EBIT phase, applies an "optimal filter" to determine a photon energy, and categorizes each pulse with an event grade. From there, the end user can interact with the data using custom analysis software written in a commercial software suite called Igor Pro.

3.2.3.5 Triggering

The SCDP first triggers the data stream. The trigger point defines (nearly) the start of a data record of a given length, which should contain the majority of the pulse decay. Some pre-trigger data are stored as well to check that all the event data is contained in the data record.

3.2.3.6 Optimal Filtering

Next, the SCDP applies an optimal filter to the pulse. The details of optimal filtering were first presented in Szymkowiak et al. [1993]; Adams et al. [2009] presents the method that is currently implemented in the SCDP. The optimal filter is a matched filter that is weighted to optimize signal-to-noise over all frequencies. It allows us to make a best estimate of the pulse height, and therefore photon energy. The premise is that each pulse, without noise, is a scaled version of the same shape, i.e.

$$H_\gamma S(t), \tag{3.18}$$

where H_γ is the amplitude of the pulse shape, and is proportional to the energy of the photon, and $S(t)$ is the invariant pulse shape.

The actual measurement of the pulse shape that we make, $D(t)$ is given by

$$D(t) = H_\gamma S(t) + N(t), \tag{3.19}$$

where $N(t)$ is the noise. This is sometimes called a "noisy pulse."

Our goal, then, is to find H_γ for each pulse. We obtain H_γ by minimizing, in the least squares sense and in frequency space, the difference between the "noisy pulse" and the model of the pulse shape, $H_\gamma S(f)$. This can be shown by

$$\chi^2 = \sum \frac{[D(f) - H_\gamma S(f)]^2}{N^2(f)}. \tag{3.20}$$

To minimize Equation 3.20, one sets the derivative of χ^2 with respect to H_γ to zero. It can be shown [Figueroa Feliciano, 2001] that after doing this, the optimal estimate for H_γ, within a normalization constant, is given by

$$H_\gamma = \sum \frac{D(f)S^*(f)}{N^2(f)}. \tag{3.21}$$

This equation is now composed of elements that we can measure. To obtain the noise power spectrum, $N(f)$, we measure many data records without an X-ray source to get $N(t)$, then perform a Fourier transform. As mentioned before, $D(t)$ is obtained by measuring the detector response to many photons of a particular energy. We then take a Fourier transform to obtain $D(f)$. $S(f)$ is found by dividing $D(f)$ by the energy of the incident photons.

We then transform Equation 3.21 back to the time domain:

$$H_\gamma = \sum D(t)F(t), \tag{3.22}$$

where $F(t)$ is the inverse Fourier transform of $F(f) = S(f)/N^2(f)$.

There are two caveats to this method: optimal filtering is only truly optimal if the detector response is linear (i.e., follows Equation 3.18), and if the noise is stationary (i.e., its power spectrum does not vary over time). These two requirements are not always true for real detectors: saturation of the detector from a high-energy photon will change the pulse shape, and Johnson and phonon noise both depend on the resistance of the detector, which changes over the duration of a pulse. Other methods of pulse analysis have been developed, with similarly good results and vary-

ing levels of complexity. See Peille et al. [2016] for a review and comparison of these methods.

3.2.3.7 Event Grades and Instrumental Response

In determining the pulse height, the SCDP flags each photon with one of three event grades: high-res, mid-res, and low-res. These correspond to the amount of time the exponential decay from the initial event is recorded before another photon on the same pixel causes a second pulse. High-res events only have one photon event for the entire data record. Mid-res and low-res pulses have a secondary pulse that rides on the tail of the primary one, the later in time after the primary pulse than the latter. High-res events are so named because obtaining a full measurement of the pulse shape over an entire record length leads to a better match to the optimal filter, thus higher spectral energy resolution.[5] Operationally, using the beryllium window or decreasing the EBIT beam current can reduce the count rate on the ECS to maximize the number of high-res events. Ishisaki et al. [2016] has more details about event grades.

Even with a perfectly monoenergetic photon beam, the ECS instrumental response is not a delta function with infinite resolution. The actual instrumental response has a Gaussian core [Porter et al., 2004, Cottam et al., 2005], with its FWHM value defining the FWHM energy resolution of each pulse. For high-res

[5]Optimizing the record length, thus, is a balance between minimizing pileup (where short record lengths would be best) and maximizing the frequency space over which we can measure a pulse, in order to maximize the energy resolution (where long record lengths would be best).

primary events on the ECS, this value is ∼4.5 eV at 6 keV. This finite energy resolution is due to the fact that the detector and system noise is white [Eckart et al., 2016]: essentially, the optimally filtered pulse height calculation for a monoenergetic photon beam will have a normal distribution of values due to these noise effects.

3.2.3.8 Gain Scale

After calculating a pulse height, it is necessary to apply a gain scale to match the instrumental response to an energy in eV. After we create a gain calibration file, we apply it to our data in Igor Pro, discussed in the next section.

Creating a gain calibration file for the ECS involves injecting species with well-known energies into the EBIT then collisionally ionizing them and recording their spectra. The species should be chosen to map out a fairly wide range in energy space, focusing on the energies around the lines of interest to the experiment. This must also be done at the experimental operating temperature, since the measured pulse height is temperature-dependent. One then inputs this spectrum into a software program called CXRS, developed by Ming-Feng Gu [private communication], that fits each line to find its centroid in instrumental units then maps it to its energy in eV. This correlation is usually fit with a fourth order polynomial to make a gain curve that extends across all relevant energies. This is illustrated in Figure 3.10. The ECS gain is fairly linear for small energies, but large signals (and thus large energies) reach a more non-linear region of the gain scale. This causes the pulse template to not fit the pulse as well, leading to a degradation in energy resolution.

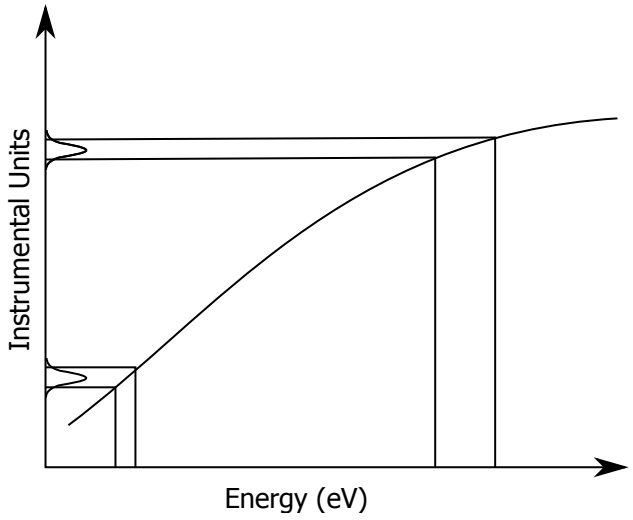

Figure 3.10 Sketch of the gain calibration procedure and resulting gain curve for the ECS. Measurements of spectral lines from K-shell elements with well-known energy centroids are used to map ECS instrumental units to a photon energy in eV. Figure adapted from Hell [2017].

The gain calibration may vary slightly on time scales of hours to days. However, if the gain scale was created contemporaneously with the relevant measurements, it is accurate to within $\sim$0.5 eV. This can be verified by applying a gain scale to an experiment and comparing the Gaussian centroid of the measured line with line energies in the literature. This accuracy is set by many parameters, including the range of species used in the gain calibration procedure and the accuracy of the polynomial fit to the gain curve, the temperature stability of the ECS over the measurement period, and the linearity of the ECS detectors. An accurate gain scale is important for line identification, however, for the CX measurements presented here, our measured accuracy is sufficient for our needs.

3.2.3.9 Final Analysis

Our photon has finally traveled from the EBIT chamber to the ECS, and has been transformed into an entry in an event list with an energy determination and a set of flags. We use the commercially available software program Igor Pro to interact with our data, as well as to adjust and apply any other post-processing tools that may be necessary, such as the aforementioned gain calibration. Other post-processing steps that may be necessary include excluding pulses due to crosstalk, applying corrections for a temperature drift of the ADR, or including or excluding pulses of a certain EBIT phase, pulse height, or time of the experiment. Finally, we extract a spectrum.

3.3 The Transition-Edge EBIT Calorimeter Spectrometer

Together, the ECS and the EBIT have enabled fundamental laboratory measurements that no other technique can achieve, demonstrated by over 40 refereed publications to date, e.g. Leutenegger et al. [2010], Beiersdorfer et al. [2003b], Thorn et al. [2009], Brown et al. [2006], Graf et al. [2009], Gu et al. [2007b]. This includes benchmarking atomic theory for charge exchange, measuring absolute cross sections of L-shell transitions for astrophysically abundant elements from Mg to Ni, and studying K-shell emission in He-like Fe and Ni, including dielectronic recombination satellite emission from lower charge states. ECS measurements even provided diagnostic laboratory data that were critical for interpreting spectra from the Hitomi mission [Collaboration, 2016].

However, upgrading from a 30-pixel Si-thermistor microcalorimeter to a kilo-pixel transition-edge sensor microcalorimeter is important for both scientific and technological reasons. State-of-the-art silicon thermistor microcalorimeters that have been optimized for astrophysical measurements achieve ∼3 eV resolution at 6 keV [Porter et al., 2006], and typical array sizes are 36 pixels. The energy resolution of these devices is hindered by a relatively small α parameter of ∼10 or less [Enss, 2005] (see Equation 3.11). TES microcalorimeters, by contrast, use a thin-film superconductor operated in its superconducting-to-normal transition as the thermometer, are read out using superconducting electronics, and have values of α close to or surpassing 100. Compared to the current-generation silicon devices, state of the art TES microcalorimeters have higher energy resolution and can allow higher count rates by a factor of ∼10–100 per pixel.

An important advantage of using TESs for astrophysical and laboratory applications is that they are scalable to large arrays. The current-generation silicon thermistor arrays like the ECS appear prohibitively difficult to scale to significantly larger pixel count primarily because each pixel requires its own wiring chain from room temperature to the 50 mK detector cold stage. In comparison, multiplexed readout schemes developed by collaborators at NIST/Boulder enable multiple TES pixels to share preamplifiers and signal wiring, so that the cryogenic wiring complexity of an $N \times N$-pixel array scales as only N, as opposed to N^2 for silicon thermistor (non-multiplexed) devices [Irwin, 2002]. In addition, TES array fabrication does not require any hand assembly, as is required for the silicon devices, which allows for more straightforward fabrication of large arrays through microfabrication.

Furthermore, in TESs, the thermal link between the detector absorber and the cold bath is chosen to be stronger than in Si-thermistor devices, which shortens the thermal decay time constant and thus increases the throughput. This will lead to higher count rate capabilities, thus shorter experiment times and a higher availability for science.

A large technological challenge is that no fully operational kilopixel TES instrument that meets the requirements for Athena or the proposed Lynx mission currently exists.[6] In preparation for these future missions, it is critical to develop a proof-of-concept operated on the ground to determine the limitations on the current baseline designs, both in hardware and software, and to address the many open questions related to the performance and optimization of large arrays of TESs.

In response to these scientific and technological needs, the microcalorimeter group at GSFC will soon deploy a kilopixel array of TESs called the Transition-Edge EBIT Microcalorimeter Spectrometer (TEMS) as a user system at the LLNL EBIT. TEMS, a result of a longstanding collaboration between GSFC, NIST/Boulder, and LLNL, will be the first fully functional flight-like array of its kind in the world. The goal of this new facility is both to produce scientific results that are improved over those using the ECS, and also to be a critical stepping stone for the X-IFU on

[6] Our collaborators at NIST/Boulder have, however, deployed several TES arrays of up to ∼250 pixels to various light sources, accelerator facilities, and laboratory facilities. These detectors are not kilopixel arrays of close-packed pixels as is required for Athena, but achieve excellent resolution. The arrays that are optimized for photon energies of < 10 keV achieve resolutions of up to 2.1 eV FWHM at 6 keV, and arrays optimized for photon energies of < 2 keV achieve resolutions as high as 1.0 eV FWHM at 0.5 keV [Doriese et al., 2017].

Property	ECS	TEMS
Thermometer type	Si themistor	MoAu TES
Energy resolution at 6 keV	4.5 eV	< 3 eV
Energy resolution at 60 keV	32 eV	25 eV (Planned upgrade)
Array size	30 pixels	1024 pixels
Pixels read out	30	252
Timing	10 μs	< 1 μs
Count rate/array	100/s	> 5000/s

Table 3.1 Comparison between the ECS and the TEMS.

Athena and the proposed detector array on Lynx. Table 3.1 shows a summary of major design differences between the ECS and the future TEMS.

3.3.1 Technical Specifications

The TEMS detector is a 32×32 pixel array with 250 μm pixel pitch that uses a Bi/Au X-ray absorber with a thin-film Mo/Au superconductor as the thermometer. With the current generation of readout electronics and geometrical constraints in the focal plane design, 252 of those pixels are wired and read out. The main detector array is sensitive to 0.1–10 keV; a second array of 8×8 pixels will be added later to cover the hard X-ray band from 0.5–100 keV, with 25 eV resolution and 70% quantum efficiency at 60 keV [Bennett et al., 2012].

The array is contained in a 15 mm $\times$ 19 mm chip, and the pixel pitch is 250×250 μm. Each pixel has a 140×140 μm^2 transition-edge sensor that is

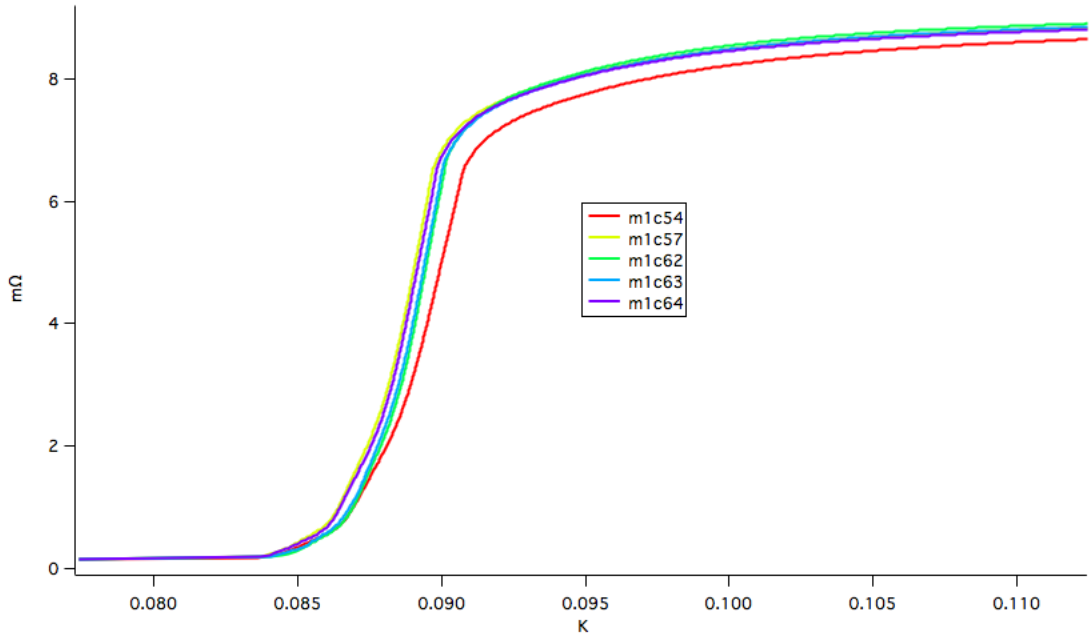

Figure 3.11 The resistance vs. temperature curve of five pixels in the TEMS array showing the superconducting-to-normal transition. The normal-state resistance is ∼8 mΩ.

composed of 50 nm of Mo and 220 nm of Au, and has a normal-state resistance of ∼8 mΩ. A figure of a transition shape of a TEMS pixel is shown in Figure 3.11. A T-shaped stem sits on the TES to support the 240 × 240 μm^2 absorber made of 1.5 μm of Au and 4.0 μm of Bi. Both the TES and the stem are supported by a silicon-nitride membrane, which provides a weak thermal link to the heat bath. There is also ∼64 μm of silicon between each pixel in order to provide a heat sink and minimize thermal cross-talk. The TES bias leads, made of Nb microstrips, are run along this frame. Figure 3.12 shows a photo of a detector chip much like the one implemented in TEMS and a schematic of one pixel.

One important requirement of large multiplexed TES arrays is the uniformity

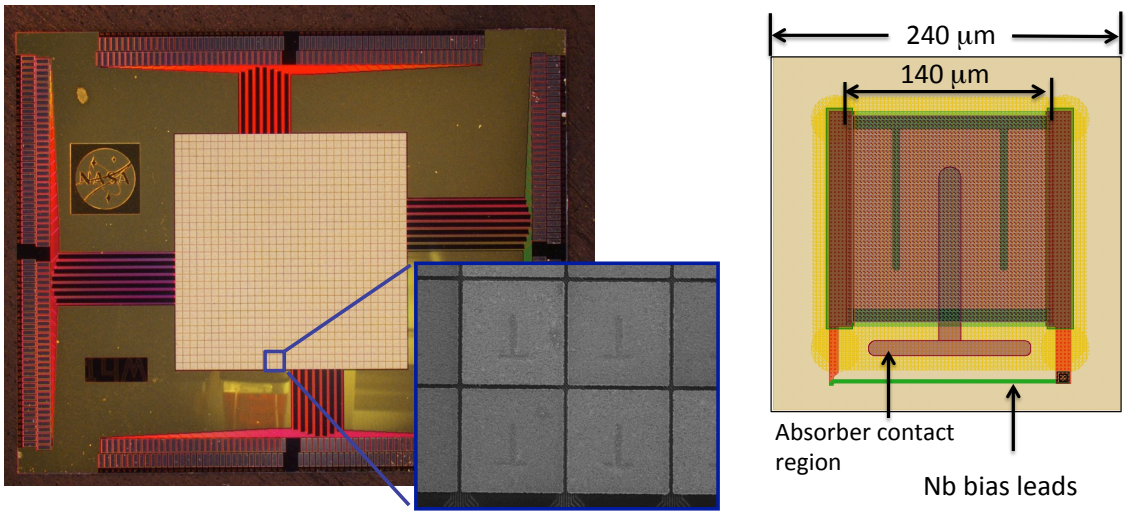

Figure 3.12 A kilopixel array like the one currently used in the TEMS, fabricated at NASA/GSFC. The inset on the left shows a magnification of a few pixels, and the cartoon on the right shows the geometry of the TES (yellow), absorber and absorber stem (tan and brown) and niobium bias leads (green). Image courtesy of Stephen Smith.

of the critical temperature (T_c) of each pixel. With TDM, each column of pixels is voltage biased by a common line, so in order for each pixel in the column to be held at the same point on its transition (R/R_{normal}), the critical temperature of the pixels must be very similar. The TEMS detector chip has an average T_c of $91 + / - 0.12$ mK across 220 currently operating pixels, exhibiting excellent uniformity.

3.3.2 Device Readout

The TEMS TESs are read out using Superconducting Quantum Interference Devices (SQUIDs), developed at NIST/Boulder, using time-division multiplexing (TDM) [de Korte et al., 2003]. In this scheme, each TES is coupled to a first-stage SQUID amplifier, and the output from each SQUID per column of pixels is read out sequentially in time. The first-stage SQUIDs from each column are coupled through a summing coil to a second stage SQUID, whose signal gets amplified by a SQUID series array. A schematic of a 2-row $\times$ 2-column SQUID TDM system is shown in Figure 3.13.

Magnetic shielding for the magnetically sensitive detector and SQUIDs from Earth's magnetic field and the 4 T magnet in the ADR consists of a superconducting niobium shield around the detector card, and a mu-metal shield around the circumference of the cryostat. The TEMS focal plane, including the GSFC-fabricated detector chip shielded by a copper collimator, flexible wiring for TES bias and readout, and NIST-supplied multiplexing and readout chips, is shown in Figure 3.14.

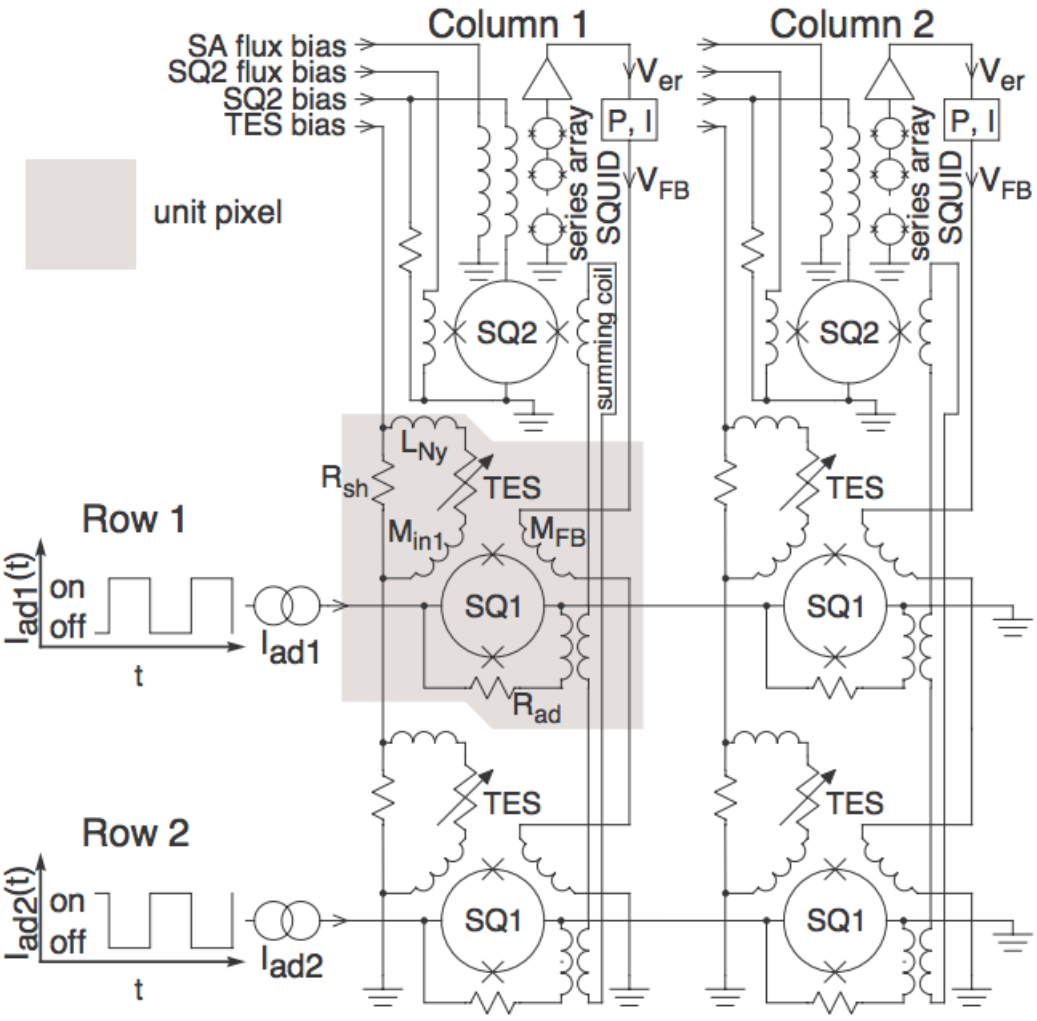

Figure 3.13 Circuit diagram for a 2-row × 2-column time-division SQUID multiplexer. Reproduced from Kilbourne et al. [2008]

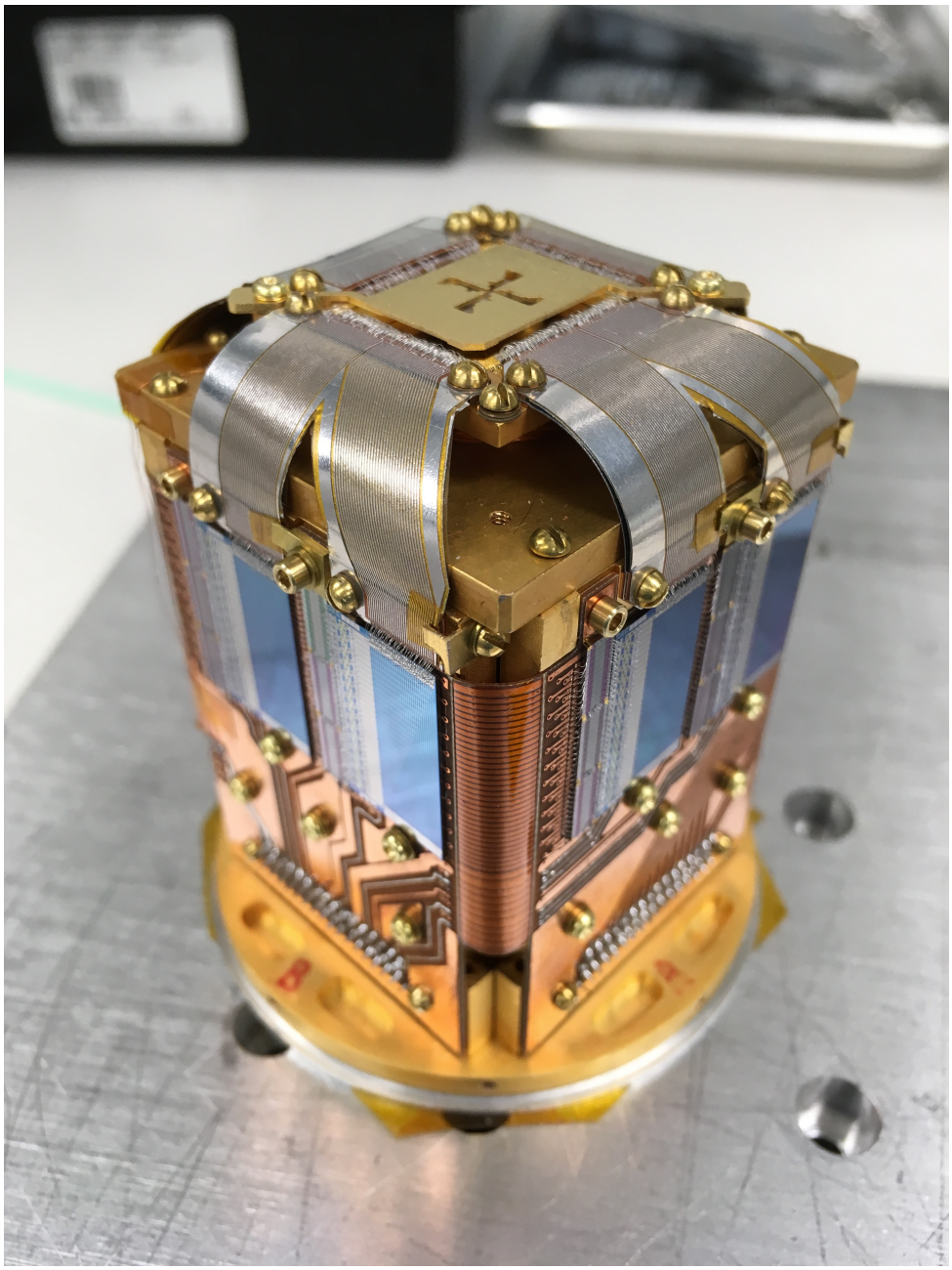

Figure 3.14 The current NIST-developed TEMS focal plane assembly, pictured here with a GSFC detector array that is obscured by a copper collimator. Only a fraction of the pixels on the chip are wired and read out (which trace out a rough "plus" pattern), and the collimator blocks X-rays from being absorbed by the pixels that are not active. This reduces the thermal crosstalk measured by the active pixels.

3.3.3 TEMS Cooling System

Like the ECS, the TEMS is operated at 50 mK in order to achieve optimal spectral energy resolution. The cooling system consists of a cryogen-free 3 K pulse tube cooler and a 300 mK closed-cycle sorption cooler that cools a single stage ADR operating at 50 mK. The 50 mK stage currently has a hold time of 60+ hours and recharges automatically under software control; the final system will have an estimated hold time of ∼120 hours at 50 mK.

3.3.4 Current Status of TEMS and Outlook

We have tested several different detector chips for the TEMS system in order to select one with the best intrinsic energy resolution for permanent installation. During one of these tests, we achieved an average FWHM energy resolution of 3 eV for 30 pixels in a 2×16 multiplexing configuration, for count rates of one per second per pixel [Smith et al., 2014c]. This shows substantial progress from the results presented in [Kilbourne et al., 2008], which demonstrated 2.9 eV FWHM resolution at the 2×8 multiplexing level. Figure 3.15 shows the spectral energy resolution of all pixels read out with this detector array during 2×16 multiplexing tests at GSFC.

The detector chip that is currently installed in the TEMS system exhibits even higher intrinsic spectral resolution and higher uniformity of the TES transition temperature across the chip. Figure 3.16 shows the 2.35 eV spectral resolution at 6 keV for one pixel in the current detector array.

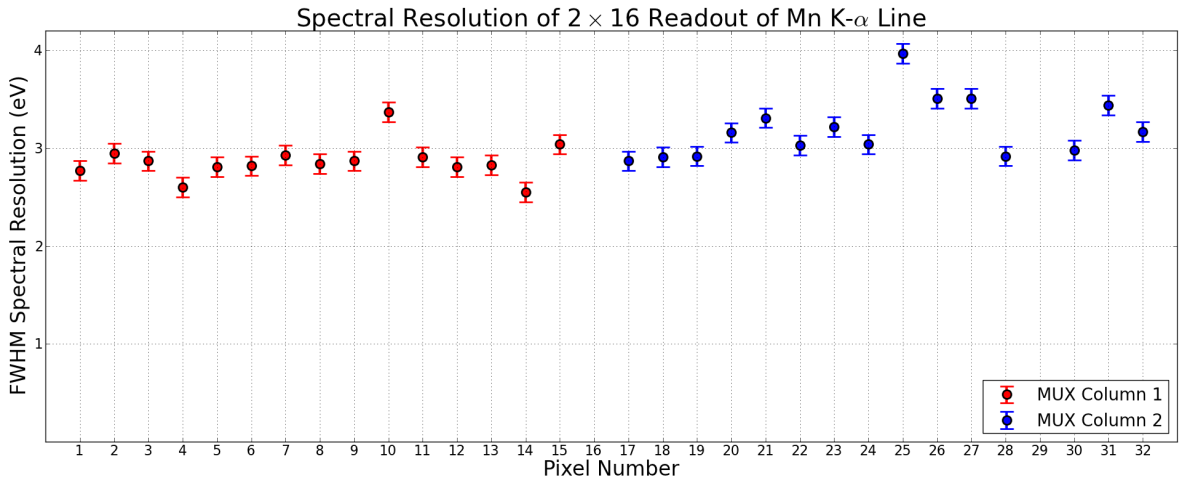

Figure 3.15 Spectral resolution of all pixels read out during a multiplexing test of 2 columns of 16 pixels each, performed on a previous iteration of a TEMS detector chip. The average resolution was 3 eV at 6 keV for all pixels.

The detector system with this chip is currently undergoing tests at GSFC to optimize the spectral resolution and performance while multiplexing all 8 columns of 32 pixels. The team is also upgrading the SCDP software to be able to handle the more complex TES data. The current pulse processing method requires expert knowledge of TES behavior and operation, and is done on a per-pixel basis. This is not feasible for a large pixel array in system that will be used regularly at a laboratory facility, sometimes for days at a time, and used by scientists of all backgrounds. Making the TEMS a turnkey system is a major undertaking, but will provide extremely beneficial lessons learned for future spaceflight applications.

Pulse analysis is not the only new complexity when moving from Si-thermistor devices to TESs. The TESs themselves exhibit variations in their pulse shape or transition shape that often depend on the operating temperature, noise conditions,

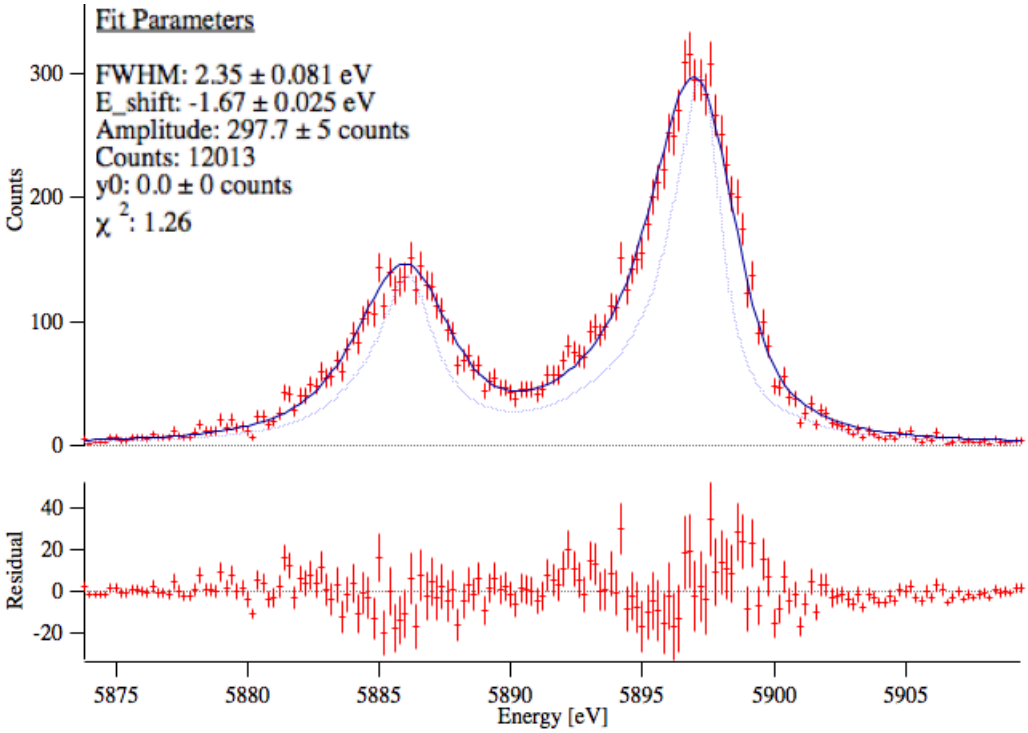

Figure 3.16 FWHM energy resolution of 2.35 eV at 6 keV for one pixel in the current TEMS detector array.

or the magnitude of the magnetic field present. Multiplexing adds further sources of operational complexity and noise. Even given these factors, results from TEMS are excellent, and progress on its development and completion is promising. Once TEMS is able to demonstrate routine resolution of <3 eV at 6 keV while multiplexing, with minimal issues such as crosstalk and gain stability, it will be delivered to the LLNL EBIT facility.

This has only been a quick summary of TEMS; a more detailed description of TESs and SQUID readout electronics is out of the scope of this dissertation. For more information about TES physics, see Enss [2005], and for further information on SQUIDs, see Clarke and Braginski [2006].

Chapter 4: Observation of Highly Disparate K Shell X-ray Spectra Produced by Charge Exchange with Bare Mid-Z ions

Now that we have discussed the theoretical and experimental tools that we can harness to gain a better understanding of the underlying atomic physics of CX, in the rest of this dissertation, we present recent results that stem from measurements of both K-shell and L-shell CX spectra. The text in this chapter is taken directly from a published paper from 2014 [Betancourt-Martinez et al., 2014c] that highlights the complex nature of the CX collision and the need for more comprehensive quantum mechanical theoretical calculations, even for the relatively simple case of K-shell ions.

4.1 Introduction

Charge exchange (CX), or charge transfer, is a semi-resonant process in which a highly charged ion captures one or more electrons from a neutral atom or molecule during a close interaction. Charge exchange is important in setting the ionization balance in laboratory and astrophysical plasmas, as a spectral diagnostic for fusion plasmas, in determining the storage time in ion traps and storage rings, and in antihydrogen production [Isler, 1977, Fonck et al., 1982, Fonck and Hulse, 1984,

Kallne et al., 1984, Rice et al., 1986, Stöhlker et al., 1998, Gabrielse et al., 2007, Greenwood et al., 2001, Cadez et al., 2003, Mawhorter et al., 2007, Greenwood et al., 2004, Simcic et al., 2010, Carolan et al., 1987, Beiersdorfer et al., 2005, Isler, 1994]. Astrophysically, charge exchange occurs in planetary atmospheres and the comae of comets interacting with the solar wind, and has been hypothesized to occur at the rim of supernova remnants [Katsuda et al., 2011, Cumbee et al., 2014]. Charge exchange also occurs between solar wind ions and neutrals in the exosphere and in the heliosphere, which adds variable foreground emission for every astrophysical observation from our solar system [Lisse et al., 1996, Cravens, 1997, Gladstone et al., 2002, Dennerl et al., 2006, Koutroumpa et al., 2009a, Dennerl et al., 2012, Bhardwaj et al., 2007, Slanger et al., 2008, Bodewits, 2007]. Astro-H, a JAXA satellite observatory scheduled for launch in 2015, features an x-ray calorimeter imaging spectrometer that will measure the first high-resolution x-ray spectra of extended objects. Correct interpretation of these observations will require accurate modeling of foreground CX.

In order to model CX spectra, we must know the n- and l-selective electron capture cross section. Classical treatment predicts a sharp peak in the n capture distribution at $n_c \sim q^{3/4}\sqrt{\frac{I_H}{I_n}}$, where I_H and I_n are the ionization potentials of hydrogen and the neutral target, respectively, and q is the ion charge [Janev and Winter, 1985]. The n-distribution is generally well-understood, and many papers show good agreement between theory and experiment for n-selective capture cross sections, as in Mawhorter et al. [2007], Otranto and Olson [2010], Igenbergs et al. [2012] and Wu et al. [2012].

The l distribution, which is dependent on collision energy, is more challenging to model correctly. One can use classical considerations to determine the electron capture state: in high-energy collisions, in the limit of strong Stark mixing, l states are assumed to be populated statistically, and high l states dominate [Janev and Winter, 1985]. In low-energy collisions, the electron does not have enough angular momentum to populate the higher l states, and statistical assumptions do not apply. This was verified in, for example, Beiersdorfer et al. [2000a].

The Lyman series x-ray emission is a powerful diagnostic for determining the state-selective capture cross section, σ_{nl}, in bare ions undergoing charge exchange with a neutral gas. Electron capture into an $l = 1$ state is dominated by direct decay from n_c, $l = 1$ to the ground state [Wargelin et al., 2008], emitting a $n_c p \rightarrow 1s$ Ly series photon. If the electron is captured into a high angular momentum state, it will decay along the Yrast chain in steps of $\Delta n = -1$ and $\Delta l = -1$, finally yielding a $2p \rightarrow 1s$ Ly-α photon. Therefore, if the electrons are captured following a statistical cross section, the strongest line in the spectrum will be Ly-α; if the electron capture cross section is largest for an np state, the $n_c p \rightarrow 1s$ Ly lines will dominate.

The hardness ratio, $\mathcal{H}$, is the ratio of the $n_c p \rightarrow 1s$ to $2p \rightarrow 1s$ emission, where n is greater than two, i.e.,

$$\mathcal{H} = \frac{\sum_{n=3}^{\infty} F_{n\rightarrow 1}}{F_{2\rightarrow 1}} \tag{4.1}$$

where F represents the flux in the denoted transition lines. The hardness ratio is expected to decrease with increasing collision energy, since as collision energy increases, so does the cross section for capture into higher angular momentum states,

producing more Ly-α photons. The hardness ratio can therefore be used as a probe of the collision velocity, allowing us to measure, for example, the velocity of the solar wind. An added benefit of the hardness ratio is that, in principle, it can be determined even with medium-resolution detectors that may not be able to resolve individual high-n Lyman lines, such as CCDs or high purity germanium solid state detectors that typically have resolutions on the order of $\sim$100 eV at 1.5 keV.

Besides the classical over-the-barrier (COB) method [Ryufuku et al., 1980, Niehaus, 1986], several other more complex charge exchange models exist which can be used to estimate total or state-selective cross sections. These include the Landau-Zener (LZ) method [Salop and Olson, 1976], the multichannel Landau-Zener (MCLZ) approximation [Janev et al., 1983], the atomic-orbital close-coupling (AOCC) method, and the molecular-orbital close-coupling (MOCC) method [Fritsch and Lin, 1991, Shimakura et al., 1993]. The classical trajectory Monte Carlo (CTMC) method [Abrines and Percival, 1966, Olson and Salop, 1977] is the most widely used approximation, due to its simplicity and its accuracy, compared to other models, in predicting experimentally-measured n-state selective cross sections.

COB and CTMC models agree qualitatively with experiments that show a decrease in hardness ratios with increasing collision velocity [Otranto et al., 2006]. Both models also agree qualitatively with experiments that show an increase in capture cross section with increasing ion charge, but have systematic uncertainties of $\sim 25-50\%$ when predicting absolute cross sections [Cadez et al., 2003, Mawhorter et al., 2007, Djurić et al., 2008]. CTMC shows better agreement with experiments at high collision energies (above $\sim$1 keV amu^{-1}), as demonstrated in comparison with

experimental results from fusion plasmas excited with a very energetic hydrogen or deuterium beam [Beiersdorfer et al., 2005]. However, discrepancies between models and experiments arise at the edge of tokamaks, where cold ions interact with molecular gas, in electron beam ion traps (EBITs), where the collision velocity is ∼10 eV amu^{-1}, and also in space, where cometary, exospheric, and heliospheric neutrals interact with low energy solar wind ions.

The COB and LZ methods do not make predictions for l-selective capture cross section, and to the extent that there are measurements of l-selective capture cross section at low collision energies, especially over a range of conditions and interacting species other than atomic hydrogen, theoretical calculations that can incorporate l, such as CTMC and AOCC/MOCC, show poor agreement with experiments [Leutenegger et al., 2010, Beiersdorfer et al., 2000a, Stancil et al., 2002, Wu et al., 2012, Mančev et al., 2013]. Furthermore, the commonly used CTMC method cannot incorporate multi-electron capture (MEC), which becomes important in the low-energy regime [Ali et al., 1994, Otranto et al., 2006].

Several comparisons between theory and experiment have been made, with varying results. Otranto et al. [2006] demonstrated that while CTMC calculations qualitatively agree with EBIT experiments where n_c decreases for increasing ionization potential, their CTMC model overestimates the flux in high-n Rydberg transitions following CX onto O^{8+}. Beiersdorfer et al. [2000a] performed experiments with EBIT-I showing that, contrary to CTMC calculations, the hardness ratio following CX with bare Ne, Ar, Kr and Xe was always nearly unity. Further, the disagreement between calculated and measured hardness ratios worsened at higher atomic

numbers. Otranto et al. [2007] presented EBIT results involving O^{8+} demonstrating that the hardness ratio can vary within nearly a factor of two by varying the neutral gas. Leutenegger et al. [2010] presented EBIT spectra of bare Ar and P that concurrently underwent CX with the same neutral gas, and contrary to the trend established in Beiersdorfer et al. [2000a] and also to previous CTMC calculations, the hardness ratios measured for Ar and P differed by a factor of two.

In this paper, we present experiments that investigate the dependence of CX line emission on the ionization potential of the neutral gas, the number of valence electrons in the neutral gas, and the atomic number of the ion. We probe whether any of these characteristics are predictive of CX spectral features, and provide empirical data towards more comprehensive and quantitatively accurate models.

4.2 Experimental Method

The measurements presented here were performed with the EBIT-I electron beam ion trap at the Lawrence Livermore National Laboratory [Beiersdorfer et al., 2003a, Beiersdorfer, 2008]. The spectra were measured using the EBIT calorimeter spectrometer (ECS) [Porter et al., 2004, 2008a]. The ECS is a non-dispersive spectrometer developed at NASA/Goddard Space Flight Center with quantum efficiency of nearly unity over a large bandwidth. The 30-pixel array of silicon-doped thermistors is divided into a mid- and a high-energy array of 16 and 14 pixels, respectively, which together have a dynamic range of 0.05–100 keV. The experiments discussed here made use of the mid-band array, which has an energy resolution of ∼4.5 eV at

6 keV.

The ECS has four internal aluminized polyimide filters used to block optical and thermal radiation at temperature stages of 77 K, 4 K, 300 mK, 50 mK, with a total aluminum thickness of 1460 Å and total polyimide thickness of 2380 Å. In addition, we used a 500 Å polyimide window outside the ECS dewar to isolate the ECS vacuum from the EBIT vacuum. These thicknesses have been experimentally verified to an accuracy of ∼10%.

Fundamentally, the EBIT operates in one of two modes: electron trapping mode and magnetic trapping mode. In electron trapping mode, after neutral species are injected into the ion trap, they are collisionally ionized by the electron beam, then confined in the trap. The ions are radially confined due to the electrostatic attraction of the electron beam, and axially confined by a voltage potential applied across three copper drift tubes. Typical thermal energies of trapped ions are ∼10 eV amu^{-1} at typical beam currents of ≥ 130 mA and trap potentials of ≥ 100 V [Beiersdorfer et al., 1996a], and typical ion densities in the trap are $\sim 3 \times 10^9$ cm^{-3}.

For a charge exchange experiment in the EBIT-I, first, ions are created during electron trapping mode, with the electron beam turned on for typically about 0.5 seconds to generate a sufficient number of bare ions of mid-Z elements. Next, in magnetic trapping mode [Beiersdorfer et al., 1996b], the electron beam is turned off and the ions are radially trapped by the 3 T magnetic field of the superconducting Helmholtz coils and the electric field of the drift tubes, so that the EBIT is effectively a Penning trap. The ions gain electrons and emit X-rays through CX with the neutral species introduced into the trap. Since the beam is off, no excitations due

to electron impact occur. Filling the K shell of most of the trapped bare ions takes about 0.5 seconds. After this occurs, the trap is dumped and the cycle is repeated. It typically requires several hours to accumulate sufficient statistics for each experiment.

We performed charge exchange experiments for the following ions and neutral gases: Mg^{12+}+CO_2, Mg^{12+}+H_2, Mg^{12+}+He, Mg^{12+}+Ne, Cl^{17+}+$C_2H_4Cl_2$, Cl^{17+}+He, Ar^{18+}+Ar, S^{16+}+He, and S^{16+}+SF_6. In the Mg experiments, there were contaminant ions present in the trap, including P, S, Si and Ar, which entered from a port on EBIT that was open in order to perform crystal spectrometer measurements. We did not observe any significant effect from these contaminants in the spectra, other than the presence of their K shell emission lines. The charge exchange cross section for ion-ion interactions is negligible. We verified that the x-rays recorded were nearly all from interactions of trapped ions with the chosen neutral gas, and not with background gases in the trap, by reducing the neutral CX partner gas injection pressure to zero while holding all other experimental parameters constant. From contemporaneous measurements, we estimate that the background CX rate for the Mg experiments was about 10% of the experimental CX rate; for all other experiments the background rate is on the order of 1%.

4.3 Analysis and Spectra

We fit Lyman series lines from H-like ions, assuming a Gaussian instrumental function [Kelley et al., 2007]. We used reference energies calculated with the Flex-

ible Atomic Code (FAC) [Gu, 2008]. We accounted for partial line blending where two transitions from different ions could be disentangled due to differing energy centroids. In a few cases, however, ion line flux could not be separated from other lines due to contaminants with transitions that overlapped with the lines of interest: for example, Mg^{11+} Ly-γ is nearly coincident with the strong Si^{12+} $1s2s\ ^3S_1 \rightarrow 1s^2\ ^1S_0$ transition. In order to account for this in our hardness ratios, we determined a lower limit assuming zero flux in Ly-γ, which appears in the text of table 4.3 and Figures 4.4 and 4.4, and an upper limit by including the entire blended line, mentioned in the caption of table 4.3. In the absence of independent measurements of the Si lines, we assert that the lower limit is the more realistic one; the Si forbidden line in CX is more likely to be stronger than the Mg^{11+} Ly-γ line.

We corrected the observed flux for attenuation from the optical and thermal blocking filters as well as frozen contaminants on the filters, which we believe is either or both of water ice or nitrogen gas frozen on the 77 K filter, or nitrogen gas frozen on the 4 K filter. Since the photoelectric absorption cross section scales very nearly as E^{-3}, either substance would produce the same transmission curve at energies above the oxygen K threshold, assuming a given optical depth at a given energy. Therefore, we make a fiducial assumption that the contaminant is water ice. We determine the thickness of water ice using the decrement in the ratio of the O Ly-α to Ly-β line strengths in electron impact excitation experiments compared to the measured ratio of 6.25 in the limit of high incident electron beam energy [Beiersdorfer, 2003]. The oxygen measurements were taken regularly during the experiments. The inferred fiducial ice layer thickness was typically $\sim$1 μm, which

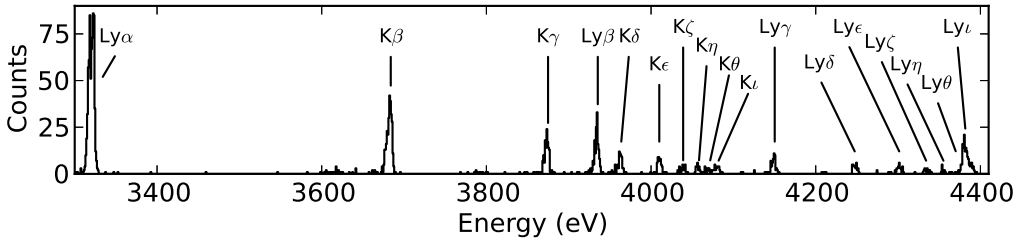

Figure 4.1 Spectrum of bare argon undergoing CX with neutral argon.

corresponds to a line flux correction of ∼10–20% in the Mg Ly band from 1300–1900 eV, and ∼1% for the S, Cl, and Ar experiments with line energies above ∼2400 eV. This corresponds to a maximum effect on the ratio of Ly-n:Ly-α of ∼10% for the Mg experiments and ∼1% for the S, Cl, and Ar experiments.

Selected spectra are presented in Figures 4.3–4.3. Lyman lines refer to the hydrogen-like ion emission; "K" lines refer to He-like ion emission. K lines can be used for various diagnostics, but in this paper we focus on the Lyman emission. Hardness ratios and other diagnostic ratios for all experiments are summarized in tables 4.3 and 4.3. Individual line fluxes are also presented in these tables.

4.4 Discussion

The hardness ratios determined for the experiments presented here span a larger range than previous experiments have shown, and can deviate widely from CTMC calculations, as can be seen in Figure 4.4. In earlier CX experiments using

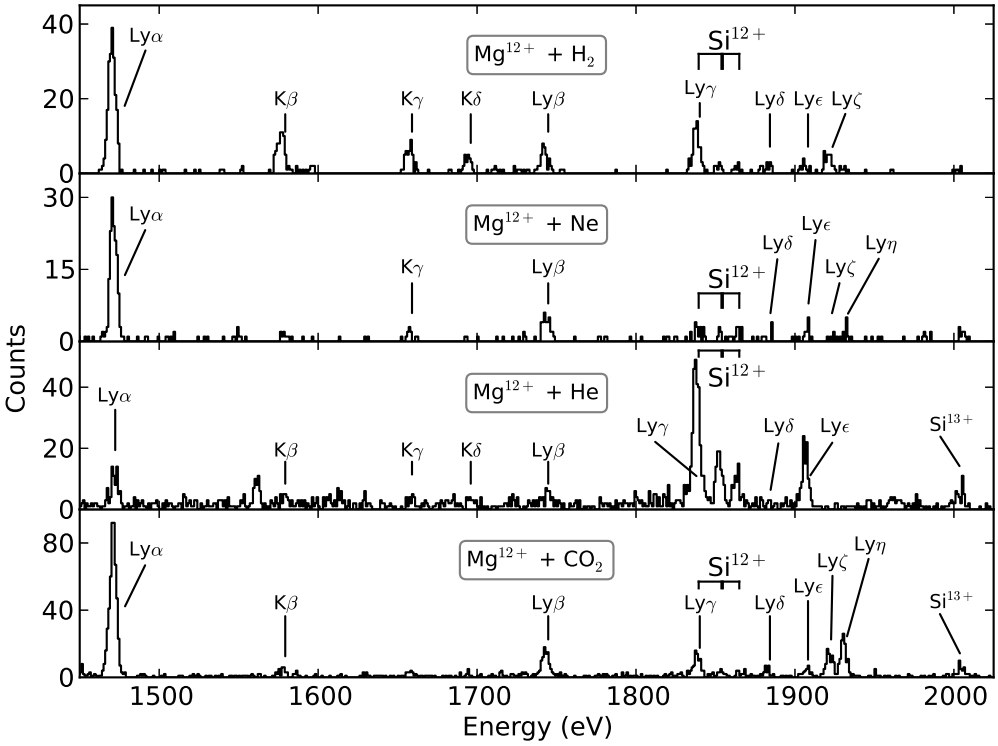

Figure 4.2 Spectra from bare Mg undergoing CX with four different neutral gases. Relevant transitions, along with background ions, are labeled.

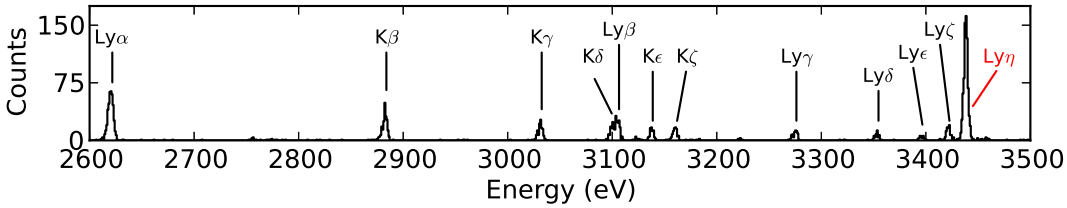

Figure 4.3 S^{16+} and He charge exchange. Note the extremely strong $8 \rightarrow 1$ transition (Ly-η), identified in red.

Table 4.1 This table summarizes the normalized H-like series line strengths and hardness ratios for the experiments presented in the text. Filter transmission- and ice-corrected line strengths are normalized to the sum of Ly-α 1 and 2. Uncertainties are one-sigma statistical errors. The flux ratio for Ly-α 1:2 was set to two in the model fits for the Mg experiments, but for the other experiments this ratio was allowed to vary and is presented in the table. The line strengths listed for the Mg^{12+} Ly-γ lines are upper limits, including both the flux in the Mg Ly-γ line as well as the Si^{12+} $1s2s\ ^3S_1 \rightarrow 1s^2\ ^1S_0$ overlapping transition. The hardness ratios listed for the Mg^{12+}experiments are calculated assuming the lower limit, i.e. zero flux in this blended Mg Ly-γ line. The upper limits on $\mathcal{H}$, which use the upper limit flux in Ly-γ, are the following: Mg^{12+}+ CO_2: 0.905 ± 0.063, Mg^{12+}+ He: 6.446 ± 0.832, Mg^{12+}+ H_2: 0.846 ± 0.087, Mg^{12+}+ Ne: 0.623 ± 0.076.

Transition	Mg^{12+}+ CO_2	Mg^{12+}+ He	Mg^{12+}+ H_2	Mg^{12+}+ Ne	P^{15+}+ He	S^{16+}+ He	S^{16+}+ SF_6	Cl^{17+}+ He	Cl^{17+}+ $C_2H_4Cl_2$	Ar^{18+}+ Ar
$1s-3p$	0.211 ± 0.022	0.610 ± 0.099	0.184 ± 0.033	0.227 ± 0.040	0.281 ± 0.075	0.32 ± 0.12	0.203 ± 0.070	0.239 ± 0.050	0.227 ± 0.030	0.204 ± 0.020
$1s-4p$	0.167 ± 0.020	3.86 ± 0.28	0.337 ± 0.044	0.133 ± 0.022	0.285 ± 0.076	0.155 ± 0.022	0.082 ± 0.016	0.253 ± 0.051	0.066 ± 0.014	0.084 ± 0.012
$1s-5p$	0.058 ± 0.011	0.319 ± 0.073	0.063 ± 0.011	0.044 ± 0.015	0.210 ± 0.057	0.114 ± 0.019	0.053 ± 0.011	0.150 ± 0.034	0.0399 ± 0.0052	0.0528 ± 0.0091
$1s-6p$	0.064 ± 0.012	1.41 ± 0.16	0.063 ± 0.012	0.095 ± 0.015	0.120 ± 0.032	0.069 ± 0.013	0.0527 ± 0.0082	0.078 ± 0.015	0.0449 ± 0.0059	0.0466 ± 0.0087
$1s-7p$	0.169 ± 0.020	0.053 ± 0.043	0.146 ± 0.026	0.030 ± 0.018	0.82 ± 0.18	0.213 ± 0.028	0.0162 ± 0.0050	0.037 ± 0.017	0.0249 ± 0.0056	0.0272 ± 0.0042
$1s-8p$	0.229 ± 0.024	0.072 ± 0.039	0.036 ± 0.014	0.080 ± 0.014	0.092 ± 0.036	1.74 ± 0.14	0.0291 ± 0.0078	1.60 ± 0.22	0.0262 ± 0.0064	0.0169 ± 0.0040
$1s-9p$	0.0054 ± 0.0078	0.074 ± 0.052	0.0133 ± 0.0050	0.0084 ± 0.0041	0.059 ± 0.029	0.0125 ± 0.0089	0.111 ± 0.019	0.026 ± 0.026	0.0184 ± 0.0072	0.0016 ± 0.0039
$1s-10p$	0.0028 ± 0.0054	0.048 ± 0.052	0.0031 ± 0.0063	0.0059 ± 0.0090	0.003 ± 0.013	0.0330 ± 0.0062	0.165 ± 0.024	0.0001 ± 0.0097	0.0130 ± 0.0099	0.181 ± 0.019
Ly-α 1:2						2.19 ± 0.36	2.22 ± 0.45	1.16 ± 0.27	1.26 ± 0.19	1.41 ± 0.19
$\mathcal{H}$	0.738 ± 0.054	2.581 ± 0.376	0.509 ± 0.059	0.490 ± 0.065	1.868 ± 0.374	2.660 ± 0.265	0.714 ± 0.116	2.383 ± 0.307	0.460 ± 0.047	0.614 ± 0.041

Table 4.2 This table presents the normalized He-like series line strengths for the experiments presented in the text except for Mg^{11+}+ Ne, which had significant line blending in the Mg forbidden (z), intercombination (y and x), and resonance (w) lines with Ne^{9+}. Filter transmission- and ice-corrected line strengths are normalized to w. Uncertainties are one-sigma statistical errors. Also presented are the He-like line ratios defined in Gabriel and Jordan [1969]: $\mathcal{R} = F_z/(F_x + F_y)$, $\mathcal{G} = F_x + F_y + F_z/F_w$, an alternate quantity giving the triplet-to-singlet capture ratio, $\mathcal{G}' = (F_x + F_y + F_z)/(F_w + F_{3+})$, the He-like hardness ratio $\mathcal{H} = F_{3+}/(F_2)$, and a ratio introduced in Leutenegger et al. [2010], $\mathcal{H}' = F_{3+}/F_w$. F represents the flux in the denoted transition lines.

Transition	Mg^{11+}+ CO_2	Mg^{11+}+ He	Mg^{11+}+ H_2	S^{15+}+ He	S^{15+}+ SF_6	Cl^{16+}+ He	Cl^{16+}+ $C_2H_4Cl_2$	Ar^{17+}+ Ar
z	1.53 ± 0.16	3.71 ± 0.59	2.90 ± 0.24	5.12 ± 0.25	1.60 ± 0.12	5.82 ± 0.38	1.520 ± 0.096	1.889 ± 0.084
x/y	1.23 ± 0.14	1.28 ± 0.24	0.861 ± 0.092	1.777 ± 0.098	1.61 ± 0.12	2.23 ± 0.21	1.65 ± 0.14	1.39 ± 0.18
$1s-3p$	0.219 ± 0.043	0.71 ± 0.16	0.347 ± 0.051	0.349 ± 0.030	0.231 ± 0.031	0.450 ± 0.051	0.185 ± 0.024	0.296 ± 0.022
$1s-4p$	0.184 ± 0.040	0.56 ± 0.14	0.209 ± 0.036	0.216 ± 0.023	0.117 ± 0.021	0.307 ± 0.038	0.107 ± 0.018	0.135 ± 0.014
$1s-5p$	0.108 ± 0.024	0.47 ± 0.11	0.125 ± 0.026	0.176 ± 0.026	0.065 ± 0.023	0.141 ± 0.023	0.062 ± 0.013	0.076 ± 0.010
$1s-6p$	0.090 ± 0.024	0.145 ± 0.086	0.030 ± 0.011	0.141 ± 0.018	0.0411 ± 0.0059	0.112 ± 0.022	0.0440 ± 0.0089	0.0616 ± 0.0092
$1s-7p$	0.114 ± 0.029	0.42 ± 0.12	0.029 ± 0.012	0.160 ± 0.019	0.0152 ± 0.0061	0.220 ± 0.033	0.0212 ± 0.0047	0.0290 ± 0.0057
$1s-8p$		0.315 ± 0.098	0.018 ± 0.018	0.0050 ± 0.0053	0.0244 ± 0.0078	0.0669 ± 0.0095	0.0137 ± 0.0047	0.0287 ± 0.0060
$1s-9p$				0.0055 ± 0.0042	0.0293 ± 0.0077	0.0002 ± 0.0033	0.0029 ± 0.0037	0.0195 ± 0.0049
$1s-10p$				0.0026 ± 0.0015	0.0012 ± 0.0041	0.0097 ± 0.0028	0.0140 ± 0.0046	0.0327 ± 0.0061
$\mathcal{R}$	1.248 ± 0.126	2.904 ± 0.420	3.365 ± 0.302	2.879 ± 0.110	0.994 ± 0.064	2.604 ± 0.200	0.922 ± 0.075	1.362 ± 0.179
$\mathcal{G}$	2.755 ± 0.269	4.991 ± 0.777	3.758 ± 0.306	6.893 ± 0.325	3.214 ± 0.215	8.053 ± 0.532	3.169 ± 0.204	3.276 ± 0.218
$\mathcal{G}'$	1.606 ± 0.129	1.378 ± 0.139	2.137 ± 0.143	3.354 ± 0.121	2.108 ± 0.122	3.491 ± 0.168	2.187 ± 0.127	1.857 ± 0.082
$\mathcal{H}$	0.191 ± 0.020	0.438 ± 0.048	0.159 ± 0.015	0.134 ± 0.010	0.124 ± 0.017	0.144 ± 0.008	0.108 ± 0.009	0.159 ± 0.013
$\mathcal{H}'$	0.715 ± 0.091	2.622 ± 0.448	0.759 ± 0.085	1.055 ± 0.090	0.525 ± 0.078	1.307 ± 0.105	0.449 ± 0.040	0.678 ± 0.053

trapped ions, the hardness ratio measured at low collision velocity was often ∼1 [Wargelin et al., 2005, Beiersdorfer et al., 2000a, Otranto et al., 2006, Leutenegger et al., 2013, Allen et al., 2008, Beiersdorfer et al., 2001]. All experiments in this work were performed at similar collision energies of $\lesssim 25$ eV amu^{-1} [Beiersdorfer, 2003], but the hardness ratios vary between ∼0.5 to ∼2.6. This demonstrates that the contribution from the np capture cross section, as normalized to the total capture cross section, occupies a broader range than previously supposed; the initially surprising variation in $\mathcal{H}$ between bare Ar and P as shown in Leutenegger et al. [2010] seems to be less of an anomaly than formerly thought.

One might expect to see $\mathcal{H}$ scale with the atomic number of the ion (as CTMC calculations in Beiersdorfer et al. [2000a], Wargelin et al. [2008] show), the number of valence electrons in the neutral, or the ionization potential of the neutral. For example, Ali et al. [2005] notes that SEC (single electron capture) from a neutral with a large ionization potential would require a smaller impact parameter, leading to a low l state of the captured electron. However, our results also show that there is no clear scaling between the l distribution of captures and any of the aforementioned parameters, as can be seen in Figures 4.4 and 4.4.

The fact that we do not see a scaling of $\mathcal{H}$ with the ionization potential in particular may stem from the relative dominance of SEC versus MEC. As pointed out by Ali et al. [2005], MEC produces multiply charged ions that autoionize until reaching a lower n, l state that radiatively decays. This leads to fewer high-n Lyman lines and thus a smaller $\mathcal{H}$. In our experiments, we find that charge exchange with helium as the neutral partner shows an especially high $\mathcal{H}$. This is likely due to a high

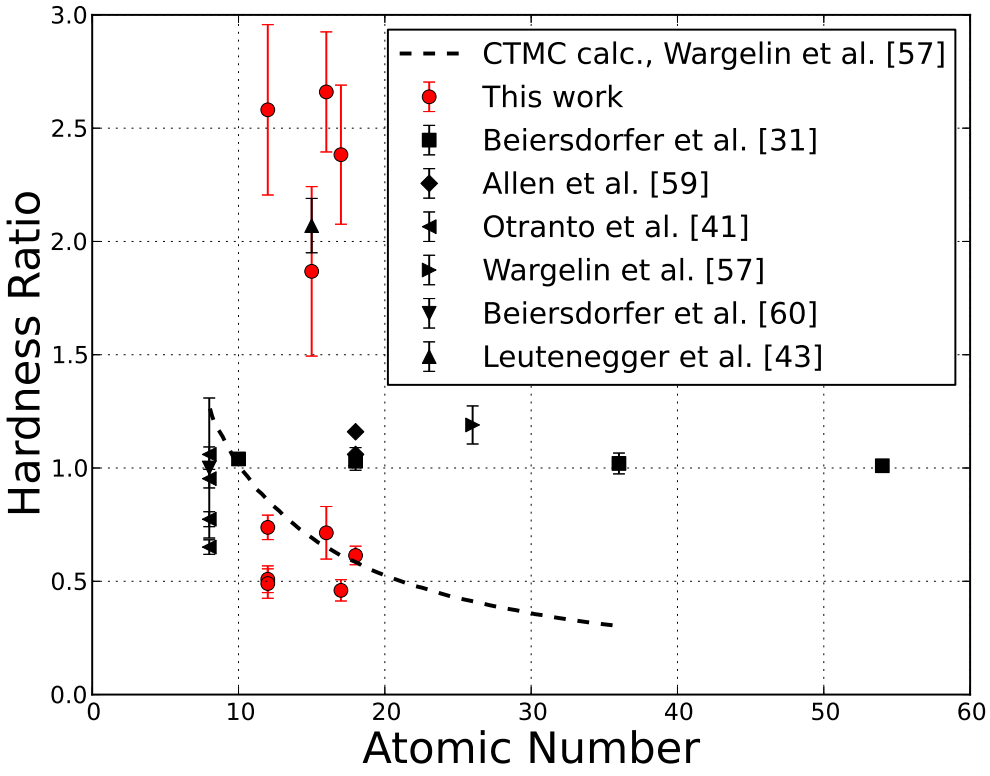

Figure 4.4 Hardness ratio as a function of the atomic number of the ion. All experiments were performed at less than $\sim$25 eV amu^{-1}.

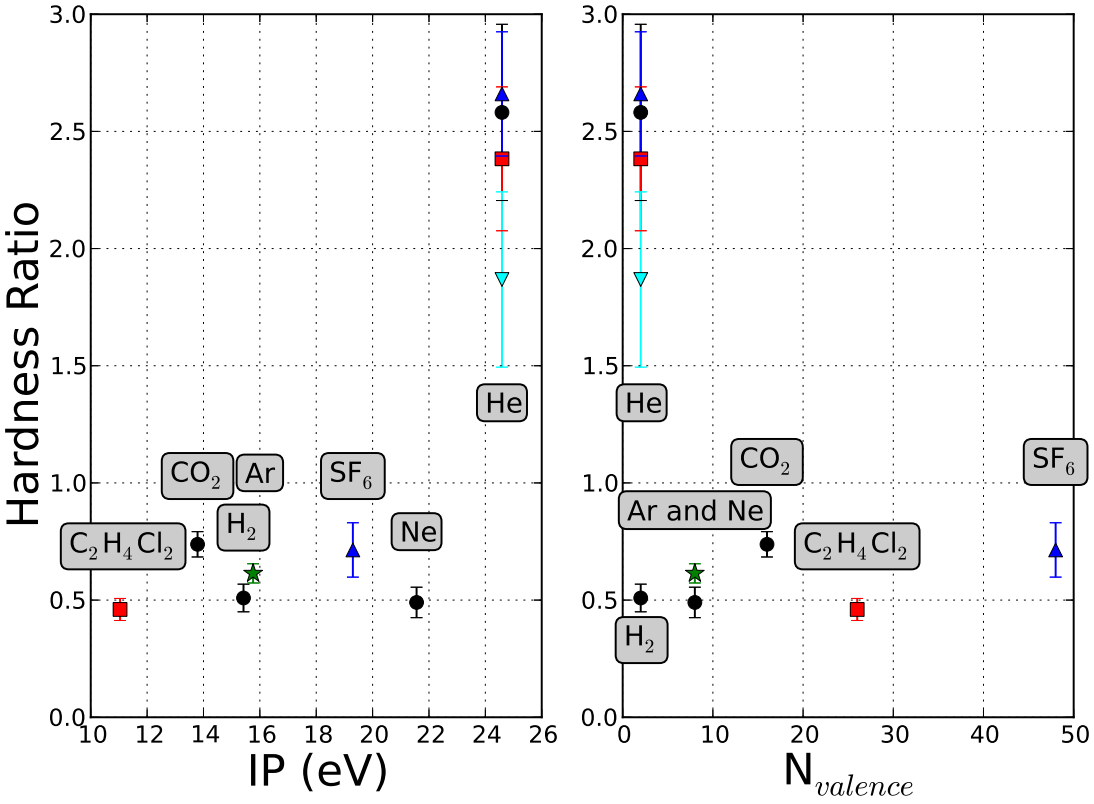

Figure 4.5 Hardness ratio as a function of the ionization potential (left) and the number of valence electrons (right) of the neutral gas. Colors and symbols represent different bare ions: Mg in black circles, Cl in red squares, Ar in green stars, S in blue upward-pointing triangles, and P in cyan downward-pointing triangles. The neutral species is indicated on the plot.

percentage of single electron capture, as Ali et al. [2005] demonstrated, in addition to the high ionization potential of He. However, we measure a low $\mathcal{H}$ ($\sim$0.5) for experiments with molecular H, even though one would expect SEC to be dominant for H_2.

We suggest that in the case of SEC, the differences we measure in hardness ratio from CX with otherwise similar neutrals stem from inherent differences in the *np* cross section of those species. These differences can likely only be understood in the context of a rigorous quantum mechanical treatment of the interaction, which must be guided by further experimental benchmarks.

The large variation in hardness ratio we have shown from charge exchange experiments performed at low collision energies, in comparison with both previous work in the literature and theoretical calculations using models such as CTMC, demonstrates that open questions still exist in determining the *l*-selective CX capture cross section distribution, and therefore the resulting x-ray spectrum and its accompanying diagnostics. This is an issue that is imperative to address now, so as to properly interpret the high-resolution spectra from the Astro-H x-ray satellite observatory and high-resolution x-ray microcalorimeters to be implemented on future space missions.

4.5 Acknowledgments

The authors would like to thank Ed Magee and David Layne at LLNL for their technical support. We also thank the anonymous referees for their helpful

comments. Work at the Lawrence Livermore National Laboratory was performed under the auspices of the U.S. Department of Energy under Contract DE-AC52-07NA27344 and supported by NASA APRA grants to LLNL and NASA/GSFC.

Chapter 5: High-Resolution Spectra of L-Shell Charge Exchange with Ne-like Ni

5.1 Introduction

Most observational and modeling efforts for CX have concentrated on K-shell ions, and we have just seen in the previous chapter that there is still much work to be done to properly understand CX interactions involving these ions. However, L-shell ions make up a non-negligible fraction of X-ray emission from a wide variety of X-ray sources. L-shell sulphur may contribute to CX in Jupiter's polar regions [Cravens et al., 2003, Gladstone et al., 2002, Elsner et al., 2005], and L-shell Si, S, Mg, Ne, Fe, and O ions, found in the solar wind [Schwadron and Cravens, 2000], may also lead to CX lines in the solar system. L-shell Ni ions, though less cosmically abundant than Fe, have been identified in spectra of stellar coronae [Behar et al., 2001, Peretz et al., 2015, Güdel and Nazé, 2009] as well as in high-resolution spectra of the sun [Phillips et al., 1982]. As high-resolution spectral measurements become more routine, it will become increasingly important to understand the behavior of Ni L-shell lines compared to those resulting from neighboring L-shell Fe ions in order to properly interpret spectral line diagnostics.

Despite its potential significance in astrophysics (see Section 1.5), the study of CX lacks a deep understanding of the subtleties in the atomic physics governing the process. Experimental data are often in conflict with models, even just for K-shell [Beiersdorfer et al., 2003a, Wargelin et al., 2005, Beiersdorfer et al., 2003b, 2000a, Otranto et al., 2007, Leutenegger et al., 2010]. Some of this disagreement may stem from the fact that multi-electron capture (MEC), which may be important to consider in CX [Ali et al., 1994, 2005, Hasan et al., 2001], is not modeled. Indeed, experiments performed with atomic H, ensuring single electron capture (SEC), agreed well with models [Beiersdorfer et al., 2005]; though this could also be due to the fact that the collision energy in the experiment was high (40 keV/amu). In general, experiments at high collision energy (above 0.1–1 keV/amu), where the detailed pseudo-molecular structure of the electron capture interaction is not as important (see Section 2.3), agree better with theoretical calculations [Cariatore and Otranto, 2013, Igenbergs et al., 2012, Otranto and Olson, 2010]. However, it is imprudent to simply ignore the cases of low collision energy or MEC. For example, solar wind ions typically have initial energies of tens of keV/amu, but this may drop to tens of eV/amu after passing through the bow shock of a comet [Wegmann et al., 1998]. As gas in the neutral medium undergoes CX with the surface layers of shock-heated gas in supernova remnants, the collision energies are dominated by the thermal motion of the hot gas, which are tens of eV/amu [Wise and Sarazin, 1989]. Ions in the ISM may also interact with nearby neutrals at these thermal velocities [Steigman, 1975, Christensen et al., 1977]. In addition, MEC likely plays an important role in SWCX, as the multi-electron neutrals CO_2, H_2O, and H_2 are abundant in cometary

comae and planetary atmospheres.

While K-shell spectra are challenging to fully understand, the situation is even worse for L-shell due to its more complex atomic structure. Compounding the problem, few experimental data of L-shell CX exist, especially at high resolution. The only data in the literature are for the low-Z elements C, N, and O in the EUV range [Bliek et al., 1998, Crandall et al., 1979, Dijkkamp et al., 1985, Folkerts et al., 1995, Lubinski et al., 2000, 2001, Soejima et al., 1992], and X-ray measurements of Kr, U [Beiersdorfer et al., 2000b, Tawara et al., 2002, 2003], Fe [Frankel et al., 2009b, Beiersdorfer et al., 2008], and S [Frankel et al., 2009b], the latter being the only previous L-shell X-ray measurement at high spectral resolution. Results from comparisons of these experiments to theoretical models, ranging from classical and semi-classical to quantum mechanical, are mixed, but tend towards agreeing at high collision energies and showing significant discrepancies at low collision energies [Soejima et al., 1992, Lubinski et al., 2000, 2001].

Performing experimental measurements of CX between astrophysically abundant L-shell ions and neutrals at high spectral resolution is a crucial step towards understanding the detailed atomic physics of CX, and benchmarking and improving CX theory. In this chapter, we present recent measurements of CX with Ni^{19+} and He and H_2 [1] with an Electron Beam Ion Trap (EBIT) and an X-ray microcalorime-

[1] One may note that we do not present measurements with atomic H, even though this is the most astrophysically relevant target. This harkens back to Section 1.7: we did in fact use an atomic H source for some experiments, but the results were unsatisfactory. Our efforts to characterize the fraction of atomic vs. molecular hydrogen from our atomic H source were limited by poor

ter. In the following chapter, we will compare our experimental results to theory.

5.2 Experimental Method

For our experiments, we used the EBIT-I electron beam ion trap at the Lawrence Livermore National Laboratory (LLNL) [Beiersdorfer et al., 2003a, Beiersdorfer, 2008] and measured the spectra with the EBIT calorimeter spectrometer (ECS) [Porter et al., 2004, 2008a]. For a more detailed description of the LLNL EBIT and the ECS, see Chapter 3. A brief description of the tools used follows.

The EBIT is a plasma source with with six radial ports, onto which we attach various spectrometers or gas injectors. The EBIT operates in one of two modes: electron trapping mode and magnetic trapping mode. For our CX experiments, we used both in sequence, beginning with electron trapping mode. In this mode, neutral species that are injected into the EBIT trap region are collisionally ionized by a tunable electron beam, then confined in the trap. These newly-created ions are radially confined due to the electrostatic attraction of the electron beam, and axially confined by a voltage potential applied across three copper drift tubes. We adjust the electron beam energy and the length of time for which the electron beam is on to achieve our desired charge state. Next, we turn off the beam and enter into magnetic trapping mode [Beiersdorfer et al., 1996b], where the ions are radially confined by the 3 T magnetic field of a pair of superconducting Helmholtz coils, and

signal to noise, so it was difficult to know this fraction with sufficient accuracy. We are currently working towards developing a more satisfactory and well-characterized method of performing CX experiments with atomic H.

axially by the electric field of the drift tubes. In this mode, CX may occur between ions and neutrals that are simultaneously injected into the trap via another radial port. These ions lower their charge state with each successive CX interaction, until most CX involves ions of a low enough charge state that the emitted photons are no longer in the X-ray band. At this point, the trap is emptied and the cycle is repeated. One cycle that includes electric trapping mode, followed by magnetic trapping mode, then finally emptying the trap, is called an EBIT cycle. This is repeated until the resulting CX spectrum has sufficient counts in each individual line.

For the experiments presented here, nickel was supplied by sublimation of nickelocene ($C_{10}H_{10}Ni$) which flowed directly into the trap region via one of the six radial ports around the EBIT. In the charge-breeding electric trapping phase, called direct excitation (DE), we tuned the electron beam energy to breed mostly F-like Ni (Ni^{19+}), which leads to Ne-like (Ni^{18+}) following single electron capture (SEC) in CX. Ne-like Ni was also present during charge breeding. This was necessary in order to avoid creating O-like, thus F-like following CX, which has several spectral lines within the Ne-like spectrum. We injected neutral He and H_2 via a ballistic gas injector connected to another radial EBIT port.

The EBIT cycle consisted of 0.35 seconds of charge breeding followed by 0.35 seconds of CX, after which the trap was dumped and the cycle repeats. Figure 5.1 shows individual X-ray counts as a function of the EBIT cycle, where the significant reduction in count rate delineates where DE ceases and CX begins. Figures 5.4–5.7 show comparisons of the DE and CX spectra.

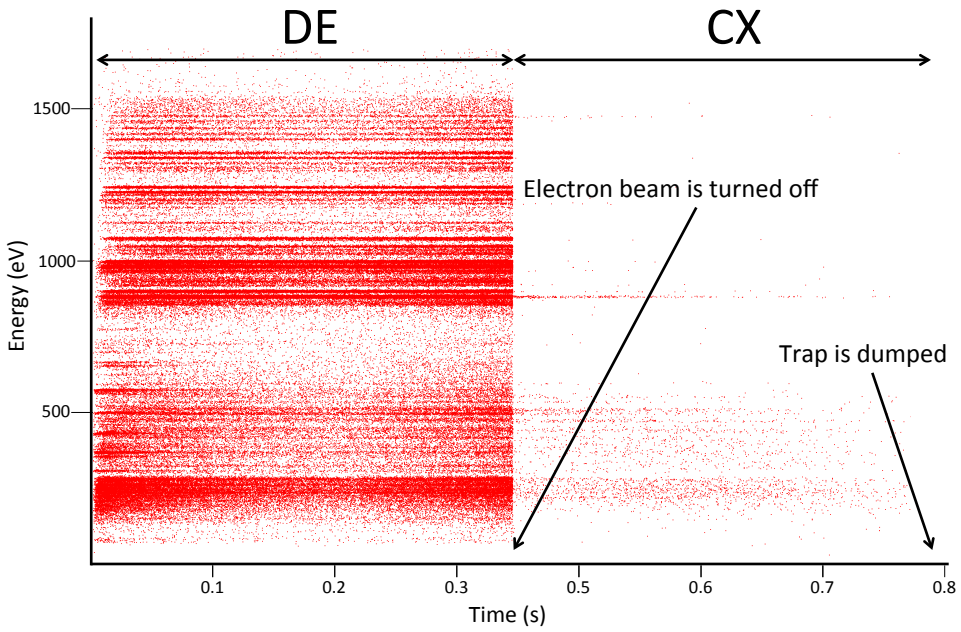

Figure 5.1 Measured X-ray energy as a function of the EBIT cycle, showing ∼35 ms of DE followed by ∼35 ms of CX.

Neutral Ni was also present during CX, along with background neutrals present in the trap such as C, N, and O, and trace amounts of Ar, which are from residual air in the EBIT vacuum space. We provide an analysis and estimate of our background CX rate in the next section. X-rays may also be produced during the CX phase from metastable states, but we exclude this from our spectra by commencing data analysis a few microseconds after the electron beam is turned off, which is long enough for these states to relax to the ground state.

Typical thermal energies of trapped ions in the EBIT are $\sim$10 eV amu^{-1} ($\sim$50 km s^{-1}). This is the approximate collision energy/velocity at which CX occurs in our experiments. CX experiments performed with EBITs are thus an ideal way to probe the important low collision energy regime, which, as mentioned in Section 5.1, is not well described by theory.

We measured our spectra with the EBIT Calorimeter Spectrometer, which is connected to the EBIT via a radial port. The ECS is a silicon-thermistor X-ray microcalorimeter developed at NASA/GSFC as part of the Astro-E/Suzaku program. It has a 30-pixel array of silicon-doped thermistors which are divided into a mid- and a high-energy array of 16 and 14 pixels, respectively. With these two arrays, the ECS has a total dynamic range of 0.05–100 keV. The experiments discussed here made use of the mid-band array, which has an energy resolution of $\sim$4.5 eV at 6 keV and an absorber quantum efficiency of nearly unity. Each X-ray measured by the ECS is time-tagged with its arrival time relative to the EBIT cycle during acquisition, which allows us to temporally distinguish the X-rays from the DE and CX phases during analysis.

The ECS has four internal aluminized polyimide filters used to block optical and thermal radiation at temperature stages of 77 K, 4 K, 300 mK, and 50 mK, with a total aluminum thickness of 1460 Å and total polyimide thickness of 2380 Å. We also used a 500 Å polyimide window outside the ECS dewar to isolate the ECS vacuum from the EBIT vacuum. These thicknesses have been experimentally verified to an accuracy of ∼10%.

5.3 Analysis

We created a gain scale to correlate the pulse height of each event measured on the ECS to a photon energy in eV (see Section 3.2.1 for an overview of the physics of microcalorimeters and Section 3.2.2 for the function of a gain calibration). We accomplished this by injecting into the EBIT several different species that have K-shell lines at well-known energies within and beyond the Ni L-shell energy band, measuring the pulse height of these lines with the ECS, and fitting a 4^{th} order polynomial to these points to map out a well-sampled gain scale across our energy band of interest.

We removed excess counts in our spectra due to cosmic ray events in the detector frame using a software algorithm that searches for nearly simultaneous events measured on multiple pixels on the ECS. We then made time cuts in our data separating the DE and CX portions of each EBIT cycle. We combined spectra from several measurements with the same experimental conditions, namely neutral gas species, Ni and neutral gas injection pressures, and background conditions, to

create one dataset for each ion and neutral combination.

We took into account X-ray attenuation from the ECS blocking filters, as well as from contaminants present in EBIT that froze on one or more filters. We believe these contaminants are water ice frozen on the 77 K filter, N_2 or O_2 gas frozen on the 4 K filter, or both. The shapes of the N_2 and O_2 transmission curves are very similar above the oxygen K edge, and our Ni L-shell lines of interest all occur above this edge. We therefore made a fiducial assumption that the contaminant is water ice, and determined the thickness of the ice by performing contemporaneous measurements of the decrement in the ratio of the O Ly-α to Ly-β line strengths in electron impact excitation experiments. The measured ratio of these lines at high electron beam energy ($\sim$ 12 keV) is 6.25 [Beiersdorfer, 2003]. From our measurements of the decrement, we calculated an ice thickness of $\sim$0.3 μm for the time period during which our experiments were performed. See Section 3.2.2 for a discussion on this calculation. Combining the effects from the ECS filters and the ice corresponds to a maximum flux correction of 42% for the strongest line in the CX spectra at $\sim$880 eV, but closer to 9% for the higher energy lines towards $\sim$1500 eV. The spectra shown in the following section are not corrected for this attenuation, but the models used in the cross section calculations described in Section 6.3 take this into account. The total effective transmission accounting for attenuation from both the filters and the ice frozen on the filters is shown in Figure 5.2.

We performed contemporaneous measurements of the background CX rate present in the trap by injecting only Ni with no other neutral gas. The only neutrals present were neutral Ni due to the continuous nature of the injection method, as

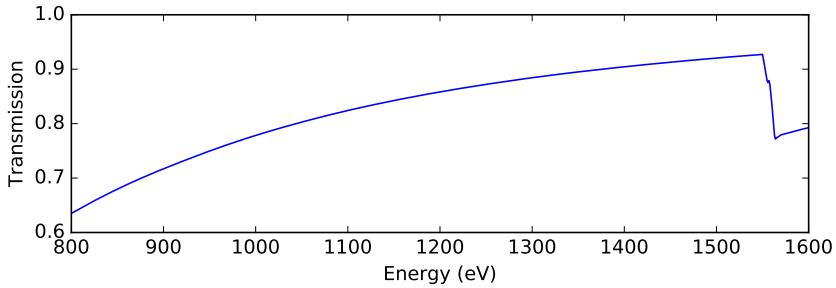

Figure 5.2 X-ray transmission in our energy range of interest of the infrared blocking filters and 0.3μm of water ice frozen on one or more of the filters.

well as C, N, and O that are often present at a low level in the EBIT chamber. While we do identify H- and He-like C, N, and O lines in our DE spectra, CX with bare, H-like, and He-like C, N, and O, do not lead to spectral lines in our region of interest. For example, even electron capture into $n = 15, l = 1$ onto O^{8+} would yield an emission line at ~868 eV, whereas the lowest energy line in the L-shell band of Ne-like Ni occurs around ~880 eV. Another common background gas is Ar. The electron beam energy for the experiments presented here was sufficient to breed primarily He-like Ar, which would lead to Li-like Ar following SEC in CX. Li-like Ar would yield spectral lines from its most likely high-n capture state according to Equation 1.2 ($n = 8 - 11 \rightarrow n = 2$), which do fall in our energy range of interest. However, we measure a negligible number of photons resulting from this species in DE, so do not expect Li-like Ar to be significant in our CX spectra.

We do perform a correction for background CX between F-like Ni (Ni^{19+}) and neutral nickel. We estimate the strength of the background contribution in our

experiments by considering the relative count rate of a pure background spectrum compared to a "signal" spectrum. We expect a background CX spectrum to have a fairly low and constant count rate over the CX phase, since the neutral gas load injected during this phase is relatively low and the ions created during DE would not have many neutral partners with which to undergo CX quickly. Indeed, we measured this in our background spectra (see Figure 5.3). Conversely, our experiments with He and H_2 injection begin with the same number of ions as in our background spectra at the beginning of the CX phase, but have a higher gas load of neutrals available for CX, so these ions quickly undergo CX, emitting X-rays and reducing their charge state with each interaction. The number of ions in the trap decreases exponentially as:

$$N_i(t) = N_{i,0}e^{-t/\tau}, \tag{5.1}$$

where N_i is the time-dependent number of ions, $N_{i,0}$ is the initial number of ions at the end of the DE phase and start of the CX phase, t is the time, and τ is the time constant. Note that $N_{i,0}$ is the same for both signal and background spectra. The average number of ions throughout the CX phase is thus

$$\overline{N_i} = \frac{1}{\phi_{CX}}\int_0^{\phi_{CX}} N_i(t)dt = N_{i,0}\frac{\tau}{\phi_{CX}}\left(1 - e^{\frac{-\phi_{CX}}{\tau}}\right), \tag{5.2}$$

where ϕ_{CX} is the total amount of time of the CX portion of the EBIT cycle. An example of the signal and background gas loads as a function of time is shown in Figure 5.3. This shows the aforementioned exponential decay of the count rate in

the CX experiment (top) and the lower, more constant count rate of the background measurement (bottom).

Before we subtract our background spectrum from our signal spectrum, we must weight the background spectrum by the relative number of background ions present in the signal spectrum ($\frac{\overline{N_i}}{N_{i,0}}$), as well as the relative integration time of each experiment ($\frac{T_s}{T_b}$, where T_s and T_b are the total integration times of the signal and background experiments, respectively). This corresponds to a spectral correction of the form

$$\text{Background-subtracted spectrum} = \text{Signal} - \text{Background} \cdot \left(\frac{\overline{N_i}}{N_{i,0}}\right)\left(\frac{T_s}{T_b}\right). \quad (5.3)$$

We measured τ by creating a histogram of all the counts in the CX phase in each signal spectrum and fitting the curve with an exponential. We then calculated an average τ for each neutral species, weighted by the integration time for each experiment that contributed to the total spectrum. We chose ϕ_{CX} at the onset of our experimental run to be ∼0.35 seconds. This background subtraction corresponded to a maximum reduction in line flux of ∼10.7% in the H_2 experiment and ∼6.6% for the He experiment.

The following sections show the background-subtracted spectra, and in Chapter 6, we use this background-subtracted data as the input for our cross section models.

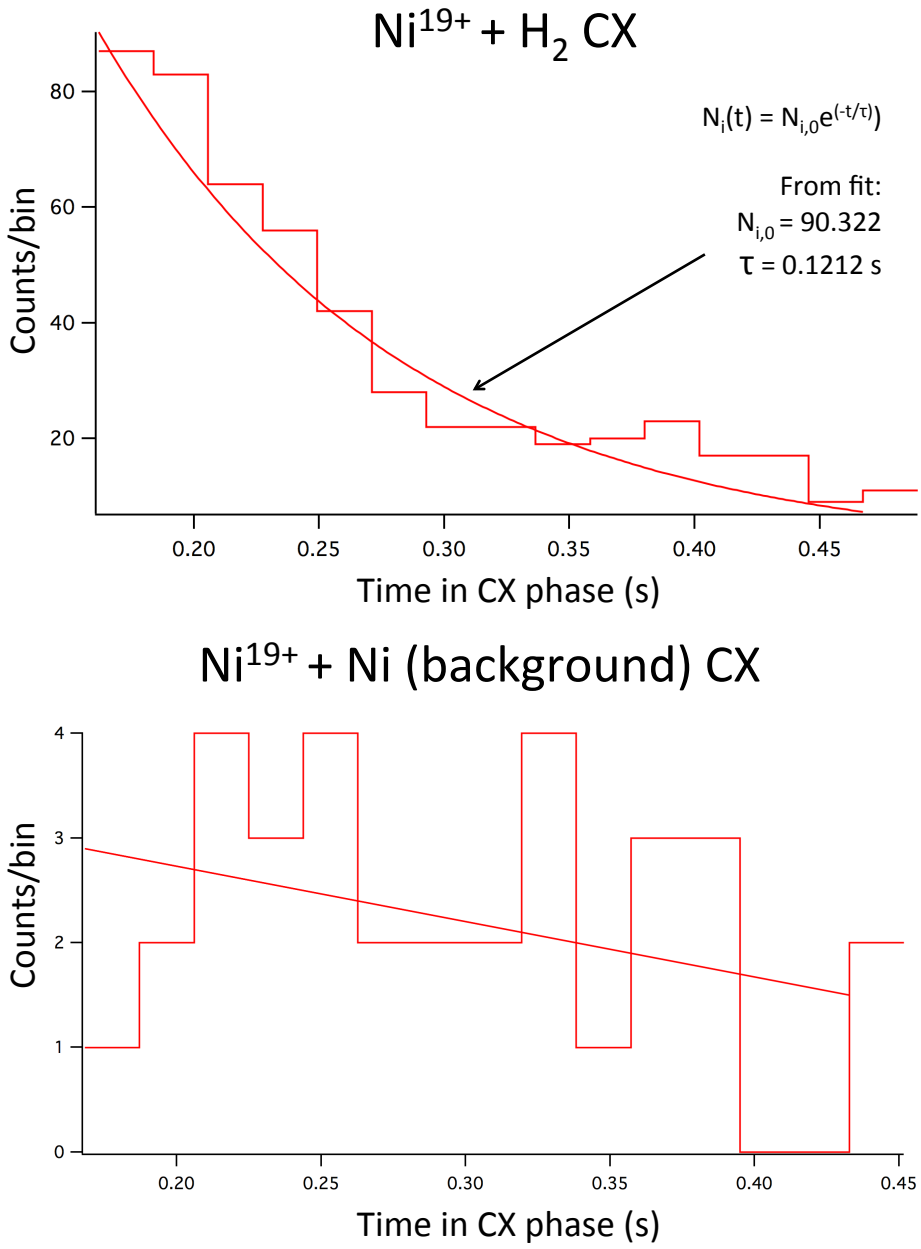

Figure 5.3 Measurements of the X-ray count rate as a function of time for our signal measurement (CX with desired ions and neutrals, top) and our background measurement (no injection of neutral partners in experiment, bottom). In the signal measurement, one can see the exponential decay of the count rate over time, where the best fit parameters for an exponential decay are shown. The background measurement shows a lower and fairly constant count rate, as expected.

5.4 Spectra

Upon measurement of the L-shell DE and CX spectra, the striking spectral differences between the DE and CX line strengths are immediately obvious. These spectra are presented in Figures 5.4–5.7. Each spectrum in these figures is approximately normalized to the peak height of the DE line near 890 eV (M2/3G) and is split into two energy bands with different y-axis scales in order to highlight the stark differences in individual line strengths.

The two largest differences between DE and CX, present in both the Ni^{19+}+H_2 and Ni^{19+}+He spectra, are at opposite ends of the L-shell spectra. At the lower energy end, the 3F, 3C, and 3G lines are greatly suppressed in comparison with the DE spectrum. In contrast, the M2/3G line is fairly strong in both CX and DE spectra, but it dominates the CX spectrum. On the high energy end, the DE spectral lines decrease in strength with increasing energy. However, in CX, the second strongest line is from a high-$n \rightarrow n = 2$ transition. This can be seen as an analog to strongly enhanced high-n Lyman lines seen in K-shell CX spectra (see Chapter 4)

The count rate is also significantly higher in DE than it is in CX. This is because in DE, an ion can be excited and radiatively de-excite many times within one EBIT cycle. However, in CX, the count rate depends on the density of the neutral species present. Typically, neutral densities are low [Beiersdorfer et al., 1996b]—we estimate this to be $\sim 10^{9-10}$ cm^3 in the experiments presented here—which leads to lower total counts in the CX spectra.

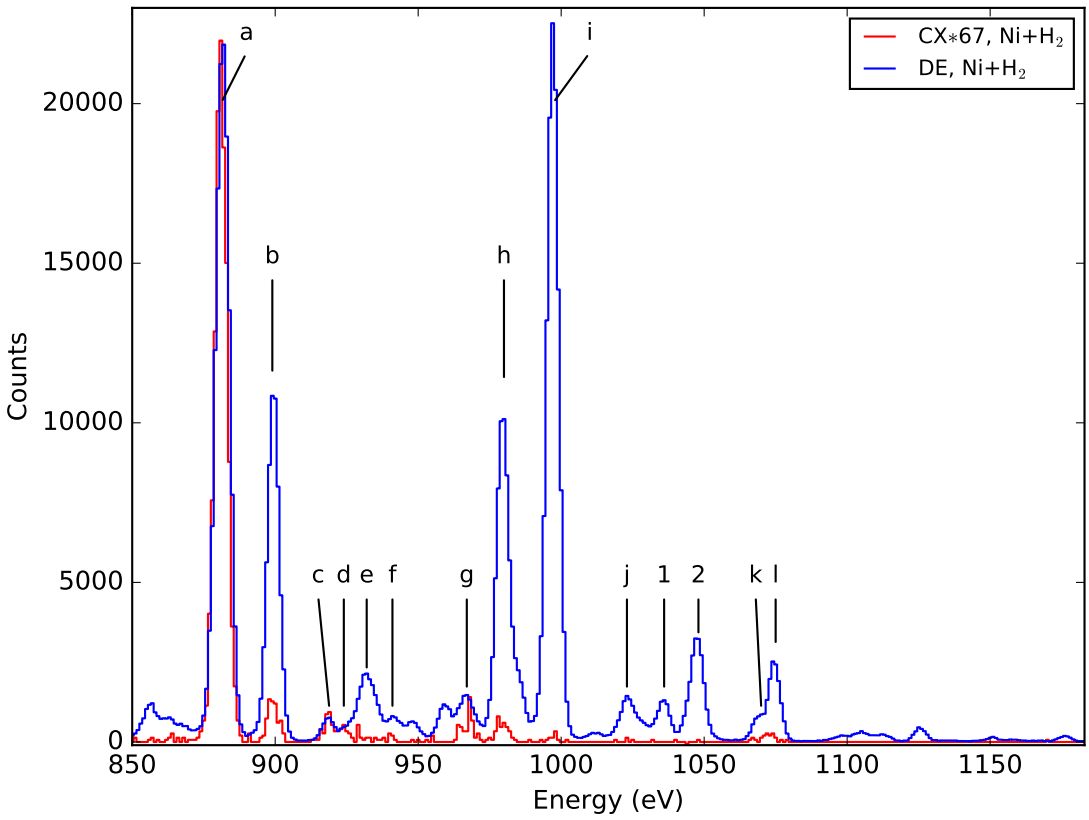

Figure 5.4 Spectra of Ni^{19+} (F-like) created in direct excitation (blue) and CX of $Ni^{19+}+H_2$ (red), from 850–1175 eV. Note the comparatively weaker 3F (line ID b), 3D (line ID h), and 3C (line ID i) lines in the CX spectrum. Line identifications correspond to the entries in Tables 5.1 and 5.2. The CX spectrum is normalized to the M2/3G line in DE (line ID a).

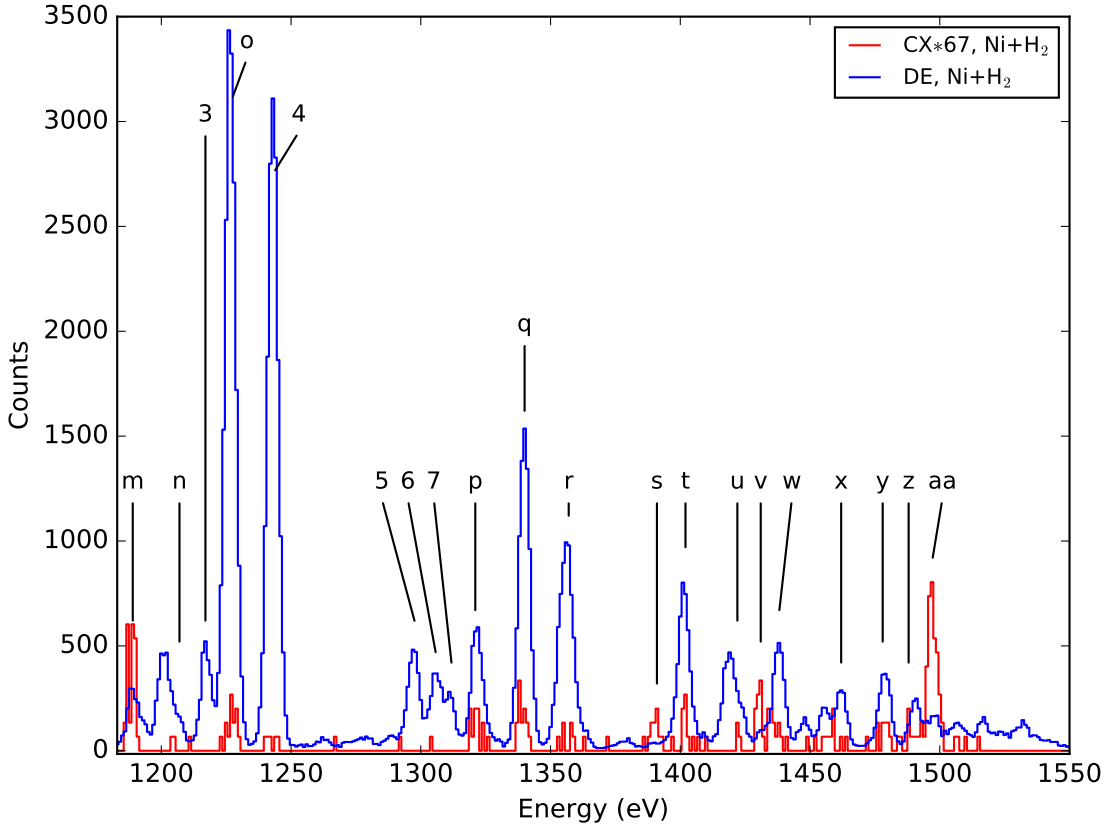

Figure 5.5 Spectra of Ni^{19+} (F-like) created in direct excitation (blue) and CX of $Ni^{19+}+H_2$ (red), from 1175–1550 eV. Note that while the lines in the DE spectrum decrease in strength with increasing energy, in CX there is a strong line near ∼1500 eV (line ID aa) resulting from a high-$n \rightarrow n = 2$ ($n \sim 11$) transition. Line identifications correspond to the entries in Tables 5.1 and 5.2. The CX spectrum is normalized to the M2/3G line in DE (line ID a).

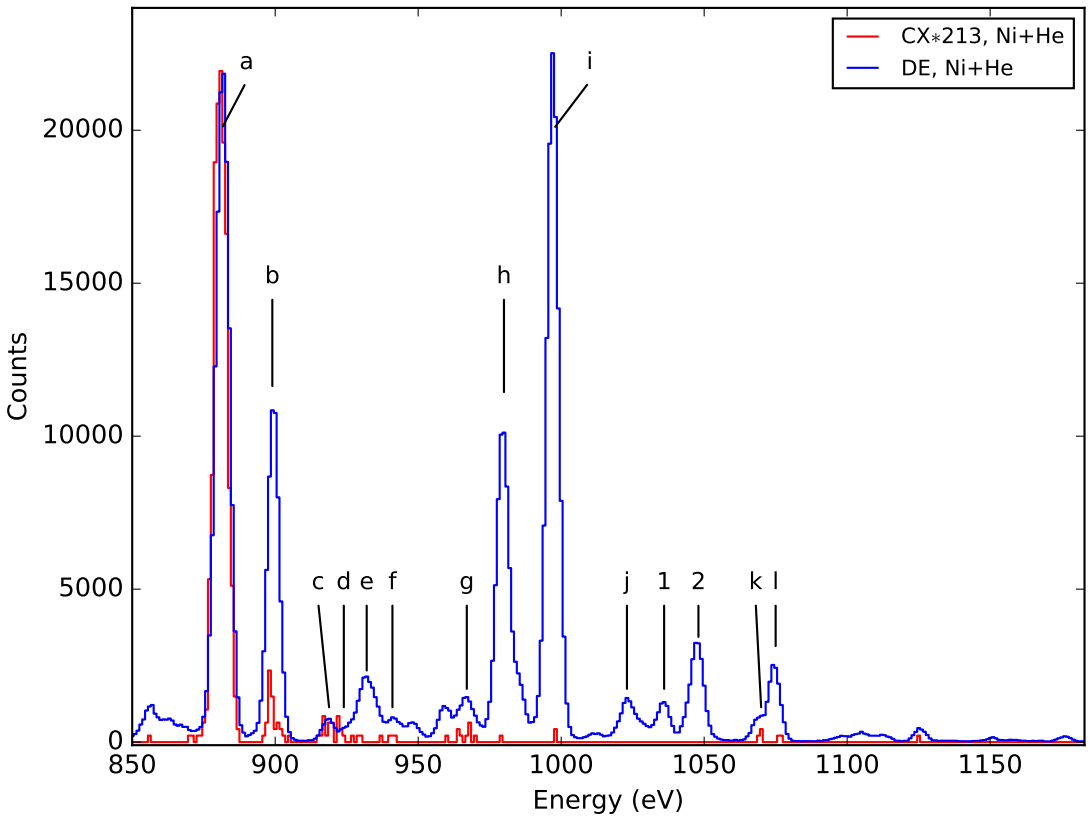

Figure 5.6 Spectra of Ni^{19+} (F-like) created in direct excitation (blue) and CX of Ni^{19+}+He (red), from 850–1175 eV. Like in the Ni^{19+}+H_2 spectra (Figures 5.4–5.5), one can note the suppressed 3F, 3D, and 3C lines (line IDs b, h, and i, respectively) in CX. Line identifications correspond to the entries in Tables 5.1 and 5.2. The CX spectrum is normalized to the M2/3G line in DE (line ID a).

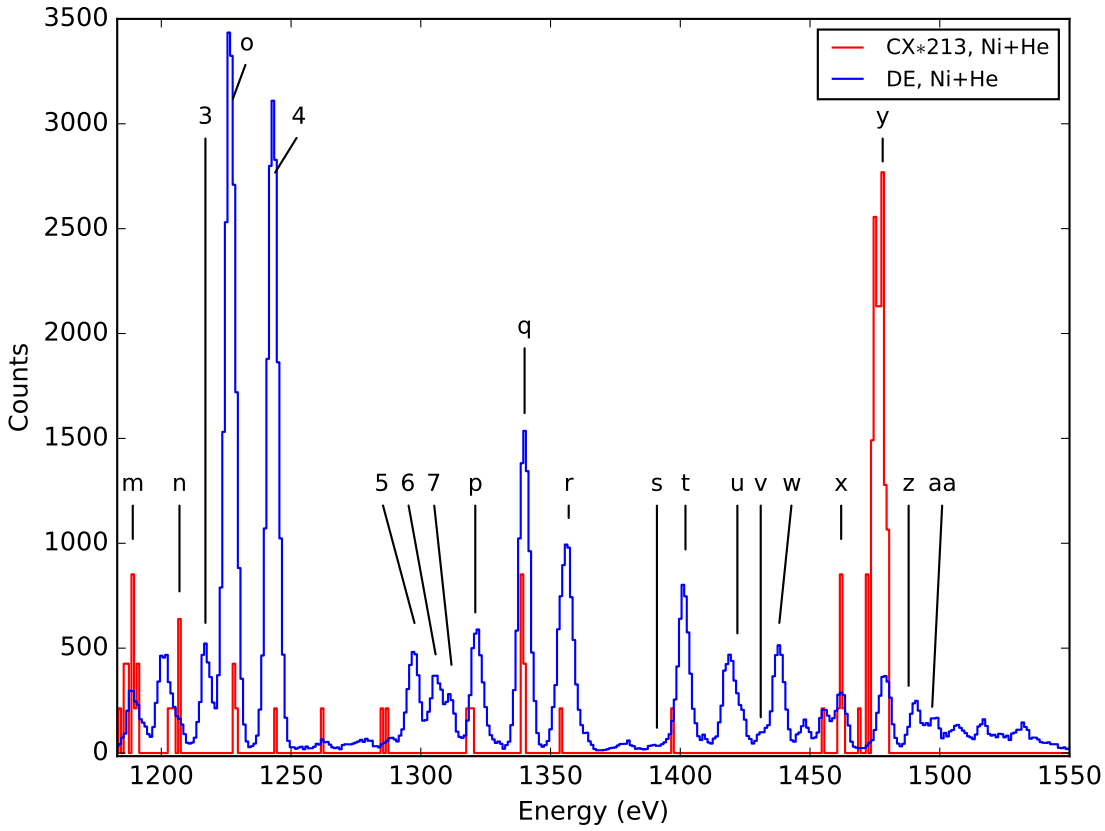

Figure 5.7 Spectra of Ni^{19+} (F-like) created in direct excitation (blue) and CX of Ni^{19+}+He (red), from 1175–1550 eV. As in the Ni^{19+}+He spectra, note the strongly enhanced high-$n \rightarrow n = 2$ line ($n \sim$8–9) near 1475 eV (line ID y). Line identifications correspond to the entries in Tables 5.1 and 5.2. The CX spectrum is normalized to the M2/3G line in DE (line ID a).

Line identifications in the CX spectra (letters, a–aa) are presented in Figure 5.8 and Table 5.1. We identified the strongest lines present in our CX spectra by aligning our DE and CX spectra in energy, selecting lines that had more than ∼2 counts in CX, and estimating the energy centroid of those lines in the DE spectrum. We then compared these line energies to calculations with the Flexible Atomic Code (FAC) and measurements of L-shell Ni lines with a high-resolution crystal spectrometer from Gu et al. [2007a]. See Section 2.1 for a description of FAC. We corrected the ionization energies to make Ne-like Ni according to Scofield [private communication], and the $3 \rightarrow 2$ transition energies to match those experimentally verified in Gu et al. [2007a]. In our identifications, we only considered lines with a branching ratio greater than 5%, except in a few cases indicated in the table. In some cases, one line may be a combination of several transitions presented in the table. Some F-like Ni lines are also included in the table; F-like lines would be present following SEC in CX with an O-like ion. Although we include them in our table, they should only be a minor contribution to the spectrum due to the fact that the O-like $2p_{1/2}2p_{3/2}^2 3d_{5/2}(J=3) \rightarrow 2p_{3/2}^2(J=2)$ transition, which should be the strongest one in the O-like series in DE [Gu et al., 2007a], is not present in our spectra.

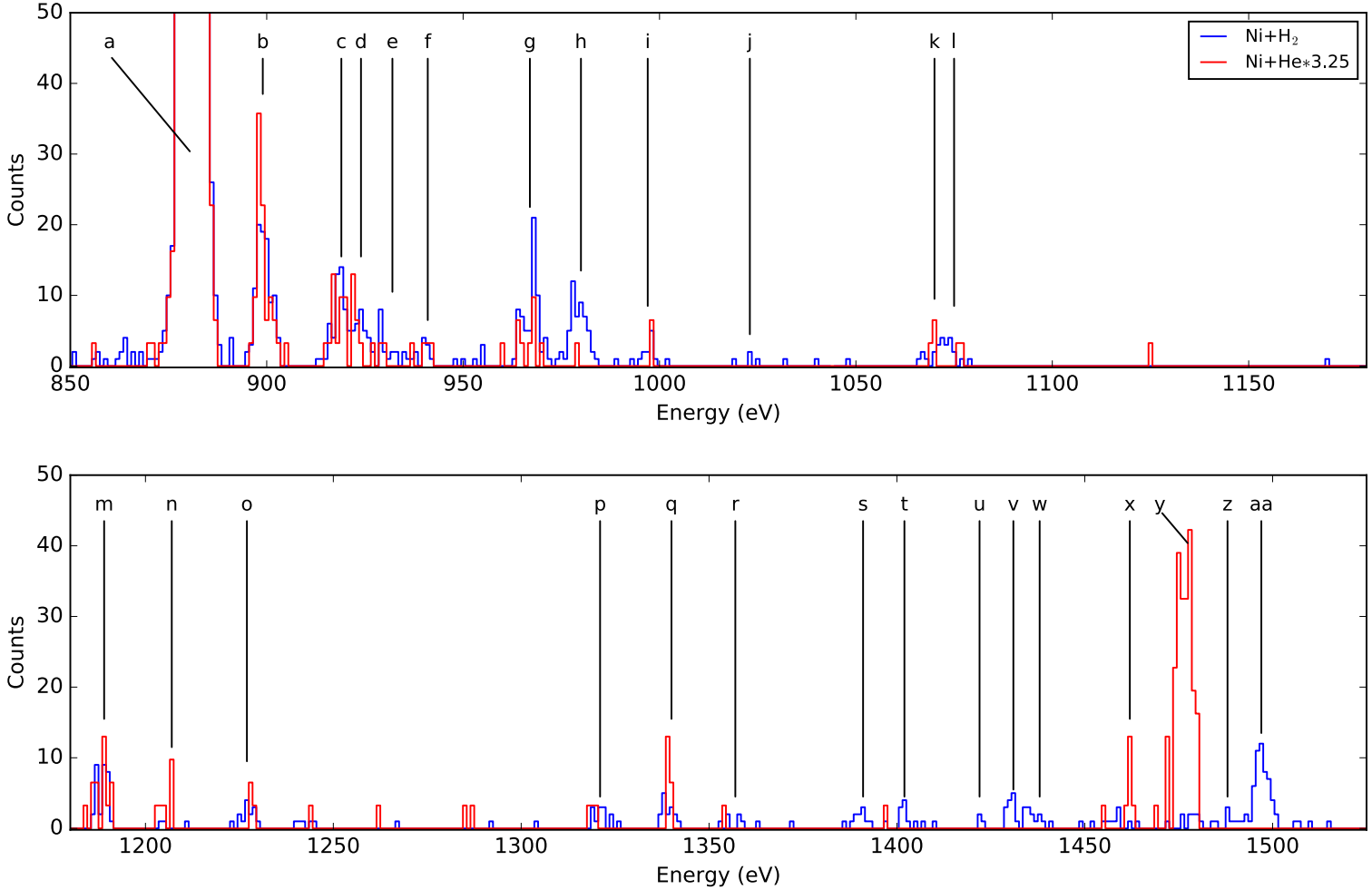

Figure 5.8 CX spectra of Ni^{19+}+H_2 (blue) and Ni^{19+}+He (red), normalized to the 3G/M2 line in the Ni^{19+}+H_2 spectrum. Lines with more than ∼2 counts are identified by letters which correspond to an entry in Table 5.1. Note the difference in the strong high-$n \rightarrow n = 2$ transitions from 1450 eV–1500 eV between the H_2 and the He spectra.

As described in Section 1.4, CX typically leads to electron capture into a high n state. The l capture state, while harder to predict, has been shown to vary with the collision energy. At high collision energies, the states are populated statistically, favoring higher angular momentum states [Janev and Winter, 1985]. After capture into such a state, the electron will de-excite via Yrast transitions, changing its l state by one with each step and eventually landing in $n = 3, 4, 5, 6$ which can then decay to $n = 2$ (see Figure 1.3). However, at the low collision energies produced with the EBIT, lower angular momentum states are favored [Ryufuku and Watanabe, 1979, Beiersdorfer et al., 2000a]. Given this, we would expect significant capture into $l = s, p$, and d in our experiments. We also naively assume that most parent F-like ions would have an electron hole in $2p$, so capture into $l = s, d$ could directly decay into $l = p$, yielding a high energy line.

The strongest line in both Ni^{19+}+H_2 and Ni^{19+}+He CX spectra is a blend of the M2 ($2p^3_{3/2}3s_{1/2}(J = 2) \rightarrow 2p^4_{3/2}(J = 0)$) and 3G ($2p^3_{3/2}3s_{1/2}(J = 1) \rightarrow 2p^4_{3/2}(J = 0)$) lines, which are not individually resolved with the ~4.5 eV resolution of the ECS. This is a stark difference from Ne-like Ni spectra following collisional excitation, where the M2/3G line is nearly as strong as the 3C line ($2p^1_{1/2}3d^3_{3/2}(J = 1) \rightarrow 2p^4_{3/2}(J = 0)$), and the 3F ($2p^1_{1/2}3s^1_{1/2}(J = 1) \rightarrow 2p^4_{3/2}(J = 0)$) and 3D ($2p^3_{3/2}3d^1_{5/2}(J = 1) \rightarrow 2p^4_{3/2}(J = 0)$) lines are also fairly strong. This can be seen in Figures 5.4 and 5.6. This result indicates that capture into a previously F-like ion with an electron hole in $2p_{3/2}$ and a radiative cascade whose penultimate state is $3s_{1/2}$ is strongly preferred. This fits with our naive view of CX at low collision energies. The relative enhancement of the M2/3G line and suppression of the 3F,

Table 5.1 CX lines identified in this work. FAC energy calculations for Ne-like and F-like ions are described in Section 2.1. All lower states for Ni^{19+} are $2p^4_{3/2}(J=0)$, and lower states for the Ni^{20+} transitions here are $2p^3_{3/2}(J=3/2)$. An asterisk indicates that the branching ratio for this transition is less than 5%, so this line is unlikely but may contribute at a low level. Such lines are only included when the measured line energy is different from the closest Ni^{19+} theoretical line energy by more than 5 eV. Names for F-like ions follow those from Gu et al. [2007a].

Line ID	Energy in DE (eV)	FAC Energy (eV)	Energy from Gu et al. [2007a] (eV)	Upper State	Name
a	882	880.753	880.827	$2p^3_{3/2}3s^1_{1/2}(J=2)$	M2
		882.888	882.96	$2p^3_{3/2}3s^1_{1/2}(J=1)$	3G
b	900	899.807	899.877	$2p^1_{1/2}3s^1_{1/2}(J=1)$	3F
c	919	920.037	918.542	$2p^3_{3/2}3p^1_{1/2}(J=2)$	E2L
d	925	926.041		$2p^3_{3/2}3p^3_{3/2}(J=2)$	
e	932	930.711	931.586	$2p^2_{3/2}3s^1_{1/2}(J=5/2)$	F4
f	941	942.002	940.346	$2p^1_{1/2}3p^1_{3/2}(J=2)$	E2U
g	967	969.255	967.947	$2p^3_{3/2}3d^1_{3/2}(J=1)$	3E
h	980	979.487	979.571	$2p^3_{3/2}3d^1_{5/2}(J=1)$	3D
i	997	997.139	997.218	$2p^1_{1/2}3d^1_{3/2}(J=1)$	3C
j	1023	1023.523	1023.475	$2p^2_{3/2}3d^1_{5/2}(J=5/2)$	F14
		1021.840	1023.475	$2p^2_{3/2}3d^1_{5/2}(J=3/2)$	F15
k	1070	1073.451		$2s^1_{1/2}3p^1_{1/2}(J=1)$	3B
l	1074	1079.017	1074.844	$2s^1_{1/2}3p^1_{3/2}(J=1)$	3A
		1076.882		$2s^1_{1/2}3p^1_{1/2}(J=2)$	*
m	1188	1190.006		$2p^3_{3/2}4s^1_{1/2}(J=1)$	4G
n	1207	1207.353		$2p^1_{1/2}4s^1_{1/2}(J=1)$	4F
o	1226	1228.023		$2p^3_{3/2}4d^1_{5/2}(J=1)$	4D
p	1322	1322.537		$2p^3_{3/2}5s^1_{1/2}(J=1)$	5G
q	1340	1338.760		$2p^3_{3/2}5d^1_{3/2}(J=1)$	5E
		1340.036		$2p^1_{1/2}5s^1_{1/2}(J=1)$	5F
		1341.376		$2p^3_{3/2}5d^1_{5/2}(J=1)$	5D
r	1356	1356.458		$2s^1_{1/2}4p^1_{1/2}(J=1)$	4B
		1358.142		$2p^1_{1/2}5d^1_{3/2}(J=1)$	5C
		1358.583		$2s^1_{1/2}4p^1_{3/2}(J=1)$	4A
s	1390	1391.931		$2p^3_{3/2}6s^1_{1/2}(J=1)$	6G
t	1401	1402.566		$2p^3_{3/2}6d^1_{5/2}(J=1)$	6D
u	1423	1419.787		$2p^1_{1/2}6d^1_{3/2}(J=1)$	6C
v	1432	1432.827		$2p^3_{3/2}7s^1_{1/2}(J=1)$	7G
w	1438	1439.425		$2p^3_{3/2}7d^1_{5/2}(J=1)$	7D
x	1462	1462.704		$2p^3_{3/2}8d^1_{3/2}(J=1)$	8E
		1463.288		$2p^3_{3/2}8d^1_{5/2}(J=1)$	8D
y	1479	1476.579		$2p^3_{3/2}9s^1_{1/2}(J=1)$	9G
		1476.658		$2p^1_{1/2}8s^1_{1/2}(J=1)$	8F
		1479.618		$2p^3_{3/2}9d^1_{5/2}(J=1)$	9D
		1480.824		$2p^1_{1/2}8d^1_{3/2}(J=1)$	8C
		1481.395		$2s^1_{1/2}5p^1_{1/2}(J=1)$	5B
		1482.437		$2s^1_{1/2}5p^1_{3/2}(J=1)$	5A
z	1490	1489.084		$2p^3_{3/2}10s^1_{1/2}(J=1)$	10G
		1491.282		$2p^3_{3/2}10d^1_{5/2}(J=1)$	10D
aa	1499	1497.226		$2p^1_{1/2}9d^1_{3/2}(J=1)$	9C
		1498.262		$2p^3_{3/2}11s^1_{1/2}(J=1)$	11G
		1499.902		$2p^3_{3/2}11d^1_{5/2}(J=1)$	11D

Table 5.2 Lines only present in the DE spectra or the ACX and SPEX-CX models described in Chapter 6, not in the experimental CX spectra. FAC energy calculations for Ne-like and F-like ions are described in Section 2.1. All lower states for Ni^{19+} are $2p^4_{3/2}(J = 0)$, and lower states for the Ni^{20+} transitions here are $2p^3_{3/2}(J = 3/2)$, except for line ID 6, which is $2p^1_{1/2}(J = 1/2)$. Line IDs 9–12 refer to the high-n transitions in the ACX model which we have determined to have energies different from those in FAC by as much as ~ 10 eV (see Section 6.2). The ACX energies were determined by Adam Foster [private communication]. All lower states for Ni^{19+} are $2p^4_{3/2}(J = 0)$, and lower states for the Ni^{20+} transitions here are $2p^3_{3/2}(J = 3/2)$, except for line ID 6, which is $2p^1_{1/2}(J = 1/2)$.

Names for F-like ions follow those from Gu et al. [2007a].

Line ID	Peak Energy (eV)	FAC Energy (eV)	Energy from Gu et al. [2007a] (eV)	Energy from ACX	Upper State	Name
1	1036	1036.373	1036.740		$2p^1_{1/2}2p^3_{3/2}3d^1_{3/2}(J = 5/2)$	F17
2	1048	1047.188	1048.044		$2p^1_{1/2}2p^3_{3/2}3d^1_{3/2}(J = 3/2)$	F20
		1048.209	1048.044		$2p^1_{1/2}2p^3_{3/2}3d^1_{3/2}(J = 5/2)$	F20
3	1217	1222.946			$2p^3_{3/2}4d^1_{3/2}(J = 1)$	4E
4	1243	1244.359			$2p^1_{1/2}4d^1_{3/2}(J = 1)$	4C
5	1298	1297.194			$2p^2_{3/2}4d^1_{5/2}(J = 5/2)$	
6	1306	1305.584			$2p^1_{1/2}2p^3_{3/2}4d^1_{5/2}(J = 1/2)$	
7	1312	1311.024			$2p^1_{1/2}2p^3_{3/2}4d^1_{3/2}(J = 5/2)$	
8	1417	1419.787			$2p^1_{1/2}6d^1_{3/2}(J = 1)$	
9	1488	∼1477–1481		∼1486–1488	$2p^1_{1/2}8l$, $2p^3_{3/2}10l$	
10	1499	∼1489–1492		∼1498–1501	$2p^3_{3/2}10l$	
11	1506	∼1494–1498		∼1504–1508	$2p^1_{1/2}9l$	
12	1518	∼1507–1509		∼1516–1519	$2p^1_{1/2}10l$	

3D, and 3C lines may thus be seen as strongly diagnostic of the presence of CX.

A key feature of CX in K-shell H-like spectra is a strong $np \rightarrow 1s$ Lyman line, where n is large [Betancourt-Martinez et al., 2014c, Leutenegger et al., 2010]. An analog to this for L-shell spectra would be a strong $ns \rightarrow 2p$ or $nd \rightarrow 2p$ line. We do in fact observe this in our spectra, with the strong line most likely being the $11s$ or $11d \rightarrow 2p$ transition in the Ni^{19+}+H_2 spectrum and $8d$ or $9d \rightarrow 2p$ transition in the Ni^{19+}+He spectrum.

The canonical equation to estimate the primary n capture state of the transferred electron is Equation 1.2, which is repeated here for convenience:

$$n_{\max} \sim q\sqrt{\frac{I_H}{I_n}}\left(1+\frac{q-1}{\sqrt{2q}}\right)^{-1/2} \sim q^{3/4}, \tag{5.4}$$

where I_H and I_n are the ionization potentials of hydrogen and the neutral target, respectively, and q is the ion charge [Janev and Winter, 1985].

Following this equation leads to an estimate of $n_{\max} \sim 9$ for Ni^{19+}+H_2 and $n_{\max} \sim 7$ for Ni^{19+}+He. Though the trend of $n_{\max}$ being inversely proportional to the ionization potential of the neutral gas is observed in our experiment (with an $n_{\max}$ of ~ 11 for Ni^{19+}+H_2 and $n_{\max} \sim 9$ for Ni^{19+}+He), this canonical estimate differs from our measurement by several n levels. This highlights the approximate nature of this equation.

We also observe emission from intermediate states such as $3d, 4s, 4d, 5s, 5d, 6s$, and $6d \rightarrow 2p$. Emission from transitions between $n < n_{\max}$, $l = s, d$ and $2p$ may result from one of three options.

First, if a high angular momentum state is populated after capture, the electron can decay via the Yrast chain as described in Section 1.4, ending in a $2p$ state. As capture into low angular momentum states is preferred in EBIT experiments, however, this is not likely to be the dominant reason for these intermediate-energy lines.

Second, electron capture into $n \sim n_{\max}$, $l = p$ may decay in one step to a $n < n_{\max}$, $l = s, d$ state, then subsequently to $2p$. We have determined via FAC calculations that the branching ratios required for this to occur are not insignificant, so this may play a role in creating these lines.

Third, these intermediate-energy transitions may result from double-electron capture into a doubly excited state, followed by autoionization of one electron while the second drops to a lower n state. This second electron would then radiatively de-excite from that lower state to $n = 2$. It has been shown experimentally that double electron capture can account for nearly half of all CX interactions [Ali et al., 2005]. Further, the relative strength of these intermediate-energy lines is higher in the Ni^{19+}+H_2 spectrum than it is in the Ni^{19+}+He spectrum. The ionization potential of H_2 is ∼15.4 eV, while the first and second ionization potentials of He are ∼24.6 eV and ∼54.4 eV, respectively. It thus follows that multi-electron capture is more likely to occur with neutral H_2 than with He, which would suggest that the dominant process creating these intermediate-energy lines in our spectra is in fact from the double-electron capture scenario.

Although these empirical observations are extremely valuable, in order to fully disentangle the relative dominance of all relevant processes, detailed radiative cas-

cade models are required. The following chapter begins to address this need.

A particularly fascinating feature of our spectra is the unexpectedly strong presence of the 3F and 3A/3B lines. These lines result from an electron hole in $2s_{1/2}$ being filled by either a $3p_{3/2}$ or $3p_{1/2}$ electron (to create the 3A and 3B lines, respectively), or a hole in $2p_{1/2}$ being filled by a $3s_{1/2}$ electron (to create the 3F line). The presence of these lines is surprising because as previously described, our naive assumption of the F-like parent ion core structure was the lowest energy configuration with a hole in $2p_{3/2}$, and we do not expect CX to influence this core configuration. We do not observe O-like Ni in our DE spectrum, which could potentially populate these levels after capturing two electrons. One possible reason for the presence of these lines could be from the effects of mixing: the energy state of a given core configuration with one excited electron may be similar to a different core configuration with an excited electron. More detailed theoretical calculations are necessary to obtain an accurate estimate of the strength of this effect.

5.5 Summary

In this chapter, we have described experiments performed at the LLNL EBIT of CX between F-like Ni and neutral H_2 and He to create Ne-like Ni. These are the first high-resolution L-shell data of Ni L-shell CX, adding to the very short list of high resolution L-shell CX data. This was also performed in the low collision energy regime, where most discrepancies between experiment and theory occur.

The spectra resulting from collisional excitation and CX are dramatically dif-

ferent. We found that a significantly enhanced M2/3G line is likely highly diagnostic of CX, and that the ratio of the higher energy lines to M2/3G may be a good indicator for the capture state, similar to the hardness ratio for K-shell spectra.

There are obvious differences between the $Ni^{19+}+H_2$ spectrum and the Ni^{19+}+He spectrum. The strong high energy line is shifted to a higher energy for the $Ni^{19+}+H_2$ spectrum, as is qualitatively predicted by the canonical equation for n_{max} (Equation 1.2), and the intermediate energy lines are stronger for the Ni^{19+}+He spectrum. It remains to be determined whether these differences are due to the difference in ionization potential of the neutral partner, the relative significance of MEC, or due to innate variations in the cross sections. With these experimental results in hand, we can now begin comparing them to theory.

Chapter 6: L-shell Ni CX: Comparisons to Models and Relative Capture Cross Section Calculations

6.1 Introduction

In the previous chapter, we presented the first high-resolution spectra of CX between L-shell Ni and two astrophysically relevant neutral species, H_2 and He. We now compare our experimental spectra with those created using the commonly-used CX models SPEX-CX [Gu et al., 2016] and ACX [Smith et al., 2014a], and show that significant differences exist. See Section 2.2 for details on these models. We also describe a pipeline we created that utilizes radiative cascade models with atomic data from FAC in order to fit our data to a model that assumes single electron capture (SEC) into various quantum states. See Section 2.1 for a brief discussion on FAC and how we use the code. We then use this model fit to extract state-selective relative capture cross sections from our experimental data.

We first demonstrate the functionality of our model with the relatively simpler case of K-shell S undergoing CX with neutral He, and compare our results to recent Multi-Channel Landau-Zener (MCLZ) state-selective cross section calculations. An overview of MCLZ theory is given in Section 2.3. We then move back to L-shell Ni

CX, and present our model fit to the data in Chapter 5, along with the state-selective cross sections we derive, and discuss our next steps.

6.2 Comparisons to Spectral Models

We used the CX spectral synthesis codes SPEX-CX and ACX to simulate spectra for interactions between Ni^{19+}+H (SPEX-CX, ACX) and Ni^{19+}+He (ACX only) to then compare to our experimental spectra.

We gave the SPEX-CX model as an input the lowest allowable collision velocity of 50 km/s, the approximate ionization temperature of 500 eV, and only considered Ni ions (zeroing out the abundance of all the other ions in the model). While this does not exactly describe our system—in particular, the monoenergetic electron beam in the EBIT does not have a thermal Maxwellian distribution in the mode in which we operated it—SPEX-CX requires a temperature, and 500 eV yielded the closest match to our spectra upon visual inspection. We then convolved the result of this model with a Gaussian line profile to match the instrumental response of the ECS (see Section 3.2.3.7).

To compare our data to the ACX model, we used the ACXION model, and again convolved the resulting spectrum with a Gaussian line profile. We set the ion and charge state to be Ni^{19+}, and considered CX with both H and He by adjusting the *fracHe0* parameter. We used two different l distributions by varying the *model* parameter: model "8," which is the default model used in ACX and which assumes a separable l distribution (Equation 1.8), and model "15," which uses a Landau-Zener

weighting function for the total L distribution (Equation 1.7). Model 15 was chosen because Landau-Zener methods are most applicable to low-energy collisions such as those in EBITs [Janev et al., 1985], and because model 15 best matched previously measured K-shell EBIT CX spectra [Betancourt-Martinez et al., 2016].

Figures 6.1–6.17 show the results of the comparison between our experimental data and these models. These figures show background-subtracted data (see Section 5.3) and model-predicted counts (i.e., the models have been adjusted to account for the X-ray attenuation in the data due to the ECS filters; see Section 3.2.3.1). Figures 6.1, 6.8, and 6.13 show the entire spectrum for each of the comparisons we perform in order to obtain a global view. Each spectrum is then split into four plots to more easily identify the differences in line strength. SPEX-CX cannot incorporate neutral He, so it is not compared to our Ni^{19+}+He data. The line identifications on the plots correspond to the entries in Tables 5.1 and 5.2. Table 5.1 presents lines that we identified in our experimental CX spectra. The lines presented in Table 5.2 correspond to lines that are present in the DE spectra or in the models, but not in our experimental CX spectra. In the figures, all model line strengths are normalized to the total number of counts in the M2/3G line in the data, so that line is not shown in the zoomed-in plots.

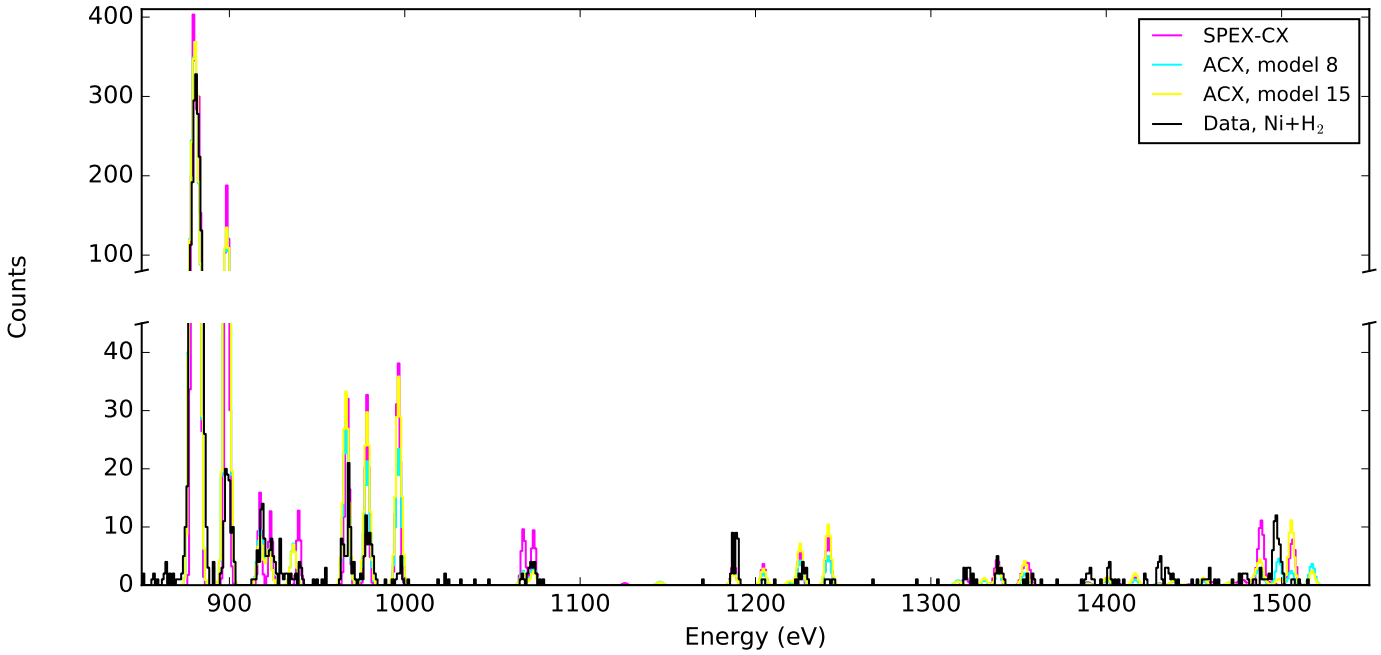

Figure 6.1 SPEX-CX model (magenta), ACX model 8 (cyan), and ACX model 15 (yellow), assuming CX between Ni^{19+} and H, plotted against Ni^{19+}+H_2 EBIT CX data (black). Note the broken y-axis. The data spectrum has been background-subtracted, and the model spectra show model-predicted counts, i.e., they have been adjusted to account for the attenuation in the data due to the ECS filters. All spectral lines are normalized to the flux in the M2/3G line in the data. Individual lines are labeled in subsequent plots.

We first compare our Ni^{19+}+H_2 data to the models assuming capture from atomic H. It is relevant to compare CX between H_2 and H because of their similar ionization potentials (15.4 eV and 13.6 eV, respectively) and number of electrons available to be captured (2 and 1), though MEC does have to be considered in the H_2 case, and intrinsic differences in the state-selective cross section may be present. Figures 6.2–6.5 show the SPEX-CX and ACX models along with the Ni^{19+}+H_2 EBIT data. Although some lines are well approximated by the models, both in strength and energy centroid, (namely c, d, g; k and l with the ACX model; and q with the SPEX-CX model), most lines are dramatically over- or under-predicted. There are strong lines in the models that did not have enough counts in the data to be initially identified according to our ∼2-count minimum threshold, and the ACX model even predicts flux at energies that do not have any Ni^{19+} transitions, according to FAC structure calculations, such as the line between 1140–1160 eV and the line to the low energy side of line ID p.

An important energy regime that the models fail to correctly reproduce is near the strong high-$n \rightarrow n = 2$ transition(s) around 1500 eV, which, in the EBIT Ni^{19+}+H_2 spectrum, is likely dominated by $11s, 11d \rightarrow 2p$ transitions (see Chapter 5). Recall that Equation 1.2 predicts the primary n level of electron capture from neutral H_2 to be 9.0. With atomic H, which is the assumption in the models, this number changes to $n = 9.6$. Models in ACX that weight this distribution should put 60% of electron capture into $n = 10$ and 40% into $n = 9$. If we compare the lines in the ACX spectra to our FAC energy calculations, it would appear that, first, ACX actually populates $n = 8 - 12$, and second, models 8 and 15 differ in

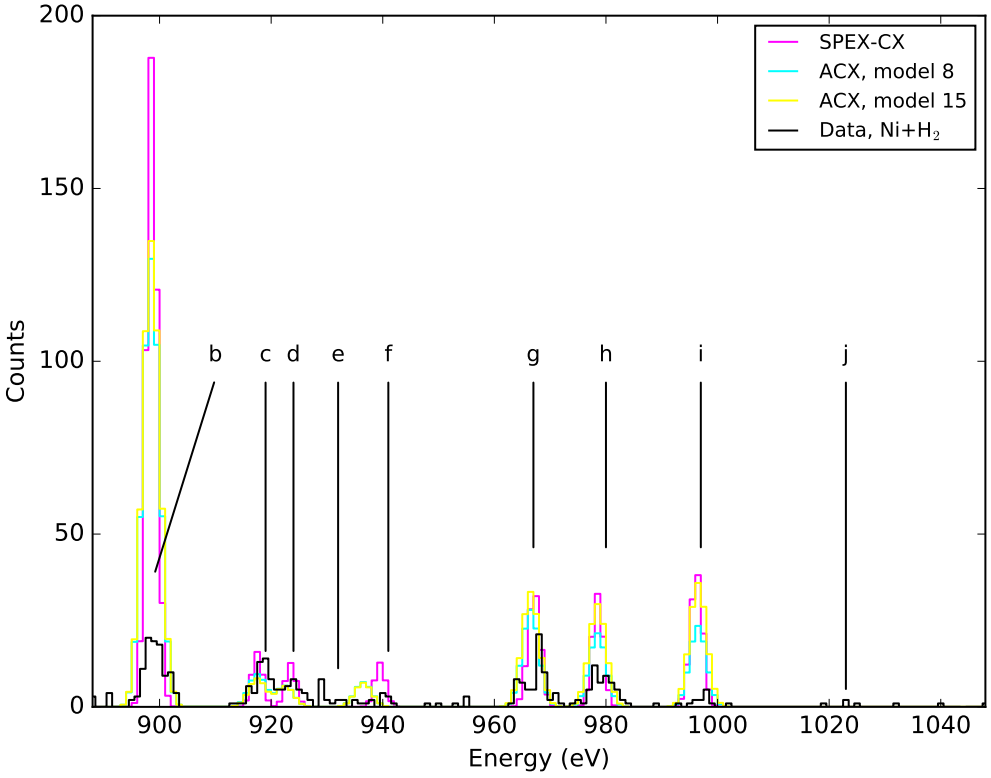

Figure 6.2 SPEX-CX model (magenta), ACX model 8 (cyan), and ACX model 15 (yellow) plotted against Ni^{19+}+H_2 EBIT CX data (black), from 888 eV–1048 eV. The data spectrum has been background-subtracted, and the model spectra show model-predicted counts, i.e., they have been adjusted to account for the attenuation in the data due to the ECS filters. All spectral lines are normalized to the flux in the M2/3G line in the data. Labels correspond to line IDs in Tables 5.1 and 5.2.

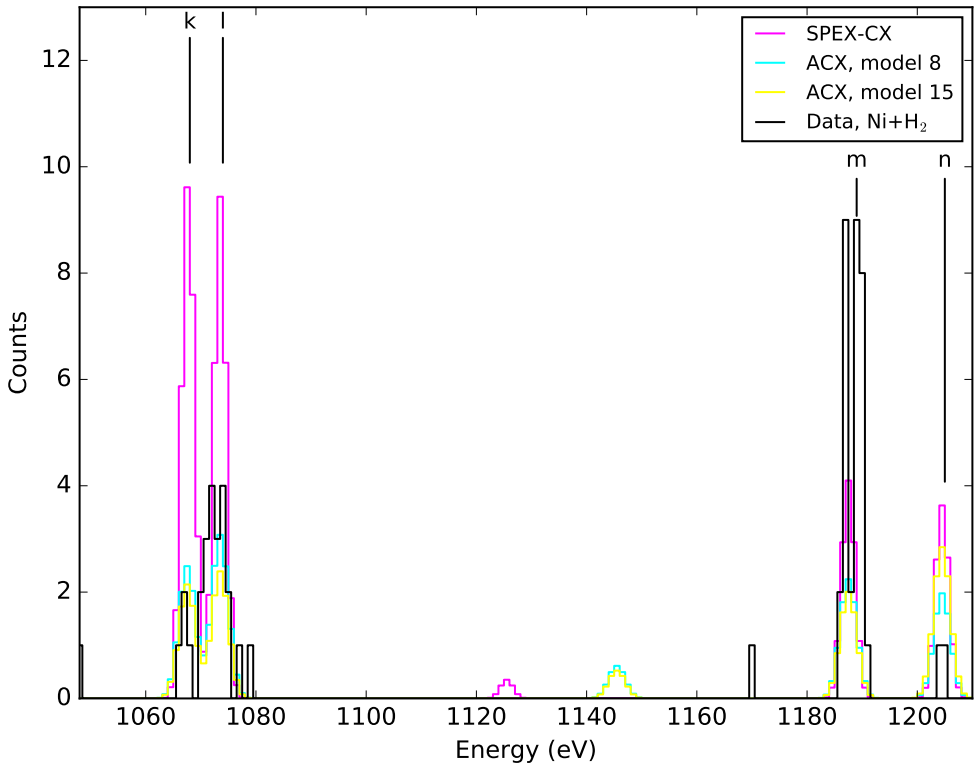

Figure 6.3 Same as Figure 6.2, but for 1048 eV–1210 eV.

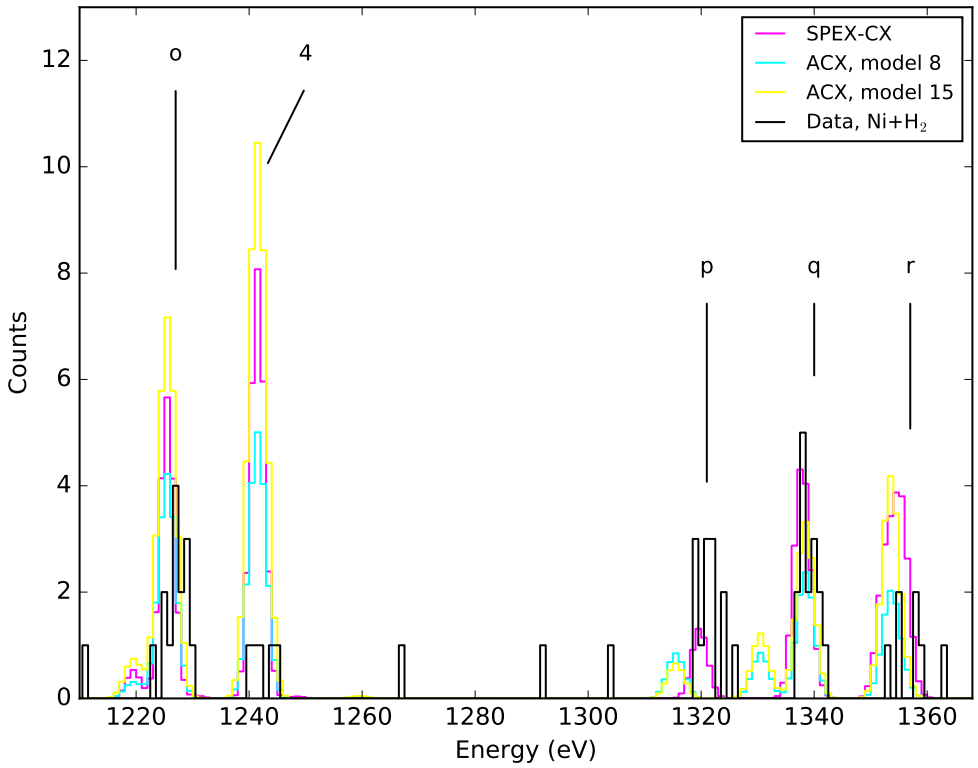

Figure 6.4 Same as Figure 6.2, but for 1210 eV–1368 eV.

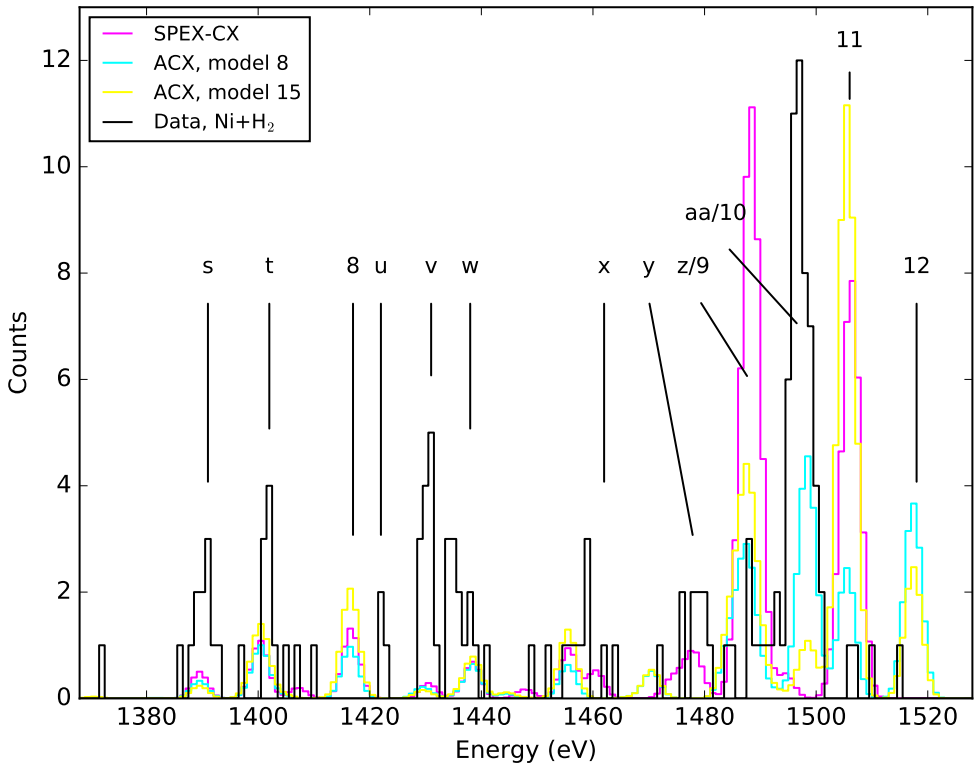

Figure 6.5 Same as Figure 6.2, but for 1368 eV–1528 eV.

their treatment of the n distribution. Figure 6.6 shows line identifications of these high-$n \rightarrow n = 2$ transitions assuming energies calculated from FAC, showing this unexpected behavior. However, we found that this behavior can be explained with further information from the authors of ACX: the line energies used in the ACX spectra differ from those of the FAC calculation by up to ∼10 eV [Adam Foster, private communication]. In addition to this energy discrepancy, ACX calculations do not include transitions that involve $n > 10$, meaning that even with line energies closer to those of our calculations, the model will be unable to reproduce certain high-n lines in our spectra. Figure 6.7 shows the same high-n line region of the spectrum, with transitions determined by the line energies used in ACX. We can see from Figure 6.6 that the SPEX-CX model behaves as we expect (see Section 2.2), i.e., it appears to only calculate capture into $n = 10$ states.

Next, we investigated whether the spectral models using atomic H as the neutral partner would better reproduce the Ni^{19+}+He data. This may be the case, as He is more likely than H_2 to undergo SEC rather than MEC. A greater contribution of SEC vs. MEC would alter the relative line strengths, especially at intermediate energies. Figures 6.8–6.12 show this comparison between models and data. This time, only lines c and d are fairly well reproduced. The models again fail to reproduce the high-n lines. This is in line with what we expect, however: besides the discrepancy in line energy as discussed above, the higher ionization potential of He should lower n_{max} relative to that of CX with atomic H, shifting the high-n lines to lower energies. We observe this in Figure 6.12.

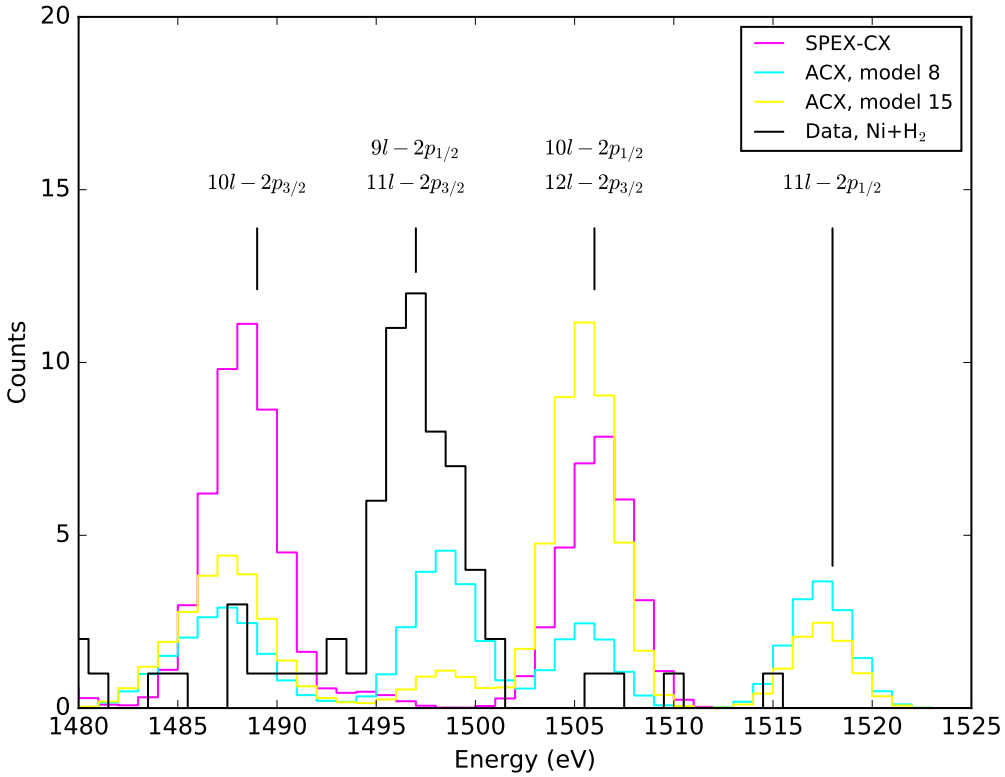

Figure 6.6 Comparison of high-n lines in the $Ni^{19+}+H_2$ data, the SPEX-CX model, and the two ACX models. Here, possible transitions contributing to each line are identified using line energies as calculated by FAC. From this analysis, it appears that the ACX model does not behave in the way we expect. This is due to the fact that the line energies differ between methods by ∼10 eV. The data spectrum has been background-subtracted, and the model spectra show model-predicted counts, i.e., they have been adjusted to account for the attenuation in the data due to the ECS filters. Lines are normalized to the flux in the M2/3G line in the data.

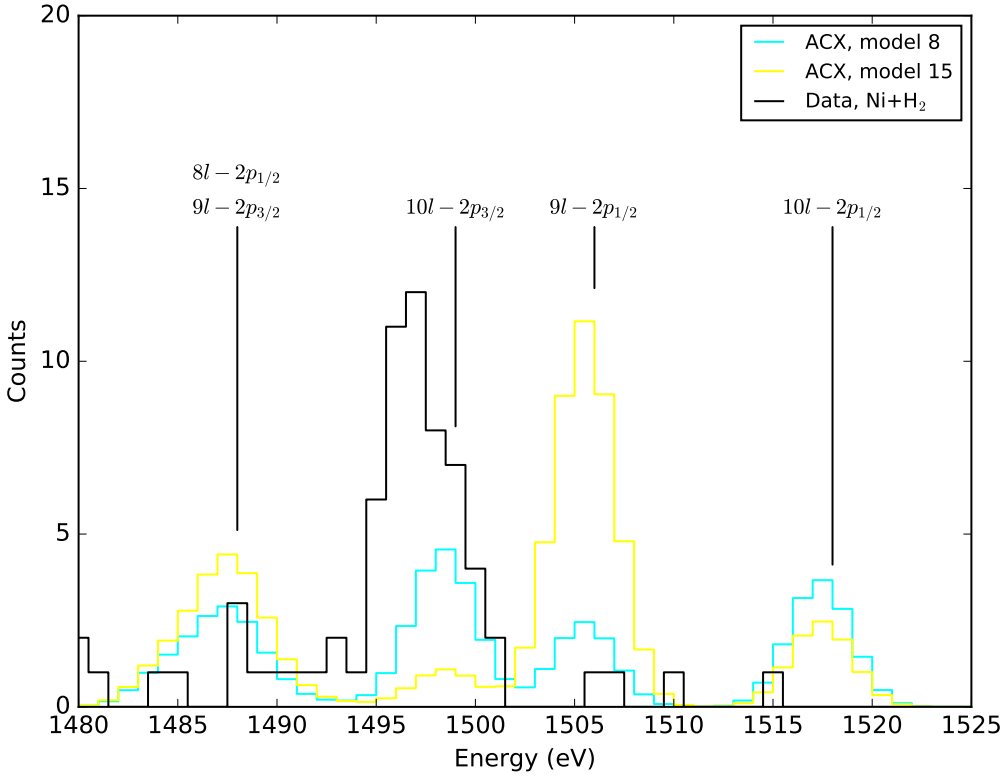

Figure 6.7 Comparison of high-n lines in the Ni^{19+}+H_2 data and the two ACX models, with transitions determined by the energies used in ACX. This shows an n- and l-distribution we would expect from ACX, unlike in Figure 6.6. The data spectrum has been background-subtracted, and the model spectra show model-predicted counts, i.e., they have been adjusted to account for the attenuation in the data due to the ECS filters. Lines are normalized to the flux in the M2/3G line in the data.

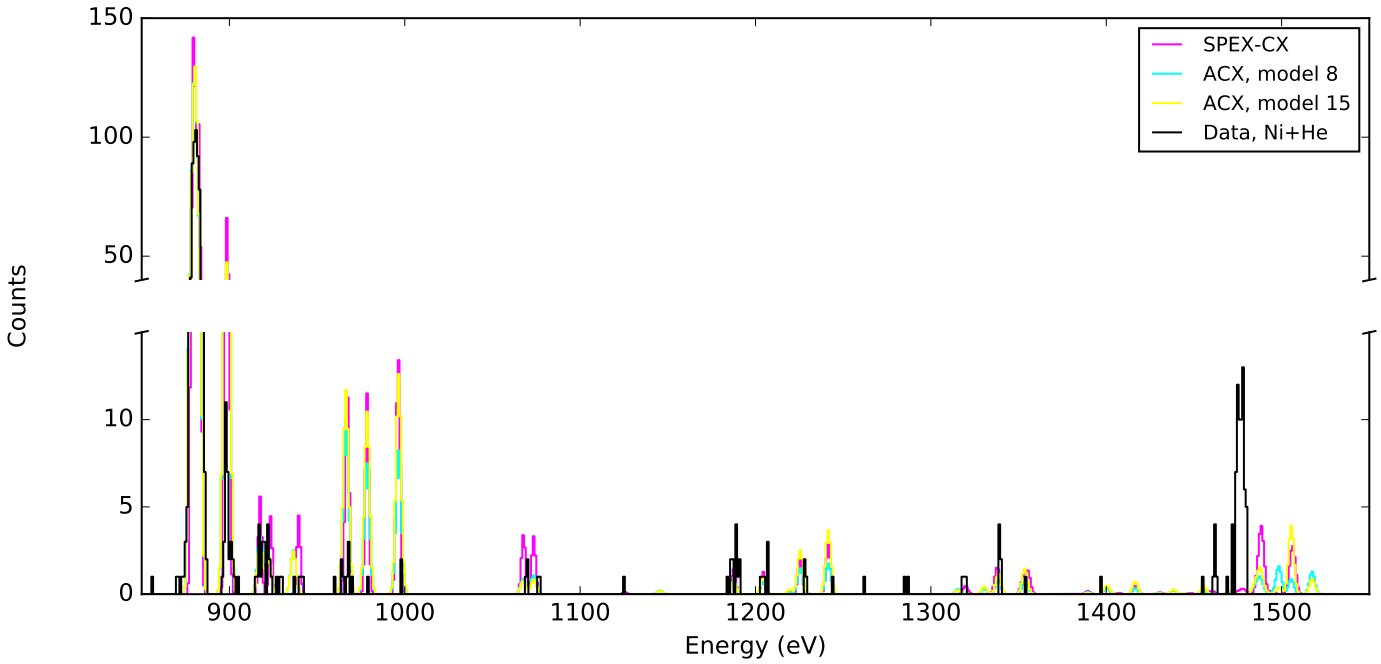

Figure 6.8 SPEX-CX model (magenta), ACX model 8 (cyan), and ACX model 15 (yellow) assuming CX between Ni^{19+} and H, plotted against Ni^{19+}+He EBIT CX data (black). Note the broken y-axis. The data spectrum has been background-subtracted, and the model spectra show model-predicted counts, i.e., they have been adjusted to account for the attenuation in the data due to the ECS filters. All spectral lines are normalized to the flux in the M2/3G line in the data. Individual lines are labeled in subsequent plots.

Finally, we compared the ACX models, which, unlike SPEX-CX, can be altered to use He as a neutral partner, to our Ni^{19+}+He data. As can be seen in Figures 6.13–6.17, however, the models and data are just as inconsistent as with the previous comparisons. Most notably, the primary state for electron capture for the experimental data appears to be $8s$ or $9s$, and neither ACX model predicts flux in this line. Instead, they predict a dominant $7d \rightarrow 2p$ transition, which is in fact what Equation 1.2 would predict.

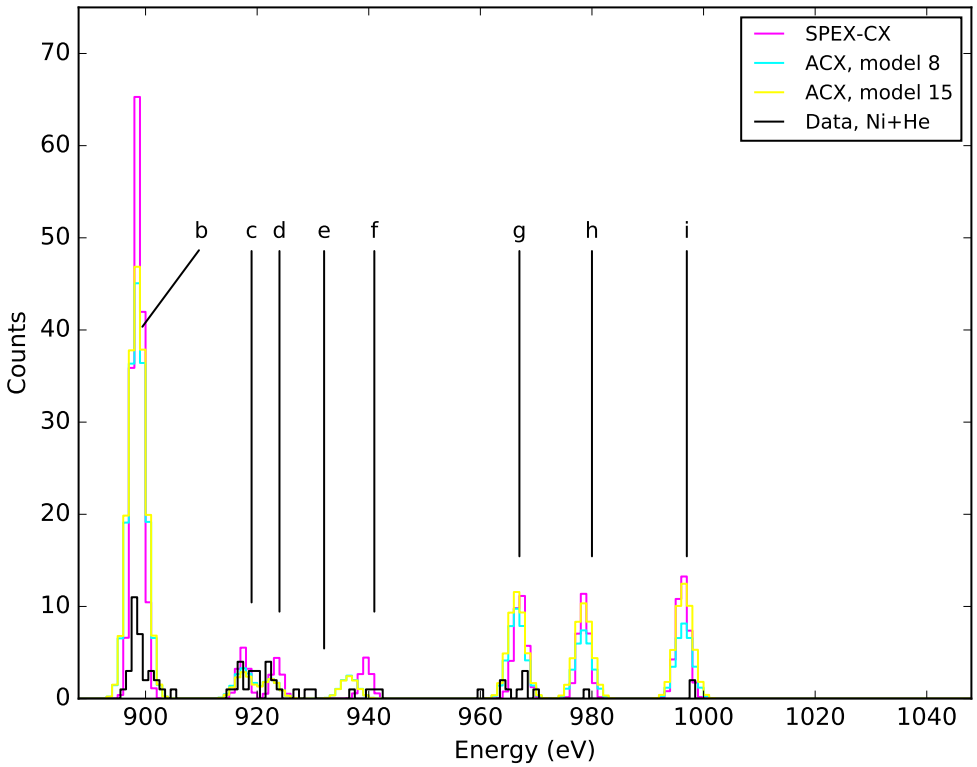

Figure 6.9 SPEX-CX model (magenta), ACX model 8 (cyan), and ACX model 15 (yellow) assuming CX with atomic H plotted against Ni^{19+}+He EBIT CX data (black), from 888 eV–1048 eV. The data spectrum has been background-subtracted, and the model spectra show model-predicted counts, i.e., they have been adjusted to account for the attenuation in the data due to the ECS filters. All spectral lines are normalized to the flux in the M2/3G line in the data. Labels correspond to line IDs in Tables 5.1 and 5.2.

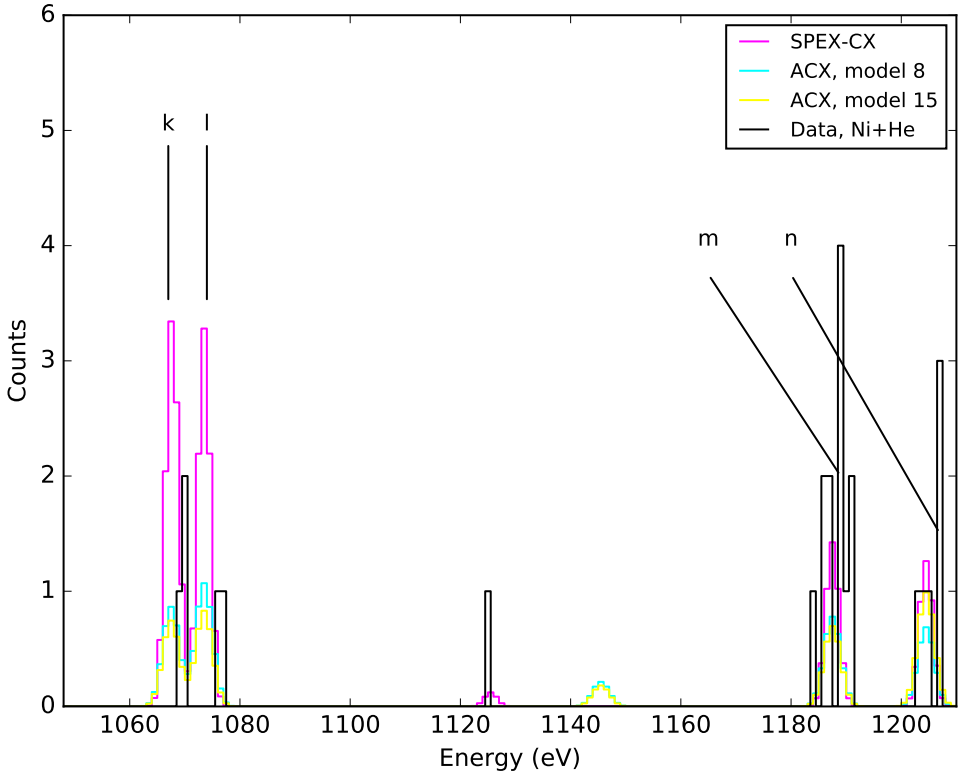

Figure 6.10 Same as Figure 6.9, but for 1048 eV–1210 eV.

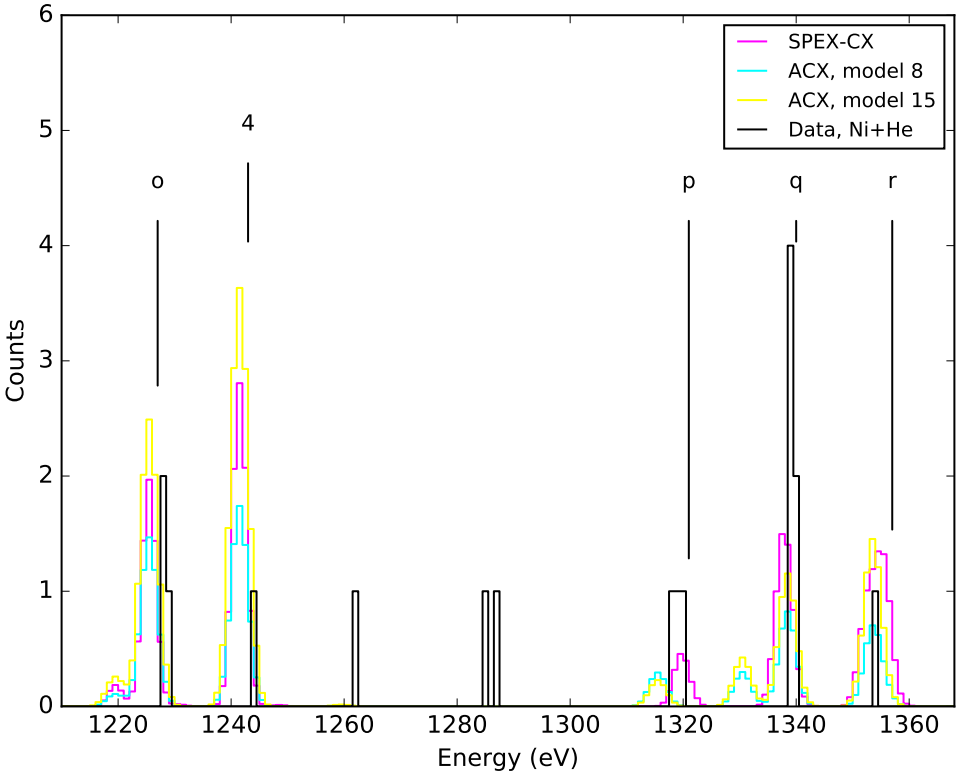

Figure 6.11 Same as Figure 6.9, but for 1210 eV–1368 eV.

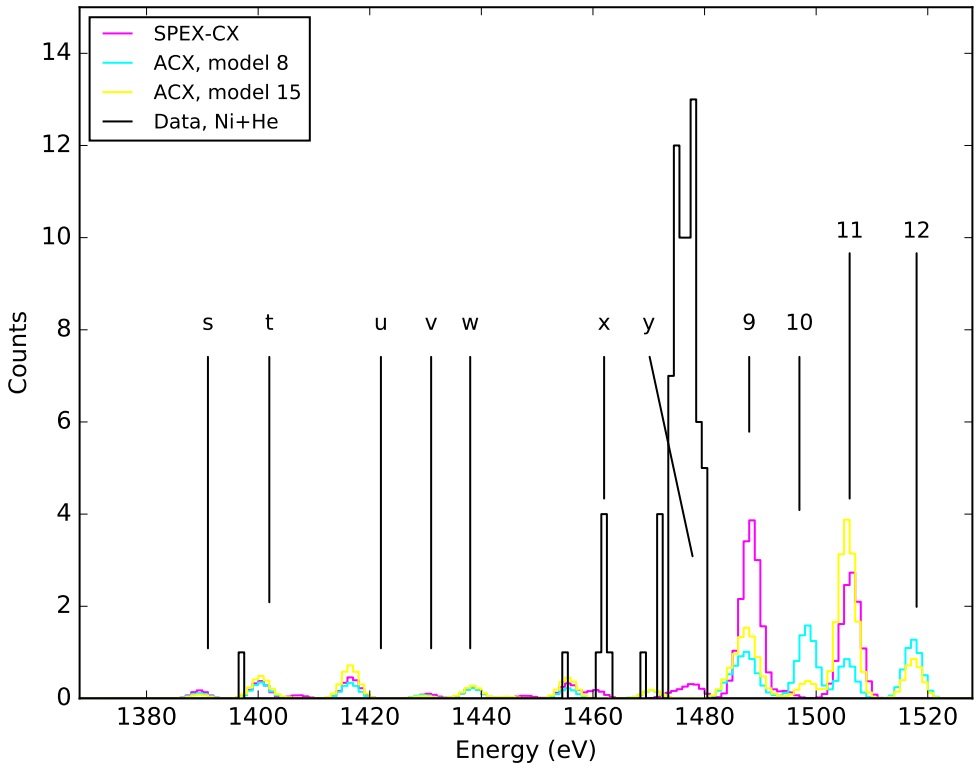

Figure 6.12 Same as Figure 6.9, but for 1368 eV–1528 eV.

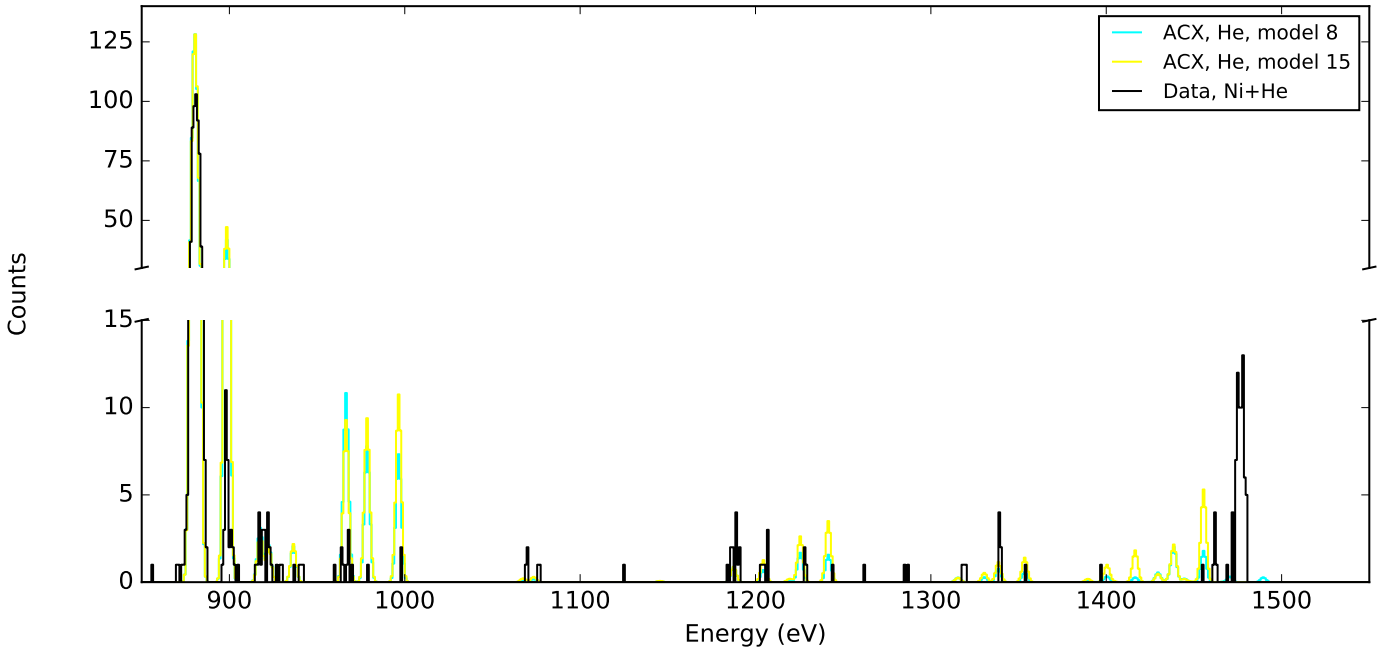

Figure 6.13 ACX model 8 (cyan) and ACX model 15 (yellow) assuming CX between Ni^{19+} and He, plotted against Ni^{19+}+He EBIT CX data (black). Note the broken y-axis. The data spectrum has been background-subtracted, and the model spectra show model-predicted counts, i.e., they have been adjusted to account for the attenuation in the data due to the ECS filters. All spectral lines are normalized to the flux in the M2/3G line in the data. Individual lines are labeled in subsequent plots.

While the availability and relative ease of use of models such as ACX and SPEX-CX are beneficial for increasing the amount of non-CX experts incorporating CX into their spectral analyses, these comparisons of models to data show that these models must be used with extreme caution. These discrepancies again highlight the need for careful energy calculations and more detailed state-selective cross section calculations, especially at low collision energies. Continuing to benchmark models such as these will aid us in spurring on this effort.

6.3 A Pipeline to Extract State-Selective Relative Cross Sections from Spectra: Method

In the absence of state-selective cross section calculations for our ion and collision energy of interest for the experiments presented here, we have created a procedure to extract these values from our data. This procedure involves four basic steps, which will be described in more detail presently. First, we calculate the atomic structure of various configurations of Ne-like Ni, beginning with a base F-like ion plus the addition of one excited electron in many different quantum states. Second, we use the atomic data to perform a radiative cascade for each of these states, creating a spectrum for each one. Third, from this set of spectra, we select a subset (which we dub a spectral basis set) that we will add together into a model to fit our data. Finally, we run our model, which uses this spectral basis set in a least-squares minimization procedure to calculate the relative weight to be applied to each spectrum in the set to create a best fit to the data. Recall that each spectrum in

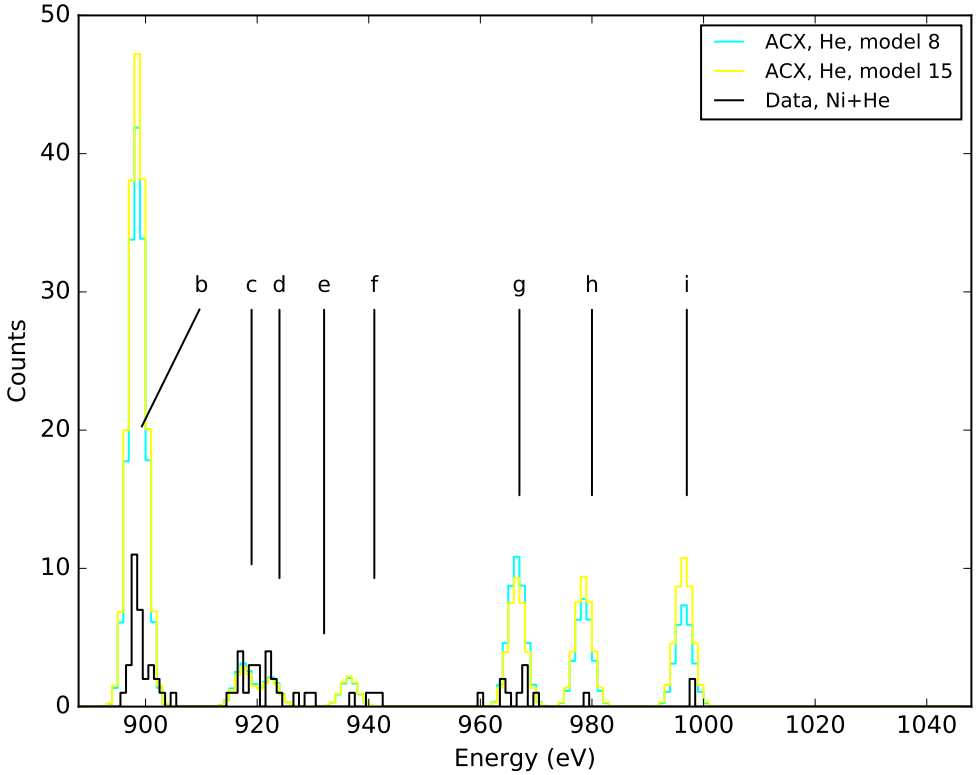

Figure 6.14 ACX model 8 with neutral He (cyan) and ACX model 15 with neutral He (yellow) plotted against Ni^{19+}+He EBIT CX data (black), from 888 eV–1048 eV. The data spectrum has been background-subtracted, and the model spectra show model-predicted counts, i.e., they have been adjusted to account for the attenuation in the data due to the ECS filters. All spectral lines are normalized to the flux in the M2/3G line in the data. Labels correspond to line IDs in Tables 5.1 and 5.2.

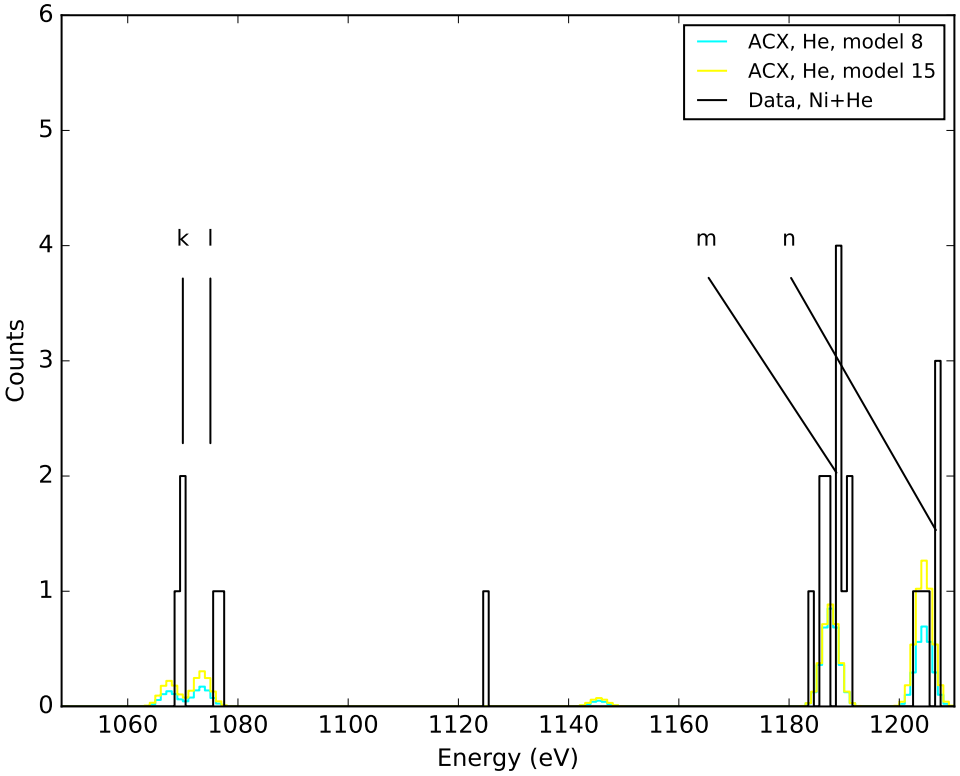

Figure 6.15 Same as Figure 6.14, but for 1048 eV–1210 eV.

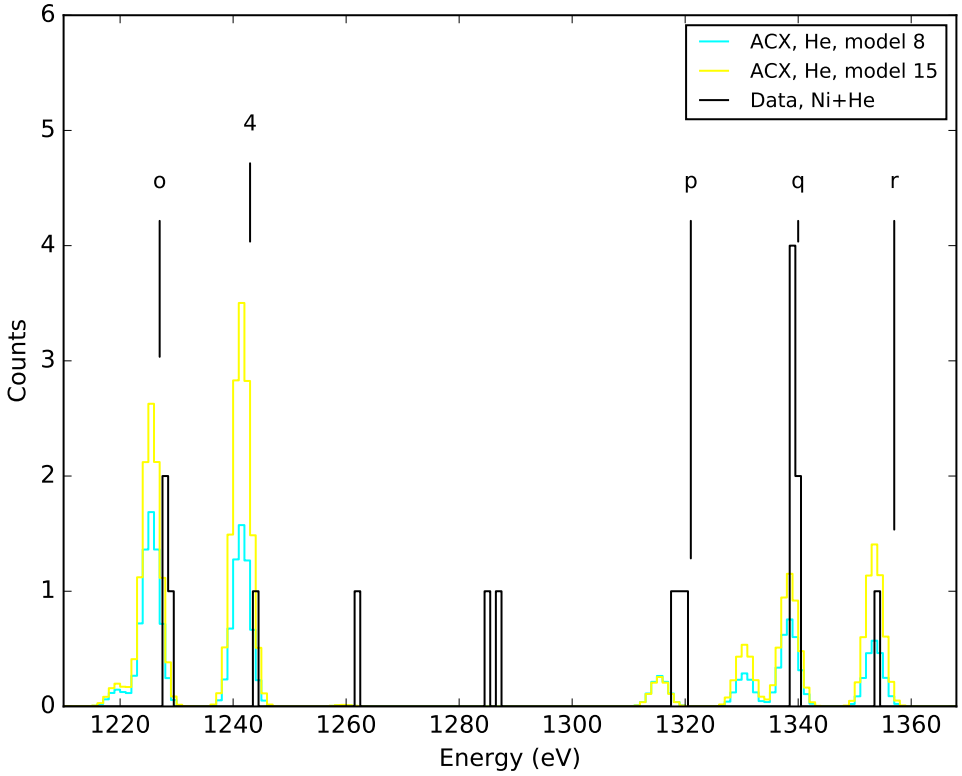

Figure 6.16 Same as Figure 6.14, but for 1210 eV–1368 eV.

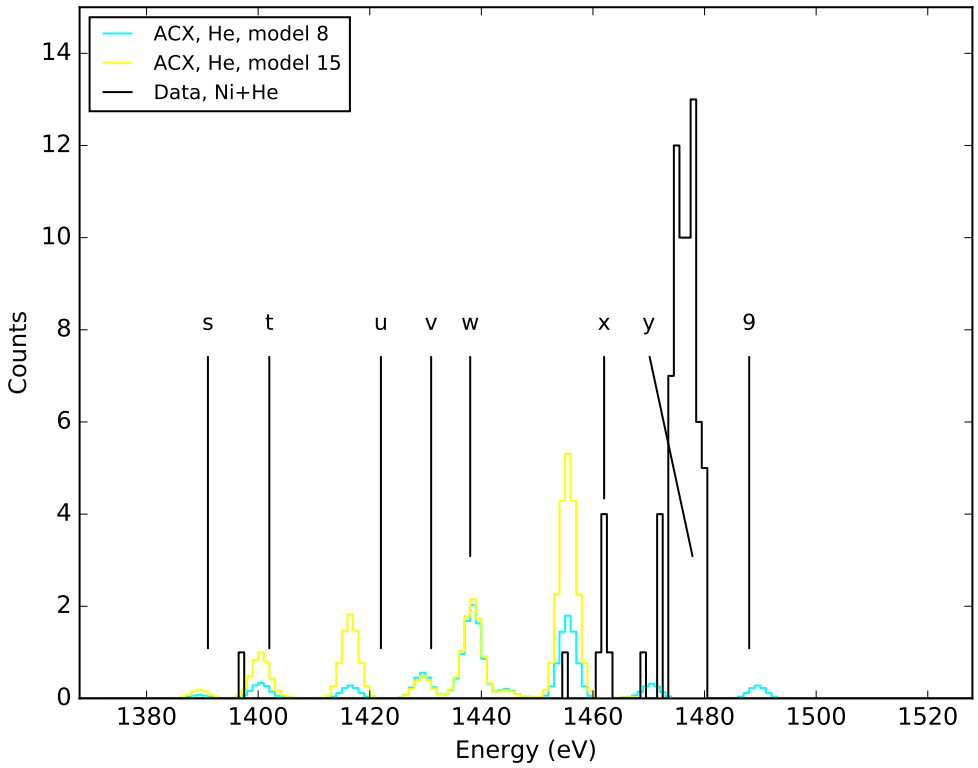

Figure 6.17 Same as Figure 6.14, but for 1368 eV–1528 eV.

the basis set is representative of electron capture into one particular quantum state; thus the weight assigned to each spectrum in the basis set after the fit corresponds to the relative cross section of electron capture into that quantum state.

For the initial step, we first consider a base F-like ion in its ground configuration. We initially assumed that the F-like ion would be in its ground state (with an electron hole in $2p_{3/2}$), but as described in Section 6.6, we later found it necessary to include core excited states (electron hole in $2p_{1/2}$ and $2s_{1/2}$). We then add one electron in an excited state to the configuration, making the F-like ion a Ne-like one. This represents the electron capture process during CX. We consider many quantum states for the excited electron, going as high in energy as $n = 15$ and including all possible l, j, and coupled J values. For each of these Ne-like configurations, we calculate the atomic structure, including level energies and transition energies between all levels, along with the oscillator strength and Einstein A coefficient for each transition. This is done with FAC, assuming jj-coupling (see Section 2.1).

Next, we calculate the radiative cascade paths for each of these excited Ne-like states in order to generate spectra. We do this by using the previously calculated atomic data, we create matrices of transition energies, Einstein A coefficients, and branching ratios between all calculated energy levels. At this stage, we choose an initial subset of excited states to consider by choosing a range of n values that might be most relevant to our experimental spectra. We choose this by examining the experimental spectra to determine the highest energy spectral line with significant flux. We then conservatively choose an n_{min} and n_{max} range for our cascade calculations that bounds this primary capture channel, where n_{max}–$n_{\mathrm{min}} > 5$. For

example, our $Ni^{19+}+H_2$ spectrum shows a strong high-n line that corresponds to the $n = 11 \rightarrow n = 2$ transition, so for our cascade calculation, we consider all configurations with the excited electron in $n = 5 - 13$. We then generate a list of all possible l, j, and J values for each unpaired electron within this range of n values. Finally, we input each of these configurations into the cascade matrix to generate a list of spectral line energies and strengths. From this linelist, we generate a spectrum of that cascade following capture. An example spectrum is shown in Figure 6.18.

At the end of this second stage, we thus have a set of spectra that corresponds to a given F-like core configuration with one excited electron that radiatively cascades to the ground state of Ne-like Ni. This is a large number of spectra—on the order of hundreds—which is certainly more than should be used to fit a spectrum with only about 15 lines. It is thus necessary to reduce the number of spectra that will make up a basis set for our fitting code. The spectra in the basis sets used in this work were chosen by visual inspection, based on their ability to produce lines present in our experimental spectra, generally limited to low values of l to reflect the low collision velocities that occur in EBIT experiments, and are biased towards the observed $n_{\max}$ from the data. In some cases, an element of a basis set may be a statistical J-weighted average of several J states. We also created several different basis sets to determine how this changed both the model spectrum generated and the resulting cross sections.

Choosing the spectra to make up a basis set may be accomplished in various other ways, for example: determining which spectra are most distinct and least degenerate; using statistical weighting to make cuts according to J value; only

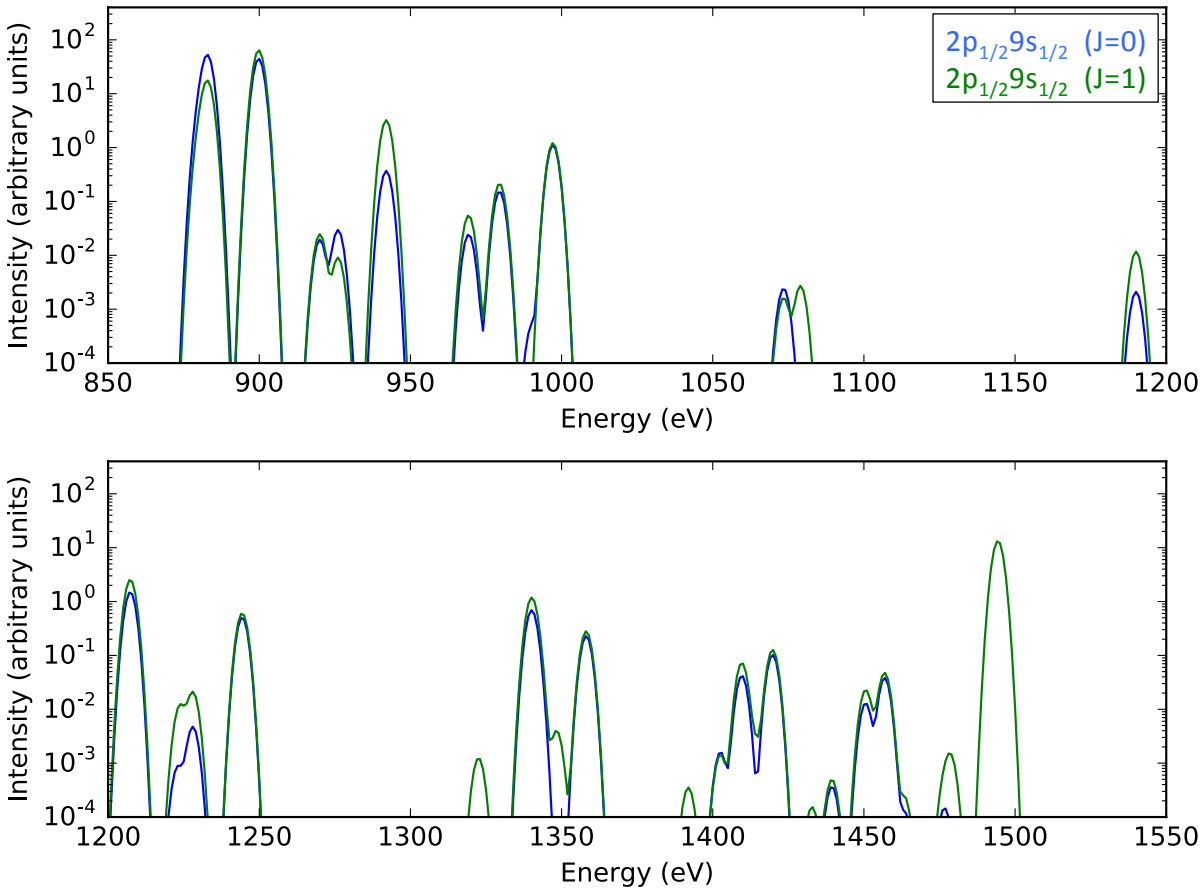

Figure 6.18 Simulated L-shell spectra for capture into Ne-like Ni configurations $2p_{1/2}9s_{1/2}(J=0)$ (blue) and $2p_{1/2}9s_{1/2}(J=1)$ (green), assuming a Gaussian response with 1.5 eV FWHM resolution.

including spectra with low values of l and a value of $n_{\max}$ as empirically determined by the data, along with other options or combinations of the above. While limiting the number of spectra in the basis set is necessary, any of these methods will lead to some error in our cross section calculation. This is because in the true experiment, a large number of capture configurations contribute to our measured spectra at some level. An added level of complication is that a set of given electron configurations that we deem to be significant might lead to very similar spectra. Thus each element in our chosen basis set may not be representative of a single n, l, j, J-resolved state, but a sum of several.

With a chosen spectral basis set, the fourth and final stage of our pipeline is then adding each spectrum in the set into our model. Our model takes as an input each element in our spectral basis set. Within each of these basis set elements, the possible free parameters are the capture state itself (i.e., the base F-like configuration and the quantum state of the additional excited electron), the Gaussian sigma of the spectral lines, and the overall weight of that particular spectrum versus all the other spectra in the basis set. In our fit, we freeze the capture state (after we have selected the ones we want to consider), tie together the sigma for all spectral lines across all the models, and only allow the overall weight of each particular spectrum in the basis set to vary.

Our fit is done through least-squares minimization, which we perform through a Python script using the package LMFIT. During the fit, each simulated spectrum is adjusted to match the ECS filter transmission (see Section 3.2.2). Each spectral bin is weighted using the Gehrels method, which is better suited for low counts

[Gehrels, 1986]. After the fit, the weight assigned to each spectrum in the basis set corresponds to the relative cross section of the n, l, j, J-resolved state that lead to that spectrum. For an example basis set with three spectra A, B, and C, this can be represented as

$$\text{Best fit to data}=(\text{Spectrum A*W1}) + (\text{Spectrum B*W2}) + (\text{Spectrum C*W3}), \tag{6.1}$$

where W1, W2, and W3 correspond to the weights given to spectra A, B, and C, respectively, after the fit.

The absolute value of each weight (or relative cross section) is arbitrary, as it corresponds to the necessary strength of that element in the spectral basis set to match a spectrum with an arbitrary number of counts. The physical result is in comparing the relative strengths of each weight. For the spectra in our model basis set that are degenerate (i.e., that result from more than one capture state), we treat the cross section as derived from the fit as that of the sum of all states included in this degeneracy. Plots of the relative cross sections extracted from our data via the method just described are shown in Figures 6.20, 6.21, and 6.22 for S+He CX, and Figures 6.28, 6.29, and 6.30 for Ni+H_2 CX.

6.4 Cross Section Calculations: Result for S+He

As an initial test of our pipeline and fitting procedure, we began with the simpler case of K-shell spectra. We fit experimental data of CX between H- and

He-like S and neutral He, first presented in Chapter 4, with the process described in the previous section. Because the gain calibration for the experiment from which the data are taken led to line energies that were shifted with respect to those in the models by ∼0.6 eV near the high-n Ly lines (possibly due to gain drift or a non-ideal polynomial fit to the gain curve; see Section 3.2.3.8), we shifted the data for these energies by hand to match the model. We created three different model basis sets to fit to the data. The spectra that formed the basis set for the best fit to the data are presented in Appendix A.

The spectrum generated with the best fit to the data is shown in Figure 6.19. In general, the fit is very good: though the He-like forbidden line near 2400 eV is slightly over-predicted and the H-like Ly-η line near 3450 eV is slightly under-predicted, most other lines are well-described by the model.

The weights for each model allow us to determine the relative cross section for each capture state described in our basis set. This is plotted in Figures 6.20 and 6.21.

Our results suggest that for H-like S in our experiments, the primary capture channel is into $8p_{1/2}$ and $8p_{3/2}$, which have nearly indistinguishable spectra. Also significant is capture into $8s_{1/2}$. This is to be expected, since capture into low l states should be preferred for low collision velocity EBIT CX experiments.

For the He-like ion, capture into low l states is also preferred, though in this case, the relative strength of capture into s is higher than that of p. Although the spectra resulting from capture into $n = 6 - 9$, $l = s$ are fairly indistinguishable, as capture into $n = 7$ is preferred for $l = p$ and f, we assume that the point

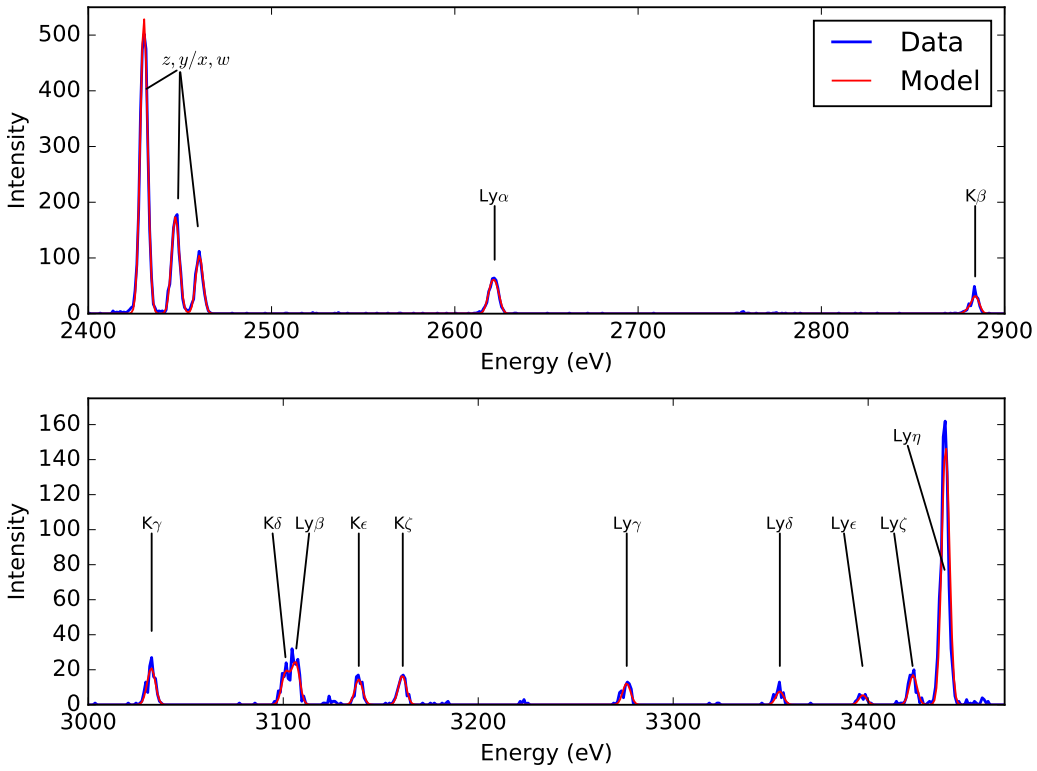

Figure 6.19 Model fit (red) to the data (blue) for H- and He-like S+He CX.

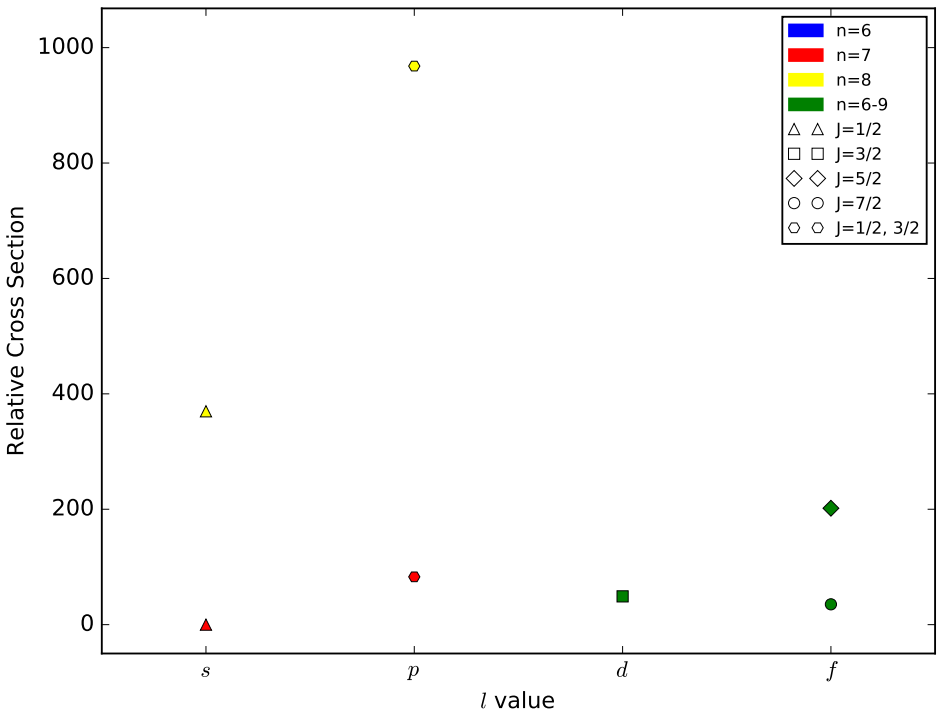

Figure 6.20 Relative n, l, J-resolved capture cross sections for H-like S+He CX. Each point reflects one quantum state of electron capture, or in the case of degenerate states, a sum of several. The color, symbol, and x-value of each point describes the quantum state presented. The absolute value of the calculated cross section is arbitrary; the relevant physics is in the relative values. This shows that the primary capture channel is into $8p$, followed in strength by $8s$.

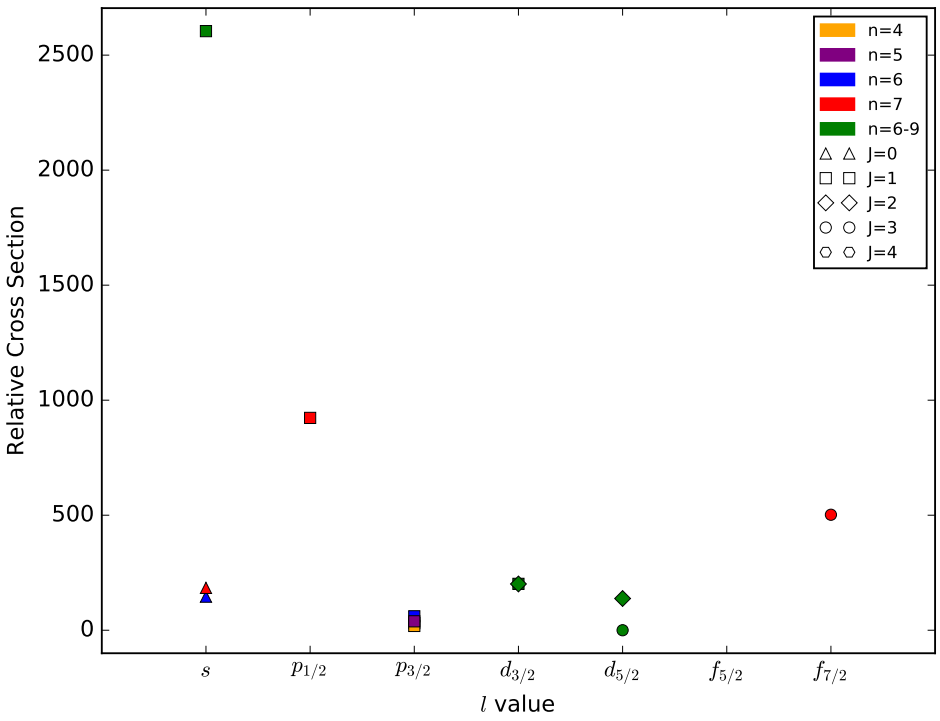

Figure 6.21 Relative n, l, j, J-resolved capture cross sections for He-like S+He CX. Each point reflects one quantum state of electron capture, or in the case of degenerate states, a sum of several. The color, symbol, and x-value of each point describes the quantum state presented. Again, the absolute value of the calculated cross section is arbitrary. Though the spectra for $n = 6 - 9$, $l = s$ are fairly indistinguishable, we deduce from the relative importance of $n = 7$ into higher angular momentum states that electrons are primarily captured into $7s$ (J=1).

corresponding to the largest cross section (at $l = s$) is also dominated by $n = 7$.

A fairly surprising result is the significance of capture into $l = f$ for both ion species. It is possible that this results from double electron capture with at least one electron in $l = p$, followed by autoionization and a simultaneous transition of the second electron into nf.

Now that we have a working procedure to go from an experimental spectrum to state-selective relative cross sections, which yields a good model fit to the data and cross sections, we will compare our results to calculations performed by Renata Cumbee using the Multichannel Landau-Zener (MCLZ) method.

6.5 K-shell S+He Cross Sections: Pipeline Model Comparison to MCLZ Calculations

Dr. Cumbee used the Kronos CX database [Mullen et al., 2016] to calculate MCLZ cross sections for CX between H-like S and neutral He. She applied a low-energy l distribution (Equation 1.7) to obtain nl resolved cross sections at a collision energy of 10 eV/amu. This method was performed assuming LS-coupling, so the levels were then transcribed to their equivalent jj-coupled states using statistical J-weighting in order to compare to our model. This process yielded a list of relative cross sections for each significant state, normalized so that the sum of all the cross sections is 1.

We then matched up the states reflected in our model basis set to those in the MCLZ calculations. The result of this comparison is shown in Figure 6.22.

We normalized each relative cross section point in both data and theory figures to its respective maximum value. In the case presented here, each cross section was normalized to capture into $8p(J = 1/2)+8p(J = 3/2)$. In the cases where one of the models in our basis set served as a template for more than one state, we adjusted the corresponding MCLZ point on the figure to reflect the sum of all states included.

For completeness, we wished to ensure that the states with the largest cross sections were presented. We thus sorted the MCLZ cross sections by strength and added four more states to Figure 6.22 that were not included in our initial model fit. With the addition of these four points, surrounded by light grey parentheses in the right-hand plot of Figure 6.22, the 16 most significant capture states are shown.

The normalized cross sections obtained from these two methods show fair agreement. Both methods find that most capture is into $8p(J = 1/2) + 8p(J = 3/2)$, with significant capture into both $8s(J = 1/2)$ and $nf(J = 5/2)$, (n=6–9). Considering only s angular momentum states, both methods predict that there is more capture into $8s_{1/2}$ than into $7s_{1/2}$.

One interesting difference between the two methods is the relative importance of $nf_{5/2}$ versus $nf_{7/2}$: the two methods show opposing results. As the MCLZ cross sections were performed in LS coupling, these two states were only separated out according to their J-weights after the cross section for the general nf state was found. It is thus to be expected that the state with the larger J value would dominate, and interesting that our model predicts the opposite to be true.

The MCLZ calculations predicted a relatively high cross section for several states that we did not initially include in our model basis set. We did not include

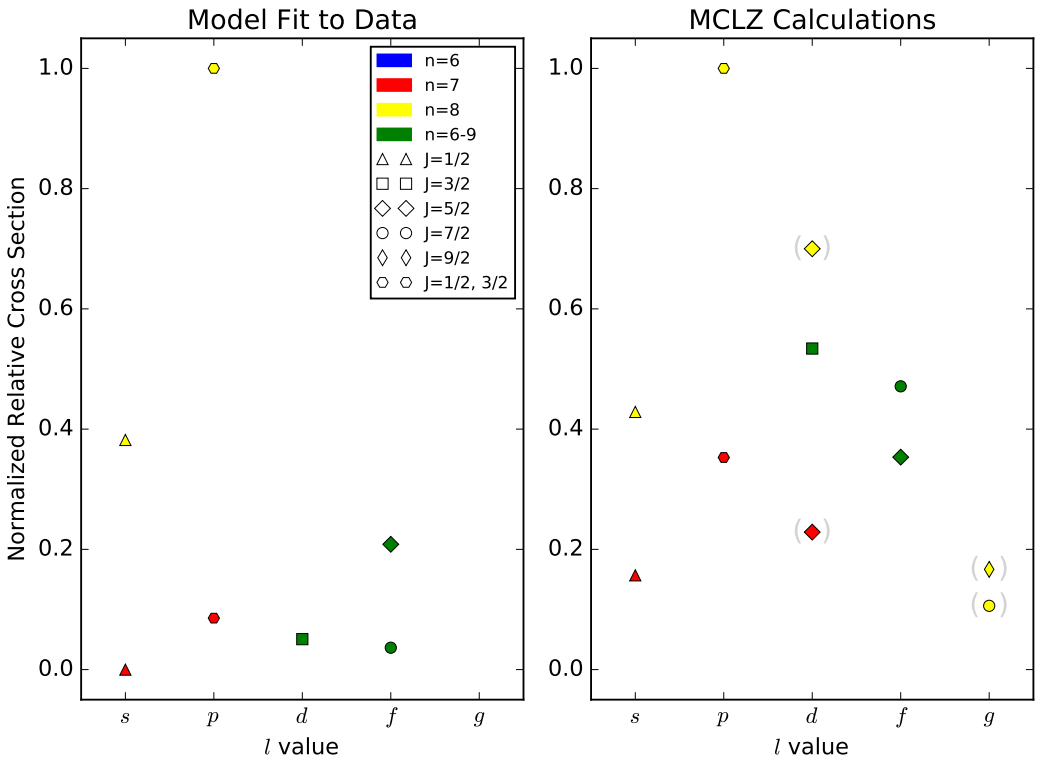

Figure 6.22 Normalized relative cross sections as obtained with the pipeline and fitting procedure described in this chapter (left) and MCLZ calculations (right) for CX between H-like S and neutral He. Each point on these plots reflects one quantum state of electron capture, or in the case of degenerate states, a sum of several. The color, symbol, and x-value of each point describes each quantum state presented. The y-value indicates the relative cross section of that state. To interpret this figure, one should compare the y-position of points of the same x-value, color, and symbol shape across the left-hand and right-hand plots. Points in parentheses refer to states that were not included in the fit presented in this chapter, but that have a high relative cross section according to the MCLZ calculations. The two methods show fair agreement; they both assign a relatively high cross section to the $8s$ and $8p$ states, but the MCLZ calculation emphasizes capture into higher l states (d, f, g) than our pipeline does.

these either because the spectra only displayed subtle differences in line strengths from spectra resulting from capture states already included in the basis set (for the cases of $7d_{5/2}$ and $8d_{5/2}$), or because we limited the maximum angular momentum state to $l = f$ (for the cases of $8g_{9/2}$ and $8g_{7/2}$). However, because of the high relative cross section of these states in the MCLZ calculation, we performed another fit to our data that included these four capture states to determine if our pipeline would identify them as important. After the fit, each of these states was assigned a weight of approximately 0, meaning they should not contribute significantly to our experimental spectrum.

We then worked backward from the MCLZ calculations to simulate the spectrum predicted by the MCLZ results in order to compare it to our data. We allowed the He-like lines to be fit according to the elements in our spectral basis set, and fixed the relative contributions of the H-like spectral basis set elements according to their MCLZ-calculated cross section. This fit/simulated spectrum and comparison to both the experimental data and our pipeline model fit is shown in Figure 6.23. It can be seen that the match between experiment and theory for the H-like lines is fairly poor; in particular, the strong Lyman-η line is greatly under-predicted. This shows that although the MCLZ calculations correctly assign the highest cross section to capture states that lead to this strong line ($8p$), it over-emphasizes the relative importance of capture states with other l values, in particular d, f, and g states. The Lyman-ζ and Lyman-α lines, as simulated in the spectrum according to the MCLZ calculations, also show poorer matches to the data than with our pipeline.

There are several next steps for this K-shell comparison, both involving the

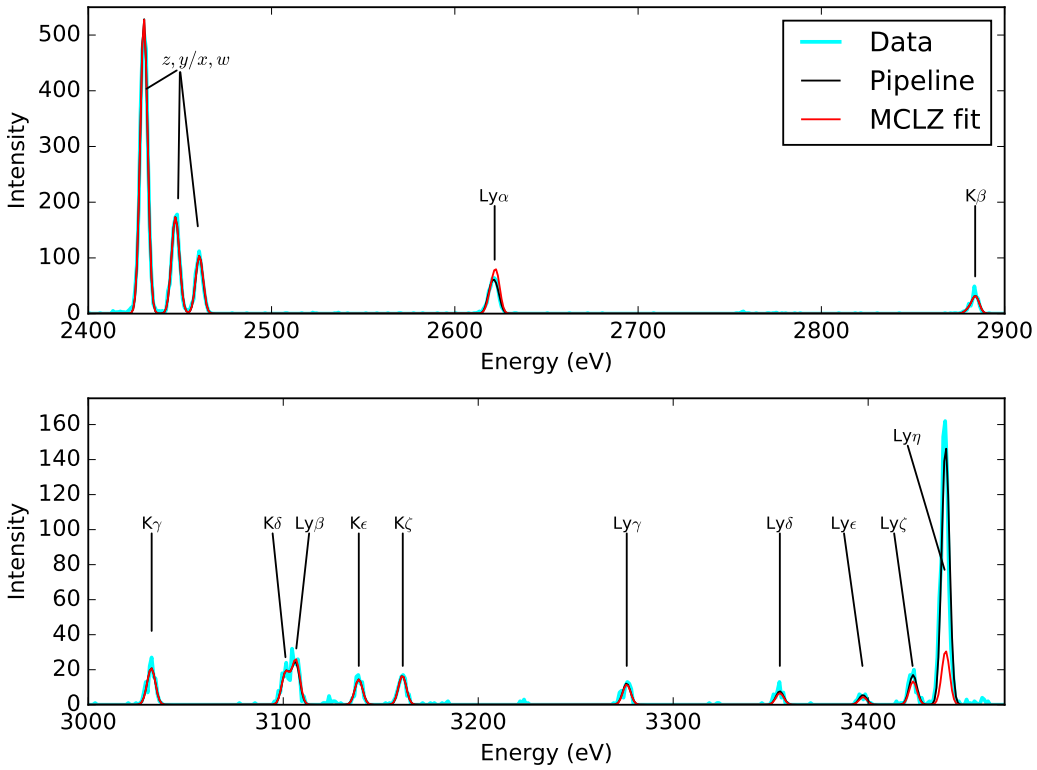

Figure 6.23 Data (cyan), model fit to the data through our pipeline (black), and simulated spectrum assuming MCLZ cross sections to set the strength of the H-like lines (red). In this simulated spectrum (red), the He-like lines are fit with our pipeline. The strength of the Lyman-α, Lyman-ζ, and Lyman-η lines, as simulated with the MCLZ cross sections, show poor fits to the data. Our pipeline performs better in all cases.

pipeline and the MCLZ calculations. With the pipeline, we hope to break the degeneracies that exist in our spectral basis set in order to distinguish as many individual quantum states as possible. This can be done by utilizing L-shell S lines, which currently are not present in our experimental spectra due to the experimental conditions at the time. On the MCLZ side, we hope to obtain results for He-like S shortly to compare to our results. Additionally, recall that MCLZ calculations for bare ions undergoing CX cannot predict an l-distribution for the captured electron; one must be applied afterwards. We thus would like to investigate how different l-distributions affect the resulting cross section calculations and simulated spectra. Mullen et al. [2016] showed that systematically shifting the l-distribution to lower values led to better agreement with EBIT data. Given our results, we expect a similar technique would also work well here. Finally, we wish to extend this pipeline and comparison with MCLZ calculations to many more K-shell ions for which we have experimental data.

6.6 Cross Section Calculations: Result for $Ni^{19+}+H_2$

We now return to our $Ni^{19+}+H_2$ CX spectrum discussed earlier in this chapter and apply our pipeline to calculate relative cross sections.

To create a basis set of spectra to model our $Ni+H_2$ spectrum, we first started with the assumption that the parent F-like ion would have the lowest possible energy configuration, $1s^2_{1/2}2s^2_{1/2}2p^2_{1/2}2p^3_{3/2}$, and only considered states with a $2p_{3/2}$ core hole. We then created spectra for $n = 8 - 11$, $l = s - g$, and all possible J values. As

described in Section 6.3, although each spectrum results from a different initial electron configuration, many of the resulting spectra appear very similar to one another. These states would thus not be able to be disentangled in the result. Thus, to compose our spectral basis set, we used spectra that were visually distinct, and noted the degeneracies for each spectrum used.

The model and residuals that resulted from this initial basis set are shown in Figures 6.24 and 6.25. The line identifications refer to those in Table 5.1. Though the fit to the M2/3G line is good, the fit to many higher energy lines is problematic. In particular, flux in lines k and l is not predicted at all, and lines b, c, d, and v are severely underpredicted. By examining the spectral basis set, we determined that this is because these lines are either weak or nonexistent in this core configuration; a better fit would require contributions from core-excited states. It is interesting to note that for lines b, k, and l, which all result from core-excited states, the SPEX-CX and ACX model predictions are either well-matched to the data or overpredict flux compared to the experiment. This suggests that these models include and perhaps even over-emphasize these core-excited states.[1]

[1]Through communication with the creators of the ACX model, we have learned that these lines do not result from direct capture into a core-excited state (e.g. $2s^1 2p^5 ns^1$). Instead, the excited states are formed during the radiative cascade. By comparing details of various transitions side-by-side, it was determined that some line strengths might differ between the two methods due to drastic differences in the atomic structure calculations between FAC and HULLAC, an atomic structure code that is implemented for certain transitions in AtomDB [Duane Liedahl, private communication]. In certain cases, the Einstein A coefficient differs by an order of magnitude. We will continue to investigate this discrepancy.

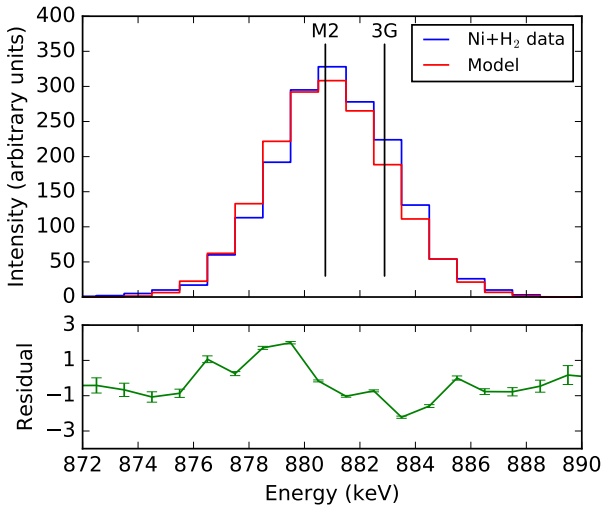

Figure 6.24 Data (blue), model fit to the data (red), and fit residuals (green) for CX between Ni^{19+} and H_2, for the M2 and 3G lines, using a model that solely includes capture states with a $2p_{3/2}$ core hole. These lines are well-predicted with this first iteration of our cross section model.

We thus created a new basis set that included spectra that were most heavily weighted in the first basis set along with spectra resulting from the $2p_{1/2}$ and $2s_{1/2}$ excited core configurations. Several states with a $2p_{1/2}$ core configuration lead to a strong b line, along with some flux in c, d, and v, and can also explain the large observed flux in the aa line. The $2s_{1/2}$ core configuration was necessary to populate the k and l lines. We performed five iterations of various combinations of these states, removing states that were repeatedly de-emphasized in the fit and replacing them with others that might contribute to flux in underpredicted lines. We adjusted the initial guess of fitting weight for certain states that we believed needed to be moved out of a local minimum, and experimented with pegging certain weights at a high or low value.

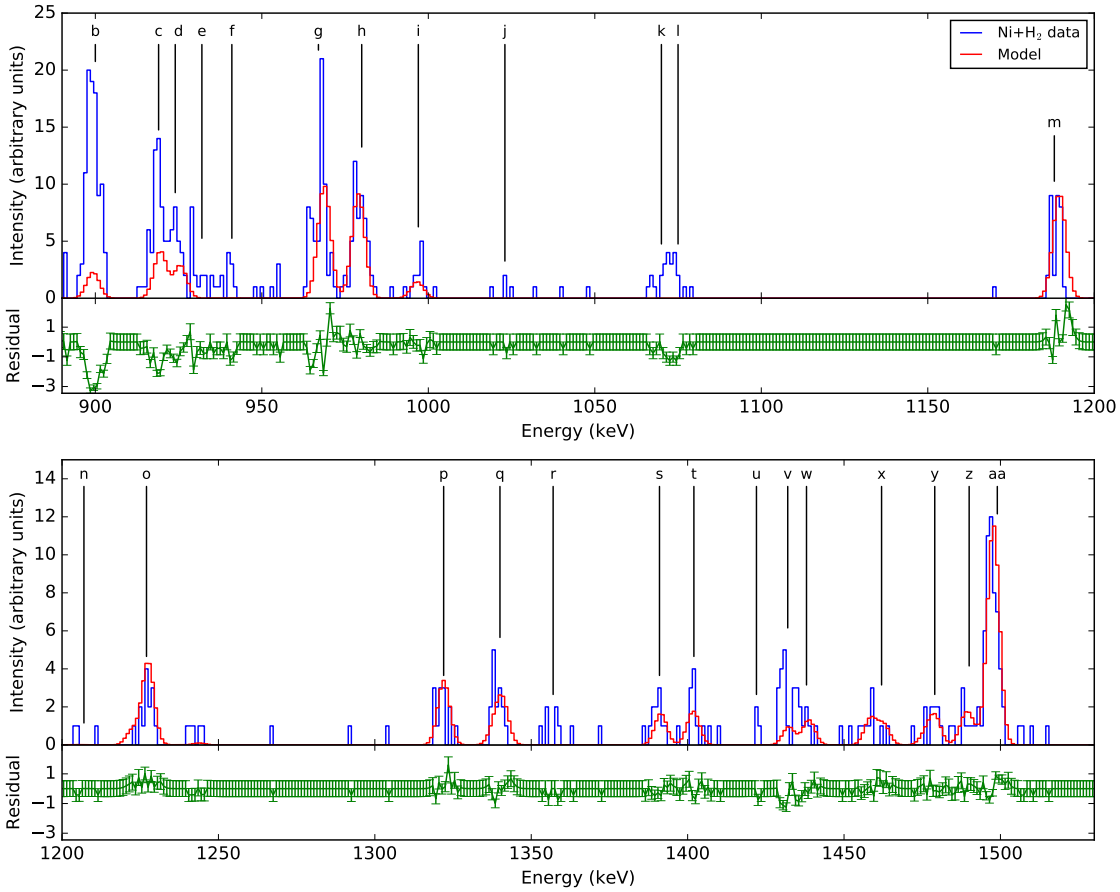

Figure 6.25 Data (blue), model fit to the data (red), and fit residuals (green) for CX between Ni^{19+} and H_2, for lines with energies between 890–1530 eV, for a model that solely includes capture states with a $2p_{3/2}$ core hole. Though the model performs better than the ACX and SPEX-CX models, it significantly underpredicts lines b, c, d, s, t, v, and w, and does not predict any flux in lines k and l. These lines are primarily a result of capture into states with $2p_{1/2}$ and $2s_{1/2}$ core hole configurations.

The result from the best fit is shown in Figures 6.26 and 6.27. The fit is generally excellent: though it still underpredicts flux in some lines, it is much improved over the initial fit that only included $2p_{3/2}$ core hole configurations, and is vastly better than the SPEX-CX and ACX models shown earlier in this chapter. Line g is the most severely underpredicted, with d, m, and v also lacking flux. The model also predicts flux in a line near 1510 eV, which is not clearly present in the data. From the shape of the residuals of the underpredicted lines, it appears that the discrepancies may be due to an energy offset between the model predicted line and the data. However, it is also possible that this underprediction is due to not including a capture state that is important, or due to errors in the FAC-calculated transition probability that generated the line strengths in the spectral basis sets.

As we saw from the MCLZ cross section calculations for CX between S^{16+} and He, higher l states like f and g may be more important than we initially assumed for low-energy EBIT experiments. However, for the fit presented here, our spectral basis set includes states with l as high as g for the $2p_{3/2}$ and $2p_{1/2}$ core configurations. Therefore, errors in the fit that can be attributed to omitting important capture states are likely not due to preferentially selecting low l states, but rather because there are many more important capture states than we can incorporate into one basis set.

In general, however, this particular potential source of error, along with any errors in the FAC transition probabilities, are likely not dominant in our current fit. These potential errors would solely alter the predicted flux in a given line, and as previously mentioned, the errors in the fit appear to primarily result from differences

in line energy between the model and data. Besides the shape of the residuals at these lines, this is also evidenced by the fact that fixing certain models with higher weights in an attempt to better match the flux in the experimental spectrum led to a higher chi-squared. In some cases, the energy mismatch is evident via visual inspection of the spectra. This is especially obvious in line g.

The main peak of line g in the data is close to the model line centroid, but there is also a low-energy shoulder that the model does not include. Interestingly, the energy centroid for that line in the data, as determined both by our analysis of the DE spectrum (see Section 5.4) and Gu et al. [2007a], is ∼967–968 eV. FAC calculates the energy of this line to be ∼969. This means that in DE, the FAC transition energy appears to be shifted from the data by almost 2 eV, however, in CX, the experimental result matches better with FAC. This difference merits additional investigation. It is possible that the low-energy shoulder on the CX line is a satellite line that results from MEC followed by autoionization and inner-shell excitation. If this is the case, however, it remains to be determined why the main line centroid would shift to a higher energy in CX. One way of testing whether the main error is in the model energy centroids is by manually correcting them to match experimental results such as in Gu et al. [2007a], and by calculating the energy of any potential satellite lines and including them in the spectra.

We do not believe the energy mismatch is due to errors in the gain calibration, since the lines with this error are scattered across the L-shell band.

From these model fits to the data, we then extracted relative cross sections for each considered capture state. Figures 6.28, 6.29, and 6.30 show these cross sections

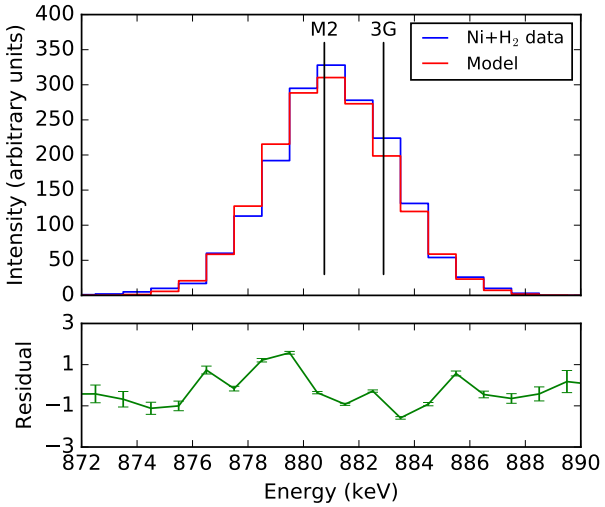

Figure 6.26 Data (blue), model fit to the data (red), and fit residuals (green) for CX between Ni^{19+} and H_2, for the energy region that includes the M2 and 3G lines. This model includes states with all three core hole configurations. Though the model appears to somewhat underpredict the flux in 3G, it is generally a good fit.

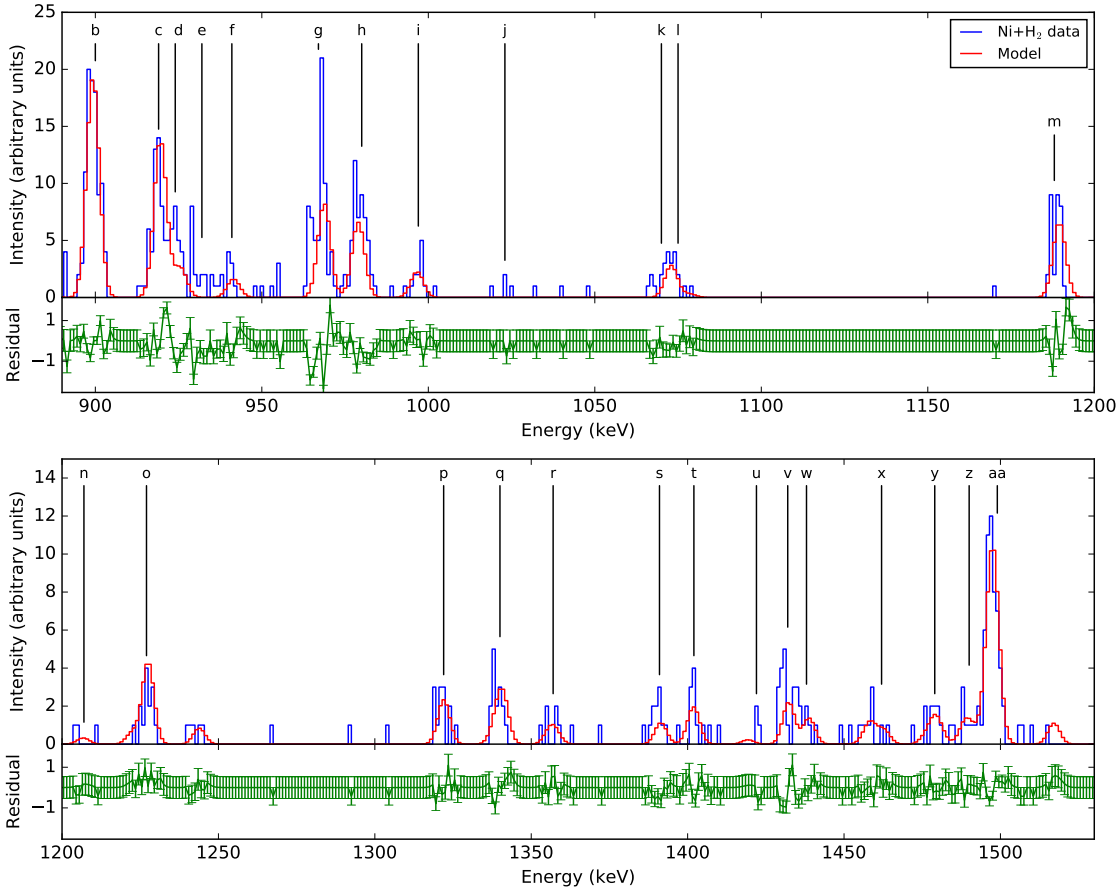

Figure 6.27 Data (blue), model fit to the data (red), and fit residuals (green) for CX between Ni^{19+} and H_2, for lines with energies between 890–1530 eV. This model includes states with all three core hole configurations. Most lines are fit very well, with the exception of lines g, h, s, t, and v. The model also predicts a line past 1500 eV where the data does not show much flux. These mismatches could be caused by not including a capture state that is relevant, by slight offsets in energy centroid of experimental lines compared to the model-predicted lines causing the fit to not weight a relevant capture state more heavily, or errors in the FAC-calculated transition probabilities that went into the model spectra.

for the $2p_{3/2}$, $2p_{1/2}$, and $2s_{1/2}$ core hole configurations, respectively. Degeneracies across electron configurations are indicated with solid black lines across points.

As can be seen in Figure 6.28, the most prominent capture channel is into $2p_{3/2}np_{1/2}(J = 1)$, where n is likely to be between 8–11. Also important is capture into $2p_{3/2}nf_{5/2}(J = 4)$ or $2p_{3/2}ng_{7/2}(J = 5)$ (n=8–11), which produce nearly identical spectra, and following that, capture into $2p_{3/2}np_{3/2}(J = 1)$ (n=8–11). Like in our S+He results, the significant capture into $l = f$ or $l = g$ that we find is surprising, given our naive assumption that capture into low angular momentum states are preferred. We note that capture into these high-l values with a $2p_{1/2}$ core hole configuration is not preferred overall. However, within the subset of $2p_{1/2}$ core hole configurations, these states have the highest cross section. This highlights the possibility of mixing between the $2p_{1/2}$ and $2p_{3/2}$ core excited configurations, as discussed in Section 5.4. Comparison to theoretical state-selective relative cross sections may help confirm whether this result is physical. We hope this work spurs on such theoretical calculations so that we can compare them to our results.

The fourth strongest capture channel is into $2p_{3/2}11s_{1/2}(J = 1)$. This spectrum is unique compared to other similar configurations with only differing values of n. The fact that $11s$ is favored over states with lower n values indicates that the primary n value of capture for the states with higher cross sections may also be 11. This highlights the fact that we must use caution applying Equation 1.2, which predicts $n_{\max}$ to be 9 for this experiment.

Another significant capture channel is into a $2s_{1/2}$ core hole configuration: $2s_{1/2}11d_{5/2}(J = 2)$. The importance of this capture channel underscores the possi-

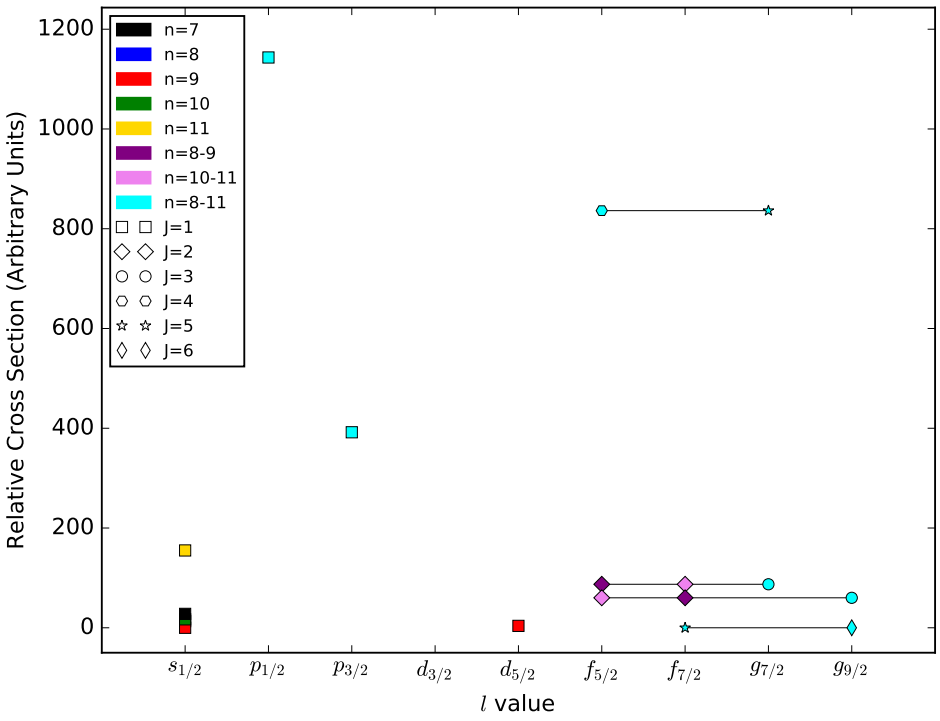

Figure 6.28 State-selective cross sections extracted from the model fit to Ni^{19+} and H_2 data, for states with a $2p_{3/2}$ core hole. Lines that span multiple points reflect degeneracies between those states. The most significant capture channel is into $np_{1/2}(J = 1)$, with $n = 8 - 11$. This ambiguity in n is due to the degenerate nature of the resulting spectra across that range of states. The next highest capture cross section is into $nf_{5/2}(J = 4)$ or $ng_{7/2}(J = 5)$, with $n = 8 - 11$. This is surprising due to the high angular momentum of those states. Comparing this figure to Figures 6.29 and 6.30, we see that the highest overall cross sections are in the $2p_{3/2}$ core hole configuration.

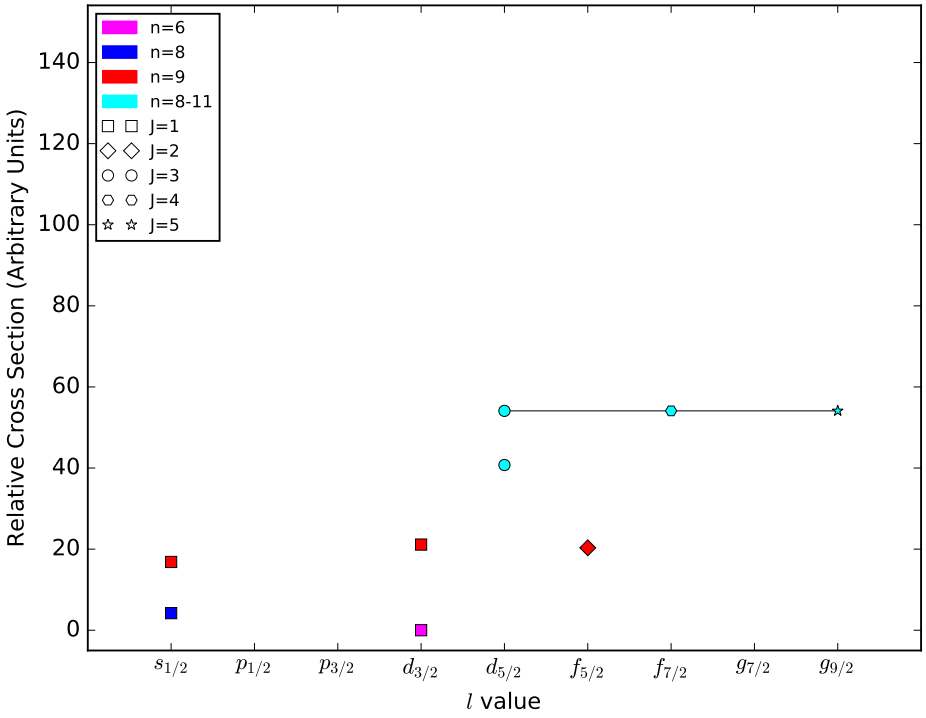

Figure 6.29 State-selective cross sections extracted from the model fit to Ni^{19+} and H_2 data, for states with a $2p_{1/2}$ core hole. Lines that span multiple points reflect degeneracies between those states. Most states with this core hole configuration do not have a very high cross section compared to the other configurations, but the primary capture channel in this configuration is for a combination of the states $nd_{5/2}(J = 3)$, $nf_{7/2}(J = 4)$, and $ng_{9/2}(J = 5)$, with $n = 8 - 11$.

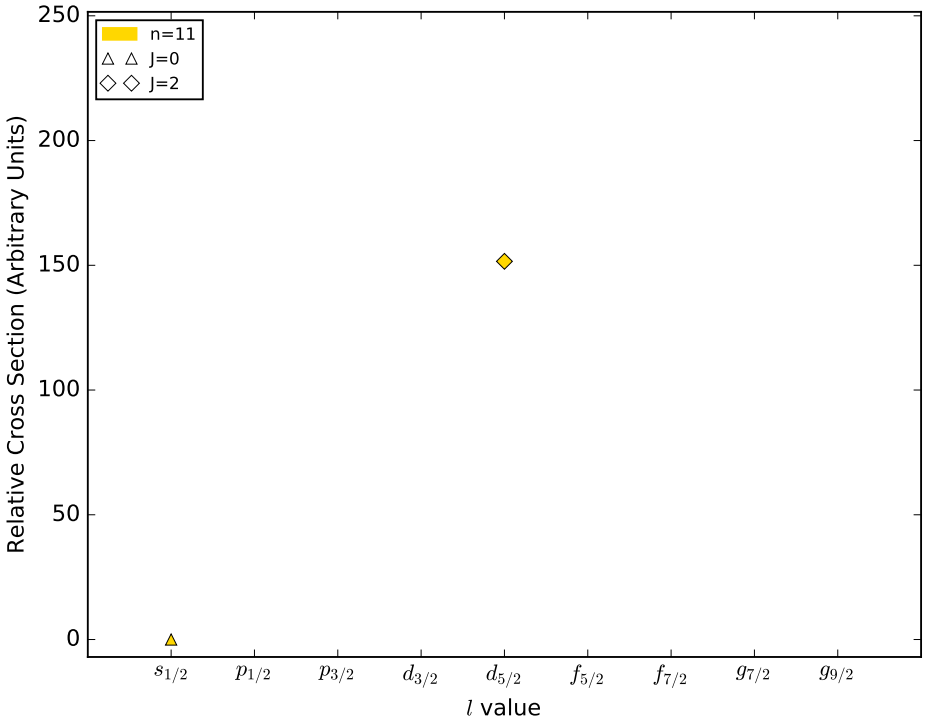

Figure 6.30 State-selective cross sections extracted from the model fit to Ni^{19+} and H_2 data, for states with a $2s_{1/2}$ core hole. The only capture channel with significant cross section in this configuration is $11d_{5/2}(J = 2)$, though it is surprising that this state is significant at all. We would naively expect the base F-like Ni ion prior to CX to have a $2p_{3/2}$ core hole, or, less likely (due to a higher energy), a $2p_{12}$ core hole. A $2s_{1/2}$ core hole has the highest energy configuration of the three. It is possible that this configuration results from MEC followed by autoionization and inner-shell excitation.

bility of $n = 11$ being the primary n value of the other degenerate states. As discussed in Section 5.4, this core configuration is unexpected due to its high energy, but perhaps this state results from multi-electron capture followed by inner-shell ionization. We will be able to better determine the likelihood of this possibility from a theoretical standpoint with total cross section calculations of SEC versus MEC for our collision energy regime and neutral species. Experimentally, by performing CX experiments with atomic H, we can ensure SEC and determine whether these core excited states are present in the resulting spectra.

6.7 Summary

In this chapter, we have compared our experimental L-shell CX data to commonly used spectral synthesis codes. The SPEX-CX and ACX models do not accurately reproduce our CX spectra, with disconcerting differences across the L-shell energy band. In some cases, energy centroids are offset from FAC energy calculations and our observed spectrum, and both models significantly overpredict flux in several lines that arise from core excited states. With further communication with the creators of these spectral synthesis codes, we hope to determine the quantitative differences between our spectra and begin to work towards a better match between experiment and theory.

We have also presented a powerful pipeline to extract relative cross sections from experimental (and if desired, simulated) spectra. We can directly compare state-selective relative cross sections calculated through this pipeline to MCLZ cal-

culations, where they are available. MCLZ calculations for S^{16+}+He CX only show fair agreement with our method, and we have shown that a simulated spectrum resulting from MCLZ calculations does not match our experimental spectrum well. This underscores the fact that more progress must be made on the theory side. However, it is important that we have a promising analysis tool that allows us to directly and quantitatively compare the results of these two methods. This pipeline can thus be used both in conjunction with and in the absence of detailed theoretical calculations.

When applying the pipeline to our Ni^{19+}+H_2 CX data, we find that a core-excited state ($2s_{1/2}$) is required to produce the k and l lines, which may result from MEC followed by autoionization and inner-shell excitation. Emission from the $2p_{1/2}$ core excited configuration may result from configuration mixing. This highlights the need for more comprehensive theoretical calculations that can incorporate these complex processes to compare to our results and guide our analysis.

We will continue to improve on this modeling process. In particular, we will focus on the errors present in our cross section calculations. Currently, our fitting procedure uses chi-squared minimization (with Gehrels weighting), which is not ideal for our case, as our spectra have many bins with low counts. In the future, we wish to experiment with different methods of calculating a fit and confidence intervals, such as the C-statistic [Cash, 1979]. Our top priority is adding confidence intervals to our calculations of cross sections in order to have a more scientifically robust result.

In the future, we can apply this method to other experimental data, including

those from techniques that achieve higher collision energies such as merged-beam experiments, in order to determine how the relative capture cross sections change. We can even apply this same procedure to spectra generated from MCLZ or other theoretical cross section calculations as verification of self-consistency. Although we can still work to make the selection of the model basis set and the determination of configuration degeneracies more robust (see Chapter 7), this pipeline is a powerful new tool that allows us to directly probe the physical processes at work during a CX experiment, and quickly visualize the spectral lines that result from any electron configuration in any H, He-, and Ne-like ion.

Our modeling pipeline has already helped us identify the most important states for electron capture, and can aid in determining more detailed diagnostics for the occurrence of CX in astrophysical observations. This combination of experiment and theory will bring us closer to understanding the detailed atomic physics of CX, properly identifying it in our astrophysical observations, and harnessing its diagnostic power.

Chapter 7: Outlook

Improving our understanding of the complex and subtle nature of CX requires incremental progress. In this dissertation, we have pushed the boundaries of our knowledge a bit further by using powerful experimental and theoretical tools where they existed already, and by developing new ones where they did not. We have shown that CX is an important process to consider in many astrophysical environments (Section 1.5), and that with high enough resolution and a large enough signal, if we properly understand the underlying atomic processes that affect CX spectra, it can be diagnostic of the velocities, elemental abundances, and densities of the emitting region (Section 1.6). Our work is far from over, however: much remains to be done in order to reach our goal of verifying and improving the accuracy of CX spectral models to within the resolution of XARM, Athena, and Lynx in order to utilize these diagnostics in the future.

There are many natural continuations of the work presented here. We will continue to develop the cross section modeling pipeline, working to make it more robust with more automated selections of basis spectral states, determinations of state degeneracy, and a quantitative error analysis. In order to cross-check our results, we will also apply our pipeline to model-predicted spectra, including those

from SPEX-CX, ACX, and future MCLZ results. MCLZ calculations for the other spectra presented in this thesis are forthcoming [Renata Cumbee, private communication], and we are looking forward to a detailed comparison of our results to this theory.

There is also much to be done on the experimental side. It is imperative to perform more high-resolution spectral measurements, especially of L-shell CX, and over a wide range of collision energies. We believe that MEC is likely a contributor to our experimental CX spectra, but disentangling its spectral effect from SEC is challenging. We can experimentally approach this challenge in two ways. The first is with time-of-flight measurements (e.g. Ali et al. [2005]) that measure the relative contribution of MEC versus SEC by identifying the charge state of the neutral target after CX. The second approach is through high-spectral resolution measurements of CX with atomic H. Using H ensures SEC, and in addition, simulates most astrophysical CX. We currently have an H source at LLNL for this purpose which operates by thermally cracking H_2 molecules into H, but this method has proved to be difficult to properly characterize. Instead, we have begun discussions with colleagues at GSFC, LLNL, and collaborators at Pacific Union College to design an H beam that results from neutralizing a proton beam from a duoplasmatron source with an alkali jet.

CX is finally starting to gain more attention in the astronomical field as we begin to see hints of it in various astrophyisical environments and learn more about the complexities of the process. To gain a better understanding of the atomic physics at work during CX, we must merge high-resolution experimental data with

comprehensive theoretical models. Observers, theorists, and experimentalists alike must thus work together to continue to learn about this fascinating process.

Appendix A: Spectral Basis Set Elements for Model Fit to S+He CX Data

This appendix shows simulated spectra for H-, then He-like S that result from electron capture into a given electron configuration in jj-coupling, then the subsequent cascade to ground. These spectra formed the basis set for a least-squares minimization fit to data presented in Chapter 4. The procedures for this fit and the generation of these spectra are described in Chapter 5.

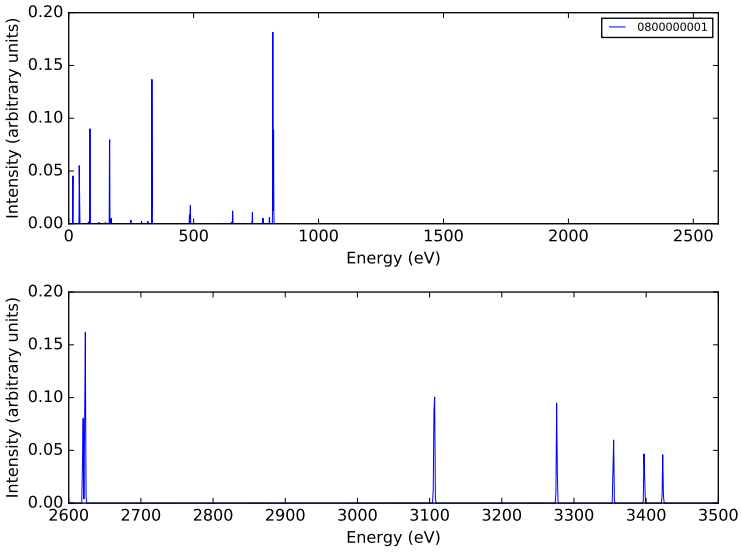

Figure A.1 Cascade spectrum of H-like S with initial electron configuration $8s_{1/2}$.

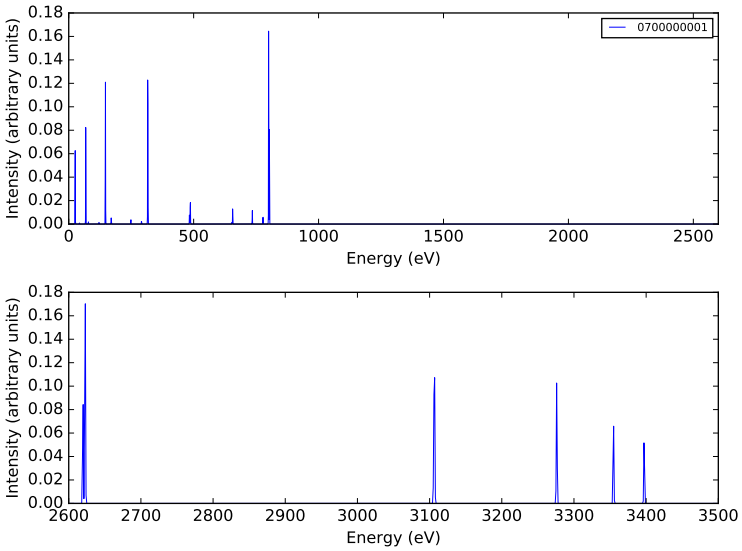

Figure A.2 Cascade spectrum of H-like S with initial electron configuration $7s_{1/2}$.

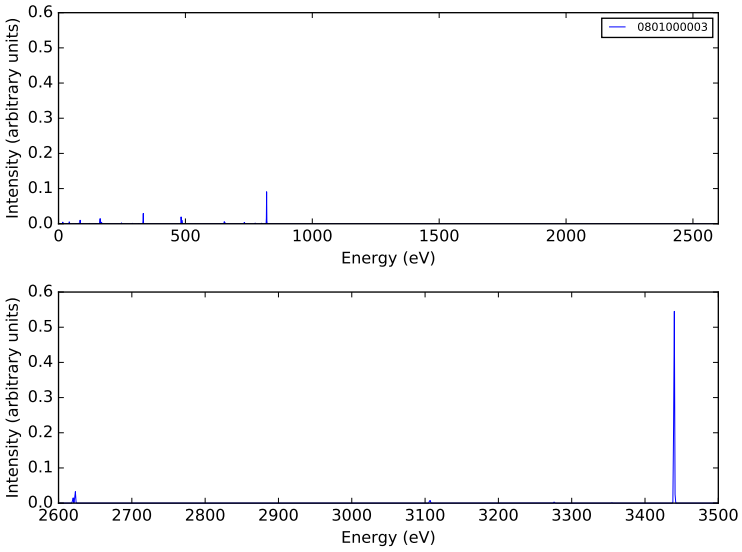

Figure A.3 Cascade spectrum of H-like S with initial electron configuration $8p_{3/2}$.

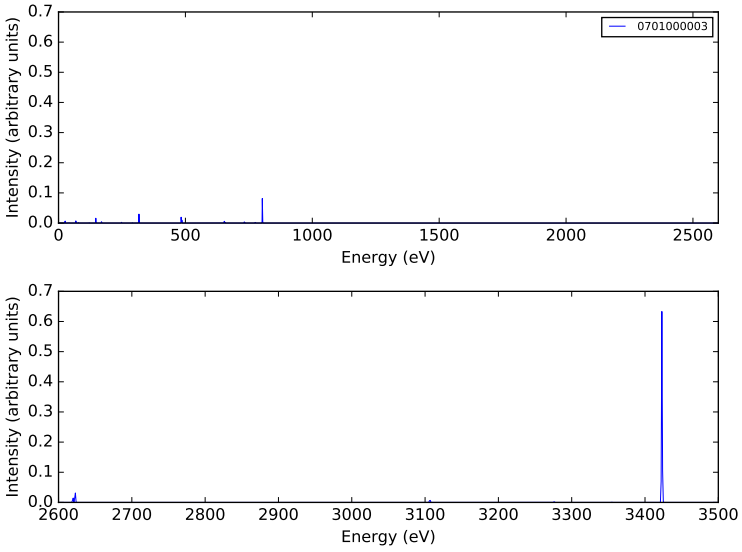

Figure A.4 Cascade spectrum of H-like S with initial electron configuration $7p_{3/2}$.

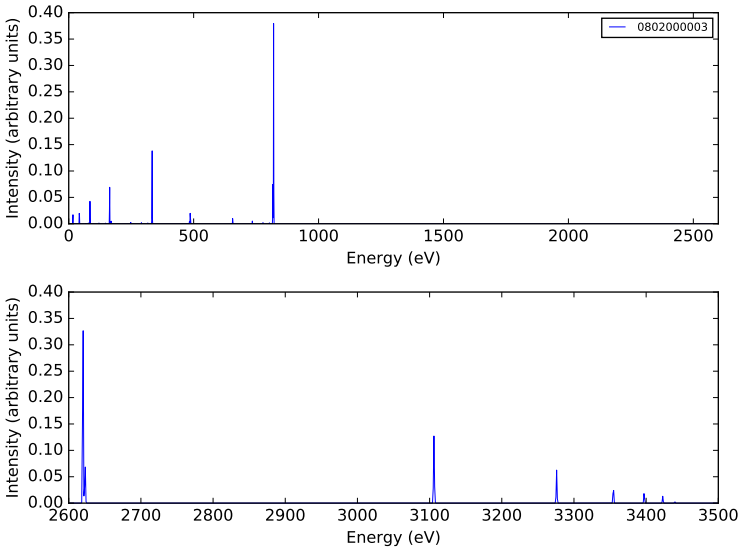

Figure A.5 Cascade spectrum of H-like S with initial electron configuration $8d_{3/2}$.

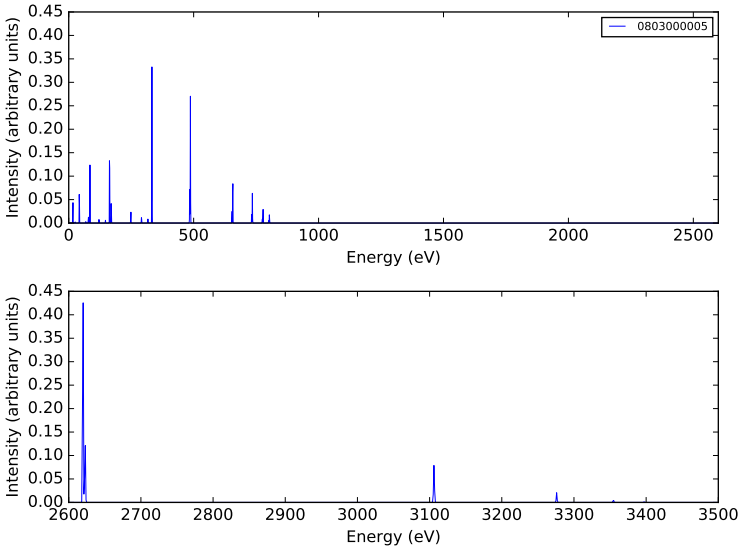

Figure A.6 Cascade spectrum of H-like S with initial electron configuration $8f_{5/2}$.

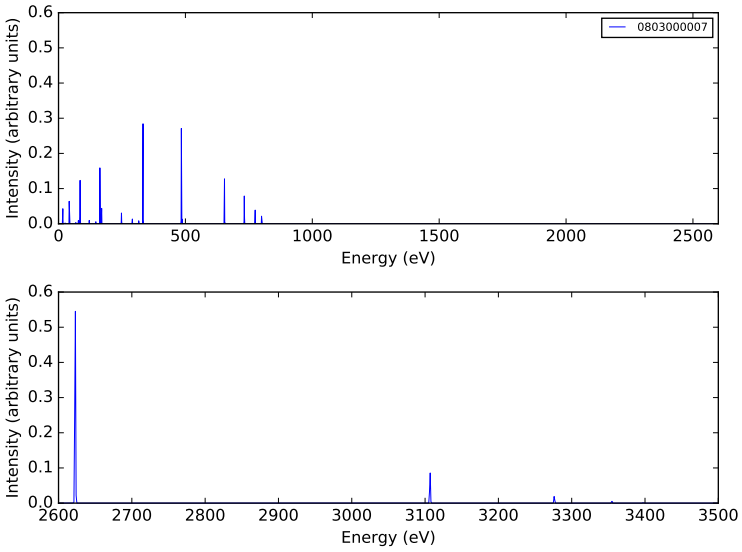

Figure A.7 Cascade spectrum of H-like S with initial electron configuration $8f_{7/2}$.

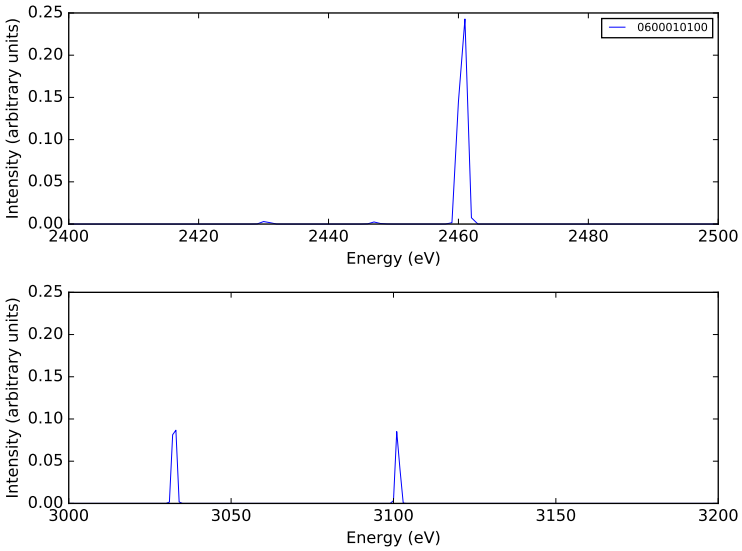

Figure A.8 Cascade spectrum of He-like S with initial electron configuration $1s_{1/2}6s_{1/2}(J = 0)$.

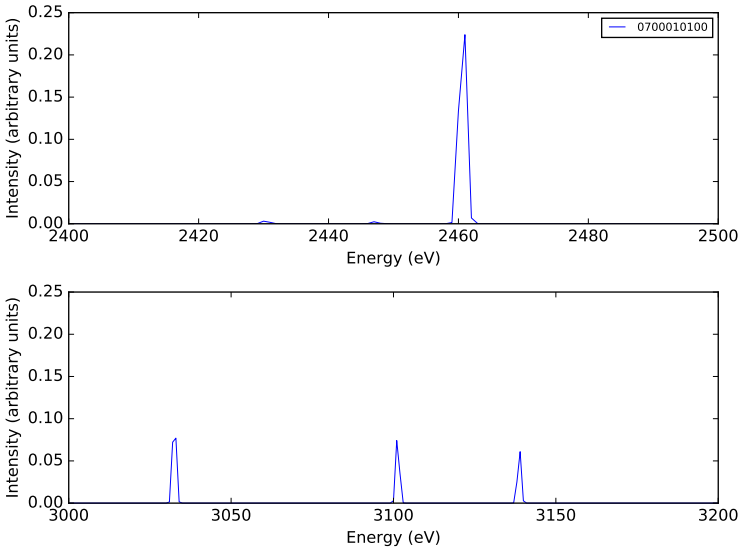

Figure A.9 Cascade spectrum of He-like S with initial electron configuration $1s_{1/2}7s_{1/2}(J = 0)$.

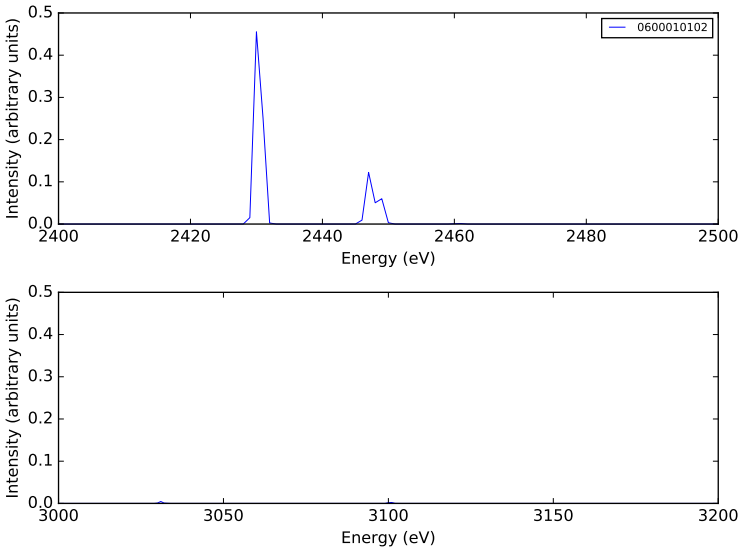

Figure A.10 Cascade spectrum of He-like S with initial electron configuration $1s_{1/2}6s_{1/2}(J = 1)$.

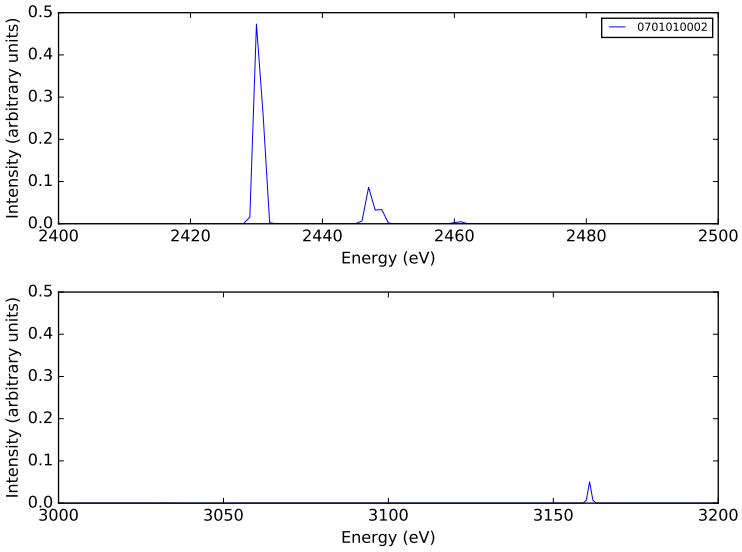

Figure A.11 Cascade spectrum of He-like S with initial electron configuration $1s_{1/2}7p_{1/2}(J = 1)$.

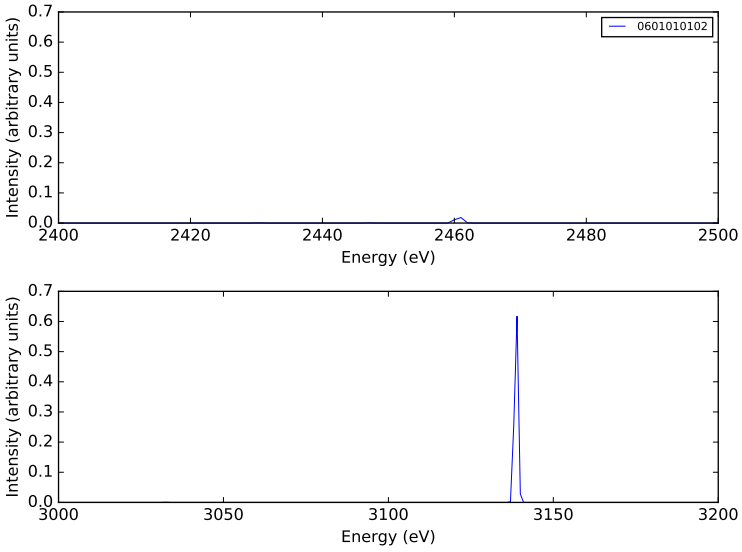

Figure A.12 Cascade spectrum of He-like S with initial electron configuration $1s_{1/2}6p_{3/2}(J = 1)$.

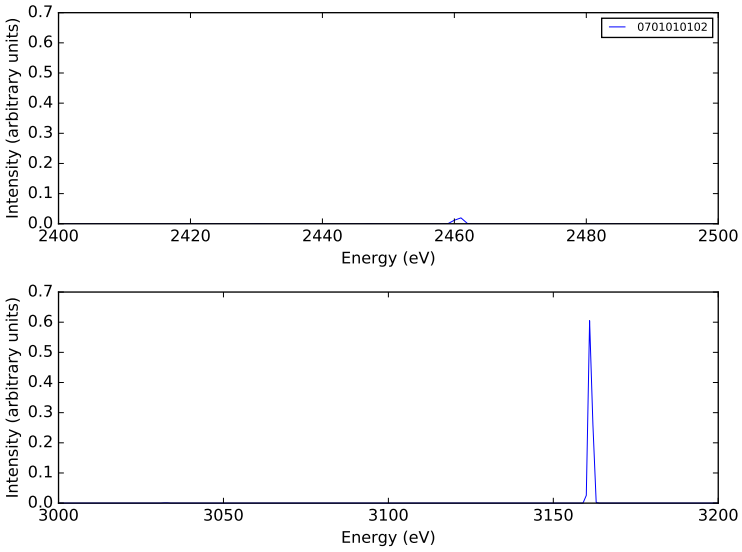

Figure A.13 Cascade spectrum of He-like S with initial electron configuration $1s_{1/2}7p_{3/2}(J = 1)$.

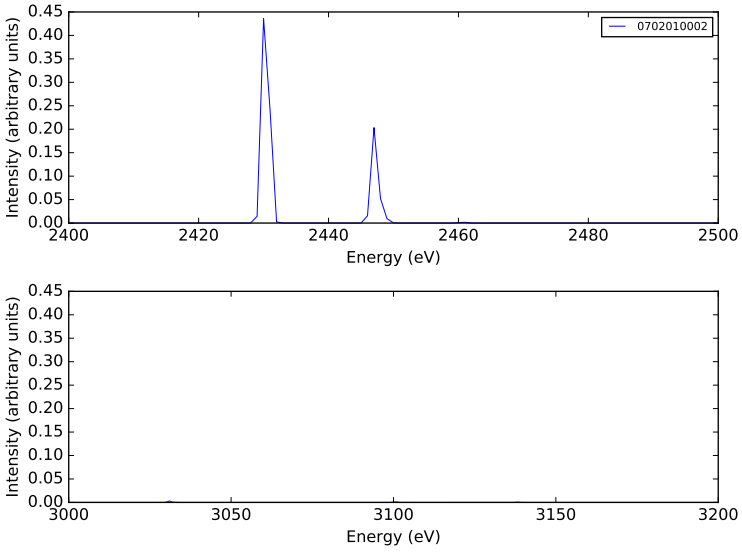

Figure A.14 Cascade spectrum of He-like S with initial electron configuration $1s_{1/2}7d_{3/2}(J = 1)$.

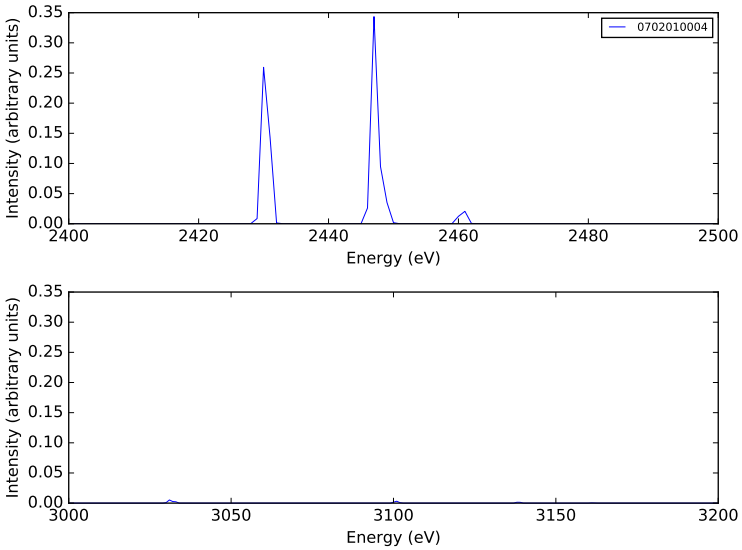

Figure A.15 Cascade spectrum of He-like S with initial electron configuration $1s_{1/2}7d_{3/2}(J = 2)$.

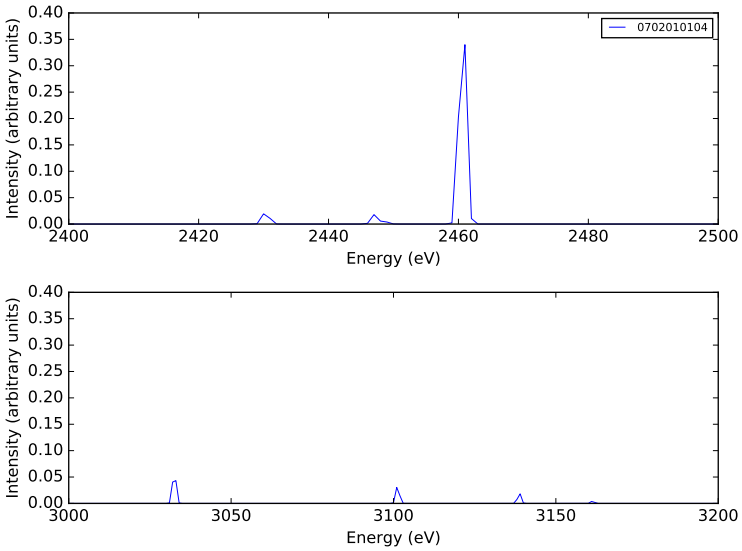

Figure A.16 Cascade spectrum of He-like S with initial electron configuration $1s_{1/2}7d_{5/2}(J = 2)$.

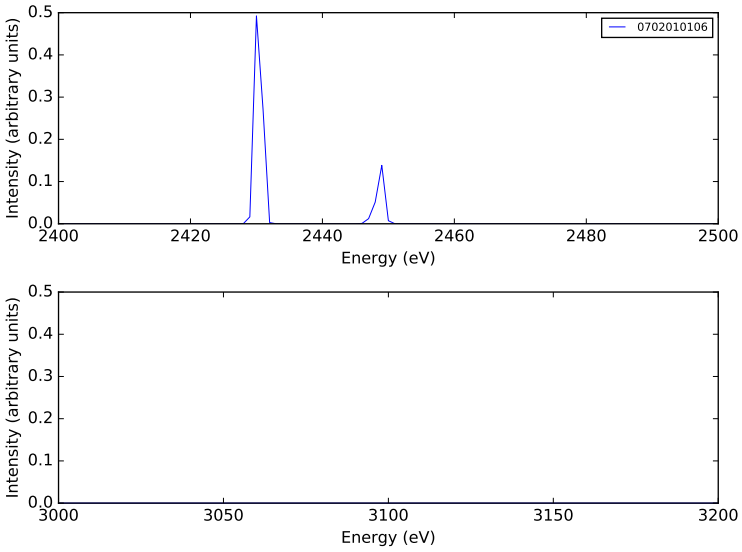

Figure A.17 Cascade spectrum of He-like S with initial electron configuration $1s_{1/2}7d_{5/2}(J = 3)$.

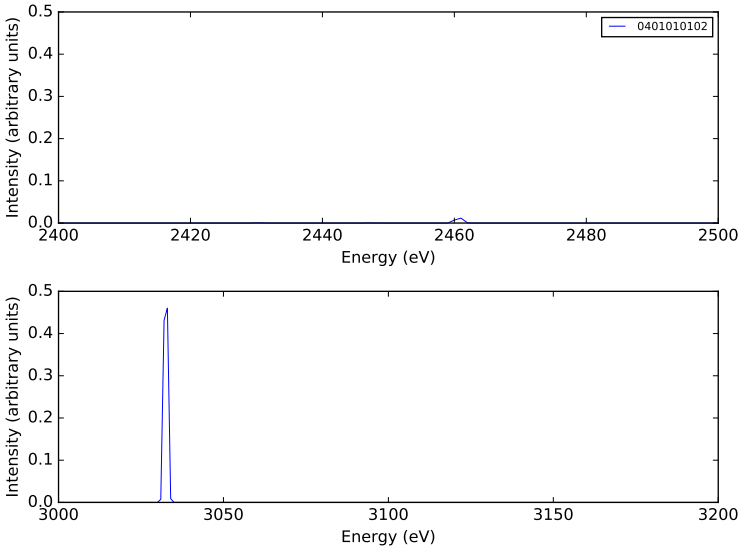

Figure A.18 Cascade spectrum of He-like S with initial electron configuration $1s_{1/2}4p_{3/2}(J = 1)$.

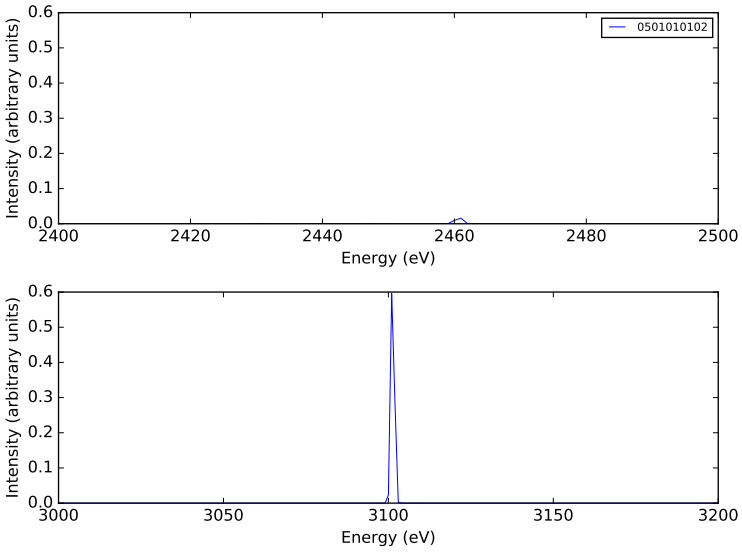

Figure A.19 Cascade spectrum of He-like S with initial electron configuration $1s_{1/2}5p_{3/2}(J = 1)$.

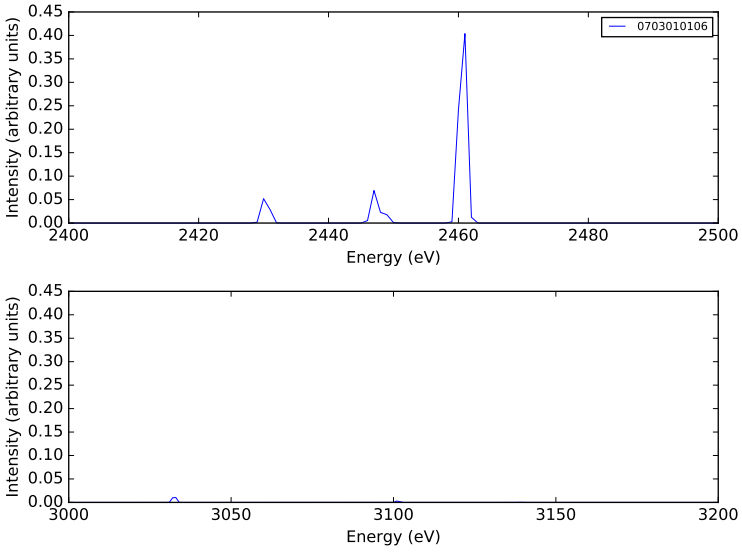

Figure A.20 Cascade spectrum of He-like S with initial electron configuration $1s_{1/2}7f_{7/2}(J = 3)$.

Appendix B: Spectral Basis Set Elements for Model Fit to Ni+H_2, Ni+He CX Data

This appendix shows simulated spectra for Ne-like Ni that result from electron capture into a given electron configuration in jj-coupling, then the subsequent cascade to ground. These spectra formed the basis set for a least-squares minimization fit to data presented in Chapter 5. The procedures for this fit and the generation of these spectra are described in Chapter 6.

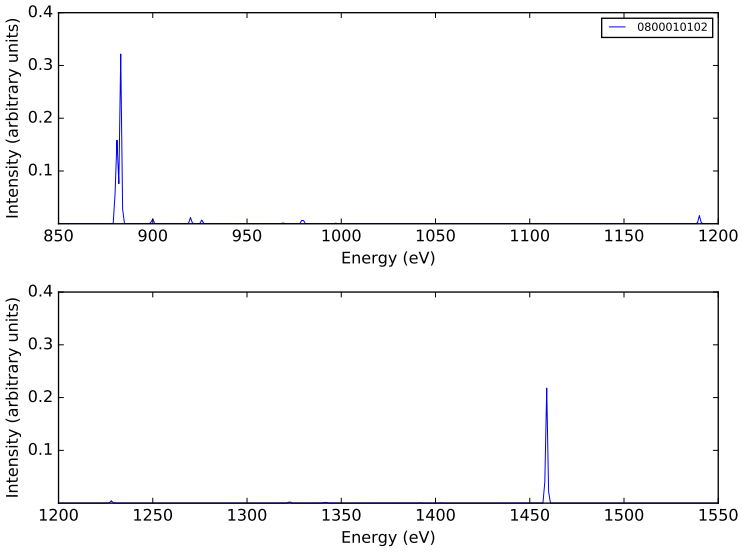

Figure B.1 Cascade spectrum of Ne-like Ni with initial electron configuration $2p_{3/2}8s_{1/2}(J = 1)$.

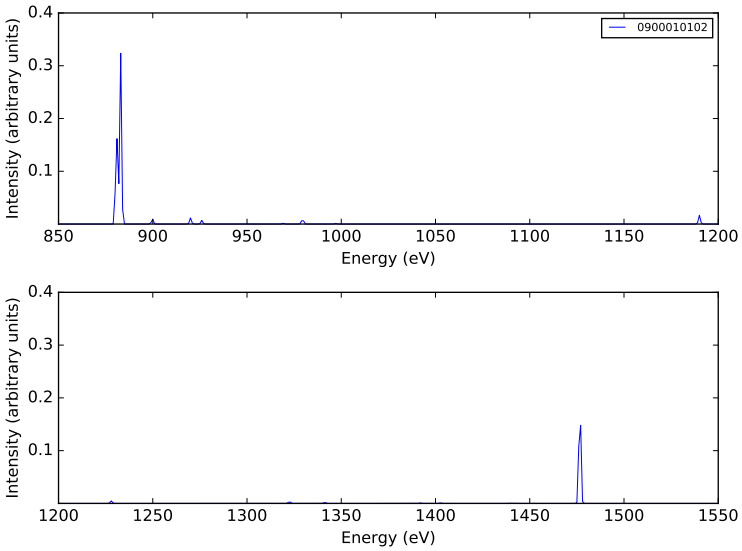

Figure B.2 Cascade spectrum of Ne-like Ni with initial electron configuration $2p_{3/2}9s_{1/2}(J = 1)$.

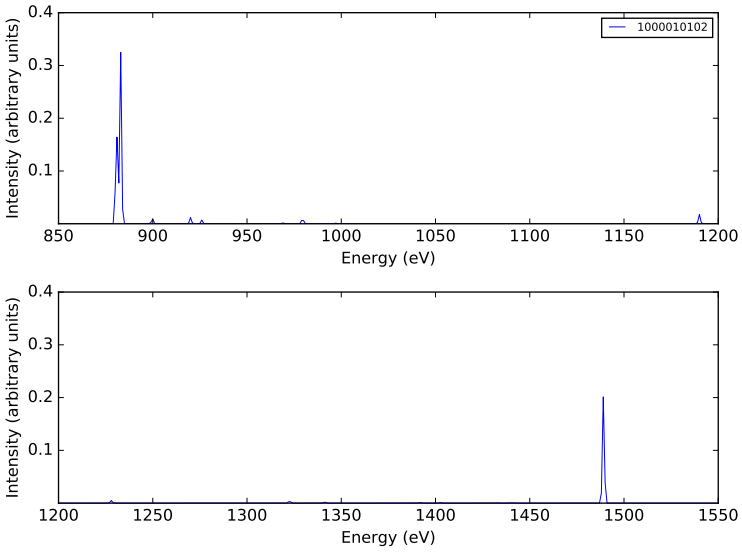

Figure B.3 Cascade spectrum of Ne-like Ni with initial electron configuration $2p_{3/2}10s_{1/2}(J = 1)$.

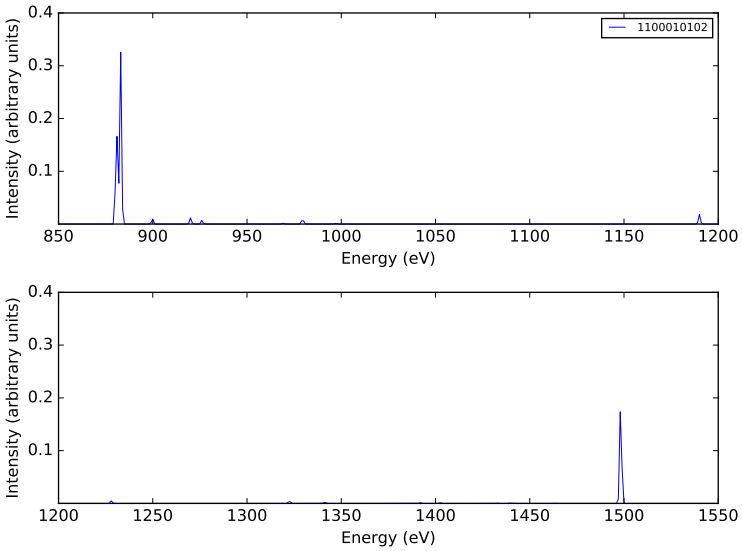

Figure B.4 Cascade spectrum of Ne-like Ni with initial electron configuration $2p_{3/2}11s_{1/2}(J = 1)$.

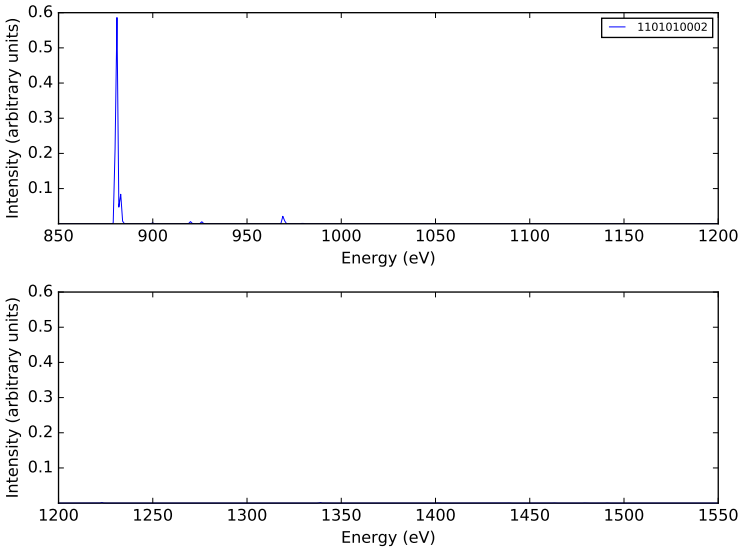

Figure B.5 Cascade spectrum of Ne-like Ni with initial electron configuration $2p_{3/2}11p_{1/2}(J = 1)$.

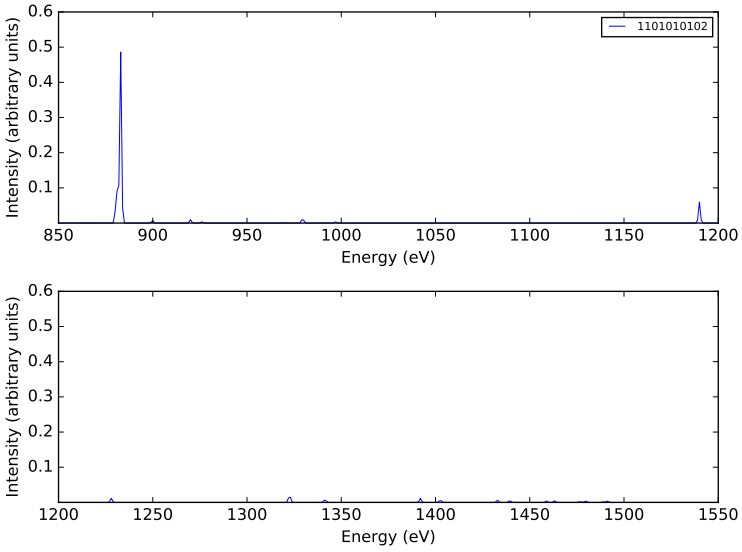

Figure B.6 Cascade spectrum of Ne-like Ni with initial electron configuration $2p_{3/2}11p_{3/2}(J = 1)$.

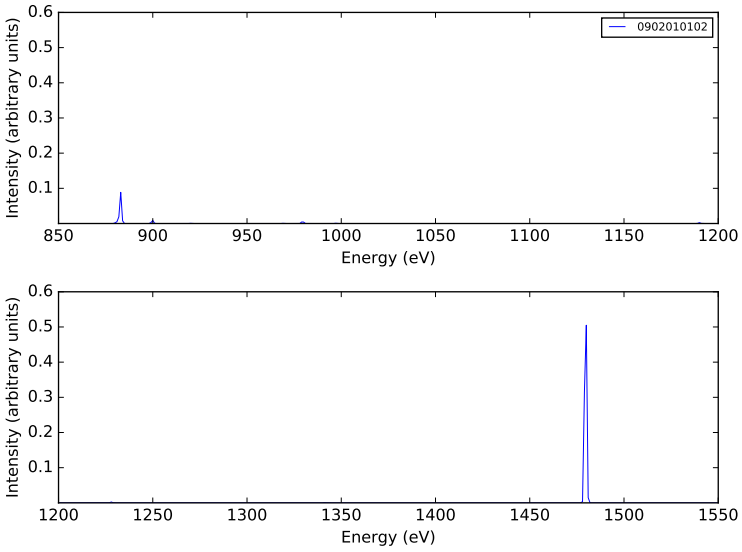

Figure B.7 Cascade spectrum of Ne-like Ni with initial electron configuration $2p_{3/2}9d_{5/2}(J = 1)$.

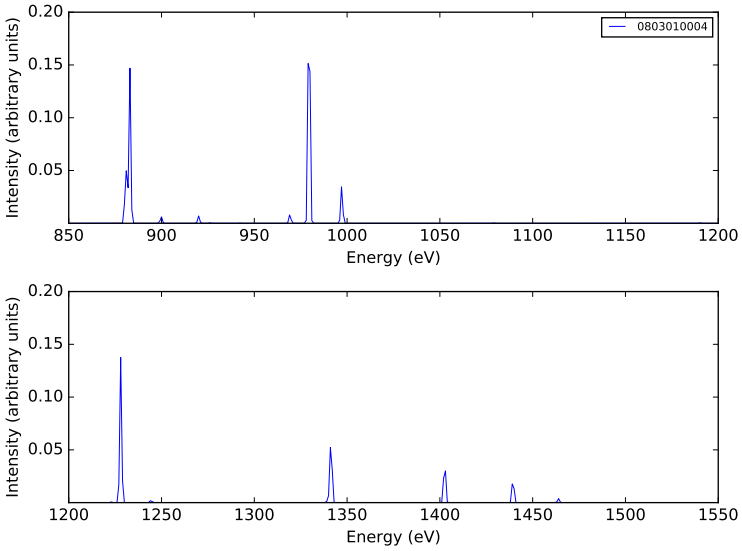

Figure B.8 Cascade spectrum of Ne-like Ni with initial electron configuration as one or a combination of $2p_{3/2}8f_{5/2}(J = 2)$, $2p_{3/2}9f_{5/2}(J = 2)$, $2p_{3/2}10f_{7/2}(J = 2)$, $2p_{3/2}11f_{7/2}(J = 2)$, $2p_{3/2}8g_{7/2}(J = 3)$, $2p_{3/2}9g_{7/2}(J = 3)$, $2p_{3/2}10g_{7/2}(J = 3)$, or/and $2p_{3/2}11g_{7/2}(J = 3)$.

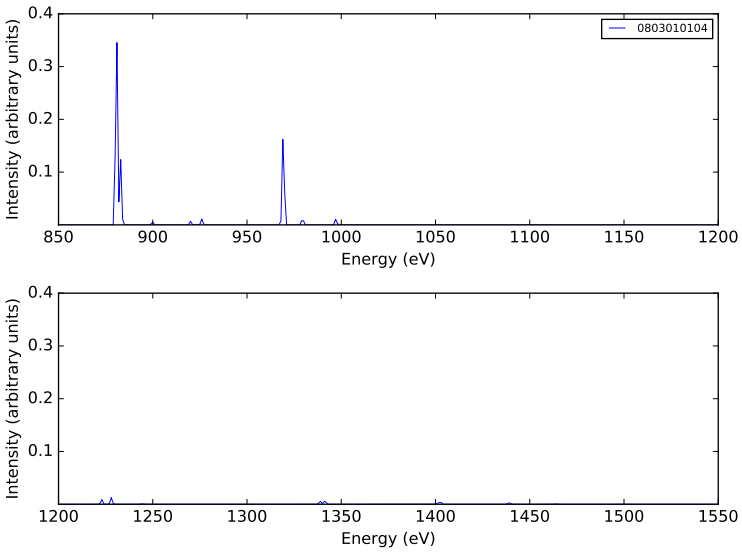

Figure B.9 Cascade spectrum of Ne-like Ni with initial electron configuration as one or a combination of $2p_{3/2}8f_{7/2}(J = 2)$, $2p_{3/2}9f_{7/2}(J = 2)$, $2p_{3/2}10f_{5/2}(J = 2)$, $2p_{3/2}11f_{5/2}(J = 2)$, $2p_{3/2}8g_{9/2}(J = 3)$, $2p_{3/2}9g_{9/2}(J = 3)$, $2p_{3/2}10g_{9/2}(J = 3)$, or/and $2p_{3/2}11g_{9/2}(J = 3)$.

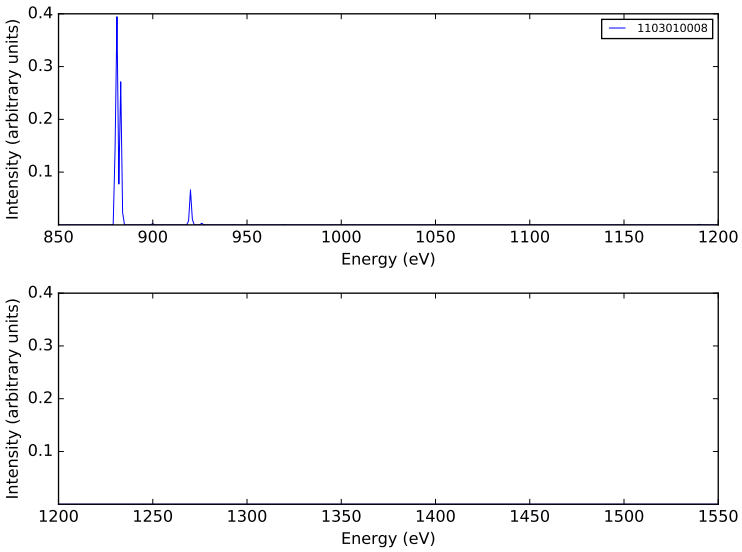

Figure B.10 Cascade spectrum of Ne-like Ni with initial electron configuration as one or a combination of $2p_{3/2}8f_{5/2}(J = 4)$, $2p_{3/2}9f_{5/2}(J = 4)$, $2p_{3/2}10f_{5/2}(J = 4)$, $2p_{3/2}11f_{5/2}(J = 4)$, $2p_{3/2}8g_{7/2}(J = 5)$, $2p_{3/2}9g_{7/2}(J = 5)$, $2p_{3/2}10g_{7/2}(J = 5)$, or/and $2p_{3/2}11g_{7/2}(J = 5)$.

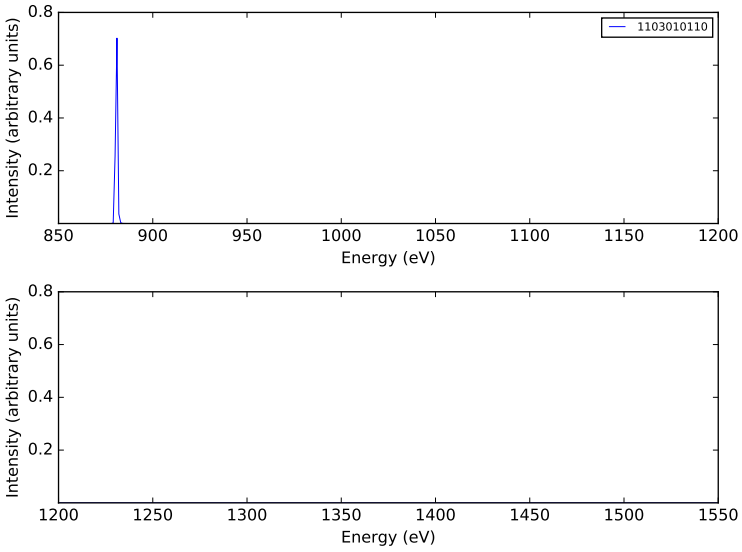

Figure B.11 Cascade spectrum of Ne-like Ni with initial electron configuration as one or a combination of $2p_{3/2}8f_{5/2}(J = 4)$, $2p_{3/2}9f_{5/2}(J = 4)$, $2p_{3/2}10f_{5/2}(J = 4)$, $2p_{3/2}11f_{5/2}(J = 4)$, $2p_{3/2}8g_{7/2}(J = 5)$, $2p_{3/2}9g_{7/2}(J = 5)$, $2p_{3/2}10g_{7/2}(J = 5)$, or/and $2p_{3/2}11g_{7/2}(J = 5)$.

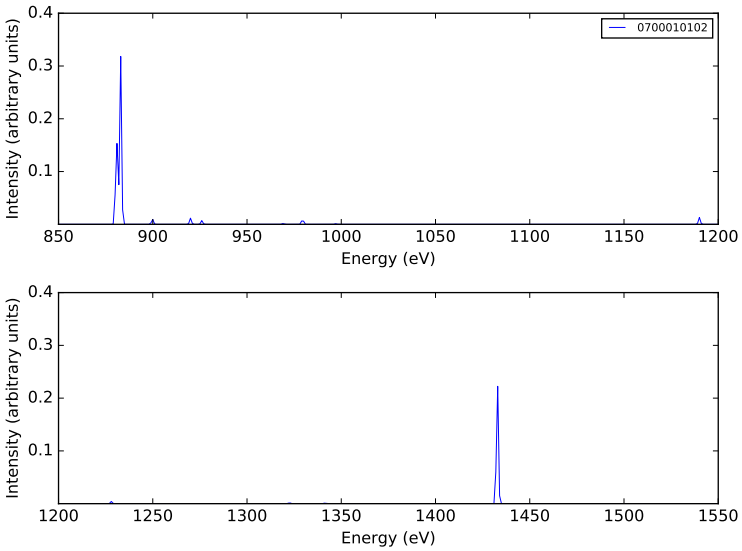

Figure B.12 Cascade spectrum of Ne-like Ni with initial electron configuration $2p_{3/2}7s_{1/2}(J = 1)$.

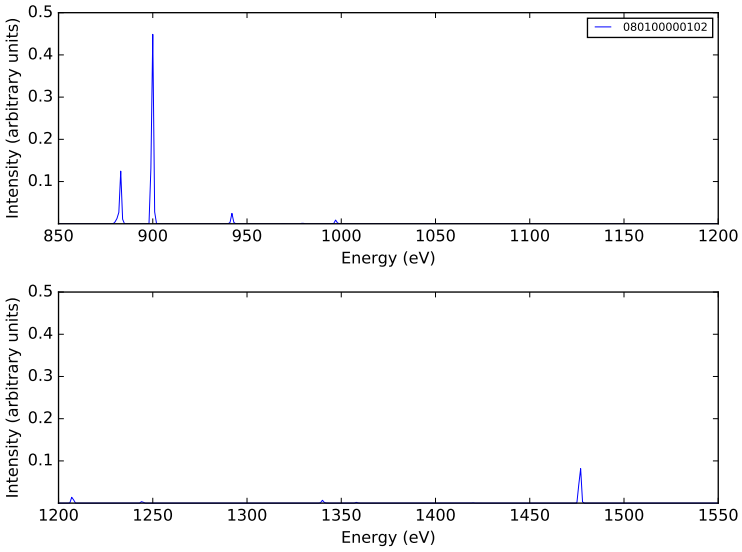

Figure B.13 Cascade spectrum of Ne-like Ni with initial electron configuration $2p_{1/2}8s_{1/2}(J = 1)$.

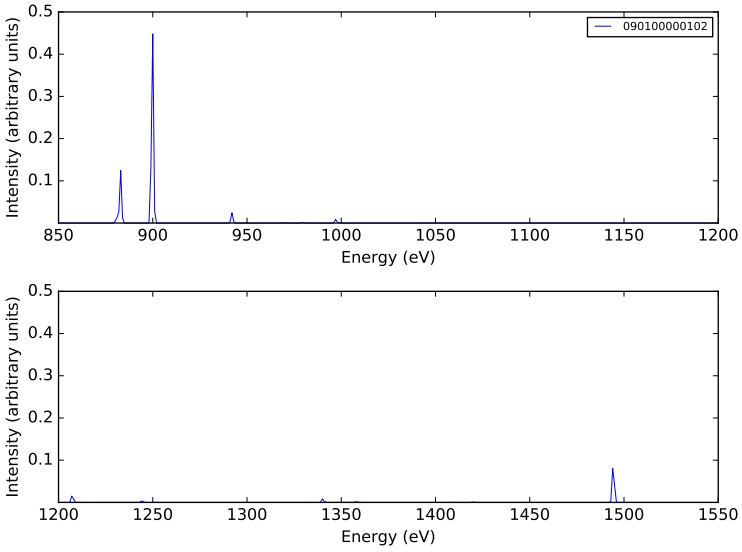

Figure B.14 Cascade spectrum of Ne-like Ni with initial electron configuration $2p_{1/2}8s_{1/2}(J = 1)$.

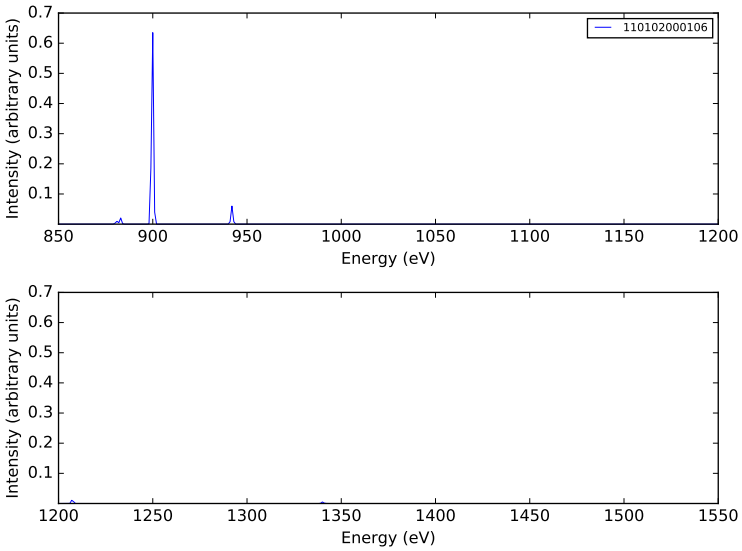

Figure B.15 Cascade spectrum of Ne-like Ni with initial electron configuration $2p_{1/2}8d_{5/2}(J = 3)$, $2p_{1/2}9d_{5/2}(J = 3)$, $2p_{1/2}10d_{5/2}(J = 3)$, $2p_{1/2}11d_{5/2}(J = 3)$.

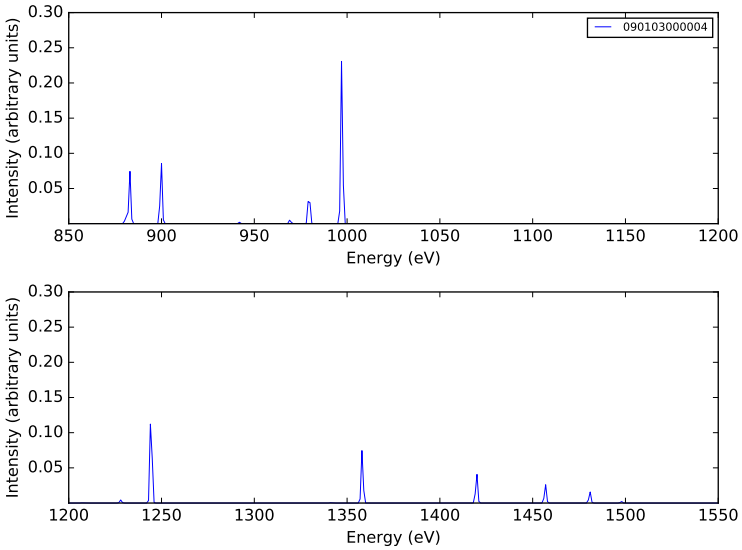

Figure B.16 Cascade spectrum of Ne-like Ni with initial electron configuration $2p_{1/2}9f_{5/2}(J = 2)$.

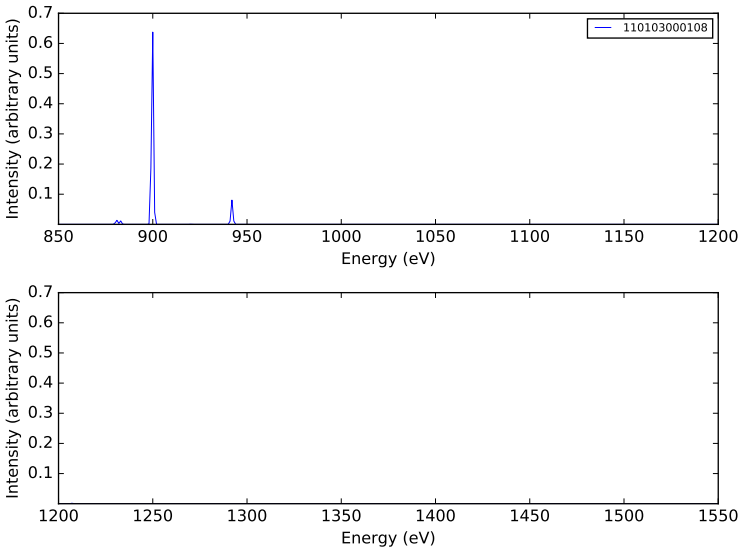

Figure B.17 Cascade spectrum of Ne-like Ni with initial electron configuration one or a combination of $2p_{1/2}8d_{5/2}(J = 3)$, $2p_{1/2}9d_{5/2}(J = 3)$, $2p_{1/2}10d_{5/2}(J = 3)$, $2p_{1/2}11d_{5/2}(J = 3)$, $2p_{1/2}8f_{7/2}(J = 4)$, $2p_{1/2}9f_{7/2}(J = 4)$, $2p_{1/2}10f_{7/2}(J = 4)$, $2p_{1/2}11f_{7/2}(J = 4)$, $2p_{1/2}8g_{9/2}(J = 5)$, $2p_{1/2}9g_{9/2}(J = 5)$, $2p_{1/2}10g_{9/2}(J = 5)$, or/and $2p_{1/2}11g_{9/2}(J = 5)$.

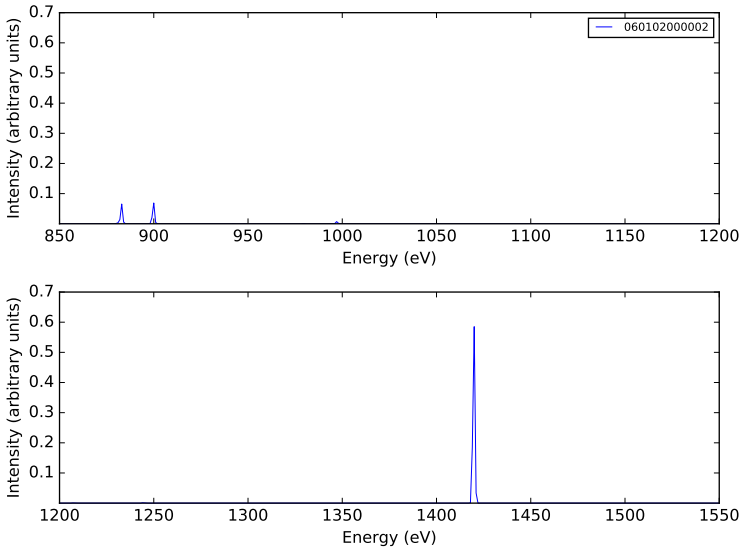

Figure B.18 Cascade spectrum of Ne-like Ni with initial electron configuration $2p_{1/2}6d_{3/2}(J = 1)$.

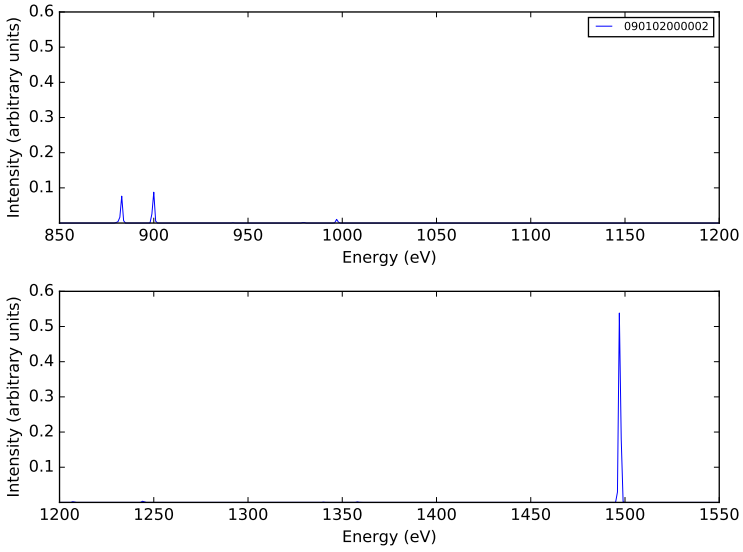

Figure B.19 Cascade spectrum of Ne-like Ni with initial electron configuration $2p_{1/2}9d_{3/2}(J = 1)$.

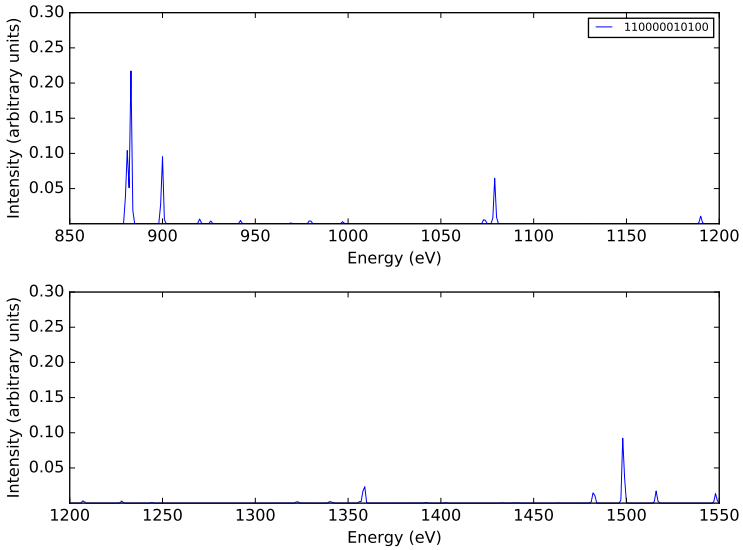

Figure B.20 Cascade spectrum of Ne-like Ni with initial electron configuration $2s_{1/2}11s_{1/2}(J = 0)$.

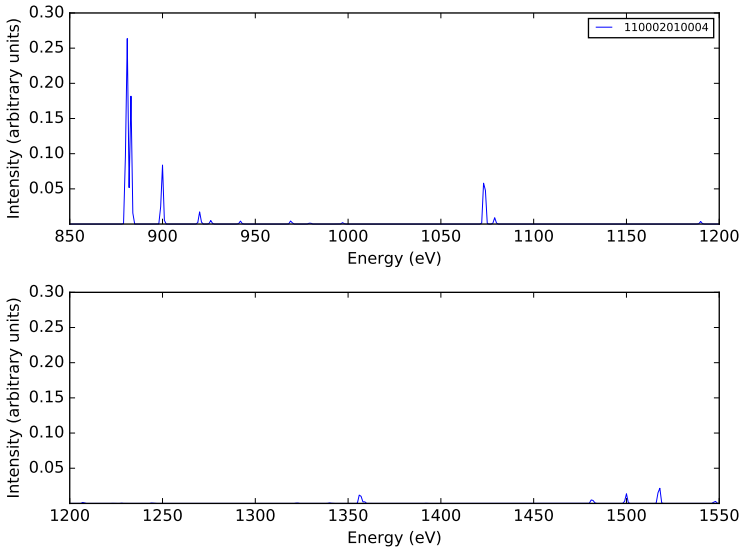

Figure B.21 Cascade spectrum of Ne-like Ni with initial electron configuration $2s_{1/2}11d_{5/2}(J = 2)$.

Appendix C: X-Ray Emission Mechanisms

X-rays are emitted from a wide variety of astrophysical objects, and one can either measure those X-rays via imaging, timing, polarization, or spectral studies. In this dissertation, I have focused on X-ray spectroscopy, which can yield a wealth of physical information, especially if at high resolution: with sufficient data from an astrophysical target or laboratory plasma, along with a correct interpretation of the underlying X-ray emission mechanisms, one can derive information about composition, temperature and density distributions, structure, turbulent and bulk velocities, and energy balance.

The first step in interpreting the spectra from the objects and regions we observe is to understand the emission mechanism. Many atomic processes involving highly charged ions can lead to the emission of X-rays in astrophysical and laboratory environments, either in the form of an X-ray continuum or via spectral line formation. Though the focus for this dissertation has been CX, in the regions where it occurs, is often just one of many processes happening simultaneously. It is thus important understand other mechanisms that can generate competing X-ray emission. For a more detailed theoretical discussion of these mechanisms, see Mewe [1999].

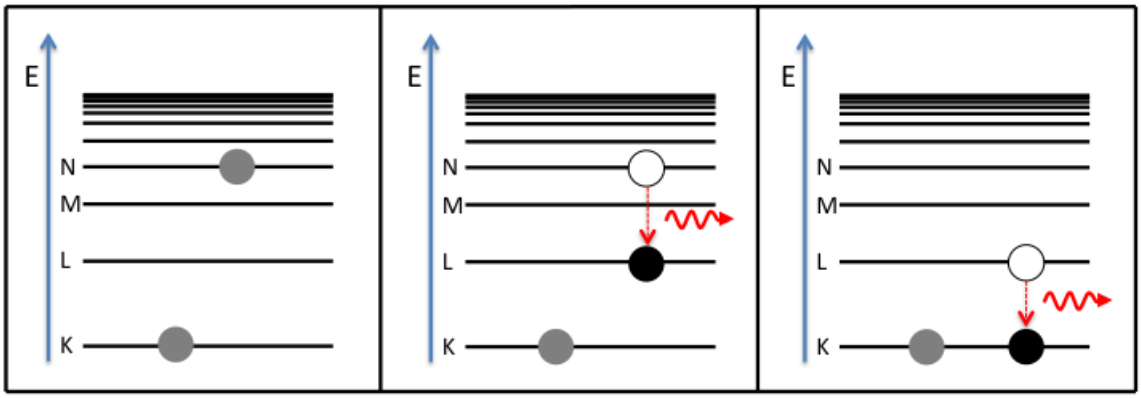

Figure C.1 Radiative cascade.

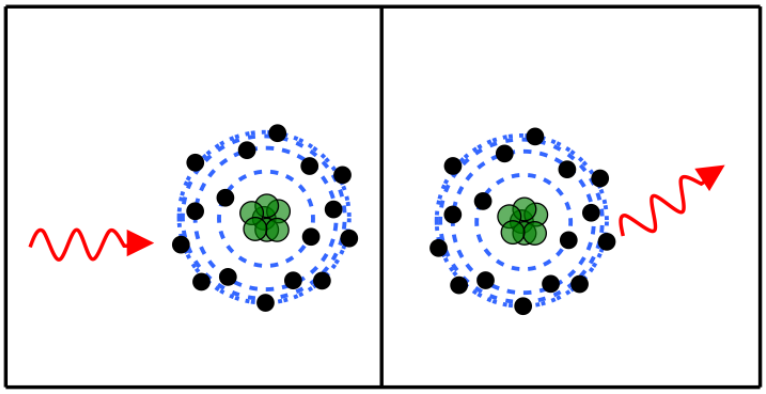

Figure C.2 Scattering of X-ray light by a neutral.

The most basic of these processes is a radiative cascade (Figure C.1): electrons in an excited state cascade down to a lower energy level, following quantum mechanical selection rules, and emitting photons at each step with an energy equal to the difference in energy between the initial and final states.

X-ray photons can also be elastically scattered by electrons in an atom. (Figure C.2).

Bremmstrahlung radiation (Figure C.3) is produced when a free electron is

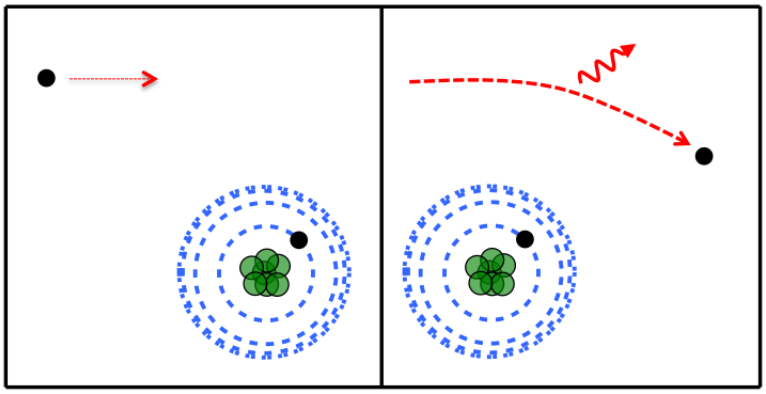

Figure C.3 Bremmstrahlung.

decelerated as it passes near an ion. To satisfy the law of conservation of energy, the electron's loss of kinetic energy from the deceleration is released back into the system as an X-ray photon. Because this loss in energy depends on several variable factors, such as the initial velocity of the electron, the charge of the ion, and the impact parameter, the resulting X-rays have a distribution of energies. Bremmstrahlung is thus a continuum process.

Electrons in an ion can be collisionally excited from one subshell to another by other electrons (collisional excitation, Figure C.4) or a photon (photoexcitation, Figure C.5). After collisional excitation, the colliding electron is left with a lower kinetic energy and the excited electron subsequently radiatively decays back to ground. Photoexcitation is a resonant process, meaning the energy of the incoming photon must exactly match the difference in energy states of the electron to be excited. If the energy of the electron collision or photon is sufficiently large, inner-shell excitation or ionization may occur.

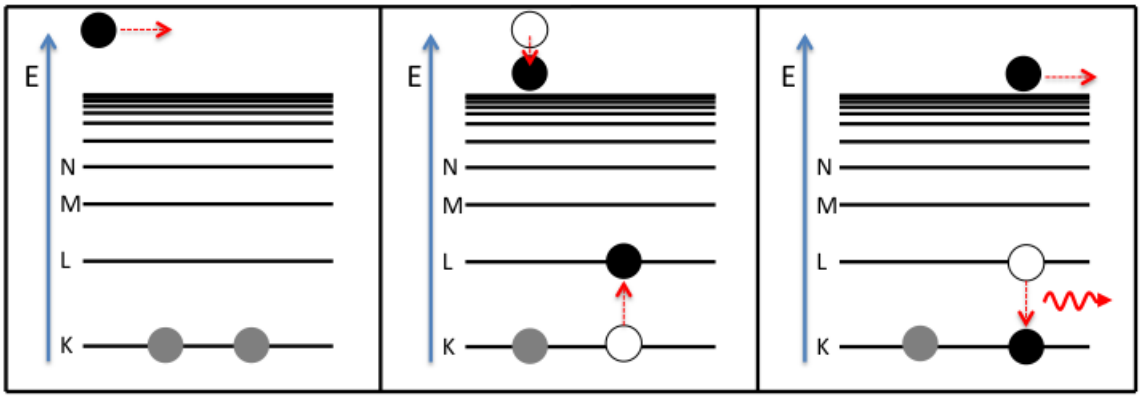

Figure C.4 Collisional excitation by electron impact.

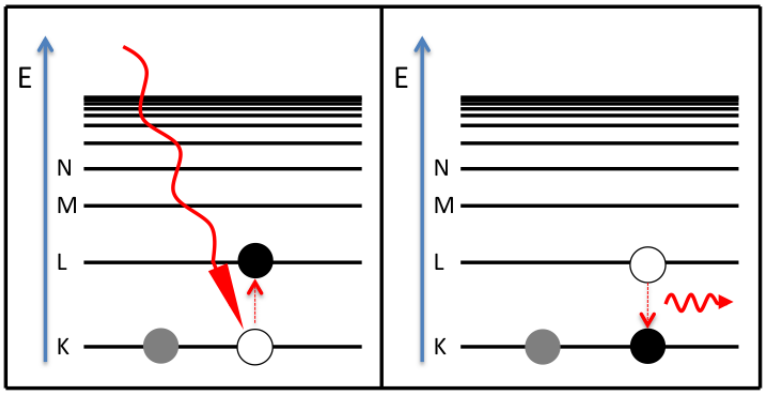

Figure C.5 Photoexcitation.

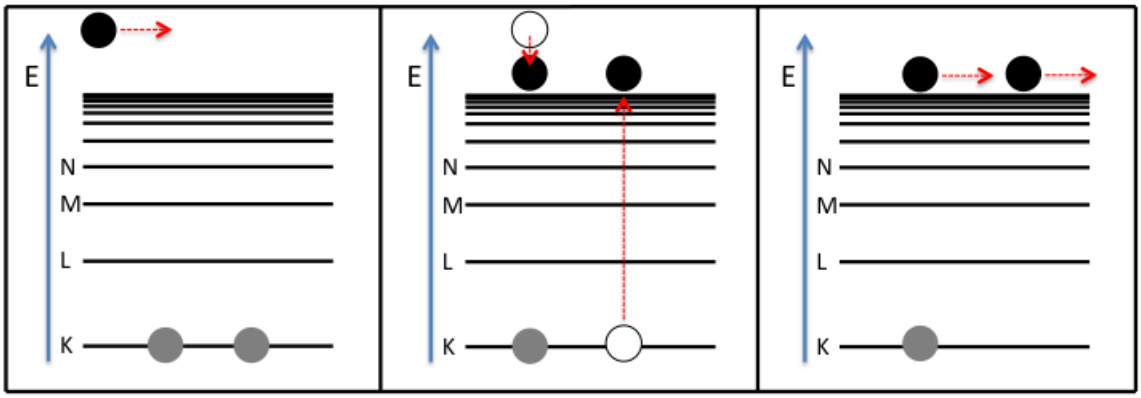

Figure C.6 Collisional ionization.

Much like excitation, electrons may be ejected from their initial subshell by a collision with an electron (Figure C.6) or stimulation by a photon (Figure C.7) in a process called ionization. The electron or photon must have energy higher than the binding energy of the electron that it ejects, and its post-collision energy is lowered by the interaction. An excited ion may also undergo autoionization (Figure C.8): the spontaneous emission of an outer-shell electron past the bound state. Auger ionization (Figure C.9) is a two-step process that involves a free electron that collisionally ionizes an inner-shell electron in the ion. A bound electron then fills the electron hole. In Auger ionization, the change in energy is transferred into another electron which gets ejected from the ion. If the change in energy instead gets released as a photon, the process is called fluorescence (Figure C.10).

Recombination is an inverse process to ionization: a free electron is captured into a bound level of an ion. In radiative recombination (Figure C.11), after electron capture, a photon is released with an energy equal to the sum of the free electron's

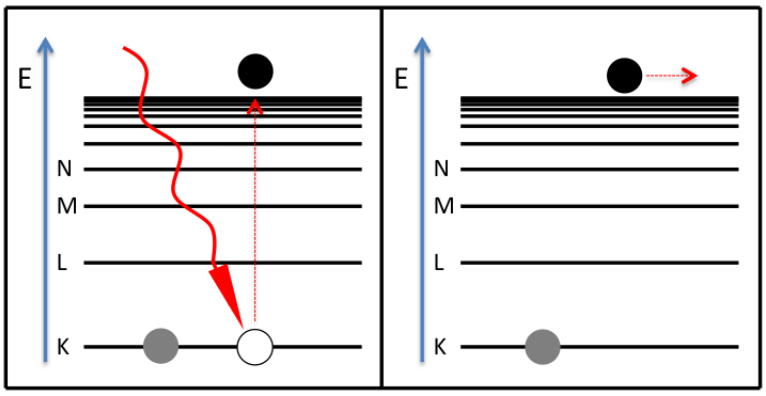

Figure C.7 Photoionization.

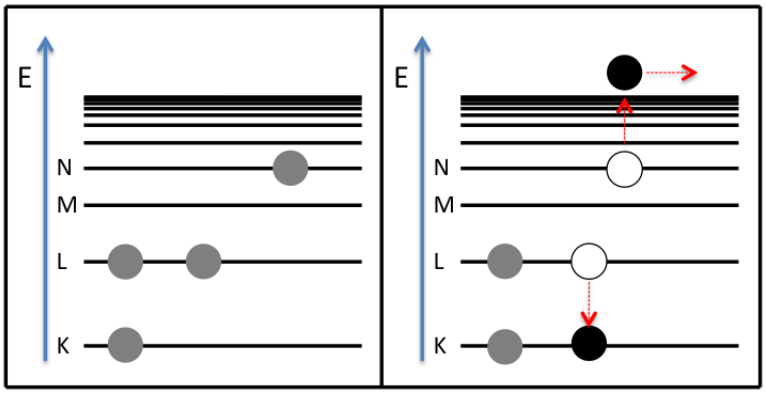

Figure C.8 Autoionization.

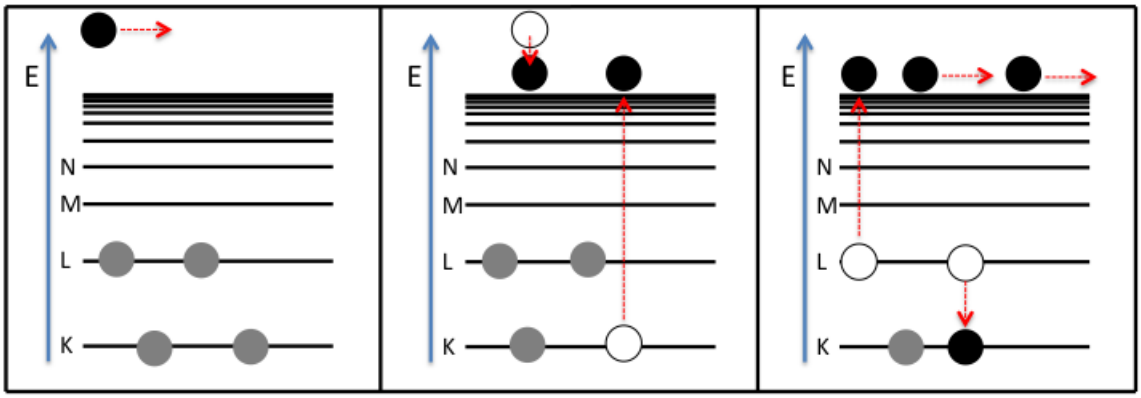

Figure C.9 Auger ionization.

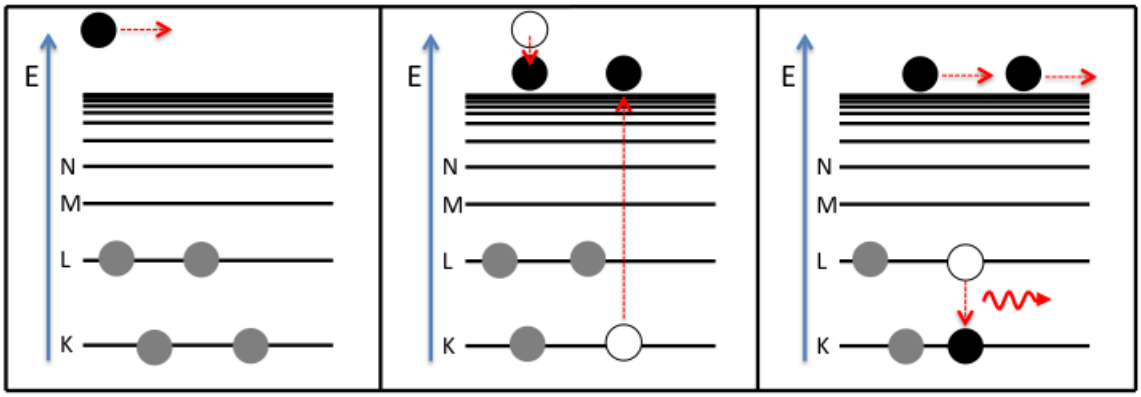

Figure C.10 X-ray fluorescence.

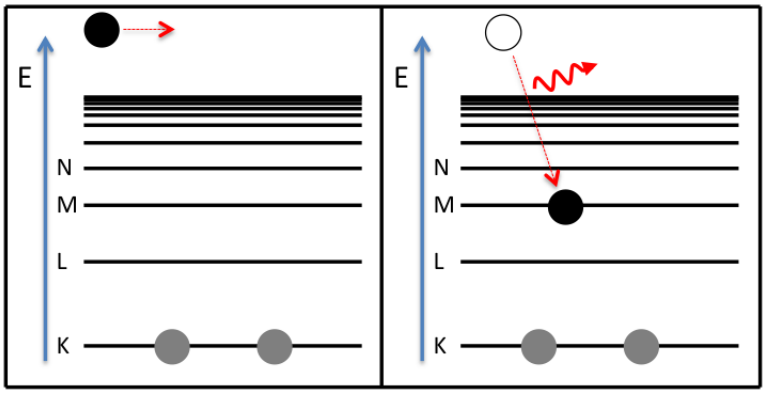

Figure C.11 Radiative recombination.

initial kinetic energy and the binding energy of the state into which it is captured. In a plasma with a distribution of free electron energies, this leads to a continuum spectrum. Dielectronic recombination (Figure C.12) is a resonant process in which the energy released during electron capture goes into simultaneously exciting a bound electron to an excited state, leading to a doubly excited ion. From here, the ion may autoionize, converting the process into an electron scattering event, or one excited electron may radiatively decay, leading to a satellite line. This satellite line will have a slightly lower energy than from a normal transition from that level due to the nearby recombined and excited electron.

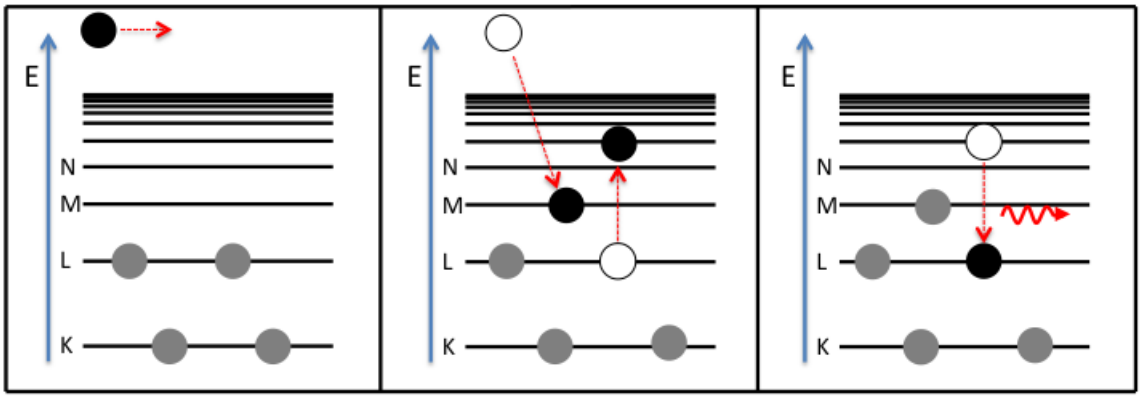

Figure C.12 Dielectronic recombination.

Bibliography

IAU colloquium no. 115: High resolution X-ray spectroscopy of cosmic plasmas. Cambridge, MA, USA, 22-25 August 1988. *COSPAR Information Bulletin*, 115: 18–18, 1989. doi: 10.1016/0045-8732(89)90127-7.

V. A. Abramov, F. F. Baryshnikov, and V. S. Lisitsa. Charge transfer between hydrogen atoms and the nuclei of multicharged ions with allowance for the degeneracy of the final states. *Soviet Journal of Experimental and Theoretical Physics*, 47:469, March 1978.

R. Abrines and I. C. Percival. Classical theory of charge transfer and ionization of hydrogen atoms by protons. *Proceedings of the Physical Society*, 88:861–872, August 1966. doi: 10.1088/0370-1328/88/4/306.

J. S. Adams, S. R. Bandler, L. E. Brown, K. R. Boyce, M. P. Chiao, W. B. Doriese, M. E. Eckart, G. C. Hilton, R. L. Kelley, C. A. Kilbourne, F. S. Porter, M. W. Rabin, S. J. Smith, D. D. Stewart, and J. N. Ullom. Real-Time Data Processing for X-Ray Spectroscopy. In B. Young, B. Cabrera, and A. Miller, editors, *American Institute of Physics Conference Series*, volume 1185 of *American Institute of Physics Conference Series*, pages 274–277, December 2009. doi: 10.1063/1.3292331.

F. A. Aharonian, H. Akamatsu, F. Akimoto, S. W. Allen, L. Angelini, K. A. Arnaud, M. Audard, H. Awaki, M. Axelsson, A. Bamba, and et al. Hitomi Constraints on the 3.5 keV Line in the Perseus Galaxy Cluster. , 837:L15, March 2017. doi: 10.3847/2041-8213/aa61fa.

R. Ali, C. L. Cocke, M. L. A. Raphaelian, and M. Stockli. Multielectron processes in 10-keV/u Ar^{q+} (5=q=17) on Ar collisions. , 49:3586–3596, May 1994. doi: 10.1103/PhysRevA.49.3586.

R. Ali, P. A. Neill, P. Beiersdorfer, C. L. Harris, M. J. Raković, J. G. Wang, D. R. Schultz, and P. C. Stancil. On the Significance of the Contribution of Multiple-Electron Capture Processes to Cometary X-Ray Emission. , 629:L125–L128, August 2005. doi: 10.1086/447768.

F. I. Allen, C. Biedermann, R. Radtke, G. Fussmann, and S. Fritzsche. Energy dependence of angular momentum capture states in charge exchange collisions between slow highly charged argon ions and argon neutrals. , 78(3):032705, September 2008. doi: 10.1103/PhysRevA.78.032705.

K. A. Arnaud. XSPEC: The First Ten Years. In G. H. Jacoby and J. Barnes, editors, *Astronomical Data Analysis Software and Systems V*, volume 101 of *Astronomical Society of the Pacific Conference Series*, page 17, 1996.

A. N. Artemyev, V. M. Shabaev, V. A. Yerokhin, G. Plunien, and G. Soff. QED calculation of the n=1 and n=2 energy levels in He-like ions. , 71(6):062104, June 2005. doi: 10.1103/PhysRevA.71.062104.

N. R. Badnell. Dielectric recombination of Fe(22+) and Fe(21+). *Journal of Physics B Atomic Molecular Physics*, 19:3827–3835, November 1986. doi: 10.1088/0022-3700/19/22/023.

S. R. Bandler, J. S. Adams, J. A. Chervenak, A. M. Datesman, M. E. Eckart, F. M. Finkbeiner, R. L. Kelley, C. A. Kilbourne, G. Betancourt-Martinez, A. R. Miniussi, F. S. Porter, J. E. Sadleir, K. Sakai, S. J. Smith, T. R. Stevenson, N. A. Wakeham, E. J. Wassell, W. Yoon, D. Becker, D. Bennett, W. B. Doriese, J. W. Fowler, J. D. Gard, G. C. Hilton, B. Mates, K. M. Morgan, C. D. Reintsema, D. Swetz, J. N. Ullom, S. Chaudhuri, K. D. Irwin, S.-J. Lee, and A. Vikhlinin. Development of x-ray microcalorimeter imaging spectrometers for the X-ray Surveyor mission concept. In *Society of Photo-Optical Instrumentation Engineers (SPIE) Conference Series*, volume 9905 of , page 99050Q, July 2016. doi: 10.1117/12.2232156.

D. Barret, J. W. den Herder, L. Piro, L. Ravera, R. Den Hartog, C. Macculi, X. Barcons, M. Page, S. Paltani, G. Rauw, J. Wilms, M. Ceballos, L. Duband, L. Gottardi, S. Lotti, J. de Plaa, E. Pointecouteau, C. Schmid, H. Akamatsu, D. Bagliani, S. Bandler, M. Barbera, P. Bastia, M. Biasotti, M. Branco, A. Camon, C. Cara, B. Cobo, L. Colasanti, J. L. Costa-Kramer, L. Corcione, W. Doriese, J. M. Duval, L. Fabrega, F. Gatti, M. de Gerone, P. Guttridge, R. Kelley, C. Kilbourne, J. van der Kuur, T. Mineo, K. Mitsuda, L. Natalucci, T. Ohashi, P. Peille, E. Perinati, C. Pigot, G. Pizzigoni, C. Pobes, F. Porter, E. Renotte, J. L. Sauvageot, S. Sciortino, G. Torrioli, L. Valenziano, D. Willingale, C. de Vries, and H. van Weers. The Hot and Energetic Universe: The X-ray Integral Field Unit (X-IFU) for Athena+. *ArXiv e-prints*, August 2013.

E. Behar, J. Cottam, and S. M. Kahn. The Chandra Iron-L X-Ray Line Spectrum of Capella. , 548:966–975, February 2001. doi: 10.1086/318999.

P. Beiersdorfer. Laboratory X-Ray Astrophysics. , 41:343–390, 2003. doi: 10.1146/annurev.astro.41.011802.094825.

P. Beiersdorfer. A "brief" history of spectroscopy on EBIT. *Canadian Journal of Physics*, 86:1–10, 2008. doi: 10.1139/P07-135.

P. Beiersdorfer, T. W. Phillips, K. L. Wong, R. E. Marrs, and D. A. Vogel. Measurement of level-specific dielectronic-recombination cross sections of heliumlike Fe xxv. , 46:3812–3820, October 1992. doi: 10.1103/PhysRevA.46.3812.

P. Beiersdorfer, A. L. Osterheld, V. Decaux, and K. Widmann. Observation of Lifetime-Limited X-Ray Linewidths in Cold Highly Charged Ions. *Physical Review Letters*, 77:5353–5356, December 1996a. doi: 10.1103/PhysRevLett.77.5353.

P. Beiersdorfer, L. Schweikhard, J. C. López-Urrutia, and K. Widmann. The magnetic trapping mode of an electron beam ion trap: New opportunities for highly charged ion research. *Review of Scientific Instruments*, 67:3818–3826, November 1996b. doi: 10.1063/1.1147276.

P. Beiersdorfer, R. E. Olson, G. V. Brown, H. Chen, C. L. Harris, P. A. Neill, L. Schweikhard, S. B. Utter, and K. Widmann. X-Ray Emission Following Low-Energy Charge Exchange Collisions of Highly Charged Ions. *Physical Review Letters*, 85:5090–5093, December 2000a. doi: 10.1103/PhysRevLett.85.5090.

P. Beiersdorfer, R. E. Olson, L. Schweikhard, P. Liebisch, G. V. Brown, J. C. López-Urrutia, C. L. Harris, P. A. Neill, S. B. Utter, and K. Widmann. X-ray signatures of charge transfer reactions involving cold, very highly charged ions. In *American Institute of Physics Conference Series*, volume 500 of *American Institute of Physics Conference Series*, pages 626–635, February 2000b. doi: 10.1063/1.1302692.

P. Beiersdorfer, C. M. Lisse, R. E. Olson, G. V. Brown, and H. Chen. X-Ray Velocimetry of Solar Wind Ion Impact on Comets. , 549:L147–L150, March 2001. doi: 10.1086/319143.

P. Beiersdorfer, E. Behar, K. R. Boyce, G. V. Brown, H. Chen, K. C. Gendreau, A. Graf, M.-F. Gu, C. L. Harris, S. M. Kahn, R. L. Kelley, J. K. Lepson, M. J. May, P. A. Neill, E. H. Pinnington, F. S. Porter, A. J. Smith, C. K. Stahle, A. E. Szymkowiak, A. Tillotson, D. B. Thorn, E. Träbert, and B. J. Wargelin. Overview of the Livermore electron beam ion trap project. *Nuclear Instruments and Methods in Physics Research B*, 205:173–177, May 2003a. doi: 10.1016/S0168-583X(03)00941-8.

P. Beiersdorfer, K. R. Boyce, G. V. Brown, H. Chen, S. M. Kahn, R. L. Kelley, M. May, R. E. Olson, F. S. Porter, C. K. Stahle, and W. A. Tillotson. Laboratory Simulation of Charge Exchange-Produced X-ray Emission from Comets. *Science*, 300:1558–1560, June 2003b. doi: 10.1126/science.1084373.

P. Beiersdorfer, M. Bitter, M. Marion, and R. E. Olson. Charge-exchange-produced K -shell x-ray emission from Ar^{16+} in a tokamak plasma with neutral-beam injection. , 72(3):032725, September 2005. doi: 10.1103/PhysRevA.72.032725.

P. Beiersdorfer, L. Schweikhard, P. Liebisch, and G. V. Brown. X-Ray Signature of Charge Exchange in the Spectra of L-Shell Iron Ions. , 672:726-732, January 2008. doi: 10.1086/522617.

D. A. Bennett, R. D. Horansky, D. R. Schmidt, A. S. Hoover, R. Winkler, B. K. Alpert, J. A. Beall, W. B. Doriese, J. W. Fowler, C. P. Fitzgerald, G. C. Hilton, K. D. Irwin, V. Kotsubo, J. A. B. Mates, G. C. O'Neil, M. W. Rabin, C. D. Reintsema, F. J. Schima, D. S. Swetz, L. R. Vale, and J. N. Ullom. A high resolution gamma-ray spectrometer based on superconducting microcalorimeters. *Review of Scientific Instruments*, 83(9):093113, September 2012. doi: 10.1063/1.4754630.

G. Betancourt-Martinez, F. S. Porter, M. A. Leutenegger, G. V. Brown, and P. Beiersdorfer. Benchmarking Charge Exchange Theory with Experiments Using an X-ray Calorimeter at an Electron Beam Ion Trap. In *American Astronomical Society Meeting Abstracts #223*, volume 223 of *American Astronomical Society Meeting Abstracts*, page 232.02, January 2014a.

G. Betancourt-Martinez, P. Beiersdorfer, G. Brown, N. Hell, M. A. Leutenegger, F. S. Porter, and C. S. Reynolds. Charge Exchange, from the Laboratory to Galaxy Clusters. In *AAS/High Energy Astrophysics Division*, volume 15 of *AAS/High Energy Astrophysics Division*, page 115.01, April 2016.

G. L. Betancourt-Martinez, J. Adams, S. Bandler, P. Beiersdorfer, G. Brown, J. Chervenak, R. Doriese, M. Eckart, K. Irwin, R. Kelley, C. Kilbourne, M. Leutenegger, F. S. Porter, C. Reintsema, S. Smith, and J. Ullom. The transition-edge EBIT microcalorimeter spectrometer. In *Space Telescopes and Instrumentation 2014: Ultraviolet to Gamma Ray*, volume 9144 of , page 91443U, July 2014b. doi: 10.1117/12.2055568.

G. L. Betancourt-Martinez, P. Beiersdorfer, G. V. Brown, R. L. Kelley, C. A. Kilbourne, D. Koutroumpa, M. A. Leutenegger, and F. S. Porter. Observation of highly disparate K -shell x-ray spectra produced by charge exchange with bare mid-Z ions. , 90(5):052723, November 2014c. doi: 10.1103/PhysRevA.90.052723.

A. Bhardwaj, R. F. Elsner, G. Randall Gladstone, T. E. Cravens, C. M. Lisse, K. Dennerl, G. Branduardi-Raymont, B. J. Wargelin, J. Hunter Waite, I. Robertson, N. Østgaard, P. Beiersdorfer, S. L. Snowden, and V. Kharchenko. X-rays from solar system objects. , 55:1135–1189, June 2007. doi: 10.1016/j.pss.2006.11.009.

R. Bingham, J. M. Dawson, V. D. Shapiro, D. A. Mendis, and B. J. Kellet. Generation of X-rays from c/Hyakutake 1996 B2. *Science*, 275:49–51, 1997. doi: 10.1126/science.275.5296.49.

F. W. Bliek, G. R. Woestenenk, R. Hoekstra, and R. Morgenstern. State-selective electron-capture measurements for N^{4+}-H and N^{4+}-H_2 collisions. , 57:221–226, January 1998. doi: 10.1103/PhysRevA.57.221.

D. Bodewits. *Cometary X-rays. Solar wind charge exchange in cometary atmospheres*. PhD thesis, University of Groningen, P.O. Box 72, 9700 AB Groningen, The Netherlands, June 2007.

D. Bodewits, D. J. Christian, M. Torney, M. Dryer, C. M. Lisse, K. Dennerl, T. H. Zurbuchen, S. J. Wolk, A. G. G. M. Tielens, and R. Hoekstra. Spectral analysis of the Chandra comet survey. , 469:1183–1195, July 2007. doi: 10.1051/0004-6361:20077410.

A. Boyarsky, O. Ruchayskiy, D. Iakubovskyi, and J. Franse. Unidentified Line in X-Ray Spectra of the Andromeda Galaxy and Perseus Galaxy Cluster. *Physical Review Letters*, 113(25):251301, December 2014. doi: 10.1103/PhysRevLett.113.251301.

G. Branduardi-Raymont, A. Bhardwaj, R. F. Elsner, G. R. Gladstone, G. Ramsay, P. Rodriguez, R. Soria, J. H. Waite, Jr., and T. E. Cravens. A study of Jupiter's aurorae with XMM-Newton. , 463:761–774, February 2007. doi: 10.1051/0004-6361:20066406.

G. V. Brown. *Spectroscopy of Fe L-shell line emission from Fe XVII- XXIV in the 10–18 A wavelength band*. PhD thesis, AUBURN UNIVERSITY, 2000.

G. V. Brown, P. Beiersdorfer, D. A. Liedahl, K. Widmann, S. M. Kahn, and E. J. Clothiaux. Laboratory Measurements and Identification of the Fe XVIII-XXIV L-Shell X-Ray Line Emission. , 140:589–607, June 2002. doi: 10.1086/339374.

G. V. Brown, P. Beiersdorfer, H. Chen, J. H. Scofield, K. R. Boyce, R. L. Kelley, C. A. Kilbourne, F. S. Porter, M. F. Gu, S. M. Kahn, and A. E. Szymkowiak. Energy-Dependent Excitation Cross Section Measurements of the Diagnostic Lines of Fe XVII. *Physical Review Letters*, 96(25):253201, June 2006. doi: 10.1103/PhysRevLett.96.253201.

H. Bruhns, H. Kreckel, D. W. Savin, D. G. Seely, and C. C. Havener. Low-energy charge transfer for collisions of Si^{3+} with atomic hydrogen. , 77(6):064702, June 2008. doi: 10.1103/PhysRevA.77.064702.

E. Bulbul, M. Markevitch, A. Foster, R. K. Smith, M. Loewenstein, and S. W. Randall. Detection of an Unidentified Emission Line in the Stacked X-Ray Spectrum of Galaxy Clusters. , 789:13, July 2014. doi: 10.1088/0004-637X/789/1/13.

E. J. Bunce, S. W. H. Cowley, and T. K. Yeoman. Jovian cusp processes: Implications for the polar aurora. *Journal of Geophysical Research (Space Physics)*, 109:A09S13, September 2004. doi: 10.1029/2003JA010280.

R. W. Bussard, R. Ramaty, and K. Omidvar. X-ray and gamma-ray line production by nonthermal ions. , 220:353–362, February 1978. doi: 10.1086/155913.

S. E. Butler and A. Dalgarno. Charge transfer of multiply charged ions with hydrogen and helium Landau-Zener calculations. , 241:838–843, October 1980. doi: 10.1086/158395.

I Cadez, J B Greenwood, J Lozano, R J Mawhorter, M Niimura, S J Smith, and A Chutjian. Absolute cross sections for single and double charge-exchange in fe q + impacting on he. *Journal of Physics B: Atomic, Molecular and Optical Physics*, 36(15):3303, 2003.

N. D. Cariatore and S. Otranto. Development and evaluation of a many-electron˘multicenter classical-trajectory monte carlo model in charge-exchange processes involving collisions of multiply charged ions and co. *Phys. Rev. A*, 88: 012714, Jul 2013. doi: 10.1103/PhysRevA.88.012714. URL https://link.aps.org/doi/10.1103/PhysRevA.88.012714.

P. G. Carolan, B. P. Duval, A. R. Field, S. J. Fielding, N. C. Hawkes, N. J. Peacock, G. Fussmann, G. Janeschitz, J. Hofmann, K. H. Behringer, and R. C. Isler. Charge-exchange-excited line radiation in a tokamak (asdex) with neutral-particle-beam injection. *Phys. Rev. A*, 35:3454–3471, Apr 1987. doi: 10.1103/PhysRevA.35.3454.

W. Cash. Parameter estimation in astronomy through application of the likelihood ratio. , 228:939–947, March 1979. doi: 10.1086/156922.

J. W. Chamberlain. Excitation in Nebulae: Charge Transfer and the Cassiopeia Radio Source. , 124:390, September 1956. doi: 10.1086/146233.

H. Chen, M. F. Gu, P. Beiersdorfer, K. R. Boyce, G. V. Brown, S. M. Kahn, R. L. Kelley, C. A. Kilbourne, F. S. Porter, and J. H. Scofield. Electron Impact Excitation Cross Section Measurement for n = 3 to n = 2 Line Emission in Fe^{17+} to Fe^{23+}. , 646:653–665, July 2006. doi: 10.1086/504708.

H. Chen, M. F. Gu, E. Behar, G. V. Brown, S. M. Kahn, and P. Beiersdorfer. Laboratory Measurements of High-n Iron L-Shell X-Ray Lines. , 168:319–336, February 2007. doi: 10.1086/510124.

R. B. Christensen, W. D. Watson, and R. J. Blint. Calculation of the Cross Section for N iv-H Charge-Exchange Significance for the Intercloud Gas. , 213:712–715, May 1977. doi: 10.1086/155201.

D. J. Christian, D. Bodewits, C. M. Lisse, K. Dennerl, S. J. Wolk, H. Hsieh, T. H. Zurbuchen, and L. Zhao. Chandra Observations of Comets 8p/Tuttle and 17p/Holmes During Solar Minimum. , 187:447–459, April 2010. doi: 10.1088/0067-0049/187/2/447.

John Clarke and Alex I. Braginski. *The SQUID Handbook Fundamentals and Technology of SQUIDs and SQUID Systems*, volume 1. Wiley-VCH, Weinheim, 2006. URL http://public.eblib.com/EBLPublic/PublicView.do?ptiID=481572.

Hitomi Collaboration. The quiescent intracluster medium in the core of the Perseus cluster. , 535:117–121, July 2016. doi: 10.1038/nature18627.

J. Cottam, K. R. Boyce, G. V. Brown, R. Fujimoto, T. Furusho, Y. Ishisaki, R. L. Kelley, C. A. Kilbourne, D. McCammon, K. Mitsuda, U. Morita, F. S. Porter, T. Saab, Y. Takai, and M. Yamamoto. The XRS Microcalorimeter on Astro-E2. In R. Smith, editor, *X-ray Diagnostics of Astrophysical Plasmas: Theory, Experiment, and Observation*, volume 774 of *American Institute of Physics Conference Series*, pages 379–382, June 2005. doi: 10.1063/1.1960957.

Robert Duane Cowan. *The Theory of Atomic Structure and Spectra*. Los Alamos Series in Basic and Applied Sciences. University of California Press, Ltd., Berkeley, 1981.

D. P. Cox. Modeling the Local Bubble. In D. Breitschwerdt, M. J. Freyberg, and J. Truemper, editors, *IAU Colloq. 166: The Local Bubble and Beyond*, volume 506 of *Lecture Notes in Physics, Berlin Springer Verlag*, pages 121–131, 1998. doi: 10.1007/BFb0104706.

D. P. Cox and P. R. Anderson. Extended adiabatic blast waves and a model of the soft X-ray background. , 253:268–289, February 1982. doi: 10.1086/159632.

D. H. Crandall, R. A. Phaneuf, and F. W. Meyer. Electron capture by slow multicharged ions in atomic and molecular hydrogen. , 19:504–514, February 1979. doi: 10.1103/PhysRevA.19.504.

T. E. Cravens. Comet Hyakutake x-ray source: Charge transfer of solar wind heavy ions. , 24:105–108, 1997. doi: 10.1029/96GL03780.

T. E. Cravens. Heliospheric X-ray Emission Associated with Charge Transfer of the Solar Wind with Interstellar Neutrals. , 532:L153–L156, April 2000. doi: 10.1086/312574.

T. E. Cravens. X-ray Emission from Comets. *Science*, 296:1042–1046, May 2002. doi: 10.1126/science.1070001.

T. E. Cravens, I. P. Robertson, and S. L. Snowden. Temporal variations of geocoronal and heliospheric X-ray emission associated with the solar wind interaction with neutrals. , 106:24883–24892, November 2001. doi: 10.1029/2000JA000461.

T. E. Cravens, J. H. Waite, T. I. Gombosi, N. Lugaz, G. R. Gladstone, B. H. Mauk, and R. J. MacDowall. Implications of Jovian X-ray emission for magnetosphere-ionosphere coupling. *Journal of Geophysical Research (Space Physics)*, 108:1465, December 2003. doi: 10.1029/2003JA010050.

R. S. Cumbee, D. B. Henley, P. C. Stancil, R. L. Shelton, J. L. Nolte, Y. Wu, and D. R. Schultz. Can Charge Exchange Explain Anomalous Soft X-Ray Emission in the Cygnus Loop? , 787:L31, June 2014. doi: 10.1088/2041-8205/787/2/L31.

Renata S. Cumbee. *Highly-Charged Ion Collisions with Atoms: Applications to X-ray Emission in the Universe*. Phd, University of Georgia, Athens, Georgia, August 2016.

P. A. J. de Korte, J. Beyer, S. Deiker, G. C. Hilton, K. D. Irwin, M. MacIntosh, S. W. Nam, C. D. Reintsema, L. R. Vale, and M. E. Huber. Time-division superconducting quantum interference device multiplexer for transition-edge sensors. *Review of Scientific Instruments*, 74:3807–3815, August 2003. doi: 10.1063/1.1593809.

K. Dennerl. Discovery of X-rays from Mars with Chandra. , 394:1119–1128, November 2002. doi: 10.1051/0004-6361:20021116.

K. Dennerl. X-rays from Venus observed with Chandra. , 56:1414–1423, August 2008. doi: 10.1016/j.pss.2008.03.008.

K. Dennerl, V. Burwitz, J. Englhauser, C. Lisse, and S. Wolk. Discovery of X-rays from Venus with Chandra. , 386:319–330, April 2002. doi: 10.1051/0004-6361:20020097.

K. Dennerl, B. Aschenbach, V. Burwitz, J. Englhauser, C. M. Lisse, and P. M. Rodriguez-Pascual. A major step in understanding the X-ray generation in comets: recent progress obtained with XMM-Newton. In J. E. Truemper and H. D. Tananbaum, editors, *X-Ray and Gamma-Ray Telescopes and Instruments for Astronomy.*, volume 4851 of , pages 277–288, March 2003. doi: 10.1117/12.461137.

K. Dennerl, C. M. Lisse, A. Bhardwaj, V. Burwitz, J. Englhauser, H. Gunell, M. Holmström, F. Jansen, V. Kharchenko, and P. M. Rodríguez-Pascual. First observation of Mars with XMM-Newton. High resolution X-ray spectroscopy with RGS. , 451:709–722, May 2006. doi: 10.1051/0004-6361:20054253.

K. Dennerl, C. M. Lisse, A. Bhardwaj, D. J. Christian, S. J. Wolk, D. Bodewits, T. H. Zurbuchen, M. Combi, and S. Lepri. Solar system X-rays from charge exchange processes. *Astronomische Nachrichten*, 333:324, April 2012. doi: 10.1002/asna.201211663.

D. Dijkkamp, D. Ciric, A. de Boer, F. J. de Heer, and E. Vlieg. Subshell-selective electron capture in collisions of C(4+), N(5+), O(6+) with H, H2 and He. *Journal of Physics B Atomic Molecular Physics*, 18:4763–4793, December 1985. doi: 10.1088/0022-3700/18/24/017.

N. Djurić, S. J. Smith, J. Simcic, and A. Chutjian. Absolute Single and Multiple Charge Exchange Cross Sections for Highly Charged C, N, and O Ions Colliding with CH_4. , 679:1661–1664, June 2008. doi: 10.1086/587782.

W. B. Doriese, P. Abbamonte, B. K. Alpert, D. A. Bennett, E. V. Denison, Y. Fang, D. A. Fischer, C. P. Fitzgerald, J. W. Fowler, J. D. Gard, J. P. Hays-Wehle, G. C. Hilton, C. Jaye, J. L. McChesney, L. Miaja-Avila, K. M. Morgan, Y. I. Joe, G. C. O'Neil, C. D. Reintsema, F. Rodolakis, D. R. Schmidt, H. Tatsuno,

J. Uhlig, L. R. Vale, J. N. Ullom, and D. S. Swetz. A practical superconducting-microcalorimeter X-ray spectrometer for beamline and laboratory science. *Review of Scientific Instruments*, 88(5):053108, May 2017. doi: 10.1063/1.4983316.

K. Ebisawa, Y. Maeda, H. Kaneda, and S. Yamauchi. Origin of the Hard X-ray Emission from the Galactic Plane. *Science*, 293:1633–1635, August 2001. doi: 10.1126/science.1063529.

M. E. Eckart, J. S. Adams, K. R. Boyce, G. V. Brown, M. P. Chiao, R. Fujimoto, D. Haas, J. W. den Herder, Y. Ishisaki, R. L. Kelley, C. A. Kilbourne, M. A. Leutenegger, D. McCammon, K. Mitsuda, F. S. Porter, K. Sato, M. Sawada, H. Seta, G. A. Sneiderman, A. E. Szymkowiak, Y. Takei, M. Tashiro, M. Tsujimoto, C. P. de Vries, T. Watanabe, S. Yamada, and N. Y. Yamasaki. Ground calibration of the Astro-H (Hitomi) soft x-ray spectrometer. In *Space Telescopes and Instrumentation 2016: Ultraviolet to Gamma Ray*, volume 9905 of , page 99053W, July 2016. doi: 10.1117/12.2233053.

T. Ehrenreich, K. Miller, P. Gee, Q. Kessel, E. Pollack, W. W. Smith, N. Djuric, J. Lozano, S. J. Smith, and A. Chutjian. Soft X-ray and Optical Laboratory Spectra to Simulate the Solar Wind on Comets: O^{5+} + CO. In R. Smith, editor, *X-ray Diagnostics of Astrophysical Plasmas: Theory, Experiment, and Observation*, volume 774 of *American Institute of Physics Conference Series*, pages 281–283, June 2005. doi: 10.1063/1.1960939.

Jrg Eichler. Chapter 2 - low-energy collisions: Basis expansions. In Jrg Eichler, editor, *Lectures on Ion-Atom Collisions*, North-Holland Personal Library, pages 15 – 43. Elsevier Science, Amsterdam, 2005. doi: https://doi.org/10.1016/B978-044452047-0/50003-6. URL http://www.sciencedirect.com/science/article/pii/B9780444520470500036.

R. F. Elsner, N. Lugaz, J. H. Waite, T. E. Cravens, G. R. Gladstone, P. Ford, D. Grodent, A. Bhardwaj, R. J. MacDowall, M. D. Desch, and T. Majeed. Simultaneous Chandra X ray, Hubble Space Telescope ultraviolet, and Ulysses radio observations of Jupiter's aurora. *Journal of Geophysical Research (Space Physics)*, 110:A01207, January 2005. doi: 10.1029/2004JA010717.

C. Enss. *Cryogenic Particle Detection*. 2005. doi: 10.1007/b12169.

E. Figueroa Feliciano. *Theory and development of position-sensitive quantum calorimeters*. PhD thesis, Stanford University, 2001.

L. Folkerts, M. A. Haque, C. C. Havener, N. Shimakura, and M. Kimura. Low-energy electron capture by N^{4+} ions from H atoms: Experimental study using merged beams and theoretical analysis by molecular representation. , 51:3685–3692, May 1995. doi: 10.1103/PhysRevA.51.3685.

R. J. Fonck and R. A. Hulse. he^{++}. *Phys. Rev. Lett.*, 52:530–533, Feb 1984. doi: 10.1103/PhysRevLett.52.530. URL https://link.aps.org/doi/10.1103/PhysRevLett.52.530.

R. J. Fonck, M. Finkenthal, R. J. Goldston, D. L. Herndon, R. A. Hulse, R. Kaita, and D. D. Meyerhofer. Spatially resolved measurements of fully ionized low-z impurities in the pdx tokamak. *Phys. Rev. Lett.*, 49:737–740, Sep 1982. doi: 10.1103/PhysRevLett.49.737. URL https://link.aps.org/doi/10.1103/PhysRevLett.49.737.

A. R. Foster, R. K. Smith, L. Ji, and N. S. Brickhouse. AtomDB v2.0: Atomic Data for X-ray Astrophysics. In *2010 NASA Laboratory Astrophysics Workshop*, page C2, May 2011.

M. Frankel, P. Beiersdorfer, G. V. Brown, J. Clementson, M. F. Gu, and L. Schweikhard. X-ray signatures of charge exchange in L-shell iron and sulfur. In *Journal of Physics Conference Series*, volume 163 of *Journal of Physics Conference Series*, page 012051, April 2009a. doi: 10.1088/1742-6596/163/1/012051.

M. Frankel, P. Beiersdorfer, G. V. Brown, M. F. Gu, R. L. Kelley, C. A. Kilbourne, and F. S. Porter. X-ray Signature of Charge Exchange in L-shell Sulfur Ions. , 702:171–177, September 2009b. doi: 10.1088/0004-637X/702/1/171.

W. Fritsch and C. D. Lin. The semiclassical close-coupling description of atomic collisions: Recent developments and results. , 202:1–97, April 1991. doi: 10.1016/0370-1573(91)90008-A.

R. Fujimoto, K. Mitsuda, D. Mccammon, Y. Takei, M. Bauer, Y. Ishisaki, S. F. Porter, H. Yamaguchi, K. Hayashida, and N. Y. Yamasaki. Evidence for Solar-Wind Charge-Exchange X-Ray Emission from the Earth's Magnetosheath. , 59: 133–140, January 2007. doi: 10.1093/pasj/59.sp1.S133.

A. H. Gabriel and C. Jordan. Interpretation of solar helium-like ion line intensities. , 145:241, 1969.

G. Gabrielse, P. Larochelle, D. Le Sage, B. Levitt, W. S. Kolthammer, I. Kuljanishvili, R. McConnell, J. Wrubel, F. M. Esser, H. Glückler, D. Grzonka, G. Hansen, S. Martin, W. Oelert, J. Schillings, M. Schmitt, T. Sefzick, H. Soltner, Z. Zhang, D. Comeau, M. C. George, E. A. Hessels, C. H. Storry, M. Weel, A. Speck, F. Nillius, J. Walz, and T. W. Hänsch. Antiproton confinement in a penning-ioffe trap for antihydrogen. *Phys. Rev. Lett.*, 98:113002, Mar 2007. doi: 10.1103/PhysRevLett.98.113002.

M. Galeazzi, M. Chiao, M. R. Collier, T. Cravens, D. Koutroumpa, K. D. Kuntz, R. Lallement, S. T. Lepri, D. McCammon, K. Morgan, F. S. Porter, I. P. Robertson, S. L. Snowden, N. E. Thomas, Y. Uprety, E. Ursino, and B. M. Walsh. The origin of the local 1/4-keV X-ray flux in both charge exchange and a hot bubble. , 512:171–173, August 2014. doi: 10.1038/nature13525.

N. Gehrels. Confidence limits for small numbers of events in astrophysical data. , 303:336–346, April 1986. doi: 10.1086/164079.

H. B. Gilbody. Measurements of Charge Transfer and Ionization in Collisions Involving Hydrogen Atoms. *Advances in Atomic and Molecular Physics*, 22:143–195, 1986. doi: 10.1016/S0065-2199(08)60336-X.

G. R. Gladstone, J. H. Waite, D. Grodent, W. S. Lewis, F. J. Crary, R. F. Elsner, M. C. Weisskopf, T. Majeed, J.-M. Jahn, A. Bhardwaj, J. T. Clarke, D. T. Young, M. K. Dougherty, S. A. Espinosa, and T. E. Cravens. A pulsating auroral X-ray hot spot on Jupiter. , 415:1000–1003, February 2002. doi: 10.1038/4151000a.

A. Graf, P. Beiersdorfer, G. V. Brown, and M. F. Gu. Measurement and Modeling of Na-Like Fe XVI Inner-Shell Satellites Between 14.5 Å and 18 Å. , 695:818–824, April 2009. doi: 10.1088/0004-637X/695/2/818.

J. B. Greenwood, I. D. Williams, S. J. Smith, and A. Chutjian. Experimental investigation of the processes determining x-ray emission intensities from charge-exchange collisions. *Phys. Rev. A*, 63:062707, May 2001. doi: 10.1103/PhysRevA.63.062707.

J. B. Greenwood, R. J. Mawhorter, I. Cadez, J. Lozano, S. J. Smith, and A. Chutjian. The Contribution of Charge Exchange to Extreme Ultra-Violet and X-ray Astronomy. *Physica Scripta Volume T*, 110:358, 2004. doi: 10.1238/Physica.Topical.110a00358.

L. Gu, J. Kaastra, A. J. J. Raassen, P. D. Mullen, R. S. Cumbee, D. Lyons, and P. C. Stancil. A novel scenario for the possible X-ray line feature at ˜3.5 keV. Charge exchange with bare sulfur ions. , 584:L11, December 2015. doi: 10.1051/0004-6361/201527634.

L. Gu, J. Kaastra, and A. J. J. Raassen. Plasma code for astrophysical charge exchange emission at X-ray wavelengths. , 588:A52, April 2016. doi: 10.1051/0004-6361/201527615.

M. F. Gu. *Experimental studies of X-ray line formation in iron L-shell ions: Resonant processes and direct excitation*. PhD thesis, Columbia University, 2000.

M. F. Gu. The flexible atomic code. *Canadian Journal of Physics*, 86:675–689, 2008. doi: 10.1139/P07-197.

M. F. Gu, P. Beiersdorfer, G. V. Brown, H. Chen, D. B. Thorn, and S. M. Kahn. Wavelength Measurements of Ni L-Shell Lines between 9 and 15 Å. , 657:1172–1177, March 2007a. doi: 10.1086/511065.

M. F. Gu, H. Chen, G. V. Brown, P. Beiersdorfer, and S. M. Kahn. Laboratory Measurements of 3–2 X-Ray Line Ratios of F-like Fe XVIII and Ni XX. , 670:1504–1509, December 2007b. doi: 10.1086/522078.

M. Güdel and Y. Nazé. X-ray spectroscopy of stars. , 17:309–408, September 2009. doi: 10.1007/s00159-009-0022-4.

H. Gunell, M. Holmström, E. Kallio, P. Janhunen, and K. Dennerl. X rays from solar wind charge exchange at Mars: A comparison of simulations and observations. , 31:L22801, November 2004. doi: 10.1029/2004GL020953.

R. M. Haberli, T. I. Gombosi, D. L. DeZeeuw, M. R. Combi, and K. G. Powell. Modeling of Cometary X-rays Caused by Solar Wind Minor Ions. *Science*, 276: 939–942, May 1997. doi: 10.1126/science.276.5314.939.

A. A. Hasan, F. Eissa, R. Ali, D. R. Schultz, and P. C. Stancil. State-selective Charge Transfer Studies Relevant to Solar Wind-Comet Interactions. , 560:L201–L205, October 2001. doi: 10.1086/324058.

B. He, J. G. Wang, and R. K. Janev. Charge exchange, excitation, and ionization in $A^{Z+} + \mathrm{H}(1s)$ collisions in strong magnetic fields. *Phys. Rev. A*, 79:012706, Jan 2009. doi: 10.1103/PhysRevA.79.012706. URL https://link.aps.org/doi/10.1103/PhysRevA.79.012706.

N. Hell. *Benchmarking transition energies and emission strengths for X-ray astrophysics with measurements at the Livermore EBITs*. PhD thesis, Dr. Karl Remeis-Sternwarte, Astronomisches Institut der Universität Erlangen-Nürnberg, Sternwartstr. 7, 96049 Bamberg, Germany, March 2017.

B. L. Henke, E. M. Gullikson, and J. C. Davis. X-Ray Interactions: Photoabsorption, Scattering, Transmission, and Reflection at E = 50-30,000 eV, Z = 1-92. *Atomic Data and Nuclear Data Tables*, 54:181–342, July 1993. doi: 10.1006/adnd.1993.1013.

D. Henley and R. L. Shelton. Suzaku Observations Of The Soft X-ray Background. In *American Astronomical Society Meeting Abstracts #210*, volume 39 of *Bulletin of the American Astronomical Society*, page 121, May 2007.

R. C. Hickox and M. Markevitch. Absolute Measurement of the Unresolved Cosmic X-Ray Background in the 0.5-8 keV Band with Chandra. , 645:95–114, July 2006. doi: 10.1086/504070.

S. Ibadov. On the efficiency of X-ray generation in impacts of cometary and zodiacal dust particles. , 86:283–288, July 1990. doi: 10.1016/0019-1035(90)90217-W.

K. Igenbergs, J. Schweinzer, A. Veiter, L. Perneczky, E. Frühwirth, M. Wallerberger, R. E. Olson, and F. Aumayr. Charge exchange and ionization in N^{7+}-, N^{6+}-, C^{6+}-H(n = 1, 2) collisions studied systematically by theoretical approaches. *Journal of Physics B Atomic Molecular Physics*, 45(6):065203, March 2012. doi: 10.1088/0953-4075/45/6/065203.

K. D. Irwin. SQUID multiplexers for transition-edge sensors. *Physica C Superconductivity*, 368:203–210, March 2002. doi: 10.1016/S0921-4534(01)01167-4.

Y. Ishisaki, S. Yamada, H. Seta, M. S. Tashiro, S. Takeda, Y. Terada, Y. Kato, M. Tsujimoto, S. Koyama, K. MItsuda, M. Sawada, K. R. Boyce, M. P. Chiao, T. Watanabe, M. A. Leutenegger, M. E. Eckart, F. S. Porter, C. A. Kilbourne, and R. L. Kelley. In-flight performance of pulse processing system of the ASTRO-H soft x-ray spectrometer. In *Space Telescopes and Instrumentation 2016: Ultraviolet to Gamma Ray*, volume 9905 of , page 99053T, July 2016. doi: 10.1117/12.2234222.

R. C. Isler. Observation of the reaction H/0/ + O/8+/ yields H/+//O/7+///excited/ during neutral-beam injection into ORMAK. *Physical Review Letters*, 38:1359–1362, June 1977. doi: 10.1103/PhysRevLett.38.1359.

R C Isler. An overview of charge-exchange spectroscopy as a plasma diagnostic. *Plasma Physics and Controlled Fusion*, 36(2):171, 1994.

N. D. James. Comet C/1996 B2 (Hyakutake): The Great Comet of 1996. *Journal of the British Astronomical Association*, 108:157–171, June 1998.

R. K. Janev. Excited states created in charge transfer collisions between atoms and highly charged ions. *Physica Scripta Volume T*, 3:208–221, January 1983. doi: 10.1088/0031-8949/1983/T3/041.

R. K. Janev and L. P. Presnyakov. Collision processes of multiply charged ions with atoms. , 70:1–107, April 1981. doi: 10.1016/0370-1573(81)90161-7.

R. K. Janev and H. Winter. State-selective electron capture in atom-highly charged ion collisions. , 117:265–387, January 1985. doi: 10.1016/0370-1573(85)90118-8.

R. K. Janev, D. S. Belić, and B. H. Bransden. Total and partial cross sections for electron capture in collisions of hydrogen atoms with fully stripped ions. *Phys. Rev. A*, 28:1293–1302, Sep 1983. doi: 10.1103/PhysRevA.28.1293.

R. K. Janev, L. P. Presnyakov, and V. P. Shevelko. *Physics of highly charged ions*. 1985.

F. Jansen, D. Lumb, B. Altieri, J. Clavel, M. Ehle, C. Erd, C. Gabriel, M. Guainazzi, P. Gondoin, R. Much, R. Munoz, M. Santos, N. Schartel, D. Texier, and G. Vacanti. XMM-Newton observatory. I. The spacecraft and operations. , 365:L1–L6, January 2001. doi: 10.1051/0004-6361:20000036.

W. R. Johnson and G. Soff. The Lamb Shift in Hydrogen-like Atoms, 1 = Z = 110. *Atomic Data and Nuclear Data Tables*, 33:405, 1985. doi: 10.1016/0092-640X(85)90010-5.

J. S. Kaastra, R. Mewe, and H. Nieuwenhuijzen. SPEX: a new code for spectral analysis of X UV spectra. In K. Yamashita and T. Watanabe, editors, *UV and X-ray Spectroscopy of Astrophysical and Laboratory Plasmas*, pages 411–414, 1996.

E. Kallne, J. Kallne, A. Dalgarno, E. S. Marmar, J. E. Rice, and A. K. Pradhan. Observations of the recombination population of n=2 excited states of Ar^{16+} in tokamak plasmas. *Physical Review Letters*, 52:2245–2248, June 1984. doi: 10.1103/PhysRevLett.52.2245.

S. Katsuda, H. Tsunemi, K. Mori, H. Uchida, H. Kosugi, M. Kimura, H. Nakajima, S. Takakura, R. Petre, J. W. Hewitt, and H. Yamaguchi. Possible Charge-exchange X-ray Emission in the Cygnus Loop Detected with Suzaku. , 730:24, March 2011. doi: 10.1088/0004-637X/730/1/24.

R. L. Kelley, K. Mitsuda, C. A. Allen, P. Arsenovic, M. D. Audley, T. G. Bialas, K. R. Boyce, R. F. Boyle, S. R. Breon, G. V. Brown, J. Cottam, M. J. Dipirro, R. Fujimoto, T. Furusho, K. C. Gendreau, G. G. Gochar, O. Gonzalez, M. Hirabayashi, S. S. Holt, H. Inoue, M. Ishida, Y. Ishisaki, C. S. Jones, R. Keski-Kuha, C. A. Kilbourne, D. McCammon, U. Morita, S. H. Moseley, B. Mott, K. Narasaki, Y. Ogawara, T. Ohashi, N. Ota, J. S. Panek, F. S. Porter, A. Serlemitsos, P. J. Shirron, G. A. Sneiderman, A. E. Szymkowiak, Y. Takei, J. L. Tveekrem, S. M. Volz, M. Yamamoto, and N. Y. Yamasaki. The Suzaku High Resolution X-Ray Spectrometer. , 59:77–112, January 2007. doi: 10.1093/pasj/59.sp1.S77.

C. A. Kilbourne, W. B. Doriese, S. R. Bandler, R. P. Brekosky, A.-D. Brown, J. A. Chervenak, M. E. Eckart, F. M. Finkbeiner, G. C. Hilton, K. D. Irwin, N. Iyomoto, R. L. Kelley, F. S. Porter, C. D. Reintsema, S. J. Smith, and J. N. Ullom. Multiplexed readout of uniform arrays of TES x-ray microcalorimeters suitable for Constellation-X. In *Space Telescopes and Instrumentation 2008: Ultraviolet to Gamma Ray*, volume 7011 of , page 701104, July 2008. doi: 10.1117/12.790027.

E. Kirsch, S. McKenna-Lawlor, A. Thompson, D. O'Sullivan, and F. M. Neubauer. Detection of energetic electron (E greater than KeV) and ion fluxes (E greater than 97 KeV) from comet P/Halley by the Giotto experiment EPA on 1986 March 13/14. , 193:303–308, March 1988.

D. Koutroumpa, F. Acero, R. Lallement, J. Ballet, and V. Kharchenko. OVII and OVIII line emission in the diffuse soft X-ray background: heliospheric and galactic contributions. , 475:901–914, December 2007. doi: 10.1051/0004-6361:20078271.

D. Koutroumpa, R. Lallement, V. Kharchenko, and A. Dalgarno. The Solar Wind Charge-eXchange Contribution to the Local Soft X-ray Background. Model to Data Comparison in the 0.1-1.0 keV Band. , 143:217–230, March 2009a. doi: 10.1007/s11214-008-9381-9.

D. Koutroumpa, R. Lallement, J. C. Raymond, and V. Kharchenko. The Solar Wind Charge-Transfer X-Ray Emission in the 1/4 keV Energy Range: Inferences on Local Bubble Hot Gas at Low Z. , 696:1517–1525, May 2009b. doi: 10.1088/0004-637X/696/2/1517.

K. Koyama, Y. Maeda, T. Sonobe, T. Takeshima, Y. Tanaka, and S. Yamauchi. ASCA View of Our Galactic Center: Remains of Past Activities in X-Rays? , 48: 249–255, April 1996. doi: 10.1093/pasj/48.2.249.

D. Krankowsky, P. Lammerzahl, I. Herrwerth, J. Woweries, P. Eberhardt, U. Dolder, U. Herrmann, W. Schulte, J. J. Berthelier, J. M. Illiano, R. R. Hodges, and J. H. Hoffman. In situ gas and ion measurements at comet Halley. , 321:326–329, May 1986. doi: 10.1038/321326a0.

V. A. Krasnopolsky, M. J. Mumma, and M. J. Abbott. EUVE Search for X-rays from Comets Encke, Mueller (C/1993 A1), Borrelly, and Postperihelion Hale-Bopp. , 146:152–160, July 2000. doi: 10.1006/icar.2000.6387.

V. A. Krasnopolsky, J. B. Greenwood, and P. C. Stancil. X-Ray and extreme ultraviolet emissions from comets. , 113:271–374, August 2004. doi: 10.1023/B:SPAC.0000046754.75560.80.

Vladimir Krasnopolsky. On the nature of soft x-ray radiation in comets. *Icarus*, 128(2):368 – 385, 1997. ISSN 0019-1035. doi: http://dx.doi.org/10.1006/icar.1997.5722. URL http://www.sciencedirect.com/science/article/pii/S0019103597957225.

NASA Jet Propulsion Lab. How comet hyakutake b2 was discovered, 1996. URL https://www2.jpl.nasa.gov/comet/hyakutake/disc2.html. [Online; accessed 29-April-2017.

R. Lallement. The heliospheric soft X-ray emission pattern during the ROSAT survey: Inferences on Local Bubble hot gas. , 418:143–150, April 2004a. doi: 10.1051/0004-6361:20040059.

R. Lallement. On the contribution of charge-exchange induced X-ray emission in the ISM and ICM. , 422:391–400, August 2004b. doi: 10.1051/0004-6361:20035625.

L. D. Landau. To the theory of energy transmission in collissions. II. *Phys. Zs. Sowjet., 2, p. 46, 1932 (English and German)*, 2:46, December 1932.

M. A. Leutenegger, P. Beiersdorfer, G. V. Brown, R. L. Kelley, C. A. Kilbourne, and F. S. Porter. Measurement of Anomalously Strong Emission from the 1s-9p Transition in the Spectrum of H-Like Phosphorus Following Charge Exchange with Molecular Hydrogen. *Physical Review Letters*, 105(6):063201, August 2010. doi: 10.1103/PhysRevLett.105.063201.

M. A. Leutenegger, G. L. Betancourt-Martinez, P. Beiersdorfer, G. V. Brown, R. L. Kelley, C. A. Kilbourne, and F. S. Porter. Charge exchange measurements with an x-ray calorimeter at an electron beam ion trap. *Physica Scripta Volume T*, 156(1):014006, September 2013. doi: 10.1088/0031-8949/2013/T156/014006.

M. A. Leutenegger, P. Beiersdorfer, G. L. Betancourt-Martinez, G. V. Brown, N. Hell, R. L. Kelley, C. A. Kilbourne, E. W. Magee, and F. S. Porter. Characterization of an atomic hydrogen source for charge exchange experiments. *Review of Scientific Instruments*, 87(11):11E516, November 2016. doi: 10.1063/1.4959919.

M. A. Levine, R. E. Marrs, C. L. Bennett, J. R. Henderson, D. A. Knapp, and M. B. Schneider. EBIT: Electron beam ion trap. In *American Institute of Physics Conference Series*, volume 188 of *American Institute of Physics Conference Series*, pages 82–101, June 1989. doi: 10.1063/1.38389.

W. Lichten. Resonant Charge Exchange in Atomic Collisions. *Physical Review*, 131: 229–238, July 1963. doi: 10.1103/PhysRev.131.229.

C. M. Lisse, K. Dennerl, J. Englhauser, M. Harden, F. E. Marshall, M. J. Mumma, R. Petre, J. P. Pye, M. J. Ricketts, J. Schmitt, J. Trumper, and R. G. West. Discovery of X-ray and Extreme Ultraviolet Emission from Comet C/Hyakutake 1996 B2. *Science*, 274:205–209, October 1996. doi: 10.1126/science.274.5285.205.

C. M. Lisse, D. Christian, K. Dennerl, J. Englhauser, J. Trümper, M. Desch, F. E. Marshall, R. Petre, and S. Snowden. X-Ray and Extreme Ultraviolet Emission from Comet P/Encke 1997. , 141:316–330, October 1999. doi: 10.1006/icar.1999.6176.

J. Liu, Q. D. Wang, Z. Li, and J. R. Peterson. X-ray spectroscopy of the hot gas in the M31 bulge. , 404:1879–1885, June 2010. doi: 10.1111/j.1365-2966.2010.16404.x.

G. Lubinski, Z. Juhász, R. Morgenstern, and R. Hoekstra. State-selective electron-capture cross section measurements for low-energy collisions of He-like ions on H_2. *Journal of Physics B Atomic Molecular Physics*, 33:5275–5296, December 2000. doi: 10.1088/0953-4075/33/23/302.

G. Lubinski, Z. Juhász, R. Morgenstern, and R. Hoekstra. Low-Energy State-Selective Charge Transfer by Multiply Charged Ions. *Physical Review Letters*, 86:616–619, January 2001. doi: 10.1103/PhysRevLett.86.616.

I. Mančev, N. Milojević, and D. Belkić. Electron correlations in single-electron capture into any state of fast projectiles from heliumlike atomic systems. , 88(5): 052706, November 2013. doi: 10.1103/PhysRevA.88.052706.

R. J. Mawhorter, A. Chutjian, T. E. Cravens, N. Djurić, S. Hossain, C. M. Lisse, J. A. Macaskill, S. J. Smith, J. Simcic, and I. D. Williams. Absolute single and multiple charge exchange cross sections for highly charged C, O, and Ne ions on H_2O , CO, and CO_2. , 75(3):032704, March 2007. doi: 10.1103/PhysRevA.75.032704.

R. Mewe. Atomic Physics of Hot Plasmas. In J. van Paradijs and J. A. M. Bleeker, editors, *X-Ray Spectroscopy in Astrophysics*, volume 520 of *Lecture*

Notes in Physics, Berlin Springer Verlag, page 109, 1999. doi: 10.1007/978-3-540-49199-6_2.

K. M. Morgan. *Transition-edge sensor microcalorimeters for a diffuse soft X-ray sounding rocket mission*. PhD thesis, The University of Wisconsin - Madison, 2015.

S. H. Moseley, J. C. Mather, and D. McCammon. Thermal detectors as x-ray spectrometers. *Journal of Applied Physics*, 56:1257–1262, September 1984. doi: 10.1063/1.334129.

P. D. Mullen, R. S. Cumbee, D. Lyons, and P. C. Stancil. Charge Exchange-induced X-Ray Emission of Fe xxv and Fe xxvI via a Streamlined Model. , 224:31, June 2016. doi: 10.3847/0067-0049/224/2/31.

M. P. Muno, J. S. Arabadjis, F. K. Baganoff, M. W. Bautz, W. N. Brandt, P. S. Broos, E. D. Feigelson, G. P. Garmire, M. R. Morris, and G. R. Ricker. The Spectra and Variability of X-Ray Sources in a Deep Chandra Observation of the Galactic Center. , 613:1179–1201, October 2004. doi: 10.1086/423164.

A Niehaus. A classical model for multiple-electron capture in slow collisions of highly charged ions with atoms. *Journal of Physics B: Atomic and Molecular Physics*, 19(18):2925, 1986.

T. G. Northrop, C. M. Lisse, M. J. Mumma, and M. D. Desch. A Possible Source of the X-Rays from Comet Hyakutake. , 127:246–250, May 1997. doi: 10.1006/icar.1997.5694.

R. E. Olson and A. Salop. Charge-transfer and impact-ionization cross sections for fully and partially stripped positive ions colliding with atomic hydrogen. *Phys. Rev. A*, 16:531–541, Aug 1977. doi: 10.1103/PhysRevA.16.531.

R. E. Olson, F. T. Smith, and E. Bauer. Estimation of the coupling matrix elements for one-electron transfer systems. , 10:1848–1855, August 1971. doi: 10.1364/AO.10.001848.

Ronald Olson. *Classical Trajectory and Monte Carlo Techniques*, pages 869–874. Springer New York, New York, NY, 2006. ISBN 978-0-387-26308-3. doi: 10.1007/978-0-387-26308-3_58. URL http://dx.doi.org/10.1007/978-0-387-26308-3_58.

S Otranto and R E Olson. State-selective charge exchange from h(1s), h(n = 2), li and na targets by very highly charged ions. *Journal of Physics B: Atomic, Molecular and Optical Physics*, 43(14):144004, 2010. URL http://stacks.iop.org/0953-4075/43/i=14/a=144004.

S. Otranto and R. E. Olson. State-selective charge exchange from H(1s), H(n = 2), Li and Na targets by very highly charged ions. *Journal of Physics B Atomic*

Molecular Physics, 43(14):144004, July 2010. doi: 10.1088/0953-4075/43/14/144004.

S. Otranto, R. E. Olson, and P. Beiersdorfer. X-ray emission cross sections following charge exchange by multiply charged ions of astrophysical interest. , 73(2):022723, February 2006. doi: 10.1103/PhysRevA.73.022723.

S Otranto, R E Olson, and P Beiersdorfer. X-ray emission cross sections following charge exchange by multiply charged ions of astrophysical interest. *Journal of Physics: Conference Series*, 58(1):165, 2007.

P. Peille, M. T. Ceballos, B. Cobo, J. Wilms, S. Bandler, S. J. Smith, T. Dauser, T. Brand, R. den Hartog, J. de Plaa, D. Barret, J.-W. den Herder, L. Piro, X. Barcons, and E. Pointecouteau. Performance assessment of different pulse reconstruction algorithms for the ATHENA X-ray Integral Field Unit. In *Space Telescopes and Instrumentation 2016: Ultraviolet to Gamma Ray*, volume 9905 of , page 99055W, July 2016. doi: 10.1117/12.2232011.

U. Peretz, E. Behar, and S. A. Drake. Coronae of stars with supersolar elemental abundances. , 577:A93, May 2015. doi: 10.1051/0004-6361/201424769.

K. J. H. Phillips, B. C. Fawcett, B. J. Kent, A. H. Gabriel, J. W. Leibacher, C. J. Wolfson, L. W. Acton, J. H. Parkinson, J. L. Culhane, and H. E. Mason. Solar flare X-ray spectra from the Solar Maximum Mission Flat Crystal Spectrometer. , 256:774–787, May 1982. doi: 10.1086/159950.

A. M. T. Pollock. A new paradigm for the X-ray emission of O stars from XMM-Newton observations of the O9.7 supergiant ζ Orionis. , 463:1111–1123, March 2007. doi: 10.1051/0004-6361:20053838.

F. S. Porter, M. D. Audley, P. Beiersdorfer, K. R. Boyce, R. P. Brekosky, G. V. Brown, K. C. Gendreau, J. D. Gygax, S. M. Kahn, R. L. Kelley, C. K. Stahle, and A. E. Szymkowiak. Laboratory astrophysics using a spare XRS microcalorimeter. In K. A. Flanagan and O. H. Siegmund, editors, *X-Ray and Gamma-Ray Instrumentation for Astronomy XI*, volume 4140 of , pages 407–418, December 2000. doi: 10.1117/12.409137.

F. S. Porter, G. V. Brown, K. R. Boyce, R. L. Kelley, C. A. Kilbourne, P. Beiersdorfer, H. Chen, S. Terracol, S. M. Kahn, and A. E. Szymkowiak. The Astro-E2 X-ray spectrometer/EBIT microcalorimeter x-ray spectrometer. *Review of Scientific Instruments*, 75:3772–3774, October 2004. doi: 10.1063/1.1781758.

F. S. Porter, R. L. Kelley, and C. A. Kilbourne. High resolution X-ray microcalorimeters. *Nuclear Instruments and Methods in Physics Research A*, 559:436–438, April 2006. doi: 10.1016/j.nima.2005.12.030.

F. S. Porter, B. R. Beck, P. Beiersdorfer, K. R. Boyce, G. V. Brown, H. Chen, J. Gygax, S. M. Kahn, R. L. Kelley, C. A. Kilbourne, E. Magee, and D. B.

Thorn. The XRS microcalorimeter spectrometer at the Livermore electron beam ion trap. *Canadian Journal of Physics*, 86:231–240, 2008a. doi: 10.1139/P07-147.

F. S. Porter, P. Beiersdorfer, G. V. Brown, W. Doriese, J. Gygax, R. L. Kelley, C. A. Kilbourne, J. King, K. Irwin, C. Reintsema, and J. Ullom. The EBIT Calorimeter Spectrometer: A New, Permanent User Facility at the LLNL EBIT. *Journal of Low Temperature Physics*, 151:1061–1066, May 2008b. doi: 10.1007/s10909-008-9788-4.

F. S. Porter, J. S. Adams, G. V. Brown, J. A. Chervenak, M. P. Chiao, R. Fujimoto, Y. Ishisaki, R. L. Kelley, C. A. Kilbourne, D. McCammon, K. Mitsuda, T. Ohashi, A. E. Szymkowiak, Y. Takei, M. Tashiro, and N. Yamasaki. The detector subsystem for the SXS instrument on the ASTRO-H Observatory. In *Space Telescopes and Instrumentation 2010: Ultraviolet to Gamma Ray*, volume 7732 of , page 77323J, July 2010. doi: 10.1117/12.857888.

P. Ranalli, A. Comastri, L. Origlia, and R. Maiolino. A deep X-ray observation of M82 with XMM-Newton. , 386:1464–1480, May 2008. doi: 10.1111/j.1365-2966.2008.13128.x.

J. E. Rice, E. S. Marmar, J. L. Terry, E. Kaline, and J. Kaline. Observation of charge-transfer population of high-n levels in Ar(16+) from neutral hydrogen in the ground and excited states in a tokamak plasma. *Physical Review Letters*, 56:50–53, January 1986. doi: 10.1103/PhysRevLett.56.50.

S. R. Roberts and Q. D. Wang. X-ray emission from charge exchange in the Cygnus Loop SNR. , 449:1340–1346, May 2015. doi: 10.1093/mnras/stv319.

I. P. Robertson, K. D. Kuntz, M. R. Collier, T. E. Cravens, and S. L. Snowden. The Heliospheric Contribution to the Soft X-ray Background Emission. In R. K. Smith, S. L. Snowden, and K. D. Kuntz, editors, *American Institute of Physics Conference Series*, volume 1156 of *American Institute of Physics Conference Series*, pages 52–61, August 2009. doi: 10.1063/1.3211834.

D. W. Rule and K. Omidvar. Charge equilibrium and radiation of low-energy cosmic rays passing through interstellar medium. , 229:1198–1210, May 1979. doi: 10.1086/157054.

H. Ryufuku and T. Watanabe. Total and partial cross sections for charge transfer in collisions of multicharged ions with atomic hydrogen. , 20:1828–1837, November 1979. doi: 10.1103/PhysRevA.20.1828.

Hiroshi Ryufuku, Ken Sasaki, and Tsutomu Watanabe. Oscillatory behavior of charge transfer cross sections as a function of the charge of projectiles in low-energy collisions. *Phys. Rev. A*, 21:745–750, Mar 1980. doi: 10.1103/PhysRevA.21.745.

E. B. Saloman, J. H. Hubbell, and J. H. Scofield. X-Ray Attenuation Cross Sections for Energies 100 eV to 100 keV and Elements Z = 1 to Z = 92. *Atomic Data and Nuclear Data Tables*, 38:1, 1988. doi: 10.1016/0092-640X(88)90044-7.

A. Salop and R. E. Olson. Charge exchange between H(1s) and fully stripped heavy ions at low-keV impact energies. , 13:1312–1320, April 1976. doi: 10.1103/PhysRevA.13.1312.

W. T. Sanders, W. L. Kraushaar, J. A. Nousek, and P. M. Fried. Soft diffuse X-rays in the southern galactic hemisphere. , 217:L87–L91, October 1977. doi: 10.1086/182545.

D. W. Savin, P. Beiersdorfer, S. M. Kahn, B. R. Beck, G. V. Brown, M. F. Gu, D. A. Liedahl, and J. H. Scofield. Simulating a Maxwellian plasma using an electron beam ion trap. *Review of Scientific Instruments*, 71:3362–3372, September 2000. doi: 10.1063/1.1287045.

N. A. Schwadron and T. E. Cravens. Implications of Solar Wind Composition for Cometary X-Rays. , 544:558–566, November 2000. doi: 10.1086/317176.

P. J. Serlemitsos, E. A. Boldt, S. S. Holt, R. Ramaty, and A. F. Brisken. X-Ray Spectrum of Cassiopeia a: Evidence for Iron Line Emission. , 184:L1, August 1973. doi: 10.1086/181275.

C. Shah, S. Dobrodey, S. Bernitt, R. Steinbrügge, J. R. Crespo López-Urrutia, L. Gu, and J. Kaastra. Laboratory Measurements Compellingly Support a Charge-exchange Mechanism for the Dark Matter ˜3.5 keV X-Ray Line. , 833:52, December 2016. doi: 10.3847/1538-4357/833/1/52.

N. Shimakura, S. Suzuki, and M. Kimura. Molecular treatment of electron capture in collisions of O^{5+} ions with H atoms at energies from 6 eV/amu to 10 keV/amu: Transfer-excitation processes. , 48:3652–3662, November 1993. doi: 10.1103/PhysRevA.48.3652.

J. Simcic, D. R. Schultz, R. J. Mawhorter, I. Čadež, J. B. Greenwood, A. Chutjian, C. M. Lisse, and S. J. Smith. Measurement and calculation of absolute single- and multiple-charge-exchange cross sections for Fe^{q+} ions impacting CO and CO_2. , 81(6):062715, June 2010. doi: 10.1103/PhysRevA.81.062715.

T. G. Slanger, T. E. Cravens, J. Crovisier, S. Miller, and D. F. Strobel. Photoemission Phenomena in the Solar System. , 139:267–310, August 2008. doi: 10.1007/s11214-008-9387-3.

R. K. Smith, R. J. Edgar, P. P. Plucinsky, B. J. Wargelin, P. E. Freeman, and B. A. Biller. Chandra Observations of MBM 12 and Models of the Local Bubble. , 623:225–234, April 2005. doi: 10.1086/428568.

R. K. Smith, A. R. Foster, R. J. Edgar, and N. S. Brickhouse. Resolving the Origin of the Diffuse Soft X-Ray Background. , 787:77, May 2014a. doi: 10.1088/0004-637X/787/1/77.

R. K. Smith, H. Odaka, M. Audard, G. V. Brown, M. E. Eckart, Y. Ezoe, A. Foster, M. Galeazzi, K. Hamaguchi, K. Ishibashi, K. Ishikawa, J. Kaastra, S. Katsuda, M. Leutenegger, E. Miller, I. Mitsuishi, H. Nakajima, T. Ogawa, F. Paerels, F. S. Porter, K. Sakai, M. Sawada, Y. Takei, Y. Tanaka, Y. Tsuboi, H. Uchida, E. Ursino, S. Watanabe, H. Yamaguchi, N. Yamasaki, and for the ASTRO-H Science Working Group. ASTRO-H White Paper - New Spectral Features. *ArXiv e-prints*, December 2014b.

S. J. Smith, J. S. Adams, S. R. Bandler, G. L. Betancourt-Martinez, J. A. Chervenak, M. E. Eckart, F. M. Finkbeiner, R. L. Kelley, C. A. Kilbourne, F. S. Porter, J. E. Sadleir, and E. J. Wassell. Uniformity of kilo-pixel arrays of transition-edge sensor microcalorimeters for x-ray astronomy applications. Submitted to IEEE Transactions in Applied Superconductivity, 2014c.

S. L. Snowden, D. P. Cox, D. McCammon, and W. T. Sanders. A model for the distribution of material generating the soft X-ray background. , 354:211–219, May 1990. doi: 10.1086/168680.

S. L. Snowden, D. McCammon, D. N. Burrows, and J. A. Mendenhall. Analysis procedures for ROSAT XRT/PSPC observations of extended objects and the diffuse background. , 424:714–728, April 1994. doi: 10.1086/173925.

S. L. Snowden, M. R. Collier, and K. D. Kuntz. XMM-Newton Observation of Solar Wind Charge Exchange Emission. , 610:1182–1190, August 2004. doi: 10.1086/421841.

K. Soejima, C. J. Latimer, K. Okuno, N. Kobayashi, and Y. Kaneko. Cross sections for single and multiple electron capture in low energy collisions of C^{4+} with H_2 O_2 and N_2. *Journal of Physics B Atomic Molecular Physics*, 25:3009–3014, July 1992. doi: 10.1088/0953-4075/25/13/009.

C. K. Stahle, R. P. Brekosky, S. B. Dutta, K. C. Gendreau, R. L. Kelley, D. McCammon, R. A. McClanahan, S. H. Moseley, D. B. Mott, F. S. Porter, and A. E. Szymkowiak. The physics and the optimization of the XRS calorimeters on Astro-E. *Nuclear Instruments and Methods in Physics Research A*, 436:218–225, October 1999. doi: 10.1016/S0168-9002(99)00624-5.

P. C. Stancil, J. G. Wang, M. J. Rakovic, D. R. Schultz, and R. Ali. Charge Transfer Data Needs for Cometary X-ray Emission Modeling. In D. R. Schultz, P. S. Krstic, and F. Ownby, editors, *Atomic and Molecular Data and Their Applications*, volume 636 of *American Institute of Physics Conference Series*, pages 144–153, October 2002. doi: 10.1063/1.1516331.

G. Steigman. Charge transfer reactions in multiply charged ion-atom collisions. , 199:642–646, August 1975. doi: 10.1086/153732.

Th. Stöhlker, T. Ludziejewski, H. Reich, F. Bosch, R. W. Dunford, J. Eichler, B. Franzke, C. Kozhuharov, G. Menzel, P. H. Mokler, F. Nolden, P. Rymuza, Z. Stachura, M. Steck, P. Swiat, A. Warczak, and T. Winkler. Charge-exchange cross sections and beam lifetimes for stored and decelerated bare uranium ions. *Phys. Rev. A*, 58:2043–2050, Sep 1998. doi: 10.1103/PhysRevA.58.2043.

A. E. Szymkowiak, R. L. Kelley, S. H. Moseley, and C. K. Stahle. Signal processing for microcalorimeters. *Journal of Low Temperature Physics*, 93:281–285, November 1993. doi: 10.1007/BF00693433.

T. Takahashi, M. Kokubun, K. Mitsuda, R. Kelley, T. Ohashi, F. Aharonian, H. Akamatsu, F. Akimoto, S. Allen, N. Anabuki, and et al. The ASTRO-H (Hitomi) x-ray astronomy satellite. In *Space Telescopes and Instrumentation 2016: Ultraviolet to Gamma Ray*, volume 9905 of , page 99050U, July 2016. doi: 10.1117/12.2232379.

Y. Tanaka. ASCA observation of X-ray emission from the Galactic ridge. , 382: 1052–1060, February 2002. doi: 10.1051/0004-6361:20011678.

Y. Tanaka, T. Miyaji, and G. Hasinger. Origin of the Galactic ridge X-ray emission. *Astronomische Nachrichten*, 320:181, 1999.

K Taulbjerg. Reaction windows for electron capture by highly charged ions. *Journal of Physics B: Atomic and Molecular Physics*, 19(10):L367, 1986. URL http://stacks.iop.org/0022-3700/19/i=10/a=007.

H. Tawara, P. Richard, U. I. Safronova, A. A. Vasilyev, S. Hansen, and A. S. Shlyaptseva. L x rays from low-energy (˜2-keV/u) ions with L-shell vacancies produced in single collisions with atoms and molecules. , 65(4):042509, April 2002. doi: 10.1103/PhysRevA.65.042509.

H. Tawara, E. Takács, L. P. Ratliff, J. D. Gillaspy, and K. Tőkési. Cascade transition X-rays from electron capture into highly charged ions in collisions with neutral gas targets. *Nuclear Instruments and Methods in Physics Research B*, 205:605–609, May 2003. doi: 10.1016/S0168-583X(03)00949-2.

H. Tawara, E. Takács, T. Suta, K. Makónyi, L. P. Ratliff, and J. D. Gillaspy. K x rays produced in collisions of bare ions with atoms: Contribution of multiple-electron transfer in Kr^{36+} , Ar^{18+} , and Ne^{10+} +Ar collisions. , 73(1):012704, January 2006. doi: 10.1103/PhysRevA.73.012704.

Sky Telescope. How yuji hyakutake found his comet, 2004. URL http://www.skyandtelescope.com/observing/celestial-objects-to-watch/how-yuji-hyakutake-found-his-comet/. [Online; accessed 25-June-2013].

D. B. Thorn, M. F. Gu, G. V. Brown, P. Beiersdorfer, F. S. Porter, C. A. Kilbourne, and R. L. Kelley. Precision Measurement of the K-Shell Spectrum from Highly Charged Xenon with an Array of X-Ray Calorimeters. *Physical Review Letters*, 103(16):163001, October 2009. doi: 10.1103/PhysRevLett.103.163001.

Los Angeles Times. Obituaries: Yuji hyakutake, 51; amateur discovered giant comet, 2002. URL http://articles.latimes.com/2002/apr/14/local/me-yuji14. [Online; accessed 29-April-2017].

T. G. Tsuru, M. Ozawa, Y. Hyodo, H. Matsumoto, K. Koyama, H. Awaki, R. Fujimoto, R. Griffiths, C. Kilbourne, K. Matsushita, K. Mitsuda, A. Ptak, P. Ranalli, and N. Y. Yamasaki. X-Ray Spectral Study of the Extended Emission, 'the Cap', Located 11.6kpc above the Disk of M82. , 59:269–282, January 2007. doi: 10.1093/pasj/59.sp1.S269.

R. von Steiger, N. A. Schwadron, L. A. Fisk, J. Geiss, G. Gloeckler, S. Hefti, B. Wilken, R. F. Wimmer-Schweingruber, and T. H. Zurbuchen. Composition of quasi-stationary solar wind flows from Ulysses/Solar Wind Ion Composition Spectrometer. , 105:27217–27238, December 2000. doi: 10.1029/1999JA000358.

S. A. Walker, P. Kosec, A. C. Fabian, and J. S. Sanders. X-ray analysis of filaments in galaxy clusters. , 453:2480–2489, November 2015. doi: 10.1093/mnras/stv1829.

B. J. Wargelin, M. Markevitch, M. Juda, V. Kharchenko, R. Edgar, and A. Dalgarno. Chandra Observations of the "Dark" Moon and Geocoronal Solar Wind Charge Transfer. , 607:596–610, June 2004. doi: 10.1086/383410.

B. J. Wargelin, P. Beiersdorfer, P. A. Neill, R. E. Olson, and J. H. Scofield. Charge-Exchange Spectra of Hydrogenic and He-like Iron. , 634:687–697, November 2005. doi: 10.1086/496874.

B. J. Wargelin, P. Beiersdorfer, and G. V. Brown. EBIT charge-exchange measurements and astrophysical applications. *Canadian Journal of Physics*, 86:151–169, 2008. doi: 10.1139/P07-125.

R. Wegmann, H. U. Schmidt, C. M. Lisse, K. Dennerl, and J. Englhauser. X-rays from comets generated by energetic solar wind particles. , 46:603–612, May 1998. doi: 10.1016/S0032-0633(97)00196-7.

M. C. Weisskopf. The Chandra X-Ray Observatory (CXO): An Overview. *ArXiv Astrophysics e-prints*, December 1999.

B. Y. Welsh and R. Lallement. Highly ionized gas in the local ISM: Some like it hot? , 436:615–632, June 2005. doi: 10.1051/0004-6361:20042611.

M. W. Wise and C. L. Sarazin. Charge transfer and X-ray emission from supernova remnants. , 345:384–392, October 1989. doi: 10.1086/167913.

D. M. Worrall, F. E. Marshall, E. A. Boldt, and J. H. Swank. HEAO 1 measurements of the galactic ridge. , 255:111–121, April 1982. doi: 10.1086/159809.

Y. Wu, P. C. Stancil, H. P. Liebermann, P. Funke, S. N. Rai, R. J. Buenker, D. R. Schultz, Y. Hui, I. N. Draganic, and C. C. Havener. Theoretical investigation of charge transfer between N^{6+} and atomic hydrogen. , 84(2):022711, August 2011. doi: 10.1103/PhysRevA.84.022711.

Y. Wu, P. C. Stancil, D. R. Schultz, Y. Hui, H. P. Liebermann, and R. J. Buenker. Theoretical investigation of total and state-dependent charge exchange in O^{6+} collisions with atomic hydrogen. *Journal of Physics B Atomic Molecular Physics*, 45(23):235201, December 2012. doi: 10.1088/0953-4075/45/23/235201.

C. Zener. Non-Adiabatic Crossing of Energy Levels. *Proceedings of the Royal Society of London Series A*, 137:696–702, September 1932. doi: 10.1098/rspa.1932.0165.